Surface water sensitivity to climate variability

Homero A. Paltán-López

School of Geography and the Environment, University of Oxford

Thesis presented for the degree of Doctor of Philosophy at the University of Oxford
College: Christ Church

Oxford, September 2018

"All models are wrong,
but some are useful"

- George E. Box

"Water is the driving force of nature"

- Leonardo Da Vinci

Acknowledgments

This DPhil is the result of four years of personal and professional growth and realizations. This would not have been possible without all the amazing people that accompanied me during the challenges I had to face and helped me to develop my potential. First, and foremost, I would like to thank my supervisor, Professor Simon Dadson whose guidance, passion for these fields, and constant remind to "roll up my sleeves" is leading me to fulfill this step. I would also like to specially thank Dr. Duane Waliser, not just for hosting me at NASA's Jet Propulsion Laboratory and collaborate in Chapter 5, but particularly for his personal support and advices during these last years. Great thanks also to Professor David Grey for sharing his experiences and views in the field which have been truly inspiring. Similarly, thanks to Professor Myles Allen for his suggestions, ideas, and collaboration to develop Chapter 6. Thanks to Dr. Judith Plummer Brackman, at the Cambridge Institute for Sustainability Leadership Cambridge, for her valuable ideas which helped the development of Chapter 7.

I would also like to thank to Dr. Katrina Charles and Dr. Jocelyne Hughes who have permitted me to be teach and be involved in the MSc. in Water Science, Policy and Management for three amazing years. At the same time, many thanks to Dr. Toby Marthews and Dr. Gary Hayman; and Dr. Nicola Gedney at the Center of Ecology and the Environment (CEH) and the Met Office, respectively, for their guidance at the early stages of this DPhil. Also, thanks to my College Advisors during these years Professor Judith Pallot and Dr. Friedderike Otto for their support as well as technical advice.

This would not have been also possible without the amazing people that shared with me these experiences. So, a great thanks to Gonzalo Griebenow, Edoardo Borgomeo, Raghav Pant, and Pablo Astudillo. Also, many thanks to also the amazing SOGE people that were here to enrich this processes: Christie Moore, Aoife Bennet, Alice Chautard, Karsten Haustein, Jaeyoung Lee, Filipa Soares, Sisi Hu, Xavi Liao, Mike Simpon, Scott Thacker, Nico Raab, Wee-Ho Lim, Rafa Moreaes, Rachel James, Iliana Cardenes, Anna Hushlak,

Negar Behzadi, Franziska Gaupp, Sarah O'Keefe, Dina Hestad, John Mittermeir, Micol Chiesa, Johanna Köhler, Sarah O'Keefe.

Thanks also to the Oxford Latin-crew for the great memories: Luis Vargas, Alejandro Espinosa, Juan Neves, Gustavito Quino, Santiago Izquierdo, Rodrigo Mendoza, Daniel Cuty, Nico Lipollis, Nico López. Also, thanks to Mike De Florio, Vicky Espinosa and Bin Guan at JPL who greatly supported me during my time there.

Finally, my thanks go to my dad, mum, brother, and aunts as they have been my inner motivation and inspiration to move forward. Also, thanks to Vero Otero and Luis Morales, as they are my family support in Europe for various years. Thanks to my friends in Ecuador who have also been part of this experience: Ernesto Carvajal, Bola García, Nico Fernández; Valeria Rivera, Caro Sampedro (Bola), Fernando Pavón, Pancho Moscoso, Pancho Montalvo, Juan Pinto. Equally, thanks to my friends in the U.K., Ignacio de Haedo and Grigoris Vasilopoulos for their support. Last, but not least, a very special thanks to Zazi for her unique and lovely support, company, conversations, and inspiration.

Publications and Outputs

The study cases presented in this thesis (Chapter 4 to 7) have been published or submitted to the following peer-reviewed journals:

- **Paltan H.,** Essery R., & Dadson, S. "*Snowmelt, runoff generation and river flow: Examining snowpack representations in a Land Surface Model.".* Re-Submitted to Journal of Hydrological Processes. (2018) – Chapter 4

- **Paltan, H.,** Waliser, D., Lim, W. H., Guan, B., Yamazaki, D., Pant, R., & Dadson, S. (2017). "*Global floods and water availability driven by atmospheric rivers."* Geophysical Research Letters, 44, 10,387–10,395. https://doi.org/10.1002/2017GL074882 - Chapter 5

- **Paltan H** , Allen M., Haustein K., Fuldauer L., & Dadson S. "*Global Implications of 1.5 °C and 2 °C Warmer Worlds on Extreme River Flows".* Environmental Research Letters, 2018. http://iopscience.iop.org/10.1088/1748-9326/aad985. – Chapter 6

- **Paltan H.,** Plummer J, Pant R, & Dadson S. *Vulnerability of Global Hydropower Potential to the Paris Agreement*. In review: Environmental Research Letters (2019) – Chapter 7

Parts of the introduction and literature review (Chapter 1) presented in this thesis are being used for the following publication (in progress):

- Dadson, S., **Paltan, H.,** Peng J., (forthcoming 2019). Hydroclimatic Risks and Climate Change. In: *Water Science Policy and Management: The Global Challenge*. Chichester: Wiley

The findings published in Chapter 5 are also being considered for the following report:

- Intergovernmental Panel on Climate Change (IPPC), Forthcoming 2018, Global Warming of 1.5 ºC, an IPCC Special report on the impacts of global warming of 1.5 ºC above pre-industrial levels and related global greenhouse gas emission pathways, in the context of strengthening the global response to the threat of climate change, sustainable development, and efforts to eradicate poverty.

Parts of the framework and tools used in this thesis were also used to collaborate in the following peer-reviewed publications:

- Kumary S., Haustein K., Javaid H., Burton C., Allen M., **Paltan H.**, Dadson S., Otto F., *Committed Aerosol Effect substantially increases Flood Risk under 1.5°C and 2.0°C Warming: A case study for Uttarakhand, India*. In review: Geophysical Research Letters

- Haustein K., Sihan L., Otto F., Hirpa F., Dadson S., **Paltan H.,** Khaled M., *A fast-track flood risk assessment*. In preparation: Geophysical Research Letters

The results of Chapter 4 were also featured in the following international media outlets:

- Buis A., NASA Estimates the Global Reach of Atmospheric Rivers, *Jet Propulsion Laboratory,* 31 October 2017. Available at: https://www.nasa.gov/feature/jpl/nasa-estimates-the-global-reach-of-atmospheric-rivers

- Schlanger Z., Invisible "rivers" in our atmosphere cause many droughts and floods here on Earth, *Quartz Magazine*, 4 November 2017. Available at: https://qz.com/1120503/nasa-invisible-rivers-in-our-atmosphere-cause-many-droughts-and-floods-here-on-earth/

- Wille V., So stark beeinflussen Flüsse in der Atmosphäre unser Klima, *Die Welt*, 16 november 2017. Available at: https://www.welt.de/kmpkt/article170636641/So-stark-beeinflussen-Fluesse-in-der-Atmosphaere-unser-Klima.html (In German).

- Nouyrigat V., Les monstres ca chés du climat, *Science and Vie*, March 2018 (p106-110) (In French)

- Redacción Tendendias, Ríos atmosféricos influyen en el globo, *El Comercio,* 12 November 2018. Available at: https://www.elcomercio.com/tendencias/riosatmosfericos-tierra-agua-investigacion-inundaciones.html. (In Spanish).

Abstract

Global water security is known to depend on, among other things, the ability of societies to cope with hydrological risks. While there are several drivers that determine the severity of these risks, climatological mechanisms play an important role in describing their spatial and temporal characteristics. These mechanisms are often described as intra-annual and inter-annual sources of climate variability. Furthermore, anthropogenic climate change is understood to importantly perturb these mechanisms and in turn magnify hydrological risks. As such, understanding the way in which these mechanisms of climate variability influence hydrological processes has become a present and pressing scientific challenge. In particular, while existing methods look to explain the role of climate variability in hydrometeorological variables, namely precipitation and temperature, more research is required to explain how these mechanisms manifest in large-scale land surface hydrological processes and extremes.

The objective of this thesis is to increase our understanding of the way that climate sources of variability influence the spatial and temporal heterogeneity of hydrological flows. This objective is addressed in a systematic way, by first exploring how hydrological flow characteristics are influenced by land surface hydrological processes in areas, with traditional rudimentary runoff representations. Building on this, this thesis secondly analyses the direct link between natural sources of climate variability and land surface hydrological processes and risks at the global scale. Lastly, the repercussions of anthropogenic climate change, in the context of current global climate agreements, in influencing hydrological extremes are explored. By examining the impacts of such extremes on global hydropower availability, a part of the ultimate consequences of hydrological risks on human systems are subsequently explored.

In order to address these aims this thesis proposes a systemic framework that connects climate sources of variability and heterogeneity of flows, by combining various physical sub-models of a Land Surface Model (LSM) and other complementary tools. As such, this framework looks to link climate sources of variability, atmospheric responses, surface hydrological variables, hydrodynamics, hydrological extremes, and societal repercussions. To demonstrate the value of the framework, this thesis presents four case studies in which

specific components and sub-models of this framework are utilized to address the mentioned objectives.

The framework proposed here has helped to unveil and quantify new drivers that control river flows and hydrological risks. This includes explaining the snowpack characteristics that determine timing and magnitude of river flow peaks in snow-dominated regions. Also, by quantifying the inter-annual variability driven by Atmospheric Rivers, this thesis found that this form of moisture transport contributes to 22% of total global annual runoff and their variability importantly drives hydrological extremes in various global locations. Furthermore, by applying this framework, this thesis found that committing to a 1.5ºC level of warming, instead of 2.0ºC, as agreed in Paris in 2015, may importantly decrease high flow occurrences in regions such central Asia or western Europe. Similarly, this thesis found that the intensification of future low flow events, resulted from future climate targets, may lead to important global water losses which in turn would make almost a quarter of current global GHP vulnerable, importantly affecting the energy share in various Asian and Sub-Saharan countries.

Contents

List of Figures

List of Tables

1. Introduction

The goal of achieving water security has been a central aim of societies throughout history. Reducing water's destructive power, while at the same time increasing its beneficial potential, has been not just a key element for economic growth, but also a source of political stability which has formed the foundation for the development of various societies [*Yang et al.*, 2004a; *Mithen*, 2012]. For example, the ability to manage rainfall and river flow fluctuations is known to have allowed the ascent and establishment of cultures such as the Sumerian, along the Tigris and the Euphrates (~5,000 BC), or the Chinese, along the Yellow river. Failure to cope with such risks has also fueled periods of political instability, which in many cases resulted in the collapse of civilizations. A remarkable example is the disintegration of the Mayan political system, which is thought to be a response to extended multi-decadal droughts (~1050 A.D.) which led to reduced agriculture production, famine, diseases and population displacements [*Kennett et al.*, 2012].

At present, the challenge of achieving water security has become more complex due to rapid demographic growth, economic fluctuations, globalization, and climate change [*Rockström et al.*, 2009; *Vörösmarty et al.*, 2010; *Grey et al.*, 2013; *Hoekstra*, 2014]. The current inability to manage variations in water have resulted in systematic crises, which in many cases have global implications. Notably, multiyear droughts and water scarcity are thought to have been important catalysts in creating political instability in Syria and

Yemen, triggering severe international conflicts [*Gleick*, 2014; *Weiss*, 2015]. At the other end of the water risk spectrum, in 2017 alone, flooding resulting from severe weather in the U.S. is thought to have led to economic losses of approximately 200 USD billion [*Halverson*, 2018]. Likewise, weather disasters are known to have caused about 75% of global human displacements during 2016 [*Internal Displacement Monitoring Centre (IDMC)*, 2017; *World Economic Forum*, 2018]. Altogether, this suggests that global sustainable development is still severely undermined by climate and water variability, and in this scenario, developing economies are more vulnerable due to the fact that their activities have a higher dependence on rainfall variability than industrialized ones [*Hall et al.*, 2014; *Bettin and Zazzaro*, 2018].

The challenge of achieving water security thus directly depends on societies' capacity to adapt to hydrological variability and build resilience to risks [*Hall et al.*, 2014]. While institutions and infrastructure are important pillars to cope with such variability, refining our estimations of climate impacts at the catchment scale is also a fundamental step towards water security [*Grey and Sadoff*, 2007]. In particular, being able to quantify the way by which intra-annual and inter-annual mechanisms of climate variability unfold in the land surface is a pressing scientific need to explain hydrological processes and risks. This need is becoming more urgent as human greenhouse emissions are increasingly becoming an additional source of climate variability which impacts in hydrological extremes are more often evident. Consequently, understanding, not just the atmospheric response of natural and anthropogenic sources of hydroclimatic variability, but also tracing their development in the land surface is a scientific challenge with large societal implications.

1.1.1 Dimensions of hydrological variability

While the most common manifestations of hydrological variability are expressed in terms of water risks, their temporal and spatial determinants are not uniform. As such, the drivers of hydrological variability are first described by their intra-annual and inter-annual natural characteristics [*Dettinger and Diaz*, 2000; *Viles and Goudie*, 2003; *McCabe and Palecki*, 2006; *Weisheimer*, 2009]. Intra-annual variability corresponds to hydrological fluctuations dictated by large-scale climatic modes, which may range from short-term inter-annual to longer decadal variations. Examples of these oscillations include El Niño Southern Oscillation, the North Atlantic Oscillation, and the Pacific Decadal Oscillation, among others. The hydrological implications of these modes have traditionally being described at regional scales [*Kenyon and Hegerl*, 2010a].

Next, inter-annual climatic variability corresponds to the seasonal, monthly and daily climatic drivers at the local or catchment level hydrology. At this scale additional large-scale low frequency climatic mechanisms also exert an influence river flow seasonality and extremes. Typical examples of these mechanisms may include the Madden-Julian Oscillation (MJO) and mechanisms of transport of atmospheric moisture from tropics to the extratropics expressed as Low-Level Jets (LLJs) and Atmospheric Rivers (ARs)[*Gimeno et al.*, 2016]. Previous research suggests that these low frequency mechanisms of climate variability have important repercussions in precipitation and other meteorological patterns with important socio-economic impacts in various locations. For instance, *Waliser and Guan*, [2017] found that ARs-associated extreme winds resulted in up to 2 USD billion insurance losses in Europe between 1997 and 2013. Yet, little still is known about possible impact of these mechanisms of climate variability in global hydrology and extremes at the land surface level. As such examining the role of these forms of variability in the surface hydrology remain as a scientific challenge.

Moreover, anthropogenic climate change is known for affecting the means and extremes of precipitation, evapotranspiration rates, and discharge of rivers [*Milly et al.*, 2002; *Hartmann et al.*, 2013; *Alfieri et al.*, 2017]. A first direct influence of the hydrological impacts of anthropogenic climate change is observed in the ongoing recession of glaciers and rising sea levels [*Barnett et al.*, 2005; *Pfeffer*, 2007]. Also, a more intense warming, which increases humidity and water transport, is thought to intensify the hydrological cycle, leading to possibly increase in flood risks [*Held and Soden*, 2006]. Likewise, climate change is also thought to reduce water availability, thus exacerbating hydrological droughts and water scarcity [*Prudhomme et al.*, 2014; *Schewe et al.*, 2014b]. Hence, the need to understand the implications of the anthropogenic influence in the climate is also a pressing scientific need which becomes highly relevant in the context of international political agreements which aim to *control* such influence. For instance, in 2015 at the Conference of the Parties (COP) of the United Nations Framework Convention on Climate Change (UNFCCC), international parties agreed to keep global warming to well below 2 degrees Celsius and to "pursue efforts" to limit warming to 1.5 degrees Celsius. Yet, while the implications of this agreement may lead to profound development and societal changes, little is known about the response of the Earth system to such temperature targets. In particular, there is a lack of understanding of the land surface hydrological response to these two climate thresholds. Consequently, there is still an insufficient understanding of the role that various natural and anthropogenic sources of climate variability play on land surface hydrology.

1.1.2 The necessity to represent hydrological variability.

The scientific challenge to better capture the hydrological implications of the natural and anthropogenic sources of variability, introduced above, requires a comprehensive quantitative knowledge of water, its variability, and its relations to society. Failure to

develop an advanced knowledge and understanding of hydrological systems leads to policy miscommunications, misperceptions and poor decision-making, which in turn aggravates the impacts water-related risks and thus water insecurity [*Di Baldassarre and Uhlenbrook*, 2012; *Grey et al.*, 2013; *Bierkens*, 2015].

However, the necessity for understanding of hydrological variability differs across variables and scales. For example, present and future variability in precipitation, temperature, and surface humidity is thought to be adequately represented [*Ma and Fu*, 2007; *Sakai et al.*, 2009; *Sun et al.*, 2012; *Kummu et al.*, 2014; *Huang et al.*, 2016]. Yet, the capacity to describe runoff and river flows in terms of trends and extremes, and not just average conditions, remains limited [*Dankers and Feyen*, 2009]. Also, at present, the characterization of runoff variability in various areas with strong atmosphere-land surface relationships still remain a challenge. For instance, the adequate quantification of the links between snowmelt-runoff generation and extreme flows remains an important challenge [*Yossef et al.*, 2012; *Sturm*, 2015]. Altogether, these conditions are aggravated when explaining the way in which the diverse natural and anthropogenic mechanisms of climate variability develop in the land surface and describe extreme hydrology. Moreover, since the impacts of more complex economic interdependencies and demographic and climate change are increasingly occurring at a global scale, there is an ongoing necessity to examine hydroclimatic processes at this scale [*Walter and Merritts*, 2008; *Wagener et al.*, 2010; *Blackbourn*, 2011; *Lorenz and Kunstmann*, 2012]..

Nonetheless, the description of the temporal and spatial response of the hydrological surface to global climatic variability is initially constrained by scarce data, or by the questionable quality of the data that would allow for comprehensive assessments. Data availability is originally affected by decline in the global network of hydroclimatic and gauging stations, which complicate the continuous and comprehensive monitoring of

changes in water-related risk characteristics [*Hannah et al.*, 2011; *Fekete et al.*, 2012]. As a response, remote sensing tools and derived products have also been used to fill this gap [*Alsdorf and Lettenmaier*, 2003]. However, using these techniques alone may also be constrained by their temporal limitations, lack of coverage in difficult terrain or cloudy areas, and errors in the sensor or in the techniques used to derive final products [*Nguyen*, 2012; *Döll et al.*, 2016]. In the same way, the measurements observed could also be mixed with numerical models to derive re-analysis products, which may enable the development of a comprehensive change record for atmospheric variables [*Lennart et al.*, 2004; *Decker et al.*, 2011; *Lindsay et al.*, 2014]. Data observed from any of these sources could thus be then used to estimate and map the state of hydroclimatic hazards at the local scale.

Regarding large-scale risks, traditional approaches have aimed to piece together local observations and modelling results in order to infer a regional estimate. For example, large scale flood damages have been previously inferred from assembling return periods derived from local-level high-flows frequency analysis. Following this approach, *Alfieri et al.* [2014] derived a pan-European flood hazard map at 100 m resolution, assuming a uniform 100-year return period for several catchments. Yet, while this approach may offer an initial insight of extreme hazard conditions, the assumption of spatially uniform flows —and thus return periods— for an entire catchment fails not just to capture atmosphere-catchment, but also the temporal interactions between upstream and downstream areas. The assumption of spatially homogeneous flows and hazards has thus been found to show inconsistent risk estimates at the large scale [*Thieken et al.*, 2015; *Mateo et al.*, 2017; *Vorogushyn et al.*, 2018].

1.1.3 Approaches to incorporate climate variability in the quantification of large-scale water hazards

An initial possibility for overcoming the spatial variability of flow occurrence is the application of multivariate distribution functions to represent hydrological hazards and risk probabilities at different sites [*Lamb et al.*, 2010; *Ghizzoni et al.*, 2012; *Keef et al.*, 2013]. While this approach has been applied mainly to flood estimates, and its sophisticated development incorporates spatial heterogeneities between stations, the fact that it provides only peaks of the hydrograph limits its practical application. For instance, the inability to represent the entire hydrograph not only overlooks the full range of hydrological variability, but also limits the further concatenation of results in hydrodynamic and impact models where continuous hydrograph simulations are required [*Falter et al.*, 2015]. Likewise, an alternative approach consists of the derivation of hydrological risks from stochastically generated sets of rainfall events [*Rodda*, 2001; *Wicks et al.*, 2013]. However, this technique may not comprehensively capture rainfall patterns, as well as initial catchment states that would ultimately lead to poor statistical description of extreme events [*Haberlandt and Radtke*, 2014].

An alternative approach, referred to as continuous hydrological simulation, avoids such simplifying assumptions by constantly simulating rainfall-runoff interactions and their consequent connection with hydrological models. While hydrological modelling efforts have traditionally looked to examine simulate the behavior of single components of the hydrological cycle, current efforts look to understand various hydrological processes that govern runoff generating and flood occurrence [*Todini*, 1988; *de Moel et al.*, 2015; *Falter et al.*, 2016]. Thus, current cascade of models are initially driven by a series of observed or synthetic climate data that would allow the implicit representation of the hydrological processes driving runoff generation and river flow dynamics. These values are then further

connected with schemes that describe surface level water dynamics and, thus, they consistently characterize the underlying processes governing hydroclimatic hazards. As such, this approach allows for the representation of the full range of hydrological variability and the underlying processes that drive hazard, such as the vertical movement of water across river networks, flood attenuations, and channel-floodplain interactions. This procedure also enables the generation of hazard metrics, which are based on the empirical distribution constructed from long-term simulation.

However, in spite of the advantages of this approach, it is not fully useful in refining our understanding of the consequences of large-scale climatic variability in surface water. Most of the challenges faced by these procedures are related to the computational costs that this effort represents [*Falter et al.*, 2016]. Moreover, the bulk of studies that characterize hydrological risks using this approach focus on flood dynamics, leaving the examination of low flows and drought events as not fully understood. As such, not only does the full range of surface water response to various natural and anthropogenic sources of climatic variability still need further investigation, but the examination of their implications on human systems or activities may also be currently poorly quantified.

However, a series of recent advances in modelling efforts offer the opportunity to examine the potential of continuously connected models. In particular, recent improvements in land surface models (LSMs) permit the combination of various sophisticated physical sub-models to continuously simulate terrestrial exchanges of surface water and energy fluxes. These modelling advances have paved the way for the combination of these sub-models and components, in order to be able to quantify the way at which various mechanisms of climate variability develop in the land surface and explain spatial and temporal characteristics of river flow and extremes.

1.2 Aims and Objectives

This main aim of this thesis is to increase our understanding of the way that natural and anthropogenic climatic sources of variability influence the spatial and temporal heterogeneity of flow. To address this aim, four research questions look to systematically address current scientific challenges introduced in the previous section:

i) How are flow characteristics influenced by land surface hydrological processes in areas with traditional rudimentary runoff representations and high climatic sensitivity?

ii) How does global land surface hydrological variables as well as extremes respond to low frequency mechanisms of natural climatic variability?

iii) Do current international climate agreements influence the characteristics of global surface hydrology and water extremes?

iv) Are there important societal repercussions from the examined natural and anthropogenic climatic sources of variability?

These questions are addressed by building on various physical sub-models of a Land Surface Model (LSM) and other complementary tools in order to enable a framework that connects climate sources of variability and heterogeneity of flows. Such framework looks to provide a tool at which the response of various sources of climatic variability respond in land surface hydrology.

1.3 Outline of Chapters

Chapter 2 corresponds to the Literature Review section. This chapter explores the previous work conducted to examine the role of climate variability in surface hydrology. It discusses in the diverse natural and anthropogenic sources of hydroclimatic variability, as well as previous studies that have continuously connected several models to infer the role of climate on hydrological risk. Chapter 3 presents the Methods and Tools that are part of this framework, along with justifying the selection of the diverse tools, techniques, and metrics utilized in the different stages of this Thesis.

The following chapters show four case studies parts of the framework presented in this thesis are used to deepen our understanding of the role of climatic variability in surface water dynamics and where the specific research questions are answered. Chapter 4 thus presents an initial test of the main schemes used in this framework by examining the snowpack properties that control timing and magnitudes of flow peaks in the Ob river basin. This catchment is selected because it is one of the world's ten largest catchments, and also because it is located in the climate sensitive Arctic region [*Serreze et al.*, 2002]. These characteristics facilitate an initial assessment of the tools used to represent the spatial and temporal heterogeneity of flows. Building on this initial experience, Chapter 5 presents a case study of the application of this framework to quantify the role of a natural and inter-annual source of climatic variability in water risks and resources at the global scale. The variability source for this case study is Atmospheric Rivers. These were selected as previous local studies in areas such as California, the UK, and the Iberian Peninsula, suggesting a possible global hydrological significance that had not been understood [*Dettinger*, 2011a; *Guan and Waliser*, 2015a; *Lavers and Villarini*, 2015b]. The people and areas exposed to this form of variability are also estimated in this chapter. Next, Chapter 6 adjusts the global framework utilized in Chapter 5 to present an innovative

examination of the influence of variability stemming from anthropogenic climatic forcings on global high flows. Anthropogenic climatic forcings are given by the estimated concentrations of greenhouse gases which would result from achieving the temperature targets agreed to in Paris in 2015 at the COP21, United Nations Climate Change Conference [*Christoff*, 2016; *Hulme*, 2016]. Lastly, Chapter 7 expands on the findings of Chapter 6 to first project the effects of the Paris Agreement in low flows and drought indicators. This analysis serves as the basis for assessing the implications of incorporating hydrological variability into vulnerability assessments, using the Hydropower sector as an example. This sector is selected because it exemplifies a major socio-economic actor whose risks and performance are heavily reliant on water dynamics [*Blomfield and Plummer*, 2014a].

2. Literature Review

2.1 Climate stressors of surface hydrology

Understanding the impacts of the interactions between climate and hydrology on different aspects of society, as summarized in the proceeding section, requires an initial description of the processes driving climatic variability. The following description divides sources of variability into natural modes and anthropogenic sources thought to influence climate. The former relates to the natural modes at different temporal frequencies which regulate natural climate over different global regions. Anthropogenic sources refer to the human-induced variations in climate. Although the full role of each of these sources is not entirely understood [*Trenberth*, 2011; *Balmaseda et al.*, 2013; *Hartmann et al.*, 2013], this review seeks to describe the major patterns and characteristics of these phenomena, and the known implications in hydrology.

2.1.1 Natural intra-annual sources of hydrological variability

Although several intra-annual variations of river flow are associated with large-scale climatic fluctuations, many are from sources that vary from region to region [*Dettinger and Diaz*, 2000]. The modes of variability presented here describe the dominant processes which are thought to modulate climate over large regions, as well as over extended time scales.

El Niño Southern Oscillation (ENSO) is probably one of the most recognized modes of variability. ENSO is associated with fluctuations of warm-temperature and cool-temperature phases in the tropical Pacific Ocean [*Neelin et al.*, 1998]. Such fluctuations are given by the states of the Walker circulation, the trade winds, and evolution of pressure with deep convection on the Pacific. The periodicity of such fluctuations are about 7 years. When not in its neutral condition, ENSO is characterized by two phases: during the warm phase, or El Niño, the factors mentioned are debilitated, which leads to a warming of Sea Surface Temperatures (SST) in the central and eastern Pacific [*Zhang et al.*, 1997; *Gershunov and Barnett*, 1998; *Wang*, 2004]. The resulting continuous reduction of the SST gradient in turn influences the trade winds, generating a positive feedback of the phenomenon. Conversely, the cool phase of ENSO, or La Niña, is described by a strong Walker Circulation and higher-than-usual warming of the western Pacific. Since ENSO influences changes in the general circulation of the atmosphere, in spite of being a regional process its impacts on temperature and precipitation patterns are global in scale.

As such, an El Niño phase is traditionally characterized by strong precipitation events in the eastern Pacific, and a precipitation decrease in the southern Pacific [*Chiew and McMAHON*, 2002]. Consequently, during this phase the coastal areas of South America, as well as island states in the Central Pacific, usually experience floods [*McPhaden et al.*, 2006; *Ward et al.*, 2014, 2016; *Emerton et al.*, 2017]. For instance, before the El Niño peak in December, most of South America has a 40 – 60% probability of observing higher than normal river flow. Likewise, the southern U.S. and several parts of Mexico see this probability increase to 70% after this peak has been reached.

At the same time, El Niño is thought to induce low flows in Northeast South America, Central America, Australia and New Zealand, and the South of Africa. Inferences in high

flow occurrences are also observed in several parts of Eastern Asia. In Europe, while the El Niño influence is not as marked as in the previously described areas, various impacts from flow magnitudes have been detected in France, Germany, and the South of Spain. In the same way, El Niño is thought to influence not just the magnitude, but also the duration of flood events in such areas.

On the other hand, La Niña usually brings conditions opposite to those described here. ENSO states are understood to influence the intensity, frequency and spatial distributions of tropical storms. La Niña conditions usually favor a greater probability of stronger and more frequent hurricanes in the Atlantic [*Pielke Jr and Landsea*, 1999]. Thus, the major El Niño phases during 1982-1983, 1997-1998 and 2015-2016, as well as major La Niña events in 1998-1999 and, 2007-2008 have led to significant economic and human losses in various locations [*Smith and Ubilava*, 2017]. For instance, hydrological shocks caused by El Niño are thought to result in about to two percent growth reduction in developing countries [*Smith and Ubilava*, 2017]. Similarly, drier and hotter weather resulting from la Niña is thought to be connected with decreases in agricultural yields and economic losses across tropical countries [*Hsiang and Meng*, 2015].

Following ENSO, possibly the largest mode of climatic and hydrological variability is the Indian Ocean Dipole (IOD). IOD refer to the pattern with anomalously low sea surface temperatures off of Sumatra, and high sea surface temperatures in the western Indian Ocean. [*Saji et al.*, 1999]. These differences in SSTs then result in surface wind anomalies in the central equatorial Indian Ocean [*Tokinaga and Tanimoto*, 2004; *Shinoda and Han*, 2005; *Horii et al.*, 2008]. As a result, surface winds invert direction from westerlies to easterlies during the peak phase of positive IOD, from September to November [*Schott et al.*, 2009]. This positive IOD phase is thus characterized by stronger trade winds and cooler SSTs in the eastern Indian Ocean. On the other hand, the ocean near East Africa typically

sees warmer waters and intensified convection. On the contrary, these patterns are reversed during the negative phase of IOD.

Another very important characteristic of IOD variability is that its origins are strongly related to the local coupling of ocean-atmospheric variables within the Indian Ocean [*Saji and Yamagata*, 2003]. Such strong local couplings are thought to also determine regional precipitation and temperature on inter-annual time scales [*Ashok et al.*, 2001; *Vinayachandran et al.*, 2009]. It is understood to be an important connection between intensification of rainfall over various parts in East Africa between October and January, during the IOD negative phase [*Reason*, 2001; *Black*, 2005; *Marchant et al.*, 2007; *Manatsa et al.*, 2012]. For instance, terrestrial water storage in the East African Lake region has been found to respond to IOD variability [*Becker et al.*, 2010]. Also, extreme floods in East African countries in 1961-1962 and 1997-1998 have been attributed to anomalous IOD conditions. These conditions are thought to have likewise exacerbated the spread of malaria in several parts of Kenya [*Hashizume et al.*, 2009]. Similarly, IOD may have influenced intense flooding over Sri Lanka, Indonesia and other parts of South Asia [*Zubair et al.*, 2003; *Yuan et al.*, 2008]. For example, negative IOD is often linked with cholera occurrences in Bangladesh, which are the result of higher sea level floods [*Hashizume et al.*, 2011].

However, the major influence of IOD may be its role on monsoon patterns over India, where it is also though to diminish the regional influence of ENSO [*Rajeevan et al.*, 2008; *Cherchi and Navarra*, 2013; *Yadav*, 2013]. Historically, significant floods in major Indian catchments, such as the Brahmaputra and Ganges, as well as extreme precipitation events, have responded to positive IOD events and La Niña conditions [*Ajayamohan and Rao*, 2008; *Pervez and Henebry*, 2015]. Conversely, drought episodes in India have been associated with anomalous IOD conditions [*Rao et al.*, 2010]. Likewise, a series of studies

have demonstrated that IOD positive phases have been the key driver of major historical droughts in southeastern Australia [*Ashok et al.*, 2003; *Ummenhofer et al.*, 2009]. At the same time, the negative phase of this mode has been associated with wet conditions in the region. IOD has also been found to influence inter-annual rainfall variations in central Brazil and in La Plata Basin in Argentina [*Chan et al.*, 2008].

Finally, it is important to note that while ENSO and IOD may be the predominant global climate modes, a number of other regional modes exist. The most important of hese are the North Atlantic Oscillation (NAO), the Atlantic Multidecadal Oscillation (AMO), and the Pacific Decadal Oscillation (PDO). NAO is thought to be the main driver of climate variability in North America and Europe [*Hurrell*, 1995; *Hurrell et al.*, 2001; *Visbeck et al.*, 2001; *Wanner et al.*, 2001; *Hurrell and Deser*, 2010]. As such, NAO is associated with changes in the surface westerlies across the North Atlantic and on to Europe, which then plays a significant determining factor in a number of atmospheric conditions, especially during winter. Positive and negative phases of NAO mode are followed by different spatial precipitation patterns. During the positive phase, warmer and wetter conditions are observed in northern Europe and the eastern United States, and colder and drier conditions are found in the northwestern Atlantic and the Mediterranean regions. These conditions reverse during a negative NAO. As such, these NAO states have been observed to modulate anomalies in snowmelt dynamics, storm surges, and variability of river flow levels in these regions, as well as major catchments in Turkey, Syria and Iraq [*Shorthouse and Arnell*, 1997; *Cohen and Entekhabi*, 1999; *Cullen and Demenocal*, 2000; *Trigo et al.*, 2004]. Likewise, recent studies have linked NAO warm states to reduced precipitation extremes in western China, the Tibetan plateau; thus also demonstrating a role in the Indian monsoon [*Feng and Hu*, 2008; *Kenyon and Hegerl*, 2010a].

Moreover, AMO is referred to as a long term fluctuation of SST in the mid- to high-latitude Atlantic Ocean, which is thought to exert a major influence on climate variability across North America and Europe [*Dijkstra et al.*, 2006; *Dima and Lohmann*, 2007; *Zhang and Delworth*, 2007]. As such, a positive AMO phase is characterized by an anomalous warm North Atlantic and a cold South Atlantic. This characteristic typically results in more intense hurricanes and more precipitation over the southern U.S. Yet, for the rest of the U.S. and for North Mexico, a warm AMO is reflected in general drier conditions and reductions in river flow levels [*Enfield et al.*, 2001; *Goldenberg et al.*, 2001; *Curtis*, 2008]. Similarly, a positive AMO has also been found to lead to strong southeast and east Asian summer monsoons, and late withdrawal of the Indian summer monsoon [*Lu et al.*, 2006; *Feng and Hu*, 2008].

Lastly, PDO is a climate mode which centers across the North Pacific Ocean. Its warm phase is characterized by warmer SST over the west coast of North America and in the eastern Pacific, as well as a cooler west Pacific [*Mantua and Hare*, 2002; *Goodrich*, 2007; *Newman et al.*, 2016]. During the negative phase, the opposite occurs. A series of studies have demonstrated PDO effects on temperature, precipitation, snowpack size and river discharge in several locations in North America [*Nigam et al.*, 1999; *Whitfield et al.*, 2010]. Typically, in this region runoff is enhanced in during cool PDOs, as well as early-onset melting due to warmer phases. A warm PDO has also been found to decrease monsoon rainfall and cause more intense temperatures over India. Similarly, in Australia PDO has been found to intensify flood risk during its cold phase [*Cai and Rensch*, 2012].

2.1.2 Natural inter-annual sources of hydrological variability

For the inter-annual time scales, the seasonality of river flow varies across catchments, and is mostly influenced by the local cycle of precipitation, evapotranspiration demand, snowmelt contribution (if any), subsurface infiltration, and local geomorphology, as well

as human inferences [*Dettinger and Diaz*, 2000]. Yet, at low frequencies, additional large-scale climatic mechanisms still exert an influence over river flow seasonality and the occurrence of extreme events. The role in surface hydrology of these sources of climate variability are also poorly understood.

As such, the Madden-Julian Oscillation (MJO) is thought to be the dominant model of tropical variability at scales ranging from one week to 90 days. It is characterized by a modulation of convective activity, which propagates eastward along the equator over the Pacific Ocean [*Matthews*, 2000; *Slingo et al.*, 2006]. MJO is most active in boreal winter and has been documented as having a strong influence on precipitation and frequency of extreme flood patterns in several global regions [*Jones et al.*, 2004]. For instance, previous studies have shown that MJO modulates the occurrence of heavy precipitation events in West Africa between March and September [*Sossa et al.*, 2017]. Likewise, several studies have reported the strong influence that MJO and its anomalies have on extreme rainfall events in Eastern China, flooding episodes in the Yangtze river, and in severe drought events in the south of China. [*Hui and Chongyin*, 2003; *Zhu et al.*, 2003; *Lü et al.*, 2012; *Li*, 2014; *Shao et al.*, 2018]. Similar influences have also been reported on the western U.S. coast, South America (as MJO *enhances* ENSO impacts), Australia, in the monsoon patterns in the Indian Ocean, Indonesia and as well as in the Middle East [*Bond and Vecchi*, 2003; *Nazemosadat and Ghaedamini*, 2010; *Shimizu et al.*, 2017].

Nonetheless, in recent years, the role that the evaporation of water from the ocean and the subsequent transport of atmospheric moisture has on the hydrological cycle has become increasingly popular [*Gimeno et al.*, 2016]. These mechanisms are also known as low-frequency mechanism of atmospheric moisture transport. Since the transport of moisture from oceans to continents is the main element of the atmospheric component of the water cycle, recent efforts focus on understanding the role that these anomalies have in the

characteristics of hydro-metrological hazards [*Stohl and James*, 2004]. As such, the two main-known large-scale mechanisms are Low Level Jets and Atmospheric Rivers.

Although the exact criteria to define LLJs differ across the literature, they are often referred to as the wind corridors found in the lower atmosphere [*Gimeno et al.*, 2016]. They are also known to carry significant amounts of moisture from tropical latitudes to high latitudes, and as such, they are key elements in the hydrology of tropical and subtropical regions [*Stensrud*, 1996; *Marengo et al.*, 2004]. LLJs are considered active during warm seasons and their origin can be either coastal or inland. LLJs thus modulate precipitation seasonality over several locations. For example, several studies have identified that moisture fluxes from the Gulf of Mexico play an important role in the hydrology cycle and in extreme events in the central U.S [*Benton and Estoque*, 1954; *Mo et al.*, 1995; *Arritt et al.*, 1997]. In Central and South America, LLJs originating in the equatorial Pacific and Atlantic, as well from the Caribbean, are known to interact with local orographic features such as the Andes or the Amazon to contribute to precipitations over these regions [*Poveda and Mesa*, 1999; *Vera et al.*, 2006; *Martinez and Dominguez*, 2014; *Poveda et al.*, 2014]. In the south and west of Africa, inflows from the Indian Ocean are thought to modulate rainfall variability and the occurrence of droughts [*Cook et al.*, 2004; *Pu and Cook*, 2012]. Likewise, in Asia and India, the strength of LLJ flows have been associated with monsoon activity, as well as with drought conditions [*Swapna and RameshKumar*, 2002; *Joseph and Simon*, 2005]. In Europe, the influence of LLJs on regional hydrology is thought to be insignificant.

Next, an increasingly studied mode of low-frequency mechanism of atmospheric moisture transport is known as Atmospheric Rivers (ARs). ARs are characterized by enhanced water vapor flux in long, narrow channels which are responsible for transporting the majority of the meridional water vapor flux over the globe (over 90%) [*Zhu and Newell*,

1998; *Ralph et al.*, 2012; *Gimeno et al.*, 2014; *Dacre et al.*, 2015]. They are thus understood be structures principally active in extratropical regions. They are generally associated with low-level moisture convergence within extratropical cyclones. Typically, their horizontal dimensions may be several thousand kilometers long, with width of about 500 km, and at any given time there may be 3–5 ARs in each hemisphere.

When ARs reach land (often referred to as landfall), their supply of water vapor has been strongly connected with large amounts of precipitation, which often results in flooding. For example, on the U.S west coast and in the U.K. they have been linked with several severe flash floods and with peak flow levels [*Dettinger*, 2011b, 2013, *Lavers and Villarini*, 2013, 2015b]. On the other hand, landfall is also relevant for water resources. For example, in California they are known to contribute between 30% and 50% of wet season precipitation, making them an essential element in snowpack formation and in regional water resource management strategies [*Guan et al.*, 2013]. Additional evidence of AR influence in rainfall has been reported in the Iberian Peninsula, Norway, Poland, France, and also in the Southern Andes, where ARs are thought to contribute to up to 80% of winter precipitation [*Viale and Nuñez*, 2011; *Lavers et al.*, 2013]. At a global scale, evidence from recent studies has identified previously unknown areas for landfall of ARs, such as south-east Asia, Australia, Africa, and Central Europe [*Guan and Waliser*, 2015a]. Also, recent estimates suggest that ARs-driven extreme winds have led to about 2 billion USD insurance losses in Europe from 1997 to 2013 [*Waliser and Guan*, 2017].

Consequently, given the damaging and beneficial characteristics that ARs may have, their study has gained scientific relevance to inform water resources and risk managers in various global locations. Yet, in spite of the regional and local importance of these low frequency mechanisms of moisture transport, there is only relatively limited understanding of the role that these processes may play in the global hydrological cycle and surface

hydrological extremes. Thus, this thesis looks to deepen our understanding of ARs in global hydrology and hydrological extremes.

2.1.3 Anthropogenic sources of hydrological variability

As reviewed in the previous sections, the processes affecting climate exhibit significant natural variability. So, while the several variables of the climate system may also show multiple states on various spatial and temporal scales, the movement of those states, aside from responding to natural variability, may also result from external sources of forcing [*Hartmann et al.*, 2013]. As such, the evidence that human activities continue to change the Earth's surface and atmospheric characteristics has increased over recent years. Changes in the atmospheric composition results either from the emission of gases and particles, or from changes in atmospheric chemistry.

These changes are measured by estimating Radiative Forcing (RF) which quantifies the net change in the Earth system's energy blance in response to some external perturbation [*Forster et al.*, 2007; *Lowe and Zealand*, 2007; *Bonan*, 2008; *Shindell and Faluvegi*, 2009; *Serreze*, 2010]. Understanding the spatial and temporal variations of forcing, along with the role of climate feedback, thus becomes essential in evaluating the potential impacts of these perturbations on the climate and land systems. A first source of forcing comes from shifts in the concentration of Green House Gases (GHG) in the atmosphere [*Hartmann et al.*, 2013]. Of these gases, the continuous increase in carbon dioxide, CO_2, is known to result in greater GHG and thus drives the increase in RF. Observations suggest that CO_2 has led to an increase in RF of 0.3 W m^{-2} per decade. Similarly, emissions from methane, CH_4, although lesser in magnitude than those from CO_2, are known to be a more powerful driver of RF. Additional GHG contributors to the increase in RF include N_2O, O_3, and

several types of dichlorodifluoromethane. Conversely, organic carbon, sulfur dioxide (SO_2), and ammonia are known to cause negative forcing.

Moreover, anthropogenic aerosols are also known to influence RF [*Charlson et al.*, 1992; *Ramanathan et al.*, 2001; *Menon et al.*, 2002]. Aerosols may then influence the climate by either interacting with Earth's radiation or with cloud processes. Yet, in spite of the significant efforts to assess aerosol properties, there are still major uncertainties in assessing their global characteristics. The main aerosol source is thought to be black carbon, which comes from wildfires and industrial pollution and absorbs radiation, which leads to a warming of the atmosphere and shading of the surface. These alterations will then result in significant consequences in ice and snow surfaces.

Lastly, it is important to consider additional natural sources that contribute to RF. The two main contributors are solar and volcanic forcing. The former corresponds to shifts in total solar irradiance [*Lean et al.*, 1995; *Cubasch and Voss*, 2000; *Lean*, 2010]. Although efforts are still required to better estimate the historical data and project these values, at present there is high confidence that over this century, solar forcing will be much lower than that contributed by GHG emissions. Volcanic eruptions are known to play an important role due to the deposit of mineral particles, sulphate aerosols, and CO_2 [*Robock*, 2000; *Shindell et al.*, 2003; *LeGrande and Anchukaitis*, 2015; *Sigl et al.*, 2015]. However, CO_2 emissions from volcanic eruptions amount to about 1% of those emitted from anthropogenic sources. As such, volcanic eruptions only have an influence on the annual and decadal climate variability, although the influence is in driving negative RF, or regional or global cooling.

At present, climate models are developed to allow the evaluation of emissions with specific climate stabilization targets. As such, these tools are widely used to examine the

response of the climate system to various forcings, which would then create productions of the state of the climate from seasonal to decadal time scales [*Hartmann et al.*, 2013]. Historically, these models have varied in their complexity and characteristics. At the moment, the primary types of global models are Atmosphere–Ocean General Circulation Models (AOGCMs), Atmosphere-only models, and Earth System Models (ESMs) [*Randall et al.*, 2007].

The main role of AOGCMs is to examine the interactions of the physical components of the climate system —namely, atmosphere, ocean, and land and sea ice— in order to make projections based on future anthropogenic forcings [*Houghton et al.*, 1992; *Solomon*, 2007; *Semenov and Stratonovitch*, 2010]. When running these types of models, the main assumption is that biogeochemical feedbacks are not relevant for the field of application to which they are applied. ESMs, conversely, are the most refined and complex models, as they add the representation of the carbon and other geochemical cycles to existing AOGCMs capabilities. Thus, the building of climate models requires that numerical models which express climate system laws first be implemented. Numerical expressions are usually resolved over spatial scales, which are represented over vertical (latitude-longitude), or horizontal grids (height, for example, for atmospheric representations). These models also require parameterizations in order to implement representations of models whose numerical modelling is impossible due to their complexity at large scale. A typical example of this includes cloud processes [*Soden and Held*, 2006].

Moreover, in order to bring together the different modelling efforts the Intergovernmental Panel on Climate Change (IPCC) provides a common framework to compare models. While the IPCC began to delineate scenarios and projections as early as 1990 as a response to the Kyoto protocol, these initial models were found not to follow the temperature and sea-level trends suggested by data at the beginning of the 21st century [*Rahmstorf et al.*,

2007]. As such, the current CMIP5 effort embraces a more detailed suite of model experiments by better constraining specifications of historical forcing (including the industrial period, from 1850-2006), as well as by including initializations of decadal predictions (from 2006 to 2100) [*Taylor et al.*, 2012]. As such, for future projections a set of concentrations are estimated for GHG, including CO_2, CH_4, and others.

Under the CMIP5 model performance, the 2013 IPCC report [*Hartmann et al.*, 2013] documents trends in the main climatic global variables. The primary relevant finding is, firstly, that in most of global areas, the multi-model mean agrees with reanalysis data [*Sillmann et al.*, 2013]. Yet in locations such as the Himalayas and other global icy regions, as well as coastal areas in western South America and Africa, there are significant biases, typically higher than >2ºC. Notable agreements are also found among models for the detection of extreme temperature events.

The simulation of precipitation is nonetheless less certain in several global regions. Important biases are found in the equatorial Western Pacific, where overly low precipitation is detected [*Collins et al.*, 2010]. On the other hand, overestimation of precipitation is found in the south of the equatorial Atlantic and the eastern Pacific [*Lin*, 2007; *Pincus et al.*, 2008]. It is also important to highlight that the representation of precipitation responds to regional processes, as well as to processes that require parameterization. The vertical improvement shown in CMIP5 models likely allowed for a more realistic simulation of precipitation extremes [*Kharin et al.*, 2013].

2.1.4 The Paris Agreement and the pursue to limit global warming

In 2015 in Paris, at the Conference of the Parties (COP) of the United Nations Framework Convention on Climate Change (UNFCCC), the parties vowed to keep global warming to well below 2 degrees Celsius and to "pursue efforts" to limit warming to 1.5 degrees

Celsius. This agreement is the result of multi-decadal international discussions. and represents the acceptable level of climate change that governments would tolerate in order to prevent additional disruption in the climate system [*Randalls*, 2010; *Rogelj et al.*, 2016a].

In order to fulfill these agreements, countries have submitted their Intended Nationally Determined Contributions (INDCs) to reduce GHG emissions. This would eventually lead to reaching a peak in global GHG, which would also allow for GHG removal in the second half of the century. As such, existing climate policies view 2°C as a safe bar that would allow for development. However, the assumption that a 2°C limit is a safe threshold as far as climate-change related tipping points are concerned has diverted attention away from the difference in impacts between a world in which global temperatures are stabilized at 1.5^{o}C instead of 2.0^{o}C. Given the sensitivity of the hydrological cycle to radiative forcing, ignoring the half-degree difference may lead to severe consequences [*Milly et al.*, 2002].

As such, in order to infer the difference in response between these two climate targets, the traditional approach would use radiative forcing protocols provided by current intermodel-comparison exercises such as the CMIP5. Utilizing the output of these exercises would, naturally, lead to a very large range of possible future temperatures as a function of model sensitivity. As such, these model efforts may not be sufficiently adequate to differentiate the risk associated with specific warming levels, such as those agreed upon in Paris [*Hulme*, 2016].

For the hydrological cycle, in particular, the distribution of global precipitation between CMIP scenario experiments does not respond uniformly between CMIP scenario experiments. This is thought to be caused by the changing role of non-CO2 forcing over the 21st century and is also due to the precipitation sensitivity to the emission-scenarios

contained by these experiments. This in turn makes it difficult to differentiate, within these models, whether the differences detected result from additional warming or from other factors. Extracting anomalies for 1.5ºC and 2.0ºC levels of warming from the traditional CMIP scenario experiments may thus not be scientifically robust [*Mitchell et al.*, 2016]

As a response to these limitations, the half a degree additional warming, projections, prognosis and impacts (HAPPI) experiment was specifically designed to simulate the specified Paris Agreement temperature targets (1.5ºC and 2.0ºC) as precisely as possible [*Mitchell et al.*, 2017]. HAPPI is an effort of various international climate groups which provides a framework for the generation of climate data describing how climate and weather extremes might differ in worlds 1.5ºC and 2.0ºC warmer than pre-industrial levels (when compared to present day conditions). This is done by separating the impact of an approximately half-degree of additional warming from uncertainty in climate model responses and internal climate. In the new protocol for both climatic targets, a set of 50-100 member-ensembles simulating future conditions over a period of ten years has been simulated with a number of AGCMs. In order to estimate the associated climate impacts since pre-industrial times, as well as in comparison to current conditions, two more experiments with the same ensemble size – one representative of the 2006-2015 period (actual experiment, in this study called the "historical scenario") and another representative for the 1861-1880 period (natural experiment) – were carried out.

All experiments use an international standard framework in which boundary conditions above the ocean are prescribed by observed or modelled SSTs and sea ice. As for fully-coupled model experiments, radiative forcing is prescribed in accordance with the expected temperature outcome based on the CMIP5 multi-model-means, as described below. Ten-year simulation periods are chosen for past, present and future, as they provide sufficient material for analysis of multi-year events, such as droughts. Each simulation

within an experiment differs from the others in its initial weather state. The use of 50–100 ten-year time segments thus in reality provides 500–1000 years of data per experiment.

For the actual experiment, the 2006–2015 decade is chosen both because it is the most recently observed period, and because it contains a range of different SST patterns over the decade. This allows for an assessment of how ocean conditions vary on inter-annual timescales, including the El Nino and La Nina events. For the natural experiment, delta SSTs taken from CMIP5 actual (historical) and natural experiments (10 year monthly means for the 1996-2005 decade) are subtracted from the OSTIA SSTs to simulate counterfactual conditions [*Donlon et al.*, 1998]. Past sea ice conditions, as well as radiative forcings, are taken directly from CMIP5 natural experiments (1996-2005).

Based on the temperature evolution over land and ocean, it is possible to estimate the SST warming required to achieve 1.5°C or 2.0°C warming for the globe as a whole. By chance, the multi-model-mean across CMIP5 GCMs under the RCP2.6 forcing scenario results in a global average temperature response at 1.55°C relative to pre-industrial levels (2091-2100 relative to 1861-1880), which is why for the HAPPI 1.5°C experiment, delta SSTs (that, as before, are added on to OSTIA SSTs for the natural experiment) from CMIP5 actual (1996-2005) and RCP2.6 (2091-2100) are used; so are future sea ice conditions and radiative forcings.

For the HAPPI 2.0°C experiments, no analogous CMIP5 simulations are available. The RCP scenario resulting in the second coolest temperatures by the end of the 21st century is RCP4.5, which reaches ~2.5°C relative to pre-industrial levels by the end of the 21st century. To calculate the future SST and sea ice conditions of a 2.0°C world we therefore take a weighted sum of the two RCP scenarios, W1 × RCP2.6 + W2 × RCP4.5. The weights are calculated such that the global-mean temperature response is 2.05°C (i.e.,

exactly half a degree above the 1.55°C response from the 1.5°C experiment), and results in W1 = 0.41 and W2 = 0.59. These weights are used to calculate the SSTs and sea ice coverage using the same methodology as in the 1.5°C experiment. The same weighting is used for the radiative forcing applied in the experiment.

As far as the effect of other forcing factors driving change, the counterbalancing nature of increased levels of anthropogenic aerosol levels (namely Organic and Black Carbon, BC and OC accordingly, as well as Sulfuric and Nitric acids, SO_2 and NO_3 correspondingly) is also briefly discussed here. While OC, SO_2 and NO_3 hamper surface warming (by reflecting Short Wave radiation), BC warms upper levels of the atmosphere (absorption). Both effects lead to a reduced hydrological cycle strength, particularly in the Asian monsoon region with high aerosol loads [*Bollasina et al.*, 2011]. Since the aerosol load is reduced to approximately 1/3 of its current levels in both of the future HAPPI scenarios, many regions will see higher rainfall increases at 1.5ºC compared to what has been observed or simulated until now. Since HAPPI does not provide GHG-only experiments, unfortunately at this point in time it is not possible to detangle potential thermodynamic and dynamic responses due to either GHGs or anthropogenic aerosols. In consequence, this thesis also looks to examine the implications of the climate variability resulted from this international agreement on global hydrological extremes.

2.2 Evaluation of hydroclimatic impacts at regional and global scales

Since water resources managers acknowledge the threat, or opportunities, resulting from climate variability to societies, there is an increasing need for policy makers to quantify their relationship. However, at the moment there is no standard method which would bring large-scale climate data to local or watershed scales [*Simonovic*, 2017]. Thus, the generic and traditional approach to assess and to attempt to incorporate the global and regional implications of hydroclimatic variability and extremes stem from the integration of diverse

modelling tools. This approach is called “model cascade” or “top-down” and is the result of feeding one model into another in order to infer the response of large scale processes into local-scale human or natural systems.

2.2.1 Cascading of processes

In water resources and risks analyses, the analysis chain typically consists of the following steps: i) retrieving global projections or historical climatic data; ii) downscaling of climate information to watershed or other finer scales; and iii) hydrological or hydraulic analyses to infer states of surface water, which would later support the estimation of the economic or social damages [*McMillan and Brasington*, 2008; *Ludwig et al.*, 2014].

The cascade process usually starts with the representation of the climate drivers of variability discussed in previous section. This step commonly gathers information from selected climate models which describe historical or projected climatic variability [*Hartmann et al.*, 2013]. For climate change studies, this stage would also include the selection of the emission scenario at which the assumption in GHG projections would be analyzed. Currently, at the CMIP5 experiment, four scenarios have been developed: RCP2.6, RCP4.5, RCP6, and RCP8.5 [*van Vuuren et al.*, 2011]. They represent a possible range of radiative forcing estimations by the end of the 21st century relative to pre-industrial levels. RCP2.6 thus represents a more optimistic future, in which annual GHG would peak by the 2020 decade, while RCP8.5 shows a scenario where GHG emissions continue to increase. Yet, as described in the previous section, more specific experiments such as HAPPI exist to project future climate scenarios.

For general climate assessments, at present about 35 global climate models developed by 21 international groups are available which run global simulations at different resolutions.

A comprehensive analysis typically evaluates the performance of all model outputs. While this option would capture the full range of uncertainty derived from GCMs, it may be computationally extensive. As such, the list is generally shortened by a first or rapid evaluation of model performances using Probability Density Function (PDF) comparisons [*Simonovic*, 2017]. This method looks to compare PDFs of simulated data with historical data in order to evaluate and select the models which returns better comparison's skill scores. This method has been typically used for water resources managers to choose from multi-model ensembles a refined set of scenarios may be constrained by uncertainties inherited from the GCM and from the exclusion of other plausible scenarios [*Clark et al.*, 2016b]. In spite of this limitation, the selection of certain GCMs has been widely used in global or large-scale studies; yet for local studies the use of scatter-plots may enrich this evaluation [*Gaur and Simonovic*, 2015]. This method looks to show likely GCMs conditions which would result in hydroclimatic extremes while also showing the uncertainty associated with the scenarios and GCM chosen.

An additional alternative for catchment-scale studies is the downscaling of information of GCMs via dynamic or statistical techniques [*Wilby and Wigley*, 1997]. The former typically relates to the development and application of Regional Climate Models (RCMs). RCMs use the initial physical conditions of GCMs to drive high-resolution simulations for a specific global region [*Corobov*, 2001; *Pierce et al.*, 2009; *Rummukainen*, 2009]. In recent years global RCM coordinated experiments have become more frequent with initiatives such as CORDEX [*Giorgi et al.*, 2009]. On the other hand, statistical downscaling corresponds to the establishment of empirical relationships between large scale climate variables (predictors), given by GCMs or RCMs, and local climatic variables (predictands) in order to project the future states of such variables [*Giorgi et al.*, 2001; *Wilby et al.*, 2002; *Maurer and Hidalgo*, 2008; *Rummukainen*, 2010; *Wilby and Dawson*, 2013]. Possibly the most common technique, within this group, is the calculation of delta

of change of observed time series which would later are used to adjust modelled projections [*Grotch and MacCracken*, 1991; *Hay et al.*, 2000; *Ruiter*, 2012]. Nonetheless, it is important to consider that downscaling climate data may add a new layer of uncertainty (given by the chosen approach) in the final results.

Lastly, is also important to consider additional sources of climate data at global scales which would derive from observations [*Overpeck et al.*, 2011; *Yang et al.*, 2013]. Since the emergence of remote sensing in the late 1970s, this tool has provided a resource for climate and weather data extraction at several scales. For instance, the Global Climate Observing System (GCOS) estimates that 26 out of 50 essential climate variables rely on the constant retrieval (and processing) of satellite data. Similarly, these data could be used to complement observation, and, via the running of physical models, to obtain meteorological reanalysis products.

2.2.2 Surface hydrological or hydraulic representations

In the cascade of processes, the output of climate models of either downscaled or direct output variables are then used to feed hydrological models. Some climate models generally deliver runoff that could be of initial utility to hydroclimatic studies. Runoff is obtained from water fluxes at the soil surface, which are converted to surface runoff [*Wolock and McCabe*, 1999]. However, such generated runoff has significant limitations associated with the climate models' inadequate ability to represent the entire hydrological cycle. This is particularly acute in the case of a deficient representation of horizontal water movement [*Teng et al.*, 2012]. As such, hydrological models can be used as complementary physical tools to represent surface hydrological states. Historically, at large scale, these models have been initially used to represent water availability from here runoff movement became an important necessity, building on this, and more recent models look to examine water resources and risks.

Hence, early approaches sought to represent the water balance over major global regions [*Xu and Singh*, 2004]. This idea was applied in order to detail baselines of global water availability computed from time series of hydroclimatic observations. Later, as macroscale hydrological models were developed in the early 1990s, water availability was estimated as total runoff accumulated over river networks [*Bierkens et al.*, 2017]. Examples of these early developments include WaterGap [*Alcamo et al.*, 1997], WBM [*Vörösmarty et al.*, 1998], and MacPDM [*Arnell*, 1999].

Next, the challenge in the hydrological modelling community consisted of representing the horizontal movement of runoff across river networks. As such, series of routing techniques were developed to translate runoff simulated from GCMs or RCMs to river flow. So these techniques seek to represent the equations governing water mass movement within a grid [*Coe*, 1998; *Lohmann et al.*, 1998; *Nijssen et al.*, 2001b; *Oki et al.*, 2001]. At present, developments seek also to represent transfers between surface and sub-surface flows [*Dadson et al.*, 2011]. Taking these developments into account, the representation of runoff movement has been traditionally grouped in three categories [*Li et al.*, 2013].

A first group corresponds to early developments which are based on linear reservoir routing techniques (LRR) (e.g., [*Miller et al.*, 1994; *Coe*, 1998; *Oki and Sud*, 1998; *Branstetter and Erickson*, 2003]). These methods are characterized for using a prescribed and temporal homogenous channel velocity which makes them computationally efficient. More some sophisticated applications of LRR methods may include a spatially variable channel velocity when applied over large regions [*Arora and Boer*, 1999; *Bjerklie et al.*, 2003; *Fekete et al.*, 2006]. Yet, the impacts of some the hydroclimatic processes, described in sections above, may occur at the daily time-scales. As such, the inadequate representation of the temporal heterogeneity of flows of LRR techniques may limit their applicability to study the links between natural and anthropogenic climate variability and runoff.

A second group of runoff routing techniques uses an Impulse Response Function (IRF) [*Lohmann et al.*, 1996, 1998; *Goteti et al.*, 2008; *Zaitchik et al.*, 2010]. They differ from the LRR methods that, instead of simulating a grid-to-grid movement of runoff, they model the lumped response from information derived from a contributing region [*Botter and Rinaldo*, 2003; *Sivapalan et al.*, 2003]. While these techniques may be highly computationally efficient, they fail to capture the spatial heterogeneity of a catchment which may be an important limitation for very intervened catchments. At the same time, they usually require extensive calibrations in order to derive their *correct* parameters. Yet, possibly their most important limitation is their difficult capacity to capture the variability of water fluxes [*Li et al.*, 2013]. Thus, this may constrain their capacity to capture interactions between climate variability and land surface hydrology.

The last group of runoff routing methods are those which are based on the application of the Saint Venant equations [*Moussa and Bocquillon*, 1996]. These models usually solve these equations by simplifying them by using techniques such as the kinematic wave method, diffusion wave method, and other simplifications [*Fread*, 1973; *De Roo et al.*, 2000; *Akbari and Firoozi*, 2010; *Lehner and Grill*, 2013]. They are characterized by their capacity to explicitly solve river flow velocities while also embracing spatiotemporal variability of a catchment. Thus, these models have facilitated the examination of the variability global water cycle. Typical application of these methods include algorithms to separate baseflow from river flow [*Arnold et al.*, 1995], estimations of spatial heterogeneity of flows [*Li and Sivapalan*, 2011], frameworks to evaluate hourly channel and floodplain dynamics in the Amazon catchment [*Beighley et al.*, 2009], routing routines in regional and global circulation models [e.g. *Arora and Boer*, 1999; *Lucas-Picher et al.*, 2003; *Cao et al.*, 2007; *Decharme et al.*, 2010; *Dadson et al.*, 2011], or global inundation and channel dynamics models [*Yamazaki et al.*, 2011].

As such, the simplification of the Saint Venant equations has permitted to represent the horizontal movement of surface water while maintaining the spatial and temporal heterogeneity of flow. This has permitted runoff routing to be incorporated into Land Surface Models (LSMs) which at the same time results in the improvement of the representation of the Earth system. LSMs simulate the exchanges of energy, water and carbon fluxes between the land surface and the atmosphere, which allows a physical representation of the hydrological cycle [*Blyth et al.*, 2006a; *Best et al.*, 2011]. While LSMs are frequently coupled with GCMs to provide the lower boundary conditions of the atmosphere, and to represent climate-land feedbacks, when run alone or *offline* they require meteorological forcing data to simulate surface conditions. The ability of an LSM to represent surface hydrology is enhanced by its capacity to reproduce river flows by routing runoff.

From here, after river flow has been incorporated into different models, the current trend has the development of models for specific water resource assessments at global or local scales [*Bierkens*, 2015; *Döll et al.*, 2016; *Simonovic*, 2017]. As such, the aforementioned models have incorporated several features that range from groundwater representations and water withdrawals, to exhaustive shifts in terrestrial water storage. However, several efforts have been carried out to develop models which specifically simulate a series of processes. For example, PCR-GLOBWB [*Van Beek and Bierkens*, 2009] and H08 [*Hanasaki et al.*, 2008] have been used to simulate reservoir operations both globally and at the catchment level. The former has also been adjusted to include other processes, such as freshwater temperature and streamflow forecast [*Beek et al.*, 2012; *Yossef et al.*, 2013]. For example, this has permitted the examination of the impact of global warming on specific systems such as thermoelectric power[*van Vliet et al.*, 2016b]. Since these models do not typically incorporate hydrodynamics, additional approaches have been sought to represent floodplain and inundation dynamics. A popular large scale model for this

purpose is CaMa-Flood [*Yamazaki et al.*, 2011] (which will be described in further sections). This model for example have been widely applied to investigate the future response of global flood and drought risks under climate change (e.g. [*Hirabayashi et al.*, 2008, 2013]).

2.2.3 Uncertainties and limitations

In spite of the significant utility of the above-described series of models in reproducing climate variability and in explaining complex physical processes, this process may reproduce a series of errors which may complicate the interpretation of results [*Maslin and Austin*, 2012]. Often the main limitation is in fact linked with the chain of processes (detailed above), which at the same time cascades uncertainties. An initial source of uncertainty thus stems from the selection of scenarios for future greenhouse gas emissions, which is affected by the way these are translated into atmospheric concentrations and forcings [*New et al.*, 2000; *Lambert and Boer*, 2001; *Allen and Ingram*, 2002]. The configuration and structure of GCMs also adds to what is regarded as the largest source of uncertainty [*Stainforth et al.*, 2005, 2007; *Graham et al.*, 2007; *Gupta et al.*, 2008; *Brekke et al.*, 2009]. GCMs are known to contain errors from the simplification and assumptions of climate and physical representations, such as cloud processes; their coarse spatial resolutions, and possible biases in the forcing data. In consequence, it is understood that GCMs do not properly project natural variability, which may constrain evaluations on decadal and multi-decadal time scales. Moreover, if downscaling techniques are chosen, their capacity to capture extremes such as storms or dry spells is also known to differ according to the type of method selected [*Wood et al.*, 2004; *Mearns et al.*, 2013; *Gutmann et al.*, 2014].

The main implication for water risk assessments is therefore that climate models (GCMs or RCMs) may not adequately represent precipitation, due to its high variability over fine

time and spatial scales [*Prudhomme et al.*, 2002; *Wilby and Dawson*, 2013]. The quality of the large number of precipitation products differ according to the type of terrain or climate represented [*Sperna Weiland*, 2011]. As previously discussed, the rudimentary representation of local runoff processes in several climate models may also limit simulation of peaks, floodplain processes and in nival catchments where frozen soils and snowmelt dynamics dominate flow occurrences [*Yossef et al.*, 2012]. This may be particularly notable in the representation of large catchments. As such there is also a scientific necessity to improve the description of runoff-river flow relationships in areas where performance is traditionally poor.

Thus, hydrological schemes as well as inundation representations, apart from containing uncertainties associated with their selection and parameterization, may also reproduce uncertainties inherited from large-scale models. River flow representation may also be constrained by hydrological models' lack of ability to represent wetlands, evaporation, and human inferences [*Nordhaus*, 2007; *Dell et al.*, 2014; *Heal and Millner*, 2014]. Resulting river flows or inundation maps may thus fail to adequately show the extensive range of socioeconomic, adaptation and policy aspects of losses and damages.

In this context, a comprehensive assessment of hydroclimatic extremes requires a characterization and understanding of these uncertainties [*Clark et al.*, 2016a]. An initial solution is the use of large or perturbed physics ensembles to force climate models which would, in turn, help to disentangle sources of errors [*Murphy et al.*, 2004; *Tebaldi et al.*, 2007; *Deser et al.*, 2012; *Kay et al.*, 2015; *Clark et al.*, 2016a]. A significant number of representations of likely futures and risks may therefore assist in the construction of informative probability distributions of hydroclimatic impacts. In this regard, the HAPPI experiment provides a comprehensive ensemble of years for the models available (50-125-time slices which really provides 500-1250 years of data).

Another alternative is the reduction of uncertainties through series of tests based on the evaluation of historical model performances [*Gupta et al.*, 2008]. These results then may help to recalibrate models until a satisfactory performance is obtained. Various metrics exist to assess such performances; for example, a common one is the examination of the relationship between simulated outputs of precipitation and evapotranspiration. This permits an initial evaluation of a model's skills to describe the water balance, and thus evaluate its capacity to capture hydrological processes. So, from here, other, more detailed scores can be developed to evaluate the ability of a model to represent large scale climate modes of variability that dominate climate variability over specific regions or for particular applications [*Pierce et al.*, 2009; *Teutschbein and Seibert*, 2012]. For instance, when evaluating hydroclimatic variability in areas such as the Pacific Coast of South America or the South of Asia, a sensible choice would be to evaluate the capacity of a model capture ENSO and Monsoon patterns respectively. On the contrary, water resources managers may be interested to assess the model's capacity to detect temporal sequences of extremes.

2.2.4 Limitations of Land Surface Models

Despite the important advances of LSMs over the last decades to represent fundamental hydrological processes, they still embrace various limitations. A first group of limitations relates to the challenges that LSMs still face when describing physical processes. For instance, various studies identify that LSMs still treat water table dynamics in a rudimentary way[*Lyon et al.*, 2008; *Koirala et al.*, 2014]. Traditionally these processes have been incorporated by using oversimplified models such as a fixed size of unsaturated soil column. At the same time, various studies have detected that LSMs fail to adequately simulate carbon and water fluxes during drought episodes [*Prudhomme et al.*, 2011; *Li et al.*, 2012; *Powell et al.*, 2013; *Tallaksen and Stahl*, 2014; *Ukkola et al.*, 2016]. This limitation has been associated to the systematic underestimation of evapotranspiration

during dry conditions. Similarly, various studies have reported that LSMs underestimate the duration of hydrological droughts while overestimating their severity [*Krinner et al.*, 2005]. Also, LSMs at present do not adequately represent groundwater flows which has led to a misunderstanding of the role that this component may play in global hydrological fluxes and water supplies. Possibly, this limitation is linked to the lack of consistent groundwater monitoring networks, reliable models, and geological data [*Pokhrel et al.*, 2016].

Also, in a broader sense, LSMs still fail to adequately account for human impacts and interventions in the water cycle [*Pokhrel et al.*, 2016]. At present, significant advances have been made towards incorporating the impacts of reservoirs and flow regulations on large scale hydrological models, yet these advances still need to be tested in various LSMs [*Chao et al.*, 2008; *Wisser et al.*, 2010; *Zhou et al.*, 2016]. Also, the simulation of the role and impacts that lakes and wetlands have on the hydrological and climate cycle still remains underrepresented in LSMs[*Stacke and Hagemann*, 2012; *Wania et al.*, 2013]. Moreover, just a limited number of LSMs have rudimentarily incorporated groundwater pumping effects in large scale water estimations [*Sophocleous*, 2002; *Maxwell and Miller*, 2005; *Krakauer et al.*, 2014]. Similarly, surface water extractions, irrigation dynamics (and their impact on regional climate and water vapor), and sophisticated representations of agricultural developments remains largely unexamined[*Adegoke et al.*, 2003; *Boucher et al.*, 2004; *Lawston et al.*, 2015]. At the same time, LSMs have not yet adequately considered sources of nutrients and their implications in the global water cycle. While various important models that consider nitrogen, ammonia, phosphorus, carbon, metals, and sediments exist [*Whitehead et al.*, 1998, 1998], they still need to be incorporated and tested within large-scale LSMs routines .

Lastly, current LSMs typically run at spatial resolutions between 10-100km. As such, various sub-grid hydrological processes remain either prescribed or underrepresented [*Wood et al.*, 2011; *Bierkens et al.*, 2015]. This issue may particularly affect the description of hydrological processes in areas with complex spatial heterogeneity in topography, soils, and vegetation. This would improve the existent description of channel processes, slope effects on solar radiation, and thus snowmelt, soil moisture and evapotranspiration dynamics. Nonetheless, the current development of hyper resolution models is constrained by their requirement of expensive computational resources[*Kollet et al.*, 2010].

2.2.5 Overview of applications of the model cascade approach

Using the aforementioned set of techniques, and following a top-down approach, several efforts have been carried out to assess hydrological states. Early efforts sought to demonstrate how climate data could be used to produce monthly water balance estimates at specific large catchments. For instance, *Vörösmarty and Moore* [1991] simulated gridded inundation dynamics in the Amazon and Zambesi basin by translating regional climatology into estimates of soil water, evapotranspiration, runoff, and discharge. Also, *Falkenmark* [1997] used WaterGap to use the results of a global climate model, along with social and economic scenarios in order to assess the state and future of water scarcity and stress. Similarly, using water balances derived from GCMs, *Arnell* [1999] projected changes in national water resources.

More sophisticated studies used the VIC Model to couple atmospheric models to infer river flow patterns over large basins for resource estimation purposes [*Abdulla and Lettenmaier*, 1997; *Lohmann et al.*, 1998]. *Fekete et al.*, [1999] used GIS and DEM data to link precipitation and evapotranspiration with observed runoff, in order to simulate global river flows, and thus close the water budget. As such, routing schemes within land surface models began to be used to estimate global river flows from climatological and

meteorological inputs. For example, *Nijssen et al.*, [2001a] studied the influences of model calibration as well as parameterization on global estimates of river flow, evapotranspiration, soil moisture storage, and snow water equivalent. Similarly, *Oki et al.* [2001] used global climate outputs to calculate water balance responses in a land surface model and obtain patterns in water uses across different sectors.

3. Methods

As mentioned in the background section, the framework applied in this thesis seeks to increase our understanding of climatic role in hydrological variability by refining the representation of the spatial and temporal heterogeneity of river flows. Hence, in order to achieve the specific objectives and study cases detailed, this thesis expands a "cascade approach" through a combination of series of models, shown in Figure 1.

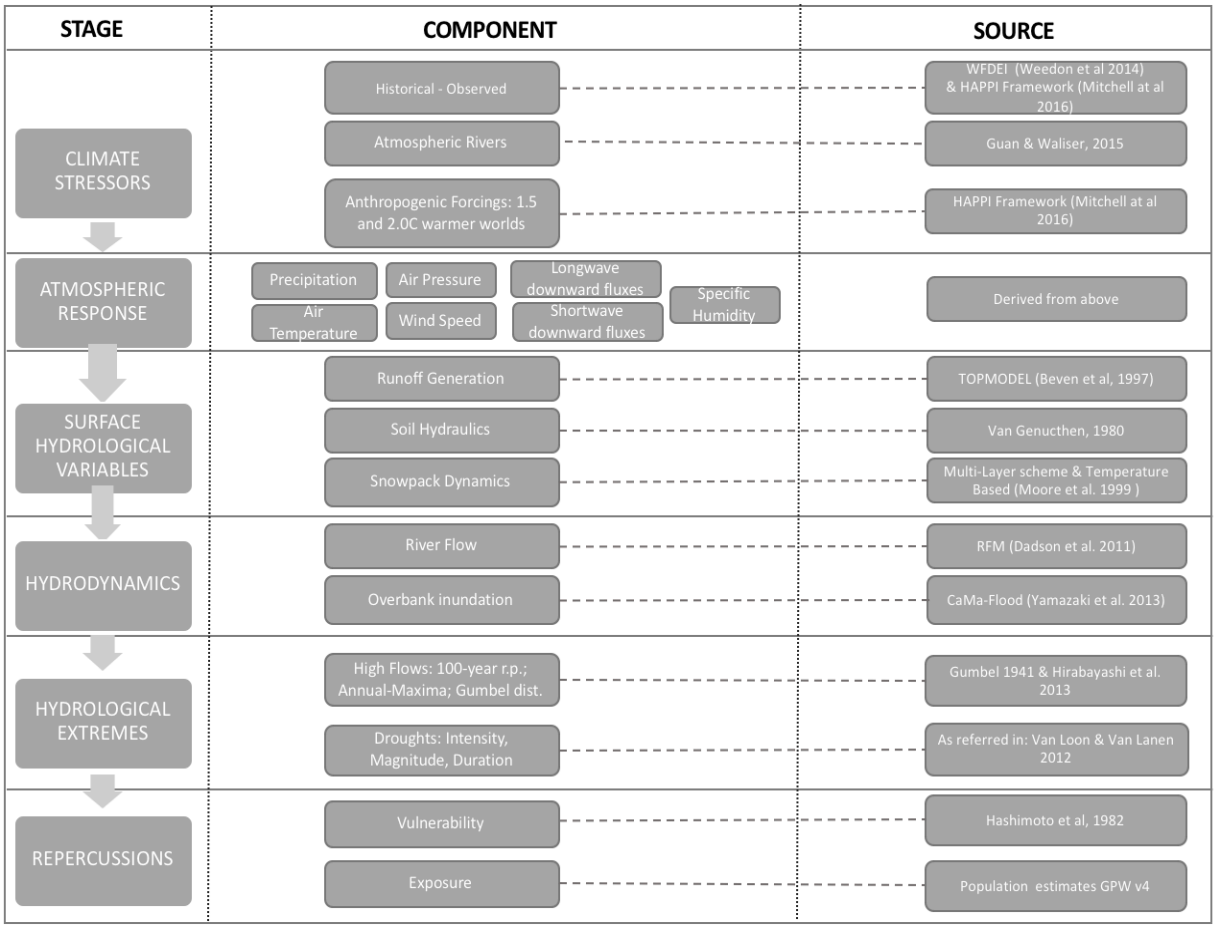

Figure 3.1 Sub-models and schemes utilized in this project. It is important to note that not all components and stages shown here were used in all four case studies.

This approach thus aims to propel a series of observed or simulated climate data that will allow representation of the hydrological processes driving runoff generation and river flow dynamics. The assessment of the role of the climatic stressors in surface hydrology is then based on the generation of *artificial* datasets that represent disrupted climate through the natural or anthropogenic sources of stress examined in this study.

As such, the initial evaluation of model performance, presented in Chapter 4, is performed by perturbing snowpack parameters in order to understand the subsequent response of river flow dynamics. This allows for generation of river flow series that capture hydrological sensitivity to snowpack changes. In Chapter 5, historical atmospheric series are perturbed by subtracting the precipitation that may have been contributed by atmospheric rivers from the historical climatology. This leads to the generation of an artificial dataset, which represents the state of hydrological variables and extremes in a world with "no-atmospheric rivers". Likewise, Chapters 6 and 7 obtain *artificial* river flow time series showing the projected state of climatic variables in global climate scenarios which are 1.5 and 2.0^{o}C warmer, as agreed to in Paris. The resultant *artificial* river flow series in all these steps thus allow for evaluation of the relative contributions of these diverse sources of climatic stress to surface hydrology and hydrological extremes.

3.1 Data Sources of Climatic Variability

The climatological data employed to drive the chain of models utilized in this framework are firstly obtained from reanalysis products. These data initially serve as the historical base at which perturbations in Chapters 4 and 5 are made. While the climatology remains the same in Chapter 4, the snowpack parameterization differs across simulations, which in turn leads to an understanding of river flow response. On the other hand, in Chapter 5 climatology, and in consequence the response of extremes, is perturbed by Atmospheric

Rivers. Next, Chapters 6 and 7 incorporate the outputs of Atmospheric Global Circulation Models (AGCMs) to obtain historical conditions and projected perturbed climatology. These data then feed the chain of models, in order to characterize the response in surface hydrology.

3.1.1 Meteorological Forcing Dataset

The first source of historical atmospheric variables used in the present thesis is the WATCH Forcing Data derived from the ERA-Interim reanalysis data (commonly known as WFDEI) [*Weedon et al.*, 2014]. The WATCH Forcing Data (WFD) is a dataset covering 1958-2001 that is based on the ECMWF ERA-40 reanalyses product via sequential interpolation to 0.5° × 0.5° resolution using the CRU land–sea mask as reference [*Boucher and Best*, 2010; *Weedon et al.*, 2011]. WFD follows elevation corrections and monthly-scale adjustments based on corrected-temperature, diurnal temperature range, cloud-cover, and precipitation monthly observations. These adjustments are corrected for varying atmospheric aerosol loading and, for precipitation, from improved gauge stations observations for rainfall and snowfall. As such WFD is a dataset created to facilitate forcing of land surface and hydrology models.

Moreover, the ERA-Interim is the latest global dataset produced by ECMWF which contains global climate reanalysis data from 1979 to date as it is continuously updated in real time [*Dee et al.*, 2011]. Gridded surface parameter outputs are provided every 3 hours describing weather as well as ocean-wave and land-surface conditions. ERA-Interim uses a wider range of satellite atmospheric data and surface observations which provide a significant improvement in surface meteorological variables, when compared to ERA-40 [*Dee et al.*, 2011]. Thus, WFDEI uses the same correction methodology as the WFD yet it is applied to the improved ERA-Interim dataset. WFDEI then is thought to provide a consistent dataset (at spatial 0.5° × 0.5° resolution) for global hydrological and land

surface models [*Weedon et al.*, 2014]. In particular, WFDEI is thought to be particularly useful to examine hydrological impacts in large catchments since the WFD bias correction methodology preserves spatial continuity over large-scales with multiple half-degree grid boxes [*Weedon et al.*, 2011].

As such, WFDEI features improved precipitation estimates (e.g., snowfall rates are provided separately from rainfall rates), wind speed, and downward shortwave fluxes (in response to changes in aerosol corrections). This dataset covers the 1979-2015 time period. It consists of monthly files containing three hourly averages at a 0.5ºx0.5º vertical resolution. In total, this dataset offers the following atmospheric variables: 10 m wind speed, 2 m temperature, 2 m specific humidity, downward longwave radiation flux, downward shortwave radiation flux, rainfall rate, and snowfall rate. This dataset is used as a historical baseline on which the perturbation experiments of Chapters 4 and 5 are performed.

3.1.2 Natural Sources of Variability: Atmospheric Rivers (ARs)

AR precipitation values were based on a global AR database developed by *Guan and Waliser* [2015]. This dataset is the product of a technique developed for the objective detection of ARs in the global domain based on detecting integrated water vapour transport (IVT) characteristics. The dataset utilized for this extraction is the ECMWF Interim reanalysis (ERA-Interim) which contains global, 6-hourly atmospheric fields at a 1.5° × 1.5° spatial resolution [*Dee et al.*, 2011]. AR are obtained from the IVT derived from specific humidity and wind fields at 17 pressure levels between 1000 and 300 hPa. As such, the technique first filters regions where IVT is above the 85th percentile, specific to each season and grid cell. Next, different criteria for AR conditions were applied with respect to IVT direction. Lastly, this technique identified landfall of ARs (with significant relevance to terrestrial hydrology) as those intersecting with the coastline, and whether the

mean AR IVT is directed from ocean to land. Biases of this product are also evaluated against the National Aeronautics and Space Administration (NASA) Modern-Era Retrospective Analysis for Research and Applications (MERRA) [*Rienecker et al.*, 2011]. The dataset covers the period 1979-2014 and contains AR shape, axis, landfall location (for AR landfall), and basic statistics for each AR detected. For this study, the Atmospheric Rivers dataset was downscaled to a 0.5ºx0.5º spatial resolution in order to meet the WFDEI dataset characteristics. This dataset was chosen due to the fact that it is the most comprehensive and spatially and temporally detailed AR product available.

3.1.3 Anthropogenic Sources of Variability: Projected Climate as Agreed to in Paris

In order to assess the response of climate variables to the temperature targets agreed upon in Paris, this thesis obtained the climatology projections and historical baselines of experiments which followed the HAPPI protocol. In total, 4 AGCMs were used, which met the requirements of either having produced runoff, or having sufficient atmospheric variables to compute runoff for the historical, 1.5ºC and 2.0ºC scenarios. Thus, the NCC/NorESM1-HAPPI model contains 125 ensemble members, and ETH/CAM4 contains 500 ensemble members for each scenario; MIROC/MIROC5 contains 50 complete time slices for the historical experiment, and 100 slices for both futures; and CCCma/CanAM4 contains 100 ensemble members for each scenario. Likewise, the spatial resolution of runoffs given by each AGCM (NCC/NorESM1-HAPPI: 1.875ºx0.625º; ETH/CAM4: 2.5ºx1.875º, MIROC/MIROC5: 1.40ºx1.40º, CCCma/CanAM4: 2.81ºx2.81º) were downscaled by bi-linear interpolation to match the resolution of our river network (described in Section 3.5, Ancillary and Validation Products).

3.2 Modelling Tools.

The following modelling tools —which are part of the framework utilized herein— were next used to simulate different states of surface hydrological variables. It should be noted that not all models which will be described were used at the same time for all case studies presented in this thesis.

3.2.1 Land Surface Model

Land Surface Models (LSMs) are tools designed to simulate the exchange of surface water and energy fluxes at the soil-atmosphere boundary, and they generally simulate surface boundary conditions for climate models. We thus incorporate parts of the JULES LSM, v4.2 [*Best et al.*, 2011] hydrological structure in order to capture the hydrological surface characteristics required for the analyses in Chapters 4 and 5. For instance, Chapter 4 requires the continuous simulation of snowmelt-runoff dynamics. In Chapter 5, the contribution of Atmospheric Rivers to terrestrial hydrology is also quantified in terms of relative contribution to total runoff, soil moisture content, and snowpack size. JULES flexible design thus has the advantage that its modular structure facilitates the simulation and representation of such processes. In this study, JULES is used at 0.5°, the horizontal resolution of WFDEI.

The configuration of JULES LSM applied in this thesis utilizes the default soil configuration of JULES [*Best et al.*, 2011], which consist of four soil layers with depths 0.1 m, 0.25 m, 0.65 m, and 2.0 m. Water in layers of the soil that become super-saturated was transferred upwards [*Clark and Gedney*, 2008]. The thermal conductivity model developed by Chadburn et al. (2015) which accounts for the physical and insulating properties of organic soils was also used. Data on soil properties were obtained from the Harmonized World Soil Database (HWSD) from FAO – IIASA [*Fischer et al.*, 2012]. The

hydraulic soil properties from HWSD were derived using the method of Cosby et al. (1984). The canopy model used accounts for radiative canopy with heat capacity and also represents snow beneath the canopy. Also, canopy radiation is treated following a multi-layer approach (10-layers) for radiation interception following the approach of *Sellers et al.*, [1992]. This approach incorporates leaf angle distribution, zenith angle, and absorption of radiation; also, this JULES configuration also assumes a decline of leaf nitrogen with canopy height. The detailed configuration of the snow model is explained in Chapter 4. Also, JULES assumes heterogeneity of land surface cover within grid cells. So, the parameterization of the land surface heterogeneity is based on nine prescribed surface types. These are broadleaf trees, needleaf trees, grasses (C3 and C4), shrubs; urban, open waters, bare soil, and permanent land ice and snow.

Also, the soil moisture equation chosen to describe the relationship between hydraulic conductivity, suction and volumetric water was the Van Genuchten formulation [*Van Genuchten*, 1980]. This formulation was chosen (in opposite to the alternative Brooks–Corey soil moisture equation) as it has shown to lead to improved runoff performance due to better representation of bare soil evaporation when tested over diverse catchment drainage areas in Europe [*Dadson et al.*, 2011].

3.2.2 Runoff Generation

Within the JULES LSM, the TOPMODEL was used to generate sub-surface runoff applied to the large-scale hydrology (LSH) scheme developed by *Gedney and Cox*, [2003]. TOPMODEL assumes that topography is a main dominant of the spatial heterogeneity of runoff. So, this model formulation is based on the hypothesis that topography controls soil hydrology, and influences the location of the water table within a catchment [Beven and Kirby, 1979]. In TOPMODEL, the topographical characteristics of an area is described by the topographic index. This index is a means of grouping runoff-producing elements in the landscape by their topographical characteristics. The topographic index is a measure of the

relative propensity for a point of soil to become saturated to the surface, given the area that drains into it, A, and its local outflow slope, β [Beven and Cloke, 2012]. Thus, as these characteristics are typically derived from DEMs it provides a physical characterization of a catchment. Also, the surface fraction of a grid-box that is saturated is obtained from the moisture conditions in the soil profile which define a critical value of the topographic index. In JULES, TOPMODEL is used to simulate an additional storage layer beneath the standard 4-layer soil column and also a modelled grid-box-mean water table depth. Subsurface runoff is obtained from any soil layer below the top of the water table. Surface runoff then is obtained when the water table reaches the surface.

The current configuration of TOPMODEL runs at a half-degree horizontal resolution in order to match the spatial characteristic of the base map ancillary data used as input. The topographic index used here offers a combination of high-resolution topographic parameter maps presented at 15-arc seconds [*Marthews et al.*, 2015a]. Chapters 4 and 5 thus obtained runoff generated in JULES using the TOPMODEL scheme.

3.2.3 A Simplified Runoff Scheme

For the hydrological assessments of the climate targets agreed to in Paris, two models (NCC/NorESM1-HAPPI and ETH/CAM4) generated runoffs as outputs. However, two AGCMs (MIROC/MIROC5 and CCCma/CanAM4) did not have a runoff-production scheme activated. A simple generation scheme was thus used to calculate runoff in those cases. For these two AGCMs, runoff was calculated by using a simple runoff production model designed to be comparable with the runoff-production models typically embedded within climate models. This simple scheme uses a Rutter-Gash canopy formulation [*Gash*, 1979] together with Penman-Monteith evaporation, calculated using available radiation

data [*Monteith*, 1965]. Soil moisture was accounted for using a two-layer model, with saturation-excess runoff computed using a generalised TOPMODEL.

The snowpack model used here was based on a temperature-based conceptual model of accumulation and melt [*Moore et al.*, 1999; *Hock*, 2003; *Beven*, 2011]. Snow accumulates when precipitation falls when temperature is below a threshold temperature T_a. When temperature is above the melting threshold, T_m melting occurs at a rate proportional to the difference between the current temperature and T_m. This is a widely-used conceptual model [*Hock*, 2003; *Zhang et al.*, 2006; *Rango and Martinec*, 2007; *Beven*, 2011] with a performance comparable to that of more parameter-rich energy balance models, despite their greater complexity.

Despite the existence of other, more sophisticated runoff schemes, this scheme is intended to be applied directly to atmospheric outputs resulting from large ensembles, such as the HAPPI ensemble. This allows for maximization of utility of the HAPPI ensemble by generating runoff when it is not provided directly. This model was also run at a half degree horizontal resolution in order to meet the spatial characteristics of the basemap ancillary data used as input (described in Section 3.5, Ancillary and Validation Products).

3.2.4 River Flow Generation

Independent of the runoff generation scheme used, runoffs were routed by implementing the grid-based hydrological routing scheme, River Flow Model (RFM), as presented by *Dadson et al.* [2011]. This model is based on a discrete approximation to the 1-D kinematic wave equation with lateral inflow. The model uses a kinematic wave approximation to the St. Venant equations for gradually-varying flow in open channels. Such an approximation relates channel flow (q) and lateral inflow per unit length of river (u) by:

$$\frac{\partial q}{\partial t} + c\frac{\partial q}{\partial x} = cu \quad \text{(Eq. 3.1)}$$

where c is the kinematic wave speed, and x and t are distance along the river reach and time, respectively. Kinematic routing is applied separately to surface and sub-surface runoff, and the routing model also distinguishes between land and river pathways by using different wave speeds. A return flow term is used to allow interactions between surface and sub-surface flow on hillslopes and in channels [*Bell et al.*, 2007]. In river cells, this term spatially integrates the fast and slow components of river flow. As such, river flows for the various study stages were calculated following this approach. Often, the kinematic wave approximation utilized in this scheme is also utilized for flood inundation forecast. The application of this scheme requires a manual configuration of individual river network features as well as the optimization of physically-based parameters [*Bell and Moore*, 1998]. In the present configuration this routing is applied separately to surface and subsurface runoff. It also allows different representations of runoff over land and river pathways. Also, a return flow term is utilized which permits the description of interactions and transfers between surface and sub-surface flow on hillslopes and in channels. Thus, this term allows the schematization of both slow and fast components of river flow.

As such, RFM river flow scheme requires river network data as input, at which river channel directions and locations are dictated. The river network used in this thesis was constructed by using the Network Tracing Method (NTM), which is a vector-based network scheme that traces the path of river networks downstream [*Olivera and Raina*, 2003]. This method works by overlaying a mesh of a certain grid size over a fine-scale joined river network to determine the coarse-scale downstream cell. This method has the advantage that it can be used in areas where digitized river networks exist, but no DTM is available, and it is usually spatially closer to the base river network. Since NTM has been found to outperform other raster-based methods, it has been widely used in previous routing studies [*Olivera and Raina*, 2003; *Bell et al.*, 2007; *Davies and Bell*, 2009], and

thus it is the river network used in this thesis. The resolution of the river network used here is half degree (0.5 ^{o}x 0.5^{o}).

3.2.5 Inundation Model

In order to examine the inundation implications of Atmospheric Rivers, runoff values were used to drive the CaMa-Flood model [*Yamazaki et al.*, 2011, 2013, 2014], which is a distributed model which routes input runoff along a prescribed river network map which indicates river flow directions for a grid cell. It estimates river discharge, river and floodplain dynamics, water depth and inundated area. This model's advantage is that it represents water storage, water level, and flooded area by making decisions based on the subgrid-scale topographic parameters using a high-resolution Digital Elevation Model (DEM). As such, despite the fact that the spatial resolution of the input runoff to run CaMa-Flood is 0.5x0.5 the model allows refinement of the spatial resolution of the output variables to 0.25^{o}x0.25^{o}.

The model assumes continuous reservoir storages for river channels and floodplains for each simulated grid cell. As such excess water from the river channel is stored in the floodplain via an explicitly parameterization of the subgrid-scale terrain characteristics of a floodplain. To calculate river and floodplain dynamics, CaMa-Flood utilizes length, width and bank height and river channel reservoir parameters; and unit catchment area, floodplain elevation profile as parameters for floodplain reservoirs. The model assumes that inundation occurs from lower to higher areas in a catchment. Also, in this model other water bodies such as lakes and wetlands are treated as floodplain storages. river flow directions and river width data in CaMa-Flood are obtained HydroSheds and from the GlobalWidth Database for Large Rivers (GWD-LR) [*Yamazaki et al.*, 2014].

Horizontal water transport at each grid is calculated by one-dimension streamlines which considers that each point has only one downstream point. So, flow velocity and river discharge rates are obtained from the local inertial equation [Bates et al., 2010] along the river network map [*Bates et al.*, 2010]. As such this water exchange is just calculated for river channels as water movement between floodplains is assumed to be insignificant, as observed by Alsdorf et al., [2010]. The method used to route runoff across river grids is the diffusive wave equation. This is a form of simplification of the St. Venant momentum equation which considers that the main parameters to describe runoff horizontal movement are pressure, bed slope and friction (leaving aside wave acceleration and advection).

A last important advantage of this model is that it is highly computationally efficient for global simulations. In Chapter 5, CaMa-Flood and its inundation options were used to assess the influence of Atmospheric Rivers on global inundation dynamics.

3.2.6 Validation Datasets

The datasets used to perform the validation of river flow, described above, differ from the catchment case study of the global analysis. For the Ob' experiment, river flows were validated against mean monthly observed data from the Regional Arctic Hydrographic Network data set, R-ArcticNET. These data were drawn from over 3,700 recording stations contained within pan-Arctic hydro-meteorological archives. The case study presented in Chapter 4 used version 4.0 of the dataset (http://www.r-arcticnet.sr.unh.edu/).

For the global analyses presented, the river flows generated were validated using the observations provided by the World Meteorological Organization Global Runoff Data Centre (GRDC) [*Fekete et al.*, 2002]. This dataset offers a collection of river discharge collected at monthly or daily time steps from over 9,000 global stations.

3.3 Metrics of Analysis

3.3.1 Validation Statistics

River flow generated during this process was validated by calculating common hydrological metrics, such as the Nash-Sutcliffe Efficiency (NSE), the bias in runoff volumes (D_v), and the ratio of the root mean squared error to standard deviation (RSR).

NSE is a normalized statistic that compares simulated residual variance (or noise) with measured observed variance in order to determine how well simulated data matches observations [*Moriasi et al.*, 2007]. This is calculated as:

$$NSE = 1 - \frac{\sum_{i=1}^{n}(O_i - S_i)^2}{\sum_{i=1}^{n}(O_i - \bar{O}_i)^2} \text{ (Eq. 3.3)}$$

Where O_i are the values observed, S_i are the simulated discharges for each time step, and n is the total number of values within the analysis period. NSE values vary between -∞ and 1.0, where 1.0 indicates perfect agreement between observed and simulated values, and performance less than zero indicates that the mean of the observations is a better predictor than the model.

Moreover, D_v, also known as the percentage bias, estimates the average tendency of the simulated data to be larger or smaller than that being observed [*Gupta et al.*, 1999]. It is calculated via the following equation:

$$Dv = \frac{\sum_{i=1}^{n}(S_i - O_i)}{\sum_{i=1}^{n}(O_i)} \text{ (Eq. 3.4)}$$

D_v values near to zero indicate a more accurate model. Positive values show a model overestimation bias, whereas negative values show underestimation. The RSR normalises the root mean square error (RMSE) by the standard deviation of the observed values. It is calculated as:

$$RSR = \frac{RMSE}{STDEV_{obs}} - \frac{\sqrt{\sum_{i=1}^{n}(O_i - S_i)^2}}{\sqrt{\sum_{i=1}^{n}(O_i - \bar{O}_i)^2}} \text{ (Eq. 3.5)}$$

The best model performances are indicated by those RSR that approach zero, which means lower residual variation.

3.3.2 Flooding and High Flow Statistics.

Once series river flow series are obtained from the steps above, the annual maxima of river discharge are obtained at each grid location. These values are thus calculated for both the *new* series that account for the perturbations in climate stressors (given by the natural or anthropogenic driver), and the historical baselines.

Annual maxima are then fitted with a two-parameter Gumbel distribution to estimate extreme values, following previous similar studies [*Gumbel*, 1941; *Hirabayashi et al.*,

2008, 2013]. It is important to note that this type of distribution may give higher probability of extremes than other types of distributions. However, changes in frequency —which are the focus of the analyses of this thesis— can be represented in spite of the extreme function selected. Next, in order to maintain consistency with conventional hydrological practices, the threshold for high flows and inundations is obtained from the flow, which is exceeded 10% of the time (referred to as Q10), or the flow or inundation with a 100-year return period. The influence of the climate stressor in the historical discharge series is thus obtained by calculating the change in the magnitude of the river discharge return period for said flow threshold.

3.3.3 Low Flow Statistics and Drought Indices.

The repercussions of the climate targets agreed in Paris, in 2015, in low flows were obtained by estimating the changes in frequency, duration, intensity (or water deficit) of hydrological drought when compared to the historical or natural baseline. Hydrological droughts were calculated by using the widely applied threshold level method [*Yevjevich*, 1967; *Hisdal and Tallaksen*, 2003; *Fleig et al.*, 2006; *Van Loon and Van Lanen*, 2012; *Van Loon*, 2015a]. This technique is known for better capturing and representing seasonal patterns and deficiencies in high-flow seasons, especially in areas with abrupt changes in river flows. As such, this approach is recommended for use in global-scale studies [*Beyene et al.*, 2014].

A drought episode is thus detected when river flow values fall below a determined threshold level. Daily threshold levels are calculated based on the 20^{th} percentile (or Q80) of flow duration curves over a moving 30-day average time window which moves through our daily river flow time series. This value is selected since it follows the values suggested in previous studies [*Van Loon and Van Lanen*, 2012]. Likewise, drought events are pooled

together if the time interval between them is 10 days or less [*Fleig et al.*, 2006]. Droughts with a duration of 15 days or less are also eliminated as they are considered minor. Lastly, the intensity of a drought event represents the deficit volume obtained by summing up the difference between the historical threshold level and the disturbed river flow in both scenarios [*Zelenhasić and Salvai*, 1987].

For Chapter 5, in order to assess the influence of Atmospheric River changes, drought intensity (or the resultant water loss) was selected as the main indicator. This indicator then served as basis for understanding how the absence of ARs influences droughts at the global scale. In Chapter 7, the influence of the climate targets agreed upon in Paris is evaluated using the three indices.

3.3.4 Gross Hydropower Potential.

In order to understand the hydropower sector's vulnerability to hydrological variability resulting from the Paris Agreement, Gross Hydropower Potential is selected as the analysis indicator. This indicator is employed because it has previously been used to provide a first outline of general regional distributions and hydropower capabilities [*Pokhrel et al.*, 2008; *Renofalt et al.*, 2010; *van Vliet et al.*, 2016b]. GHP can then later be applied by more sophisticated energy and economic models in order to further evaluate sites suitable for project selection, technologies required, economic implications, etc. Gross Hydropower Potential (GHP) is defined as the hydropower generation capacity possible if all natural water flows contained as many 100% efficient turbines as possible [*Zhou et al.*, 2015].

GHP calculation was based on the approach proposed by *Lehner et al.* [2005] and *Gross and Roppel* [2012]. Multi-model ensemble means and gridded streamflow runs (obtained using the above-described step) are combined with gridded elevation differences, water density, and gravitational differences, following Equation (3.6):

$$GHP = Q * m * g * \Delta H \text{ (Eq. 3.6)}$$

Where GHP is expressed in Watts, in each grid cell; Q is volumetric flow rate expressed in m^3/s; m is water density (1000 kg/m^3); g is the gravitational acceleration (9.807 m^2/s), and ΔH is the elevation difference (m) calculated in a grid cell. Elevation differences within a cell were obtained from the GMTED2010 Global Grids DEM at 7.5-arc-seconds (~225 m) [*Danielson and Gesch*, 2011]. So, this study obtained global GHP for both of the climate scenarios agreed to in Paris (1.5°C and 2.0°C), and for the historical baseline.

3.3.4 Measuring Exposure and Vulnerability

In order to calculate the number of people exposed to the influence of Atmospheric Rivers, in Chapter 5 this thesis uses a gridded population dataset provided by GPWv4 [*Center for International Earth Science Information Network - CIESIN - Columbia University*, 2016] as reference. This is a raster file that models global human population distribution (counts and densities). The inputs for this dataset are the 2005-2014 round of Population and Housing Censuses. Although the dataset provides series of projections, this thesis utilizes the 2015 estimates. The output resolution is 30 arc-seconds, which is approximately 1 km at the equator. The number of people exposed to ARs was thus obtained from overlapping the grids where their influence on droughts and floods is "major" (>50% of annual low flow or high flow episodes is due to their absence or presence, accordingly) with GPWv4.

Next, system vulnerability is calculated from the measures of system performance proposed by Hashimoto et al. (1982), and later applied to drought risks in water resources [*Jinno*, 1995; *Kjeldsen and Rosbjerg*, 2004; *Jain and Bhunya*, 2008]. Vulnerability, then, is a measure describing how significant or severe the likely consequences of a failure may be.

For hydrological variability, Chapter 7 understands failure as a grid's lack of capacity to deliver water above a certain critical threshold. In this Chapter, the vulnerability threshold is determined by the already-calculated drought threshold. If the drought threshold is met or superposed, the gird will be classified under a state of failure, as there will not be sufficient water to deliver GHP. Thus, Hashimoto et al. (1982) and Jinno (1995) proposed measuring vulnerability based on total water deficit (deficit volume, or drought intensity) experienced during a drought event. In this formulation, vulnerability thus considers the probability of each event to be equal (1/M), where *M* is the number of failure events, and vulnerability is calculated as the mean value of the deficit events *v(j)*, following Equation (3.7):

$$Vulnerability = \frac{1}{M}\sum_{j=1}^{M} v(j) \quad \text{(Eq. 3.7)}$$

4. Snowmelt, runoff generation and river flow: Examining snowpack representations in a Land Surface Model

Homero Paltan[1]
Simon Dadson[1]
Richard Essery[2],
[1]School of Geography and the Environment, University of Oxford, Oxford, UK
[2]School of GeoSciences, University of Edinburgh, Edinburgh, UK

*Paper submitted to the Journal of Hydrological Processes, September 2018

4.1 Abstract

Accurate representation of the hydrology of nival regions is essential due to the important role that snow plays in the surface energy budget and the global hydrological cycle. Yet, in spite of this role it is not very clear the snowpack characteristics which majorly describe river hydrology and peaks in cold regions. So, in this paper we examine the key representations of the snowpack properties that determine river flow characteristics in a snow-dominated catchment. We also examine how the physical snowpack properties, control river flow timings and magnitudes order to address this aim we evaluate the response of river flows response in the Ob' catchment (Siberia, Russia) to various configurations of snowpack processes within a Land Surface Model (LSM). We first detect that the horizontal (layer) composition of the snowpack importantly influences river flow scores by the way it describes observed seasonal snow cover fractions and snow water equivalent values. Within the snowpack, we found that the capacity of it to retain liquid water is the major regulator of river peak flows in this catchment. When this characteristic is poorly represented, daily peak flows in the melting season are poorly represented leading also to a decrease in river flow scores. Also, in spite of the possible sources of uncertainties that we identified, our simulations show that the detected biases are randomly and not systematically and thus they don't influence the hydrological performance at the catchment scale. Thus, our results indicate key elements of the snowpack which should be constantly monitored in cold regions in order to quantify freshwater fluxes to the ocean and assess water resources response to changing climate.

4.2 Introduction

Snow plays an important part in the climate system by affecting the exchange of heat between the surface and the overlying atmosphere [*Cohen and Rind*, 1991; *Vavrus*, 2007; *Sturm*, 2015]. The snowpack reflects 30-50% of incoming solar shortwave radiation and it insulates the underlying soil layers, which reduces the exchange of moisture and heat between the boundary layer and the land surface. Also, snow cover affects the atmospheric circulation in mid- and northern latitudes via an increase in surface pressure which favours a more negative North Atlantic Oscillation pattern [*Cohen and Entekhabi*, 1999]. More generally, snow is a major component of the hydrological cycle not just because it increases near-surface soil moisture (by about 25%) but also because it stores water and regulates the timing and amount of runoff entering streams and rivers (Shelton 2009; Vavrus 2007 Rango 1993).

Consequently an adequate understanding of the key processes which dictate river hydrology in cold areas is seen as an important challenge to better estimate the role of snow in the Earth System in the face of climate change [*Barnett et al.*, 2005; *Adam et al.*, 2009]. As such, the implications of changes in temperature and precipitation patterns are understood to lead to reduced snowfalls and in consequence smaller snowpacks. A reduced snowpack thus decreases the chance of it to act as water reservoir. This, in turn may lead to earlier snowmelts and reduced summer soil moisture, which would then alter the frequency and height of peak flows and produce longer periods of low flows [*Barnett et al.*, 2005]. As such cold regions are regarded as highly more prone to hydrological extremes such as spring floods or summer droughts.

In order to examine the interactions of the snowpack with other elements of the land surface and atmosphere, Land Surface Models (LSMs) have been used as key tools [*Sun*, 2004; *Dutra et al.*, 2012]. The principal role of LSMs is to partition net incoming radiation

into an upward flux of long wave radiation, sensible heat (SH) and latent heat flux (LE). LSMs are also used to track water through the soil column and to diagnose rates of surface runoff and evaporation [*Pitman*, 2003; *Best et al.*, 2011]. Due to the complexity of representing snow in models some LSMs, such as the NOAH LSM, or the OPER scheme in ECMWF, have opted to represent the snowpack as a zero-layer model (Niu et al. 2011; Dutra et al. 2010). In this approach the upper soil layer is adapted to represent snow. When snow is on the ground the surface layer temperature is not allowed to exceed 0^{o}C and the model gives the bulk of snow a set of constant properties such as thermal conductivity, snow thickness and density. As the heat capacity of snow is neglected, the heat flux used to melt snow is computed as a residual term in the surface energy balance.

Yet, the fact that snow accumulation and ablation processes operate at finer temporal and spatial scales than those captured by a LSM [*Parajka et al.*, 2010] has hitherto limited the utility of LSMs in investigations of physical processes in cold regions [*Hancock et al.*, 2013]. Whilst simple representations of snow, given by zero-layer snow models, have given good agreements with observations, they may also lead to biases in soil temperature (leading to inadequate representations of the snow cover fraction – SCF) and snow water equivalent (SWE) [*Essery et al.*, 2006; *Best et al.*, 2011; *Sultana et al.*, 2014]. SWE is an essential indicator of snowpack dynamics, especially from a hydrological point of view, because it accounts for the snowpack growth and decay independently of local variations in snow density, which is heterogeneous in space and variable in time [*Ferguson*, 1999]. SCF controls the moisture content in the near-surface soil layers and its seasonal melting regulates the annual runoff cycle [*Vavrus*, 2007]. Also, a simple representation of the snow may overlook its capacity of the snowpack to store or freeze liquid water [*Blyth et al.*, 2011].

In contrast to the zero-layer model, more complex representations of snow physical processes have been used by characterizing multiple layers of snow. For instance, In JULES LSM the multi-layer model was presented in Best et al. (2011). This model offers

the ability to define a number of snow layers, each with prognostic thickness, temperature, density, ice content and a liquid water content. In this model the number of snow layers is constantly updated according to the snow depth, subject to a prescribed maximum number of permitted layers. As the snow depth increases, the lowest layer increases in thickness until it reaches twice its prescribed thickness; the layer then splits in two, the upper part staying fixed in thickness and the new lowest layer continuing to thicken. In northern regions, a multi-layer model has been observed to give better simulations of snow and soil temperatures which in turn has increased the representation of permafrost and thaw soil dynamics [*Dankers et al.*, 2011; *Dutra et al.*, 2012; *Burke et al.*, 2013]. As such, this provides indication that representing various layers of snow may lead to more adequate simulations of river flow in cold regions.

Nonetheless, the way by which both snowpack representations differ when simulating river flow is still not clear. Similarly, it is not totally understood how the physical snowpack properties, defined in multi-layer scheme, control river flow timings and magnitudes. This may help to describe the snow properties which in turn affect hydrological extremes in cold regions. As such, the aim of the present study is to investigate the key representations of the snowpack properties that determine river flow characteristics in a snow-dominated catchment. To answer this, we first investigate how river flow characteristics respond to the incorporation of a scheme with more complex set of physical snow processes. For this we test how the skill with which snow and river hydrology are predicted a LSM changes when a more complex snow scheme is used instead of a simple one. From here, we evaluate the river flow response (defined as magnitude and timing of flows) to various snowpack properties, represented by the multi-layer snow scheme.

4.3 Materials and methods

4.3.1 Study Region

We run our simulations in the Ob' River, western Siberia, Russia (Figure 4.1). The Ob' basin is the largest river basin in the Arctic and the eighth largest river in the world with a drainage area of almost 3,000,000 km^2 [*Grippa et al.*, 2005]. The Ob' contributes about 400 km^3 freshwater per year to the Arctic Ocean via the Kara Sea, which represents 15% of the total input [*Shiklomanov et al.*, 2000; *Prowse et al.*, 2006]. Permafrost is not expected to be a major controller of physical processes in the basin as most of it does not include permafrost.

The human population in the basin is almost 30 million[*Yang et al.*, 2004b]. Specially, the Upper Irtysh, Ishim, Tobol and Lower Irtysh sub basins are characterised for its intense agricultural and industrial activities. In this side of the basin there are identified five dams and reservoirs.

Figure 4.1 Base map of the Ob' Basin: Main Ob' and tributaries, location of dams, reservoirs, and gauge stations. Minor areas of continuous (>90%) and discontinuous (50-90%) permafrost obtained from Brown et al. (1998)

4.3.2 Model Description

The properties of the snowpack are tested on the Joint UK Land Exchange Scheme (JULES) version 4.2 which is the stand-alone version of the land surface scheme used in the Hadley Centre climate models [*Blyth et al.*, 2006b; *Best et al.*, 2011]. JULES simulates the interactions of different land surface processes such as vegetation dynamics, the carbon cycle and the hydrological cycle from time-varying inputs of air temperature and humidity, wind speed, shortwave and longwave radiation, and precipitation.

We used the WATCH Forcing Data methodology applied to ERA-Interim data (WFDEI) global gridded reanalyses product [*Weedon et al.*, 2014] covering the period 1979–2011. The dataset consists of monthly files containing three hourly time steps at a 0.5º resolution, which dictates the spatial resolution of our study. Also, we used the default soil configuration in JULES, which consist of four soil layers with depths 0.1 m, 0.25 m, 0.65 m, and 2.0 m. Water in layers of the soil that become super-saturated was transferred upwards, following Clark and Gedney (2008). The thermal conductivity model developed by Chadburn et al. (2015) which accounts for the physical and insulating properties of organic soils was also used. Data on soil properties were obtained from the Harmonized World Soil Database (HWSD) from FAO – IIASA [*Fischer et al.*, 2012]. The hydraulic soil properties from HWSD were derived using the method of Cosby et al. (1984). Additional details concerning the default configuration of the model can be found in Best et al. (2011).

4.3.2.1 Snow Dynamics in JULES Existing JULES representations allow the partitioning of snowfall between snow on the canopy and the underlying ground [*Essery et al.*, 2006]. Snow from the canopy is removed either by sublimation or by prescribing a canopy

snowmelt rate. This partitioning, in turn has been found to enhance the capacity of LSMs to estimate sublimation and simulate runoff [*Essery and Clark*, 2003].

Next, JULES uses two schemes to represent snow on the ground, as introduced previously [*Best et al.*, 2011]. The zero-layer scheme merely represents snow by adapting the top soil level to show snow processes. Under this scheme snow is prescribed a constant thermal conductivity and a constant density. While the heat properties of snow are neglected, an increased soil layer thickness and the different conductivities between snow and soil lead to a decrease in the thermal conductivity of the surface soil layer. Also, when snow is on the ground the surface soil temperature is not allowed to exceed O^{o}C. Then, the heat flux used to melt snow is obtained as a resulted from the surface energy balance. Thus, meltwater produced under this scheme is partitioned into soil infiltration and runoff yet there is no account for storage of liquid water in the snowpack. This has led this model not to refreeze water in the snowpack and thus melt water too rapidly.

On the other hand, the multi-layer snow scheme uses a prescribed number of snow layers with different thicknesses. Under this scheme, each layer represents a specific snow depth at each time step, so the number of layers and depth is indeed dynamic. So variable snow layers are then first used to represent snowpack decreases due to ablation and compaction. When a layer is at the base of the snowpack, its thickness is variable until it reaches twice its prescribed thickness. Then the layer splits in two with the upper part locking its thickness while the lower one keeps thickening. The process is progressively reversed when snow depth and accumulation decrease.

When the multi-layer snow scheme is used it dynamically uses the surface heat flux, calculated by the surface energy balance of JULES. Then the ground heat flux calculated by this scheme is passed to the soil module. Next, when the temperature fluxes of a layer

are calculated to exceed a given threshold the layer ice mass is reduced. This consequently increases the layer liquid mass. Then, when the liquid content of a layer exceeds its prescribed capacity, the excess water is passed to the layer below. Lastly, the water flux at the base of the snowpack is used by the hydrological model to produce runoff, infiltrate it in the soil.

Lastly, JULES also provides diagnostic and prognostic options to calculate snow albedo. The diagnostic option a snow-free albedo and an albedo for deep snow are given for each surface type. So, this simple option fails to estimate the interactions between snow ageing and the surface ground. Conversely, the prognostic option uses a sophisticated spectral snow model [*Wiscombe and Warren*, 1980]. This snow model uses a prognostic grain size value which evolves at each time step as such, it characterizes the ageing of snow. As a result, being able to represent the time evolution of the snow albedo is thought to lead to a more coherent physical understanding of snow processes.

We ran our baseline simulations by activating the snow multi-layer and the zero-layer models in JULES v4.2. For each model we used the default configuration which includes values for the thermal capacity and conductivity of laying snow. However, the simple representation of snow requires a constant value for the density of lying snow (which remains constant) and the indication of the temperature at which snow albedo equals cold snow albedo.
The more complex model is activated when the maximum number of snow layers is defined. So, we permitted a maximum of 3 layers (with default snow depths of 0.1, 0.15, and 0.2 m). Default parameters include: density of fresh snow (snow density is automatically computed) and liquid water holding capacity of lying snow. Also, in JULES in order to simulate this process a canopy representation that simulates the partitioning of snowfall between canopy interception and throughfall has to be activated. So, in addition

a ratio of maximum canopy snow load to leaf area index has to be given. This multi-layer snow representation also requires the activation of a spectral scheme to calculate snow albedo. In this case default values for grain size for fresh snow, maximum size of grain size, snow grain area growth rate for melting snow, cold fresh snow and cold aged snow, and maximum albedo for fresh snow have to be given. For each of these parameters we used the default values. Layers, density of fresh snow, liquid water holding capacity, canopy, spectral

4.3.2.2 Runoff Generation TOPMODEL was used to model runoff generation because its more detailed physical representation of the basin has shown, in some locations, a more realistic seasonal cycle of subsurface runoff, more accurate simulations of dry season flows and improved representation of peak flows [*Clark and Gedney*, 2008; *MacKellar et al.*, 2013]. This model formulation is based on the hypothesis that topography controls soil hydrology and influences the location of the water table within a catchment. [*Beven and Kirby*, 1979]. In JULES, Gedney & Cox (2003) implemented a generalized version of TOPMODEL by using it to simulate an extra layer beneath the standard 4-layer representation of soil moisture. The critical parameter required by TOPMODEL is the topographic index, which provides information about the terrain. In this study we used the 15 arc-second resolution global map of topographic index developed by Marthews et al. (2014).

4.3.2.3 Runoff Routing and River Flows. Runoff routing based on the River Flow Model (RFM) developed by Bell et al. (2007) and Dadson et al. (2011). This model uses a kinematic wave approximation to the St. Venant equations for gradually-varying flow in open channels. Such approximation relates channel flow (q) and lateral inflow per unit length of river (u) by:

$$\frac{\partial q}{\partial t} + c\frac{\partial q}{\partial x} = cu \quad \text{Eq. (1)}$$

where c is the kinematic wave speed and x and t are distance along the river reach and time respectively. Kinematic routing is applied separately to surface and sub-surface runoff and the routing model also distinguishes between land and river pathways by using different wave speeds. A return flow term is used to allow interactions between surface and sub-surface flow on hillslopes and in channels (Bell et al., 2007). In river cells this term spatially integrates the fast and slow components of river flow. The river network and drainage directions used were calculated using the Network Tracing Method (NTM) which has been shown to provide accurate river network data for routing purposes [*Olivera and Raina*, 2003; *Bell et al.*, 2007; *Davies and Bell*, 2009]. In particular, we used a finer-scale flowpath grid calculated from the algorithm developed by Paz et al. (2008) applied to the HydroSHEDS topography dataset [*Lehner et al.*, 2008].

4.3.3 Assessment of performance

4.3.3.1 River Flow River flow performances from different configurations are compared against mean monthly observed data from the Regional Arctic Hydrographic Network data set, R-ArcticNET. These data were drawn from over 3,700 recording stations contained within pan-Arctic hydro-meteorological archives. In this study we used version 4.0 of the dataset (http://www.r-arcticnet.sr.unh.edu/). In spite of the great abundance of stations in the Ob', in this study we use 12 validation sites which meet our time frame requirements, having a record longer than ten years within our period of study. The location of each river gauging station is shown in the base map of the basin (Figure 4.1) above. A description of the principal characteristics of each river gauging site is presented in Supplementary Table S4.1. Hereafter, sites will be referred to by their code number instead of their name.

Our main measure of performance for river flows is the Nash-Sutcliffe Efficiency (NSE). NSE is a normalized statistic that compares simulated residual variance (or noise) with measured observed variance in order to determine how well simulated data match observations [*Moriasi et al.*, 2007]. It is calculated as:

$$NSE = 1 - \frac{\sum_{i=1}^{N}(Oi - Si)^2}{\sum_{i=1}^{n}(Oi - \overline{O})^2} \quad \text{Eq(2)}$$

Where is O_i are the observed values and S_i are the simulated discharges for each time step and n is the total number of values within the period of analysis. NSE values vary between -∞ and 1.0, where 1.0 indicates perfect agreement between observed and simulated values and performance less than zero indicates that the mean of the observations is a better predictor than the model.

We also calculated two error-based statistical indicators commonly used in hydrology: the bias in runoff volumes (D_v), and the ratio of the root mean squared error to standard deviation (RSR). Dv, also known as the percentage bias, estimates the average tendency of the simulated data to be larger or smaller than that being observed [*Gupta et al.*, 1999]. It is calculated via the following equation:

$$Dv = \frac{\sum_{i=1}^{N}(S_i - O_i)}{\sum_{i=1}^{n} O_i} \quad \text{Eq(3)}$$

Values of D_v close to zero indicate a more accurate model. Positive values show a model overestimation bias whereas negative values show underestimation. The RSR normalises the root mean square error (RMSE) by the standard deviation of the observed values. It is calculated as:

$$RSR = \frac{RMSE}{STDEV_{obs}} = \frac{\sqrt{\sum_{i=1}^{n}(O_i - S_i)^2}}{\sqrt{\sum_{i=1}^{n}(O_i - \overline{O})^2}} \quad \text{Eq(4)}$$

The best model performances are indicated by those RSR that approach zero, which means lower residual variation.

4.3.3.2 SCF and SWE In order to complement river flow simulations, we compare our results with observed datasets for SCF and SWE. We evaluated JULES SCF results with snow cover data derived from MODIS instrument inboard on Terra Satellite: Snow Cover Monthly L3 Global CMG (MOD10CM) dataset V5 at 0.05° resolution [*Hall et al.*, 2006]. This snow cover dataset consists of monthly averaged values from the daily global products. We resampled these data to 0.5° horizontal resolution using a bilinear interpolation method which weights the average of the four nearest cell centers of a point. Later we evaluated our results between March 2000 and December 2011 which is the data period available by the satellite observations. When compared with ground station this dataset has a reported accuracy of 93% under clear skies and this performance may improve depending on the land cover type and snow conditions. (Hall & Riggs 2007).

Also, Snow Water Equivalent (SWE), derived from JULES is compared with satellite data obtained from the Advanced Microwave Scanning Radiometer (AMSR-E) inboard of Aqua satellite: Level 3 AMSR-E Monthly Global Snow Water Equivalent EASE-Grids [*Tedesco et al.*, 2004]. A microwave sensor is chosen as it tackles the lack of direct measurements in the region and, unlike optical sensors, its observations are not constrained by the presence of clouds. In spite of the lack of consistent reference observations, a previous study obtained high accuracy values (about 90%) in a similar Northern Basin when using AMSR-E's SWE to map snow covered areas [*Tong and Velicogna*, 2010]. Given the temporal availability of the data we evaluated our results for the years 2002–2011. This dataset was resampled from its original 25 km resolution to 0.5° to match the resolution of our simulations (using a bilinear interpolation method, explained previously). We computed monthly averaged values of SCF and SWE for the months in which observations were available. Then we identified grid boxes where the difference between means was statistically significant with a $p \leq 0.05$ in order to identify those locations with a statistical difference between simulated and observed values, and thus to identify where there were simulation errors. Conversely, in those grid boxes where means were similar

we concluded that our model performed well. In order to account for spatial autocorrelation in our local (grid) t-tests we adjusted the degrees of freedom used in the statistical tests as suggested by von Storch & Zwiers (1999).

4.4 Results

The performance statistics to simulate river flow of both snow models, as compared to observed data, are presented in Table 1. We identify a clear improvement in the simulation of river discharge when the multi-layer snow model is used instead of the zero-layer model. With exception of station 10100, NSE values show an acceptable level of model performance throughout the basin. At most of the points, in particular where NSE values exceed 0.7, our multi-layer simulations suggest that JULES satisfactorily represents hydrological variability when using a more complex snow model. This finding is also supported by the calculated RSR, which shows that results produced using the multi-layer snow model show a lower residual variation than those obtained with the zero-layer model. This includes the station 11048 where NSE values show similar results between both models but when included RSR, a slight better performance is observed in the multi-layer option.

Table 4.1 Performance statistics of river flow. Nash-Sutcliffe efficiency, Bias in runoff volumes (percentage bias), and Root Mean Square Error- standard deviation ratio (RSR). Comparisons of the JULES Zero-Layer Snow Model and the Multi-Layer Snow Model against discharge observed at 12 validation stations in the Ob' basin.

	Nash-Sutcliffe efficiency (NSE)		**Deviation of runoff volumes (Dv)**		**RMSE-observations standard deviation ratio (RSR)**	
Validation Station	**Zero-Layer**	**Multi-Layer**	**Zero-Layer**	**Multi-Layer**	**Zero-Layer**	**Multi-Layer**
11801	0.1	0.75	-0.47	-0.27	1	0.52
11048	0.59	0.59	0.16	0.24	0.72	0.69

11056	0.42	0.69	-0.10	0.07	0.82	0.62
11061	0.30	0.78	-0.27	-0.05	0.93	0.55
11545	-0.77	0.51	-0.63	-0.42	1.37	0.69
11414	0.28	0.43	0.34	0.21	0.86	0.83
12554	0.23	0.26	0.36	0.35	0.87	0.86
11542	0.06	0.63	-0.14	0.04	1.00	0.63
10100	-0.65	-0.74	0.90	0.92	0.95	0.97
10246	0.71	0.8	0.10	0.03	0.61	0.52
10023	0.61	0.75	0.01	0.21	0.72	0.57
10021	0.64	0.82	-0.07	0.13	0.66	0.48

Moreover, Dv values indicate that when the multi-layer is activated, biases detected in the zero-layer diminish for most of the points. For example, underestimation at point 11601 decreases from -0.27 to -0.05. It also should be noted that at station 10023, where the multi-layer model shows improved performance when assessed by NSE and RSR, the positive bias in the model is in fact greater. This finding suggests that in this particular station the multi-layer model improves the seasonality of runoff production but causes an overestimation of runoff in general. However, this is only one exception and in general the results presented here indicate that using multi-layer model improves the way water is released from the snowpack into rivers.

The river flow simulations using the multi-layer model is shown in the Supplementary Figure S4.1. As expected, relatively small flows are observed in the main channel until March (about 4,500 $m^3 s^{-1}$ of discharge at the river mouth) as most of the basin remains frozen. As the snowmelt season begins, river flows increase dramatically, peaking during June when almost all snow has melted and water has been released from the snowpack. For instance, between April and June in the main Ob' from about 6,500 $m^3 s^{-1}$ to about 20,000 $m^3 s^{-1}$, and at the river mouth flow increases from about 8,000 $m^3 s^{-1}$ to over 31,000 $m^3 s^{-1}$. During July and August high values of river flow (about 20,000 $m^3 s^{-1}$ at the river mouth) and runoff are also observed although snow melt (as well as SCF) is relatively low.

Besides emphasizing the importance of the spring pulse, this finding suggests that during the summer river flow is maintained from other sources such as rainfall. To explore this option, we produced monthly averaged runoff ratios (Figure 4.2). This figure shows that whilst for most of the year, in the Middle Ob' sub basin, rainfall is an important constituent of runoff in the basin, snowmelt makes an important contribution during spring and early summer. During summer months although there are reportedly high precipitation rates and prior observations suggest that this moisture is lost to evaporation and thus has a minor impact on total river flow [*Serreze et al.*, 2002]. Thus, this permits us to emphasize the key role that snow properties and processes play in the Ob' hydrology.

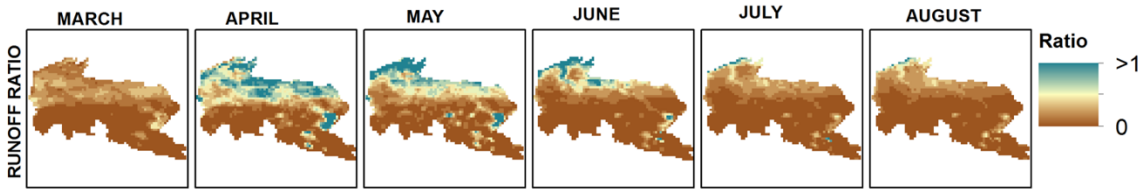

Figure 4.2 Ob' basin runoff-ratio during the melting period (March – August). Ratio between generated runoff and input precipitation. Averaged simulated values between 1979-2011.

4.4.1 SWE and SCF

In order to investigate the difference in river flow responses between the two snow schemes, we examine how they simulate SWE and SCF. In general, we note that the zero-layer model gives unrealistic lower estimates of SWE and SCF across the basin as surprisingly low SCF values were found during winter (typically SCF < 0.35) (See Supplementary Figure S4.2).

In contrast, the multi-layer model, shows a greater spatial variability of SWE and more reasonable SCF results during winter. For the multi-layer scheme, calculated mean differences, Supplementary Figure S4.3, show that during winter months although most of

the basin shows an acceptable agreement between simulated and observed snow cover fraction some important areas show minor discrepancies. Most of them are found in sub basins outside the main Ob' and are mainly caused by overestimates during winter in our simulations. In such areas our simulated SCFs would typically range between 0.99 – 1.00 versus values between 0.94-0.98 as observed by the satellite at the beginning of the season. By contrast, during spring months, the cover fraction is underestimated, especially in the Middle Ob' sub basin. For instance, in April typical simulated values range between 0.4 and 0.6 whereas satellite values range between 0.6 and 0.85. These described patterns are also seen during autumn and summer months – although to a lesser degree.

For SWE, reasonably good agreements were observed in most parts of the basin throughout the year and especially in late autumn and winter. The most significant biases documented were found during the melting season and along the main river channel where our values, when compared to the satellite retrievals, are overestimating SWE. For instance, in May in the lower parts of the river our simulations show snow masses values of 20 kg m-2 versus 8 kg m-2 detected by the satellite.

In a lesser extent, some minor areas in the Ishim, Tobol and Upper Ob' sub basins show discrepancies during winter months given by lower SWE simulated values than those detected by the satellite. For instance, an inspection in the Tobol sub basin during the winter months indicates that SWE is approximately five times lower than the observed value.

4.4.2 Snowmelt and runoff production

The discrepancies when simulating SWE and SCF of the single-layer scheme are then transmitted when producing snowmelt (Supplementary Figure S4.4). We show that this scheme produces less snowmelt and runoff than the multi-layer model during spring and summer months too. Also, when the zero-layer model is used, snowmelt is initiated earlier in the basin (as seen in the DJF plots of snowmelt).

In order to quantify the contribution of the snowpack to runoff, we analysed the link between snowmelt and total runoff, shown in Supplementary Figure S4.5. During the spring, snowmelt contributes over 80% of the total runoff. This fraction is greatest in the Lower, Middle and Upper Ob' sub basins which emphasizes the relevance of these two areas. By contrast, in the other sub basins this value usually does not exceed 50%. As the melting season progresses, snowmelt contributes a lower fraction of the total runoff. For instance, during May, the ratio of snowmelt to total runoff in the Middle Ob' sub basin ranges between 40 and 70%. At this time of the year the snowpack normally generates 25 $m^3 s^{-1}$ of freshwater.

In the sub basins outside the main Ob', although snow ratio is relatively high (about 70%), its real contribution to total runoff is relatively significant (<5ms^{-1}). Naturally, during June and throughout the summer this ratio is reduced to zero in most parts of the catchment in spite of finding patches of snow pack in the Middle Ob' that continue releasing minor quantities of water (<0.5 $m^3 s^{-1}$).

4.4.3 Mechanisms responsible for improved model performance

Next, in order to understand the physical components of the model which have the greatest impact on river flow we have performed additional simulations to determine the physical mechanisms responsible for the improvements that the multi-layer model offers (Figure 4.3). Apart from density of snow (which is automatically computed) and the number of snow layers the most significant improvements of the multi-layer model are the way in which the model computes albedo and the representation of the liquid water holding capacity of the snowpack. The default multi-layer snow model uses prognostic snow properties to calculate snow albedo principally given by characteristics of the snow grain. This option provides the ability to track the time evolution of the snowpack and alter the spectral properties of snow albedo accordingly.

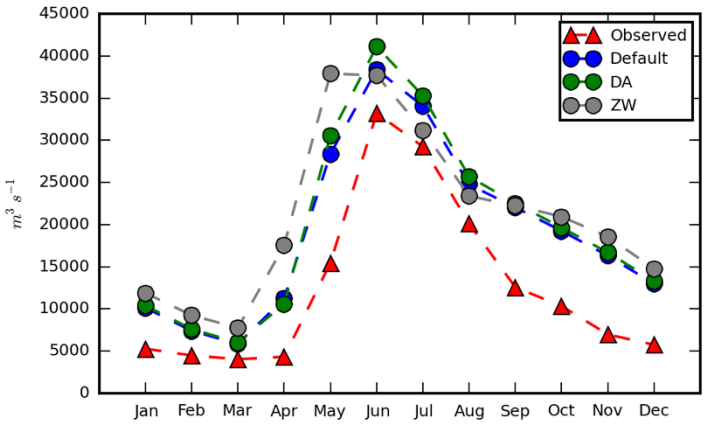

Figure 4.3 Hydrographs showing averaged river flow monthly values for the period 1979-2011 for different configuration of the multi-layer snow model at the station 11801 (mouth of the river).

Default is the multi-layer snow model version used in this study where the spectral albedo scheme is activated and the fraction of liquid water holding capacity of lying snow has a value of 0.05. DA uses the diagnostic albedo instead of the spectral scheme. ZW has a zero liquid water retention in the snow model.

To investigate this question, we first deactivated the option that enables to use this prognostic snow albedo scheme and instead used a simpler option that calculates snow albedo using only snow depth without including the effects of snow aging on the surface albedo. Secondly, we altered the liquid water retention capacities of our model. We set the fraction of liquid water holding capacity of lying snow to zero.

Our experiment suggests that the ability of the multi-layer snow model to represent snow liquid water retention more realistically plays a major role in determining the simulated patterns of river flow. When this component of the model is not used, the river flow at the mouth peaks a month earlier and the overestimation of winter and spring flow is larger. Conversely, the impact of the prognostic albedo scheme is not as significant as the capacity to retain water. The main impact detected is the increase in summer flow when this option is deactivated. These observations are supported also by the calculation of river flow

validation statistics at the mouth of the river. When the spectral albedo scheme is disabled NSE is reduced to from 0.75 to 0.72 (Dv: -0.28, RSR: 0.53) whereas when the snow liquid water retention is not used this value goes down to 0.48 (Dv: -0.36, RSR: 0.71).

Finally, in order to determine the influence of the representation of the capacity of the snowpack to retain liquid water in a snow scheme, we analysed daily outputs of SWE and liquid water content in a typical point in the Middle Ob for a snow-rich and a snow-poor winter (Figure 4.4). As shown previously both models have a similar performance during the cold months. However, between April and May, where the melt of the snowpack is strong, both cases show that the zero-layer model abruptly reduces the snowpack. In contrast, for the same period, the multi-layer model smoothly represents daily SWE peaks that are preceded by periods where the liquid water content rises. Similarly, the presence of SWE peaks at this time scale also shows that the function used to represent the retention of liquid water also allows the possibility of water refreezing before leaving the snow. Thus the ability to simulate the retention of water of the snowpack produces a more detailed representation of the SWE spring peaks. This is a key characteristic that determines the frequency of simulated river flow pulses and thus, in turn influences total hydrological performances.

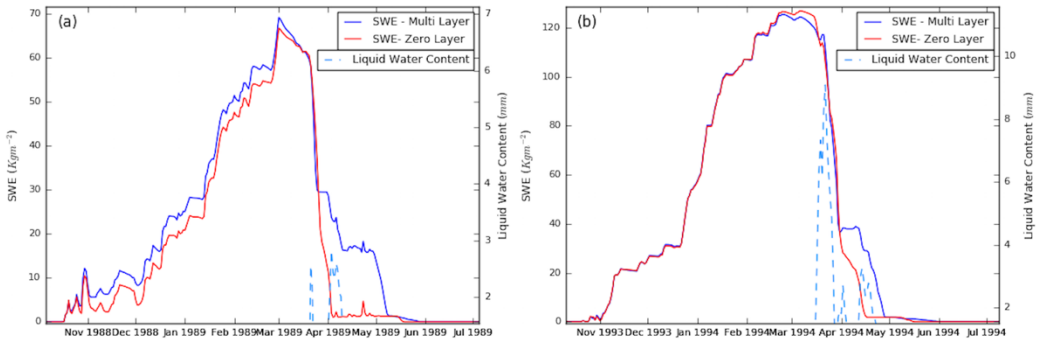

Figure 4.4 Daily outputs of SWE and liquid water content for two seasons. a) 1988-1989, a now-poor winter b) 1993-1994, a snow-rich winter. Location of the point Upper Ob in the Middle Ob' near the 10246 station.

4.5 Discussion

Our analysis shows an acceptable agreement across the basin between simulations using the more physically sophisticated multi-layer snow model and satellite observations. However, in some parts of the basin model performance is hampered by erroneous representation of SCF and SWE. Our results show that in these locations JULES freezes soils and melts snow too early, which in turn affects snow cover fraction value. The implications of this feature are seen in both higher simulated SCF during autumn and lower values at the beginning of spring particularly in the sub basins outside the main Ob'.

Furthermore, in order to explore the biases that lead to overestimation of SWE in the melting season, we explored three possible sources of uncertainty. First, we consider uncertainty in the validation dataset used in this study. Although a lack of clear validation of SWE products persists due to the absence of robust reference values, previous studies have identified that the most probable cause of error in Siberia is the fact that the AMSR-E algorithm does not account for the large grains that typically develop in snow packs (Frei, et al. 2012). Additional causes of uncertainty include surface heterogeneity and masking of the passive microwave signal by liquid water in the snow pack (Tedesco and

Narvekar, 2010). Nonetheless, these product errors have been linked to overestimation of the winter snowpack suggesting that this error in our simulations may be larger. A second source of uncertainty may be given by the driving data. This issue has been addressed by Hancock et al. (2014) and Menard et al. (2015) who, by examining snow values at single sites, suggested that possible biases in the WFDEI dataset in cold sites might be interpreted as biases in the ability of models to simulate snow processes (which is our third source of uncertainty). So in order to explore this option two points typical of the upper middle Ob' and the lower Ob' sub basins are plotted (Figure 4.5). Here we find that in spite of the good agreement between the simulated and observed SWE during the winter months (suggesting a correct accumulation of snow during winter months), in spring our experiment fails to melt all the snowpack leading to a lag of one month in the melting period. This observation suggests that when sufficient snow is provided by the driving dataset the modelled snowmelt rate is not enough to adequately represent the spring melting variability thus showing a deficiency in the model to melt snow. This discrepancy then may lead to spring underestimations of the total runoff and river flow generated by the model.

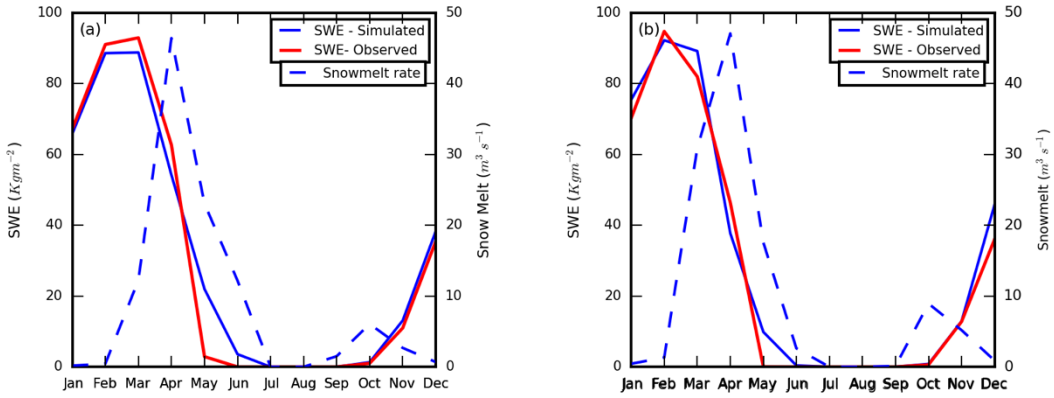

Figure 4.5 Monthly averaged values of SWE simulated and observed values and calculated snowmelt rate. a) Near the intersection between the main Ob and Biya (upper part Sub-Basin 2). b) Near the intersection between Irtysh and Ob (Sub-Basin 6).

In the limited areas where our model underestimated SWE, it is important to consider, as mentioned previously, that AMSR-E tends to overestimate winter snowpack specially under wet snow conditions. This finding suggests that the extent by which mistakes in the interpretation of the validation of the product or biases in the WFDEI dataset contribute to this error in these areas is not clear. In the areas with the largest errors we do not take into consideration snow losses to sublimation as forest cover is not dominant here (the areas mostly present tundra and agricultural fields).

4.5.1 Snowmelt-contribution

In spite of the identified errors, our results show that the multi-layer model captures a strong seasonal link between meltwater and runoff generation, as calculated by our snowmelt:runoff ratio. This contribution is much lower in the sub basins that do not constitute the main Ob. Also we highlighted the strong contribution of spring rainfall to this runoff. In line with this, a previous study by Yang et al. (2002) investigated the dependence of spring runoff on winter cover thickness finding just a weak correlation (R=0.14-0.27) for the years 1935–1999. However, in their study winter snowfall was used as the main indicator for analysing the snowpack rather than snow water equivalent. Thus, our results, which take into account these measures, show an improvement in the representation of processes that dominate the runoff generation in the Ob'.

4.5.2 Impacts on River Flow

We showed that a more complex representation of snow physics improves the simulations of both magnitude and timing of flow across the basin (with just one exception, point 10100). Moreover, our best model performances were obtained in the Upper, Middle and Lower Ob' sub basins where NSE values for the multi-layer are typically over 0.75. A visual inspection of satellite data in this area shows that this part of the basin is

characterised in general by a more natural land cover with less human influence. The differences between points with acceptable and poor performances are also shown in the hydrographs representing the simulated and observed flows at the selected stations (Supplementary Figure S4.6). We find a more accurate simulation of timing and flow peaks of the multi-layer snow model (in particular for downstream points).

We also find that the main difference between those points with high NSE values and those with poorer performances is the erroneous representation of summer and spring flows (for both the zero-snow model and the multi-layer model). This is observed in the sub basins outside the main Ob' (NSE not greater than 0.5 for the multi-layer model) and specially in the station 10100 where this bias is particularly acute (NSE: -0.74, dv:0.92 RSR: 0.97). As discussed above, in this sub basin our simulations tend to underestimate SWE which may cause less water to be released during spring months and which may then consequently produce less runoff. However, for station 10100 in particular, we detected that snowfall in the WFDEI data is between two and three times lower than in other areas where satellite SWE values show similar values. This finding suggests that the poor NSE observed at station 10100 might be due to biases in the WFDEI snow dataset (as explained above), which then affect snow accumulation-masses, resulting in very poor simulation of runoff. Moreover, the zero-snow model tends to persistently overestimate simulated river flow in particular during the spring pulse and also in autumn. This may be surprising since this model underestimates SWE and SCF values. This finding suggests that when this option is used, the capacity of the snowpack to hold water may not be adequately represented, and in contrast additional physical processes (such as soil infiltration) may be regulating the generation of runoff and the subsequent calculated river flow.

It is important to note that the discussed errors found in areas outside the main Ob' do not compromise the estimate of total river discharge, which implies that this error is reduced as the river flows downstream. This finding may be explained by the relatively small runoff contribution of these areas to the main Ob'. Thus this result suggests that the total

downstream discharge of the Ob' can be predicted accurately by JULES when using a more sophisticated snow model. Comparison of the simulated hydrograph with the observed one at the point 11801 (river mouth) shows that the timing of the simulated flow is represented adequately.

Additionally, a study by Yang et al. (2004) found that specially along the Irtysh river, decreases in summer flow are due to both water uses along the river valley for agricultural and industrial purposes and reservoir regulation aimed to reduce summer flooding. They also identified an increase in the winter peak due to reservoir release for power generation, although the effect of these interventions was found to be negligible during winter. Taken together, these observations suggest that in the sub basins outside the main Ob' anthropogenic water uses may also constitute a source of the uncertainty. Nonetheless, the impact of these discrepancies on the model's simulation of flow at the catchment outlet is negligible. Acceptable NSE values are found at both the gauging station at the intersection with the Irtysh (station 11061) and near the mouth of the Ob' river (station 11801) suggests that the Upper, Middle and Low Ob' sub basins dominate the total discharge into the Arctic Ocean. A repercussion of this is that in spite of the local site-specific mismatches that we have identified, possibly originated by biases in the WFDEI that have been already addressed by Ménard et al. (2015), the scale of our simulations (basin scale) seems to compensate for possible errors originated by the forcing data. This finding would suggest that such errors are therefore random and not systematically biased

Lastly, a satisfactory accumulation of snow over the winter months, and subsequent acceptable performances of river flow simulation also indicate a general improvement of catchment hydrology when using the WFDEI dataset at this scale. This contrasts with previous studies that detected that an insufficient snow accumulation when JULES was driven with Princeton, WATCH–CRU, or WATCH–GPCC datasets lead to early snowmelts in this region [*Hancock et al.*, 2013]. Additionally, Brun et al. (2012) found adequate model performances when snow depth, snow duration and SWE values were

calculated driving the Crocus snowpack model under the Interactions between Soil–Biosphere–Atmosphere LSM (ISBA) with ECMWF ERA-Interim data. That study found that driving datasets that used GPCC data rather than CRU for scaling and correcting precipitation provide better snow results. Our river flow results suggest that using the WFDEI GPCC corrected dataset at a basin scale may lead to acceptable simulations of river hydrology.

4.5.3 Implications of an adequate representation of snow and river flow

In the Arctic, where we performed this study, this representation is of critical importance because the observed regional changes in recent decades are often attributed to feedbacks relating to snow cover. In particular, models suggest that the observed increase in regional precipitation, mainly in late autumn and winter, will intensify due to human-induced climate change [*Min et al.*, 2008; *Collins et al.*, 2013]. This increase is driven mainly by a strong amplification of local evaporation, during winter, and also due to enhanced pole-ward moisture transport from lower latitudes, during summer and autumn [*Cai*, 2005; *Bintanja and Selten*, 2014]. The hydrological consequences are stronger water vapour feedbacks, more snowfall and greater snow depths which in turn would favour larger increases in river discharge into the Arctic Ocean [*Ye et al.*, 1998].

Consequences of shifts in the hydrological regime, along with regional warming, may in turn lead to profound downstream consequences. For instance, inundation dynamics in the Arctic control the production and release of methane from wetlands (Wania et al. 2013; Gedney et al. 2004). Additionally, characteristics of river flow discharge are thought to exert a major control on the primary production in the Arctic Ocean via the transport and delivery of nutrients (Li et al. 2009). Additionally, recent satellite observations suggest that warm waters from Arctic rivers intrude landfast sea ice barriers (Nghiem et al. 2014). This process accelerates melt of sea ice leading to an increase in open water extent which in turn causes greater absorption of solar heat intensifying the feedbacks between ocean

and the global energy budget. So, adequately modelling the timing of freezing and melting of soils improves the capacity to estimate the insulating effect that snow cover has on soils during winter months. In the Arctic this may increase our understanding of permafrost extent if this model is applied to areas with extensive permafrost.

Moreover, river ice and ice-jams are thought to be an important component of Arctic hydrology and particularly high peaks characteristics [*Prowse and Beltaos*, 2002; *Beltaos*, 2008; *Lindenschmidt et al.*, 2016]. Ice jams occur during the onset of spring flood along Arctic and several temperate rivers; yet recent warming trends are leading to recurrent midwinter thaws and ice breakups. As the incoming river flow rises in order to accommodate both the keel of the jam and the considerable hydraulic resistance of its underside, flood threat increases [*Beltaos*, 2010]. Thus, river-ice induced flooding have been reported to impact properties, transport infrastructure, ecosystems, hydropower production, and human lives in various northern and temperate locations[*Beltaos*, 1995; *Morse and Hicks*, 2005; *Ettema et al.*, 2009; *Hicks*, 2009]. In order to adequately describe these processes, current ice jams numerical models face with the challenge to couple water flow, ice dynamics, and thermal processes [*Beltaos*, 2008]. Various tools tend to simplify the effect of moving ice on water motion and the its extent, the thickness of a given ice cover, the formation of sheet-ice fronts and their interaction with the main jam release wave [*Shen*, 2010]. So, while river ice models still are evolving, various one-dimensional and two-dimensional frameworks at present exist to simulate the fundamental mechanical, thermal processes and phase changes that govern thermal-ice transport along a river channel (see: [*Lal and Shen*, 1991; *Shen et al.*, 1995, 2000; *Healy and Hicks*, 1999; *Blackburn and Hicks*, 2003; *Liu et al.*, 2006, 2006; *She and Hicks*, 2006]. Nonetheless, the current configuration of JULES, and other LSMs, still fail, to our understanding, to incorporate such river ice or ice jam schemes when simulating river flows in cold regions.

As such, this study does not account for the role of ice jams in the river flow characteristics of the Ob' catchment.

4.6 Conclusions

In this study we have shown that a more complex representation of snowpack structure and processes (provided in the JULES LSM by the multi-layer snow model) improves estimates of snow water equivalent and snow fraction in the Ob' basin. We found that the ability of the LSM to represent the capacity of the snowpack to retain liquid water is crucial to simulate river flow. In particular, this function allows the model to refreeze water before leaving the snowpack which leads to the representation of SWE peaks at daily timescales during the melting season. This produces a more real representations of spring flow pulses and thus better hydrological metrics. In contrast, the absence of this feature in the zero-layer model leads to abrupt melting of the snowpack which in turn may explain the flow overestimation calculated for this model.

Our statistical comparisons also showed few discrepancies between modelled and observed data. These were found in the sub basins that constitute the main Ob' and the Upper Irtysh, Ishim, Tobol and Lower Irtysh sub basins. Such regional differences suggest three possible sources of uncertainties that may drive errors in the evaluation of snow – river flow links. The first one is given by the validation datasets, which corresponds to a possible overestimation of our reference snowpack in this case. A second one is given by the meteorological forcing data. We identified areas where snow seems not to accumulate sufficiently during winter leading to lower runoff and river flow values in the melting. A third source of uncertainty is due to flaws in the model. For instance, we found areas where snow accumulated adequately during winter but a delayed spring pulse lead to lower hydrological performances. In addition, anthropogenic interventions, such as flow attenuation, are not accounted for here, which may also explain poor model performances in areas with more intervened land use. Nonetheless, at the catchment scale we note that

river discharge at the mouth of the Ob' is reproduced well. This suggests that biases detected are therefore random and not systematic so at this scale, river flow is better represented when a more complex set of physical parameters are used in a snow model in a LSM.

Finding that a more physically-realistic representation of snow leads to better simulation of river hydrology is crucial to assess the effects that a changing climate will have in cold regions and how this in turn would determine feedbacks in the climate and physical system.

5. Global floods and water availability driven by atmospheric rivers

Homero Paltan[1,2*], Duane Waliser[2], Wee Ho Lim[3,4], Bin Guan[2,5], Dai Yamazaki[6,7], Raghav Pant[3], Simon Dadson[3]

[1]School of Geography and the Environment, University of Oxford, Oxford, UK.

[2]NASA Jet Propulsion Laboratory, California Institute of Technology, Pasadena, CA.

[3]Environmental Change Institute, University of Oxford, Oxford, UK.

[4]Institute of Geographic Sciences and Natural Resources Research, Chinese Academy of Sciences, Beijing, China.

[5]Joint Institute for Regional Earth System Science and Engineering, University of California, Los Angeles, California, USA.

[6]Institute of Industrial Science, University of Tokyo, Tokyo, Japan

[7]Department of Integrated Climate Projection Research, Japan Agency for Marine-Earth Science and Technology, Yokohama, Japan.

*Published Article: Paltan, H., Waliser, D., Lim, W. H., Guan, B., Yamazaki, D., Pant, R., & Dadson, S. (2017). Global floods and water availability driven by atmospheric rivers. *Geophysical Research Letters*, 44, 10,387–10,395. https://doi.org/10.1002/2017GL074882

5.1 Abstract

Whilst emerging regional evidence shows that atmospheric rivers (ARs) can exert strong impacts on local water availability and flooding, their role in shaping global hydrological extremes has not yet been investigated. Here we quantify the relative contribution of ARs variability to both flood hazard and water availability. We find that globally, precipitation from ARs contributes 22% of total global runoff, with a number of regions reaching 50% or more. In areas where their influence is strongest, ARs may increase the occurrence of floods by 80%, whilst absence of ARs may increase the occurrence of hydrological droughts events by up to 90%. We also find that ~300 million people are exposed to additional floods and droughts due the occurrence of ARs. ARs provide a source of hydro-climatic variability whose beneficial or damaging effects depend on the capacity of water resources managers to predict and adapt to them.

5.2 Introduction

Key water resources and flood risk management decisions depend on our understanding of drivers of hydrological variability [*Gleick*, 1989; *De Loe and Kreutzwiser*, 2000; *Trenberth*, 2005; *Blöschl et al.*, 2007]. The magnitude and timing of runoff responds to hydro-climatic variability across sub-seasonal to inter-annual time-scales. This variability is strongly connected to the large scale transport of moisture in the atmosphere which is in part controlled by large-scale atmospheric modes of variability such as El Niño–Southern Oscillation (ENSO), North Atlantic Oscillation (NAO), Pacific/North American (PNA) teleconnection, the Indian Ocean Dipole and others [*Mestas-Nuñez and Enfield*, 1999; *Viles and Goudie*, 2003; *McCabe and Palecki*, 2006; *Kenyon and Hegerl*, 2010b]. Apart from these large-scale modes, regional and local-scale climates also modulate narrow, elongated corridors of enhanced water vapor transport in the lower troposphere, known as atmospheric rivers (ARs) [*Guan et al.*, 2013; *Guan and Waliser*, 2015b]. ARs are understood to be responsible for over 90% of the total tropical-temperate vertically integrated horizontal water vapor flux [*Zhu and Newell*, 1998; *Ghanbarian-Alavijeh et al.*, 2010; *Gimeno et al.*, 2014; *Dacre et al.*, 2015; *Guan and Waliser*, 2015b]. Their typical horizontal dimensions might be several thousand km long with width ~500 km [*Ralph and Dettinger*, 2011], and at any given time there may be 3–5 ARs in each hemisphere [*Zhu and Newell*, 1998].

Several prior analyses have documented the local implications for water resources of AR-driven precipitation. For instance, in the West Coast of the U.S. and in Europe, ARs supply on average about 30% of total precipitation [*Lavers and Villarini*, 2015a] leading to peak historical floods in Washington state [*Neiman et al.*, 2011; *Ralph and Dettinger*, 2011; *Lavers and Villarini*, 2015b]. Also, the influence of these rains on water supplies has been quantified in California where ARs contribute 30–50% of river flow [*Dettinger*, 2011a]. In Europe, AR-triggered rainfall has been observed in the Iberian Peninsula, Norway,

Poland, France, and Great Britain, where ARs have been found to contribute to extreme winter flooding [*Lavers and Villarini*, 2015a; *Ramos et al.*, 2016]. In the Southern Andes they are also thought to drive ~80% of total winter precipitation [*Viale and Nuñez*, 2011]. Globally, a recent study has documented considerable hitherto unknown landfall and inland penetration of ARs in areas with less extensive records, such as South-East Asia, South America, South Africa, Australia, and Central Europe [*Guan and Waliser*, 2015b]. Thus, the new global areas of AR landfall and penetration, along with the previous documented strong local influence of ARs suggest that ARs may be an important driver of global terrestrial hydrology.

In this paper, we utilize a global AR database to evaluate for the first time, what is the influence of these horizontal moisture transport extremes in shaping global land surface hydrology and its variations? To answer this question, we first quantify the contribution of ARs to global runoff, to soil moisture content and to snowpack size. Next, using a uniform observation and modeling methodology, we identify new regions and catchments of the globe where ARs dominate the magnitude and occurrence of hydrological droughts and floods. Lastly, we calculate the additional population exposed to hydrological drought and flood hazards due to ARs.

5.3 Methods and Data

5.3.1 Land surface hydrology

We run a Land Surface Model (LSM) in order to generate snow water equivalent (SWE), total runoff, and total soil moisture under *control* meteorological conditions. For this we force the Joint UK Land Exchange Scheme (JULES) (for details see [*Blyth et al.*, 2006b; *Best et al.*, 2011]) with the meteorology obtained from the latest WFDEI global gridded reanalysis product covering the period 1979–2010 (GPCC corrected) [*Weedon et al.*, 2014] and the default configuration of the model. Soil properties are obtained from the

Harmonized World Soil Database (HWSD) from FAO – IIASA [*Fischer et al.*, 2012] and the hydraulic soil properties used here are derived following the method of Cosby et al [*Cosby et al.*, 1984]. The temporal time step of our control meteorological conditions is 3 hours and the spatial resolution is 0.5º x 0.5º. In our *perturbed* simulation we derive AR precipitation values based on a global AR database [*Guan and Waliser*, 2015b] and then we subtract the precipitation fraction corresponding to ARs for this at each time step. The difference between the control and perturbed runs is in the precipitation forcing. At any given time step, the control run is driven by a global map of the reanalysis precipitation. The perturbed run is driven by a version of the reanalysis precipitation where precipitation falling inside of detected AR boundaries during that time step is removed. Also, various AR detection techniques exist in the literature, often emphasizing different aspects of ARs and indicative of complementing views on the AR definition. In this study, we take a broad definition of ARs, which, as in *Zhu and Newell*, [1998], does not limit the existence of ARs to the extratropics or by any other regional requirements.

In both cases, we use the default configuration of JULES which, when given total precipitation, partitions rainfall and snowfall at the given near surface air temperature of 274.0 K. Precipitation below this threshold is assumed to be snowfall. We also activate the default multi-layer scheme model in JULES, which permits a maximum of three layers (snow depths of 0.1, 0.15, and 0.2 m) where the density of fresh snow is set to 100 kg m^3. This model also partitions snowfall between that which is intercepted by the canopy and that which falls beneath it and uses a spectral scheme to calculate snow albedo. The default configuration represents soils with four vertical layers, each with its own temperature and soil moisture. Runoff is generated using TOPMODEL, which has been shown to provide a detailed physical representation of the basin leading to improved simulations of the seasonal peaks, subsurface runoff, and dry season flows[*Clark and Gedney*, 2008]. The topographic supporting datasets for TOPMODEL is calculated using an improved

topographic index based on a 15 arc-second resolution global map [*Marthews et al.*, 2015b].

5.3.2 River routing and hydrological extremes

Daily generated runoff from both the control and perturbed simulations are used to drive the CaMa-Flood model [*Yamazaki et al.*, 2011] in order to generate daily river discharge at a spatial resolution of 0.25°x0.25°. At each grid location, the annual maxima of river discharge are extracted from the computed daily values. Then these annual maxima are fitted using a two-parameter Gumbel distribution following previous studies [*Gumbel*, 1941; *Dankers and Feyen*, 2009; *Hirabayashi et al.*, 2013].

For consistency with conventional practice in hydrology, we define the threshold for droughts and floods in terms of flow-duration percentiles, which are quoted as exceedance probabilities. We define the threshold for hydrological drought as the flow which is exceeded 90% of the time (hereinafter referred to as Q90) [*Sheffield and Wood*, 2011; *Van Loon*, 2015a]. We define the high flow threshold as that flow which is exceeded 10% of the time (referred to as Q10). Then a change in extreme discharge magnitude was calculated as percentage in change in the hydrological thresholds, Q90 and Q10, between the control and perturbed simulation. Thus, the contribution of ARs to low and high flows are obtained as the change in the magnitude of the return period of river discharge for Q90 and Q10 flows respectively. In our analyses, we do not account for human interventions and flow regulations such as dams or reservoirs.

Next, we assessed how the presence of ARs increase the periodicity of exceedance of hydrological droughts and floods events. So we follow a similar approach used by Dettinger and Cayan to assess the role of ARs in fluctuations of drought episodes in the California Delta [*Dettinger and Cayan*, 2014]. We first aggregate the gridded daily river discharge into monthly subsets for both the control and the disturbed simulation. Later, a rule is applied that if the minimum value within an aggregate is less than the Q90 value

(obtained from previous steps), the aggregate is considered as one with an event of hydrological drought. Similarly, if the maximum value within an aggregate is seen to exceed the Q10 value, we consider such aggregate as one with a high flow. So, for each grid location, and simulation, we obtain a record of the frequency of events that were categorized as hydrological drought or flood. For each grid location, we then calculate how the absence of ARs increases the occurrence of hydrological drought events; and how the presence of ARs increases the occurrence of high flows events.

5.3.3 Exposure to droughts and floods

We calculate the number of people exposed to areas with strong hydrological drought and flood signals driven by variability of ARs storms. For droughts, we define the signal as strong in locations where the absence of ARs increase the occurrence of droughts events by more than 50%. We then delineate catchment boundaries using data from GRDC [*Global Runoff Data Centre*, 2007]. From here, we select those catchments where the drought signal is dominant. We estimated the population exposed to droughts by overlaying a gridded population dataset provided by GPWv4 [*Center for International Earth Science Information Network - CIESIN - Columbia University*, 2016] with the pattern of catchments showing a strong AR-driven drought signal.

Last, in order to calculate people exposed to floods driven by ARs, we compute flood hazard maps from both, the *control* and the *perturbed* simulations. Flood hazard is computed using the close relationship, given by a cumulative distributive function, between flooded area and floodplain water depth or total water storage (sum of river and floodplain storage)[*Yamazaki et al.*, 2011]. For this, we fit the two-parameter Gumbel distribution using the annual maxima of river water depth maxima (which is used as proxy for total water storage). From this distribution, we derive the 100-year flood inundation fractions for both simulations. We then estimate the increase in flooded area due to ARs.

Using the GRDC data we then calculate the population exposed to AR-driven floods by multiplying the population of each grid by the fraction of its flooded area.

5.4 Results

5.4.1 Land surface hydrology

The mean annual contribution of ARs to global runoff is 22% (Figure 5.1a). ARs contribute more than 50% of the mean annual runoff on the east and west coasts of North America, the south-eastern part of South America, location in the south of Chile, France, northern Spain and Portugal, the United Kingdom, Southeast Asia and New Zealand. The inland advection of moisture associated with ARs exerts a smaller influence (less than 30% of mean annual runoff) on the spatial pattern of runoff in southern parts of the Amazon basin, southern Africa and India. Moreover, ARs contribute an additional 15–25% to soil moisture in these areas as well as in Australia, Iran and continental Europe (Figure 5.1b).

The moisture associated with ARs also exerts a significant control on the accumulation of the snowpack in the northern hemisphere (but notably not in western Europe; Figure 5.1c). Our analysis is in agreement with earlier local results that ARs contribute approximately 40% of the moisture stored in the snowpack of the Sierra Nevada mountain range [*Guan et al.*, 2013], but we demonstrate here that their influence is much wider. We also show a yearly contribution to the snowpack that ranges between 25 and 50% in areas extending to Alaska, Quebec, the Pontic Mountains in Turkey, and the Altai and Hangai Mountains in Mongolia (Figure 5.1c). In mountainous areas, our findings indicate that precipitation driven by ARs supplies approximately 34% of the snowpack throughout the year in the Alps, 11% in the Himalayas and 68% in the Southern Andes (see Supporting Figure 5, S1).

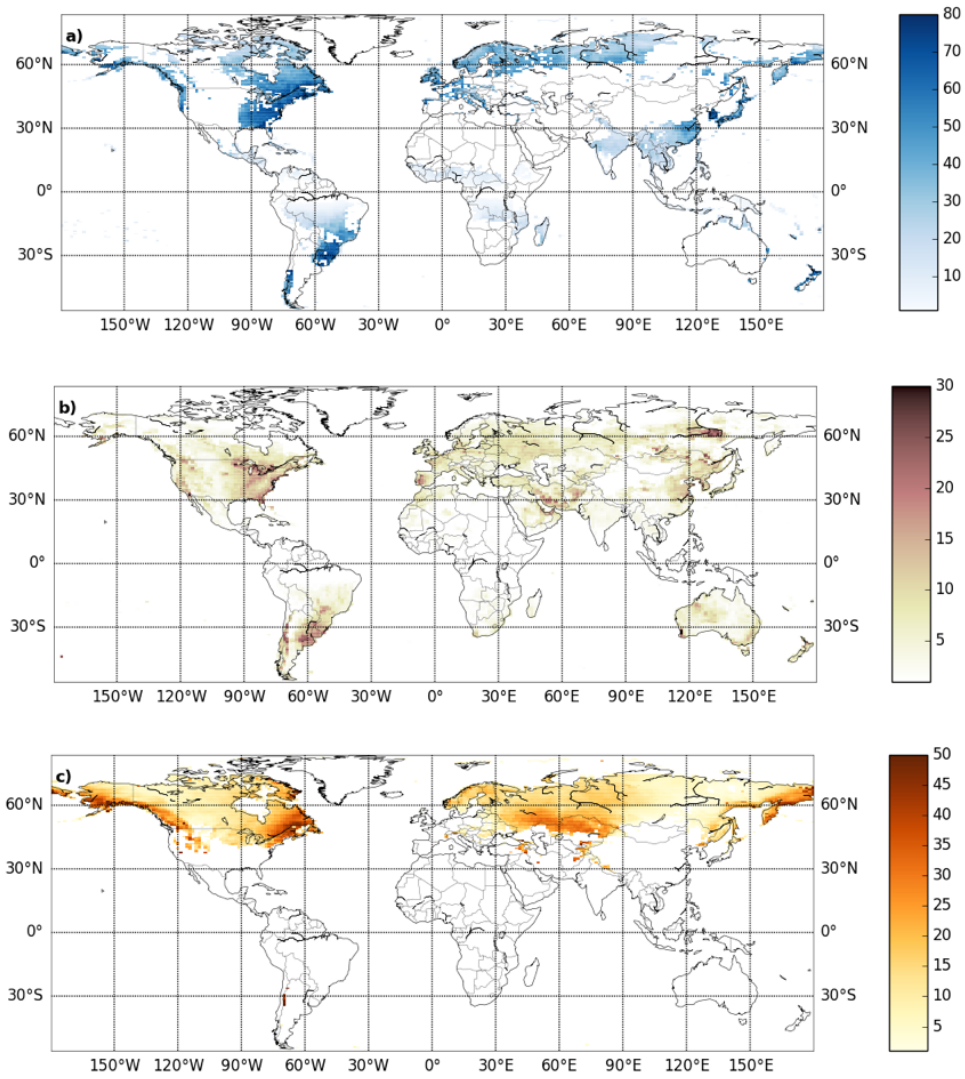

Figure 5.1 Mean annual contribution of ARs to hydrological land surface variables. Mean annual (1979-2010) contribution (%) of ARs to a) runoff, b) total soil moisture content, c) snow water equivalent.

5.4.2 Contribution of ARs to the intensity of extreme flows

The contribution of ARs to flow extremes across global major catchments is shown in Figure 5.2. The catchments where the impact is most notorious are located in extra-tropical regions (north of 30^{o}N and south of 30^{o}S) including rivers in the California's Central Valley, inland catchments in the south of South America, the Iberian Peninsula (Douro catchment), in Turkey and Iran (for example Great Kivar in Iran and Dicle Firat in Turkey), and the Murray-Darling in Australia. In these catchments, the contribution ARs typically contribute to >80% to both low and high flows. Also, in catchments such as the Thames (U.K.) and the Escaut (France-Belgium) the contribution of ARs to low flow is ~80% despite showing smaller contributions to the high flow (about 40%). Also, catchments where ARs contribute considerably (~ 50%) to both high and low flows are found along the coast of the Gulf of Mexico in the U.S., the Uruguay river in South America, the Colorado in Argentina, the Seine and Rheine in Europe, the Tigris-Euphrates and Aral in Eurasia, the Amur in Asia (Russia and China). Also, significant contributions to extreme flows (~40%) can be found in several major catchments such as the, the Parana in Brazil, the Po and Elbe in Europe, catchments in Siberia, and several catchments in China. A smaller regional influence (<20%), is found in tropical basins such as the Mississippi in the U.S, the Amazon, catchments in Central America, the Congo and other African rivers, and the south of Asia including the Himalayan-fed catchments. Nonetheless, other several small catchments show also an important impact of ARs (Supporting Figure 5, S2). For example, we detect that in several areas in the UK, New Zealand, and Australia, ARs may contribute to up to 80% of high and low flows. Similarly, in large catchments such as the Mississippi, the Paraná in Brazil, and Amur, we detect high standard deviations (~30) in our catchment measures (see Supporting Table S1) which reflects very important contributions (80%) to high flows in several sections of such catchments. Our findings are also demonstrated by calculating flow duration curves of six catchments, across different

regions, where we have detected a major influence of ARs; see Supporting Figure 5, S3. For instance, in the Sacramento catchment, flows of 1,000 m3/s are likely to be exceeded less than 5% of the time when there are no ARs. By contrast, in the presence of AR-driven precipitation, the likelihood of river flow exceeding 1,000 m3/s increases to approximately 20%. In contrast, the likelihood of exceedance of the reference low flow of this river (210 m^3/s) decreases from 90% when ARs are present, to 60% when they do not make landfall.

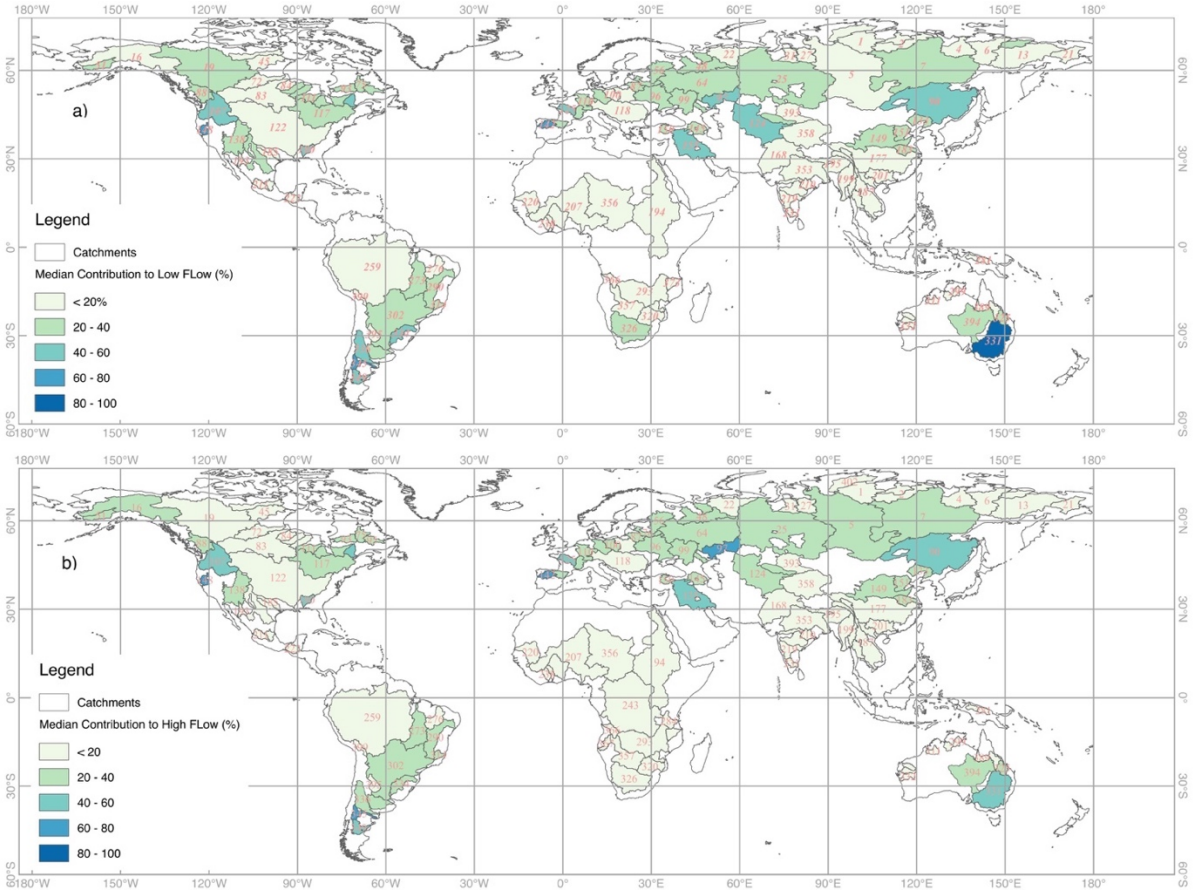

Figure 5.2 Median contribution of ARs to extreme flows: a) Low flows and b) High flows. Low flow is defined here as the Q90 flow, so this is the flow that is expected to be equaled or exceed 90% of the time.

High flow is defined here as the Q10 flow, so this is the flow that is expected to be equaled or exceeded 10% of the time. Period 1979-2010. Contributions of <1% were removed and also catchments with a drainage area < 75 km^2 are not shown here. Also, the Po and Thames catchments are not plotted in this figure. A list of catchments IDs, and values for the catchments not shown in this figure is presented Supplementary Table S5.1.

5.4.3 Contribution of ARs to the occurrence of droughts and floods

The role of ARs in the occurrence of events of hydrological droughts and floods is shown in Figure 5.3. We detect that in several temperate catchments the frequency of periods of hydrological drought increases when AR-driven moisture fluxes are absent (Figure 5.3a). In the most significant cases, the absence of ARs can increase the frequency with which such hydrological drought events occur by up to 90%. Regions where this behaviour is observed include the Central Valley in California (previously documented by [*Dettinger and Cayan*, 2014]), The Missouri River in the U.S., the Canadian shield, the Parana, the Iberian Peninsula, the Mediterranean coast of Europe, the Amur in Russia and China, the area around the Black Sea, north of in Iran and the Yellow River in Asia. A strong signal is also detected in the Murray-Darling outlets and in New Zealand. Also, in the Orange River of South Africa and in the Indus basin an important impact of the absence of ARs is also identified. Lastly, we observe a minor influence of ARs in low flow episodes in Arctic basins such as the Ob' in Russia and the Yukon area, in Canada (20%).

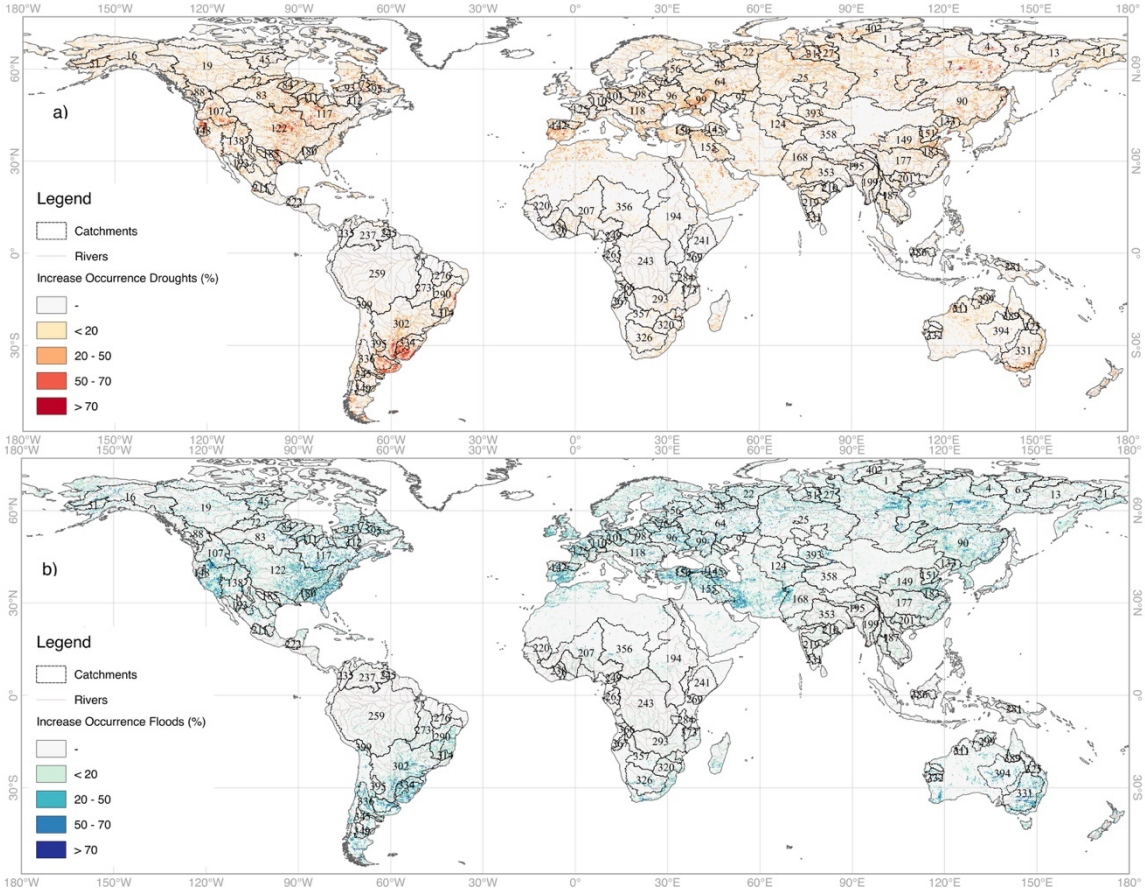

Figure 5.3 Role of ARs in the frequency of occurrence of hydrological droughts and floods: a) Increase in the occurrence of droughts events due to the absence of ARs, and b) Increase in the occurrence of flood events due the presence of ARs.

A hydrological drought event is detected when, within a monthly aggregate of daily flows, its minimum value is observed to be below the Q90 threshold. A flood event is detected when, within a monthly aggregate of daily flows, its maximum value is observed to be above the Q10 threshold. Total increase in the occurrence of events for the period 1979-2010. Catchments with drainage area <75 km^2 are not labelled. A list of catchment ID is presented in Supplementary Table S 5.1.

The role of AR-driven fluxes in increasing the periodicity of high flow events is shown in Figure 5.3b. This observed signal is more widespread than that for hydrological droughts. For instance, in the Central Valley in California (particularly in the upper parts and at the

coastal ends of those catchments), periods of high flows follow closely the variation in the occurrence of ARs. Such strong signal has been previously detected by, for example, Ralph et al. [2006] who attributed flood events between 1997-2004 in the Russian River, California to AR conditions. Similarly, Neiman et al.[2011] found a close link between AR landfall and annual peak daily flows in Western Washington between 1980-2009. We also find that on the North American east coast, ARs increase the occurrence of flooding events in the Mississippi river and in other several small catchments. In addition, ARs significantly impact the occurrence of high flows in Turkey, Spain, and France (in the Seine and Loire rivers ARs have increased the occurrence of high flow events by 80%). Also, in Britain, Germany (e.g., the Rhine river) and in Eastern Europe, ARs may increase the occurrence of high flows by 40%. A similar pattern is observed in Central Asia and in China (up to 50% in the lower parts). In Australia and New Zealand, the signal is confined to coastal regions, for example in the Murray-Darling basin ARs increased by 80% the occurrence of high flow events. In Africa, we find a significant signal in north and southeast Africa, for example in Morocco (the Moulouya River, 40%) and in the Orange River in South Africa (up to 25%).

5.4.4 Societal risks and hazard associated with atmospheric rivers

We calculate the population exposed to droughts and flood hazards that stem from ARs by representing detected high and low flow episodes across major global catchments (see Supporting Figure 5, S4). We detect that on average approximately 350 million people have been directly exposed to hydrological droughts that may result from the occurrence of ARs. The catchments with the greatest exposed populations are: the Parana and Uruguay Rivers, the Mississippi (principally around the Missouri tributary) and the St. Lawrence Rivers in the U.S., and the Dnieper and Don basins in Eurasia (especially in the region between Russia and Ukraine).

By contrast, approximately 300 million people across the globe are exposed to additional flood risk due to the occurrence of ARs. The most significant areas with increased exposure are found in California, the Mississippi basin, in the Parana river, in Iberian Peninsula, southern Iran, the Amur and Yangtze river and the Murray-Darling Basins (see Supporting Figure 5, S5). This finding suggests that improved understanding, and in turn modeling and prediction capabilities, of the way in which ARs influence hydrometeorological variability will benefit water managers, flood forecasters and civil protection authorities.

5.5 Discussion and Conclusions

The presence or absence of ARs significantly drives global hydrological variability, which occurs on seasonal and inter-annual time-scales and is controlled by the frequency with which specific regions and catchments are affected by ARs in a hydrological year. Consistent with the original (global) formulation of ARs developed by [*Zhu and Newell*, 1998], also captured in the formulation by Guan and Waliser [2015], we find that the impacts of ARs extend beyond the extratropical areas commonly examined (e.g. western N. America and Europe), and are also not restricted to the extratropics. We also recognize that other modes of climate variability may contribute to the flow events calculated here but we are emphasizing the connection to extreme, synoptic horizontal transports (often referred to as Atmospheric Rivers). For example, as the above definitions were developed to include the transient, filamentary moisture transport in the Asian monsoon, the high-peak flow events detected in this region could include contribution from the monsoon flow. Similarly, this broad AR definition may also be applicable to areas where individual Low-Level-Jet (LLJ) features are linked with deep convection and consequently strong precipitation and high peak flows – albeit those specifically with long narrow "river-like" features of moisture transport. For instance, in the central United States, the AR known as 'Maya Express' corresponds to the region of enhanced moisture transport within the Great

Plains LLJ which has been connected to heavy precipitation in the area [*Dirmeyer and Kinter*, 2009; *Lavers and Villarini*, 2013]. This potential connection between LLJs and ARs may also be observed in areas where this link has been documented such as India, Southeast Asia, Australia and Oceania, Southern Brazil, Chile, Central Africa or Iran where ARs have been documented to overlap LLJ s[*Gimeno et al.*, 2016].

While a few previous reports highlight the major global impacts of ARs in coastal regions close to the areas where ARs make landfall [e.g. Guan and Waliser, 2015], our findings highlight that significant advection of moisture inland makes an important contribution to runoff, soil moisture and snowpack accumulation (Figure 5.1a, 5.1b and 5.1c) in many areas of the globe, and thus ARs importantly shape global terrestrial hydrology. In the areas where AR-driven precipitation makes a significant contribution to the annual water supply, the prolonged absence of ARs may result in intense hydrological droughts. For instance, Dettinger [*Dettinger and Cayan*, 2014] attributed multi-decadal drought in the California Delta, including the recent extreme drought, to fluctuations in precipitation arising from the lack of large AR-driven storms. In this study, we have identified areas across the globe which may be exposed to similar drought patterns. Our findings are also consistent with the paths of moisture that are thought to be the primary source for heavy precipitation in mountain ranges the U.S. Intermountain West as noted by [*Alexander et al.*, 2015]. Regionally, our findings also support the importance explored by [*Rutz et al.*, 2015] of the evolution of ARs in the U.S West Coast.

Nonetheless, in our perturbed simulation, we do not account for the atmospheric implications of removing AR-driven precipitation. For instance, we do not alter the radiation fields to account for clouds that transport ARs-driven precipitation. Also, we do not account for further interactions between soil moisture and temperature at the near-surface [*Seneviratne et al.*, 2010]. At the same time, the representation of plant responses

in JULES has been found to leave wetter soils thus decreasing the likelihood of detecting droughts [Prudhomme et al., 2014]. As a result, our drought estimates are conservative and our study provides a broad, global consideration of the hydrological impacts of ARs, which allows comparisons between one region to the other. Also, in our drought estimations we do not account for water management options such as water transfers that might be hampered by water deficits due to AR-related variability. For example, in California the Sierra Nevada contributes about 70% of the annual water supply to Los Angeles with a population of nearly 5 million people [*Negin et al.*, 2015]. In consequence, we presume that our estimates of the population exposed to droughts are underestimated as ARs indirectly amplify the propagation of drought risk into societies. Thus we also acknowledge the existence of other types of droughts not addressed in this study (e.g. soil moisture drought or socio-economic drought, see [*Van Loon*, 2015a]) that may develop into more complex categories of droughts.

Similarly, we have identified global areas where the contribution of ARs to high flows may result in floods. Also, we find that in areas such as California, the Mississippi Catchment in the United States, Parana in Southern Brazil, the Murray Darling basin in Australia, Turkey, and in areas of the Amur River in China, ARs are not only major contributors to high flow events and also, via variability that leads to their absence, but also, they play an important role in the occurrence of hydrological droughts. Nonetheless, in spite of this hydrological significance the skill associated with forecasts of AR-driven precipitation remains limited [*Wick et al.*, 2013] and improvements in monitoring and modelling of these ARs offer scope for improving natural hazard risk reduction. The extent to which the global occurrence and intensity of ARs will be affected by future climate change is expected to increase, regional assessments have projected intensification owing to higher atmospheric moisture content under warming scenarios [e.g., *Dettinger*, 2011; *Lavers et al.*, 2013].

Taken together, our findings demonstrate that through extreme horizontal moisture transfers, ARs exert a widespread and strong control on spatially heterogeneous patterns of hydrological variability to a greater extent than previously understood which enhances our understanding of hydrological risks. Improvements in the ability of models to predict ARs will be important for water resource management and flood hazard assessment; and warrant further attention in the light of future climate change.

5.6 Acknowledgments

This work was supported by the National Aeronautics and Space Administration. This research in part was carried out on behalf of the Jet Propulsion Laboratory, California Institute of Technology. WHL acknowledge funding support from the CAS President's International Fellowship Initiative (2017PC0068) and the National Key Research and Development Program of China (2016YFA0602402).

Our model outputs containing the daily land surface hydrological variables for both the control and disturbed simulations are available here: https://figshare.com/s/97f8d14ed5fe66e74eb6. Also, our outputs containing the gridded extreme river flow and river depths values (control and disturbed) can be downloaded here https://figshare.com/s/fad4d001515e42ae17e9 and here https://figshare.com/s/d796d04c113c87c81c58 respectively.

6. Global implications of 1.5 °C and 2 °C warmer worlds on extreme river flows

Homero Paltan*[1], Myles Allen[2], Karsten Haustein[2], Lena Fuldauer[2], Simon Dadson[1]

1. School of Geography and the Environment, University of Oxford, Oxford, UK.

2. Environmental Change Institute, University of Oxford, Oxford, UK.

*Published Article: Paltan H , Allen M., Haustein K., Fuldauer L., & Dadson S. "*Global Implications of 1.5 °C and 2 °C Warmer Worlds on Extreme River Flows"*. Environmental Research Letters, 2018. http://iopscience.iop.org/10.1088/1748-9326/aad985.

6.1 Abstract

Targets agreed to in Paris in 2015 aim to limit global warming to "well below 2 °C and to pursue efforts to limit the temperature increase to 1.5 °C above pre-industrial levels". Despite the far-reaching consequences of this multi-lateral climate change mitigation strategy, the implications for global river flows remain unclear. Here we estimate the impacts of 1.5ºC vs 2.0ºC mitigation scenarios on peak flows by using daily river flow data from a multi-model ensemble which follows the HAPPI Protocol (that is specifically designed to simulate these temperature targets). We find agreement between models with regard to changing risk of river flow extremes. Moreover, we find that the response at 2.0°C is not a uniform extension of the response at 1.5 ºC, suggesting a non-linear global response of peak flows to the two mitigation levels. Yet committing to the 2.0ºC warming target, rather than 1.5ºC, is projected to lead to an increase in the frequency of occurrence of extreme flows in several large catchments. In the most affected areas, predominantly in South Asia, while region-specific features such as aerosol loads may determine precipitation patterns, we estimate that under our 1.5ºC scenario the historical 1-in-100-year flow occurs with a frequency of 1-in-25 years. At 2.0ºC similar increases are observed in several global regions. These shifts are also accompanied by changes in the duration of rainy seasons which influence the occurrence of high flows.

6.2 Introduction

The Conference of the Parties of the United Nations Framework Convention on Climate Change (UNFCCC) in its Paris Agreement in December 2015 agreed to hold "the increase in the global average temperature to well below 2 °C above pre- industrial levels and to pursue efforts to limit the temperature increase to 1.5 °C above pre-industrial levels". The simplicity of these targets led parties to the treaty to embrace a common climate strategy with the aim of preventing the risks and impacts associated with unabated climate change [*Hulme*, 2016; *Rogelj et al.*, 2016b; *Schellnhuber et al.*, 2016].

Yet, the assumption that a 2°C limit is a safe bar as far as climate-change related tipping points are concerned, has diverted attention away from the difference in impacts between worlds in which global temperatures are stabilized at 1.5^{o}C instead of 2.0^{o}C. Overlooking these thresholds may have important consequences given the sensitivity of high flows to radiative forcings [*Milly et al.*, 2002]. In particular, early studies projected an increase in annual runoff and flow peaks in snow-dominated catchments as a result of climate change [*Nijssen et al.*, 2001a]. From here, several studies have projected increases in high flow and flood frequency in Southeast Asia and eastern Africa, although important shifts have also been calculated for other regions such as the northern Andes, North America, and Eastern Europe. [*Okazaki*, 2012; *Hirabayashi et al.*, 2013; *Dankers et al.*, 2014; *Koirala et al.*, 2014]. As such, the impacts of extreme river flows on human lives, socio-economic development, and monetary losses may be particularly important in a changing climate [*Peduzzi et al.*, 2009; *Wake*, 2013; *Arnell and Lloyd-Hughes*, 2014; *Jongman et al.*, 2014; *Winsemius et al.*, 2015; *Arnell and Gosling*, 2016].

More recently, by downscaling climate projections and finding the corresponding year in which various levels of atmospheric warming are exceeded, a positive increase in future flood risk has been projected [*Alfieri et al.*, 2017]. While the future increment in flood

risks is important when compared to its historical baseline, the impacts appear to be more important at 4.0°C if compared to the less evident shifts observed between 1.5°C and 2.0°C.

Yet, since climatological biases in current climate models experiments, such as the Coupled Model Intercomparison Project, remain of the order of 0.5°C these efforts may not be sufficient to differentiate the risk associated with these two levels of warming [*Hulme*, 2016; *Mitchell et al.*, 2016]. For the hydrological cycle, in particular, the distribution of global precipitation between CMIP scenario experiments does not respond uniformly between CMIP scenario experiments due to the changing role of non-CO_2 forcing over the 21st century and also due to the precipitation sensitivity to emission-scenarios. This, in turn, makes it difficult to differentiate whether detected differences result from additional warming or additional factors. So, extracting anomalies for 1.5°C and 2.0°C levels of warming from the traditional CMIP scenarios driven experiments may not be scientifically robust [*Mitchell et al.*, 2016].

With such concerns in mind, The HAPPI protocol was specifically designed to simulate the specified Paris Agreement temperature targets (1.5°C and 2.0°C) as precisely as possible by separating the impact of an additional approximately half degree of warming from uncertainty in climate model responses and internal climate variability [*Mitchell et al.*, 2017]. So, unlike other multi-model exercises, HAPPI does not exclusively rely on prescribed radiative forcing protocols to project the future temperature evolution, but robustly constrains it using prescribed future Sea Surface Temperatures (SSTs) as well. This effectively reduces the influence of model sensitivity and results in a narrowly defined range of future temperature targets. Thus, the HAPPI Protocol provides an improved framework for the analysis of the impacts of an additional half degree of warming.

In this study, we estimate the extent to which global peak river flows seen under a 1.5°C scenario differ from those under a 2°C scenario. In particular, we investigate where shifts in high flow occurrence would be more important under these climate scenarios. We follow the HAPPI experimental protocol, to use the multi-model-ensemble daily output of four atmosphere-only general circulation models (AGCMs). Total runoff values were used to drive a river-flow routing scheme to calculate daily river flows for the: a) present baseline (2006–2015), b) 1.5°C scenario, and c) 2°C scenario. From here we compute river flow extreme statistics to calculate changes in high flow occurrence and magnitude.

6.3 Methods

6.3.1 HAPPI experiments and data

The HAPPI protocol provides three 10-year simulation periods with prescribed atmospheric forcing, sea-surface temperature and sea-ice coverage. The three scenarios are: 1) The reference or historical period which is the 'current decade' from 2006–2015, 2) a future decade that is about 1.5 °C warmer than pre-industrial levels, and 3) a future decade that is about 2.0 °C warmer than pre-industrial levels. In this protocol, the reference experiment chosen is 2006-2015 because it is the most recently observed period. This period also contains a range of different SST patterns over the decade, allowing for an assessment of how the ocean conditions vary on inter-annual timescales, including important El Niño and La Niña events.

For each scenario, we used the output of four HAPPI AGCMS: CanAM4 (100 ensemble members); CAM4-2degree (100 ensemble members); NorESM1-HAPPI (125 ensemble members), and MIROC5 (50 ensemble members). Each simulation (ensemble member) within an experiment differs from the others in its initial weather state. So, the use of 50-125 ten-year time slices really provides 500 years of data for the MIROC5 experiment,

1000 years for CanAM4 and CAM4-2degree; and 1250 years for NorESM1-HAPPI. Such extensive record (500-1250 years) in turn provides the basis for robust calculations. More details of the HAPPI protocol is found in the Supplementary Information S6.1

6.3.2 Runoff

The AGCMs used in this study have a land surface scheme which is coupled to the overlying atmosphere. For two models, NCC/NorESM1-HAPPI and ETH/CAM4-2degree, runoff was stored in the HAPPI archive. The other two models (MIROC/MIROC5 and CCCma/CanAM4) did not have a runoff-production scheme activated for use in the present experiment and so we applied a comparable runoff-generation scheme to calculate runoff in those cases. This in turn enabled us to use those models alongside the members of the ensemble for which runoff data were available.

So, for these two AGCMs we calculated runoff by using a simple runoff production model designed to be comparable with the runoff-production models typically embedded within climate models. Our scheme uses a Rutter-Gash canopy formulation [*Gash*, 1979] together with Penman-Monteith evaporation calculated using available radiation data [*Monteith*, 1965]. Soil moisture was accounted for using a two-layer model with saturation-excess runoff computed using a generalised TOPMODEL [*Clark and Gedney*, 2008].

The snowpack model used here was based on a temperature-based model of accumulation and melt [*Moore et al.*, 1999; *Hock*, 2003; *Beven*, 2011]. Snow accumulates when precipitation falls while temperature is below a threshold temperature T_a. When temperature is above a threshold for melt, T_m melting occurs at a rate proportional to the difference between the current temperature and T_m. This conceptual model is widely used [*Hock*, 2003; *Zhang et al.*, 2006; *Rango and Martinec*, 2007; *Beven*, 2011] and gives performance comparable with that of more parameter-rich energy balance models, despite their greater complexity [*Parajka et al.*, 2010].

We acknowledge the existence of other more sophisticated runoff schemes yet ours is intended to be applied directly to atmospheric outputs resulted from large ensembles such as the HAPPI ensemble allowing us to maximize the utility of the HAPPI ensemble by generating runoff when it was not provided directly. Comparison of our simulated runoff indicates good latitudinal agreement with observations provided by the World Meteorological Organization Global Runoff Data Centre (GRDC) [*Fekete et al.*, 2002] (See Supplementary Figure S6.4).

6.3.3 Runoff Routing

Total runoff derived from NCC/NorESM1-HAPPI and ETH/CAM4 models or calculated from CCCma/CanAM4 and MIROC/MIROC5 were routed by implementing the grid-based hydrological routing scheme as presented by Dadson, Bell, and Jones (2011). This scheme is based on the discrete approximation to the 1-D kinematic wave equation with lateral inflow [*Oki and Sud*, 1998]. This routing model routes flows along the path of steepest descent. Resistance to flow is handled via a wave celerity parameter. This algorithm has been widely used in various large-scale hydrological studies as well as various existing climate and land surface model configurations. Further details are available in Bell et al. (2007). We also selected this scheme as it is computationally tractable when dealing with a global problem with many hundreds of ensemble members, as with the HAPPI experiment.

Also, in this scheme the river network data used was constructed by using the Network Tracing Method (NTM) which is a vector-based network scheme that traces the path of river networks downstream [*Olivera and Raina*, 2003]. This method works by overlaying a mesh of a certain grid size over a fine-scale joined river network to determine the coarse-scale downstream cell. This method has the advantage that it can be used in areas where digitized river networks exist but no DTM is available and it is usually spatially closer to

the base river network. As NTM has been found to outperform other raster-based methods, it has been widely used in previous routing studies [*Olivera and Raina*, 2003; *Bell et al.*, 2007; *Davies and Bell*, 2009]. The resolution of the river network used here is half degree (0.5^{o} x 0.5^{o}).

Also, the spatial resolution of runoffs given by each AGCM (NCC/NorESM1-HAPPI: 1.875^{o}x0.625^{o}; ETH/CAM4: 2.5^{o}x1.875^{o}, MIROC/MIROC5: 1.40^{o}x1.40^{o}, CCCma/CanAM4: 2.81^{o}x2.81^{o}) was downscaled to match the resolution of our river network. The downscaling was performed by applying a bilinear interpolation technique. Apart from its simplicity, this technique has been found to provide a more realistic spatial gradient instead of patches of same runoff values from an AGCM in cells with finer resolution [*Koirala et al.*, 2014]; as consequence this method has been used in a range of global hydrological studies [*Qian et al.*, 2006; *Materia et al.*, 2009; *Ukkola and Prentice*, 2013; *Koirala et al.*, 2014].

The final results of our study are presented at the scale of the routing model (0.5^{o} x 0.5^{o}). We acknowledge that this increase in the spatial representation of runoff may result in our overlooking or underrepresenting runoff processes that operate at finer scales, which are represented by using statistical distributions of sub-grid runoff generation. We note that our routing scheme does not account for human interventions and flow regulations such as dams and reservoirs, or changes in land use and river interventions. We acknowledge the importance of these anthropogenic interventions, but they are not the subject of our study. Models that incorporate complex anthropogenic processes do not typically offer computational simplicity appropriate for use with large ensembles. The comparison of derived river flows with observations derived from GRDC can be found in Supplementary Figure S6.5.

6.3.4 River flow extreme statistics

The change in high flow hazards between the historical and future conditions (1.5 °C and 2 °C warming scenarios) was calculated from the probability of the historical 100-year return period river flow magnitude to be exceeded at the 1.5 °C and 2 °C warming scenarios. We selected the 100-year return period as the reference river flow in order to keep consistency with previous hydrological studies [*Dankers and Feyen*, 2008; *Hirabayashi et al*., 2008; *Ward et al*., 2013]. So, time series (500-1250 years) of simulated annual maximum daily river flows in the historical scenario (2006-2015) were fitted to a two-parameter Gumbel distribution [*Gumbel*, 1941]. As a result, the magnitude of the 100-year return period river flow of the historical scenario was calculated at each grid and for each AGCM. Lastly, the return period of the historical 100-year river flow was calculated for the time series of the 1.5 °C and 2 °C warming scenarios.

A two-parameter Gumbel distribution was selected as it provides relatively stable distribution parameters showing adequate results in similar previous studies [*Hosking and Wallis*, 2005; *Dankers and Feyen*, 2008; *Hirabayashi et al*., 2008, 2013]. Also, while these previous studies acknowledge that the type of extreme distribution function selected may impact the probabilities of extreme flows, it does not affect the estimation changes in the frequency and tendency of them, which is the aim of this study. Similarly, Hirabayashi et al. (2013) used the probability plot correlation coefficient test to find that globally 76% of the AGCMs adequately fit to the Gumbel distribution (coefficient > 0.96 at 95% of significance). Grids that did not fit this distribution were mostly found in arid regions which has also been found in similar studies [*Hirabayashi et al*., 2008].

6.4 Results

We detect regions where the shift in occurrence of global historical extreme flows at 1.5°C and at 2.0°C differ as calculated by our ensemble of four AGCMs (Figure 6.1). First, we identify regions that show an initial increase in the frequency of occurrence of historical high flows at 1.5°C and then progressively increases at 2.0°C. These regions include South America (Amazon catchment), central Africa, central-western Europe, the South of the U.S. (Mississippi river area), central Asia, and Siberian catchments. In these regions, the median increase of the frequency of the current 1-in-100-year flow is once in 70–90 years at 1.5°C, and at 2.0°C this frequency increases to at least once in 50 years. Moreover, we find that in most of central and eastern China, the southern part of the Amazon catchment, the Blue Nile, and in northern India, the 1-in-100 year flow at 1.5°C ranges between 1-in-50 to 1-in-60 years, whereas at 2ºC such an event ranges between 1-in-25 to 1-in-35 years.

Second, we identify areas where the frequency of the 1-in-100-year flow increases at 1.5°C but does not change appreciably between 1.5ºC and 2.0°C. Notably these areas are located in South and South East Asia (south of the Yangtze river) and the Indus river basin. In these regions under a 1.5°C scenario, the current 1-in-100-year flow increases in frequency to 1-in-50-year return period. However, we also identify some areas, such as South-East Asia, where the current 100-year flood occurs 1-in-25 years in the future. In North America and Eastern Europe, the current 100-year return period flow increases in frequency only slightly, to once in 80 years at 1.5°C.

We also find some regions which see a decrease in the frequency of high flows between the present day and 1.5°C or 2.0ºC or both. These regions are located in the northern part of South America, areas of the Western Coast of the United States (Colorado River) and Canada, South Africa (Orange River), Scandinavia, and in some parts of Eastern Europe. In most of these regions, we note that the current 1-in-100-year flow decreases in

frequency to approximately 1-in-150 years, with little further decrease at 2.0°C. Lastly, we find that in the area of the Murray-Darling basin in Australia, there is a shift from historical high flows not changing in a world 1.5°C warmer (projected return periods between 90-125 years), whilst under a 2.0°C scenario the return period decreases to approximately 1-in-70 years.

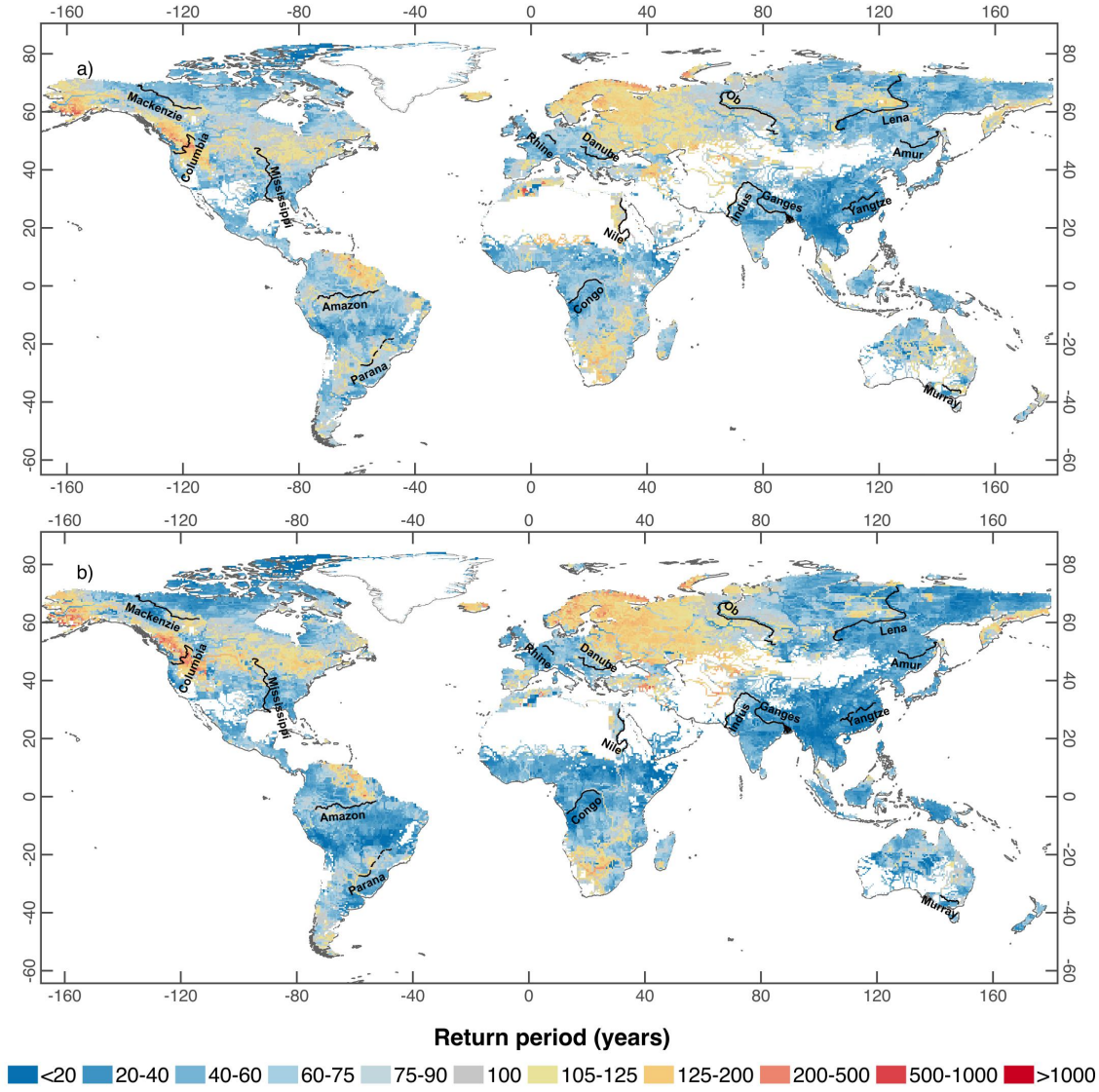

Figure 6.1 Multi-model median return period (years) for future river flow corresponding to the historical 100-year flow under a) at1.5ºC scenario b) at 2ºC scenario.

Grid boxes where the historical averaged annual flow is <10 m^3/s were screened out. Blue colors indicate a more frequent historical 100-year flow whereas red colors indicate a reduction in the frequency.

6.4.1 Physical characterisation of high flows

In order to understand the physical reasons that induced shifts in high flow frequencies, we calculated the change in both the number of frost days and the number of days where precipitation has occurred between the two scenarios in comparison to the historical baseline (See Figure 6.2). We find an important decrease in the number of frost days at 1.5°C which slightly increases at 2.0°C. This decrease is greater in North America, and central and eastern Europe (Figure 6.2a,b). This finding suggests that globally the role of snowmelt in the generation of high flows will decrease as snow accumulation reduces. Exceptions to this pattern are found in the South and East Coast of the U.S. and in the south of South America. In these areas, particularly in the U.S, where we estimate an increase in the occurrence of high flows, snow dynamics and possibly longer periods of snow accumulation may be important drivers of high flow events.

The change in the number of days with precipitation between the two climate thresholds (Figure 6.2 c,d) shows a diverse regional response. For example, in most of the regions where we estimate a progressive increase in the frequency of high flows between 1.5°C and 2.0°C, such as central-western Europe or South America, the number of days with precipitation typically decreases or does not importantly change at 1.5°C and also at 2.0°C. This is also accompanied by a decrease in average annual precipitation magnitudes at both scenarios (See Supplementary Figure S6.2). This result suggests that in these areas extreme precipitation, will likely dominate the occurrence of high flows, despite the reduction in the number of rain days. An important exception is observed in Siberia, where we see an increase in the frequency of high flows accompanied by a slight decrease in the number of days with precipitation.

In regions where the increase in high flow occurrences is important at 1.5°C but minor at 2.0 °C, such as the South of Asia, we find that, at this first temperature target, the frequency of rain days decreases as well as total annual precipitation magnitudes. Yet at 2.0°C days

with precipitation are either more common (especially in North America) or show a lower reduction compared with that detected at 1.5ºC. Similarly, annual precipitation magnitudes show a slight increase when compared to the historical reference period. This finding suggests that, in these regions, the role of shorter wet seasons and storms in high flows, which at 1.5ºC seems to be more important, will decrease at 2.0ºC. So, in these regions, the difference between the two climate targets, and thus flow occurrences, may be associated with shifts in durations and characteristics of the wet season. In the regions where we observe a decrease in the occurrence of high flows, we also detect a decrease in the number of days with precipitation and annual precipitation magnitudes.

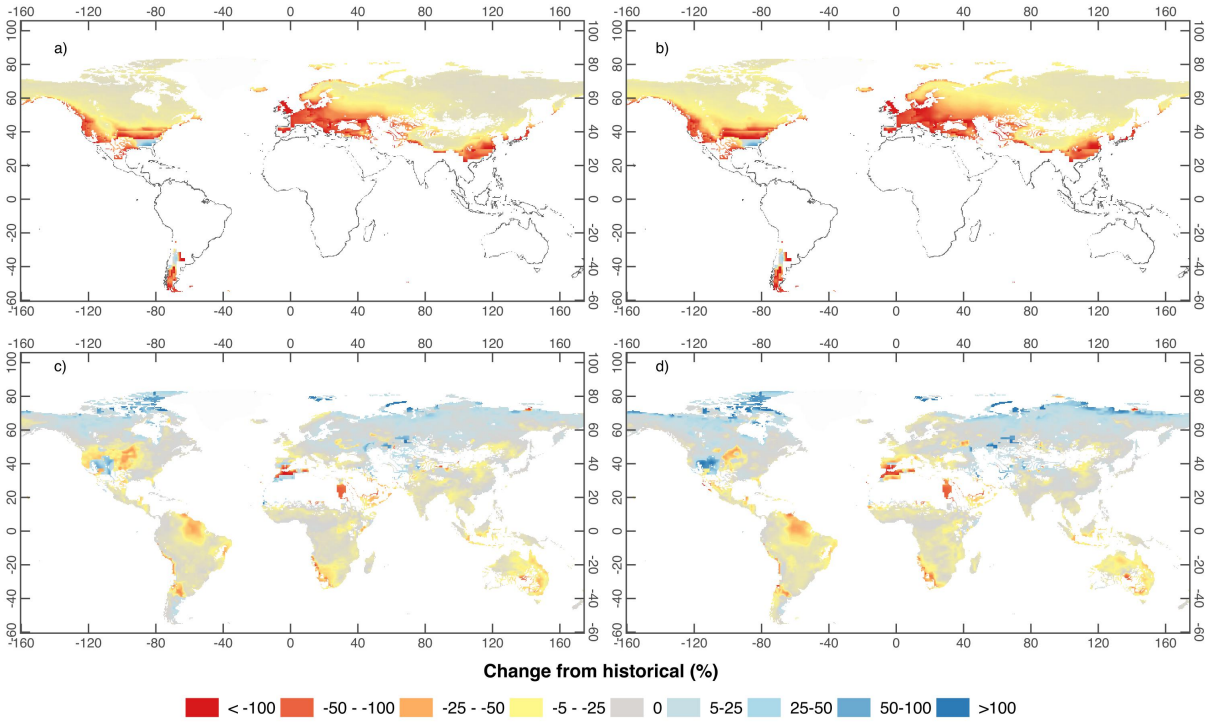

Figure 6.2 Multi-model median change (%) in the number of frost days between the historical and: a) 1.5ºC scenario, b) 2.0ºC scenario.

A frost day is that where estimated temperatures are less than 0ºC. Figure 6.2 c) and b) is as a) and b), correspondingly, but for the number of days with precipitation. We define a day with precipitation as that where estimated daily precipitation is greater than 2 mm/day. This threshold is selected as it adequately describes the range of global *light* precipitation (0.1 – 5mm/day) [*Qiaohong et al.*, 2017].

6.4.2 Multi-model consistency and biases in results

The change in high flow frequency at 1.5°C and 2.0°C, although consistent in sign between models across most parts of the globe, differs in specific regions (See Figure 6.3). Globally, we find that 49% of land grid cells at 1.5°C and 43% at 2.0°C show a high consistency in the tendencies described above (consistency defined as an agreement in trajectory of 3 out of 4 models). This high level of consistency is seen particularly in regions where we find an increase in high flow frequency, such as the South of Asia, India,

or East Africa. Conversely, in just about 7% of land grid cell at 1.5°C and 4% at 2.0°C just one model agrees with the tendency mapped above. Typical regions with lower consistencies can be found in Northern Russia and parts of the tropics. In these areas our projections are subject to an important spread across the AGCM ensemble.

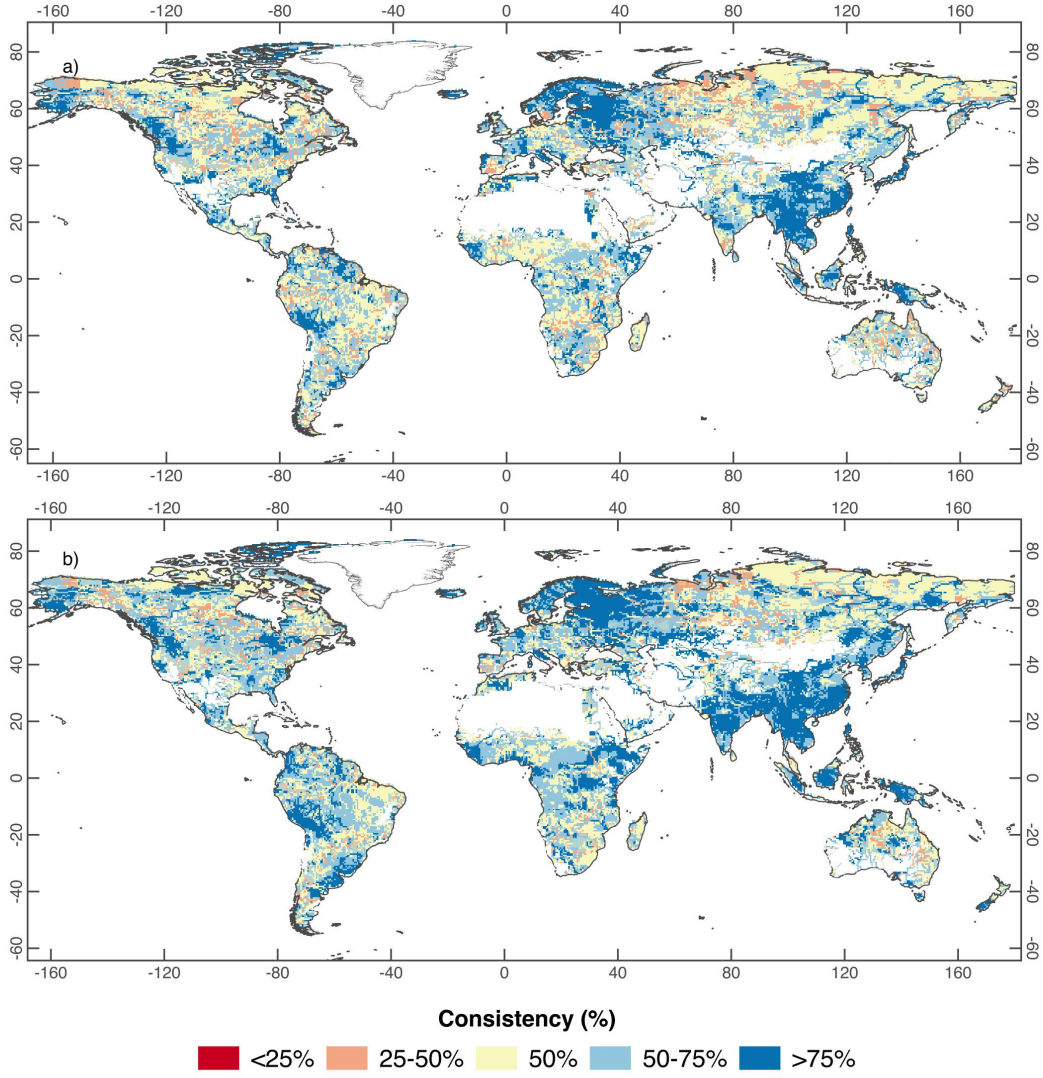

Figure 6.3 Consistency in projected river flow change for the four AGCMs used in this study.

Consistency is expressed as a percentage of the total the number of models that agree with the tendency in the direction of change (increase or decrease) of the historical return period.

Additionally, the examination of the way each AGCM simulates the changes in high frequency helps to disseminate further model biases (Supplementary Figure S6.1). For

instance, NCC/NorESM1-HAPPI generally projects greater increases in the frequency of occurrence of the reference high flow in the tropics. Thus, it simulates a more pronounced increase in high flow from the historical reference return time of 1-in-100 years to approximately 1-in-40 years at 2.0°C for larger areas (e.g., central South America and South Asia). Also, MIROC/MIROC5 and CCCma/CanAM4 show greater increases in reference extreme flow frequencies in northern regions. We also find that ETH/CAM4-2degree generally produces lower river flows outside the tropics.

Moreover, by examining the way each AGCM represents precipitation and then runoff (Supplementary Fig S6.3 for precipitation and S4 for runoff), we estimate whether existing biases (such as the lower river flow in ETH/CAM4-2degree) are due to deficiencies in the AGCM, runoff generated, or the river routing model. Using zonal means, we find that each of the four AGCMs slightly overestimates mean precipitation in the tropics compared with the Global Precipitation Climatology Centre dataset, GPCC [*Becker et al.*, 2011] (maximum precipitation bias ~30%).

This tropical overestimation persists for mean runoff in MIROC/MIROC5 and, to a lesser extent, in CCCma/CanAM4 when compared with observed river flow data obtained from the World Meteorological Organization Global Runoff Data Centre, GRDC [*Fekete et al.*, 2002]. ETH/CAM4-2degree and NCC/NorESM1-HAPPI on the other hand, show an importantly reduced runoff in the tropics compared with the other two AGCMs. In contrast, extra-tropical overestimation of precipitation in MIROC/MIROC5 does not lead to equally overestimated runoff in those regions. It is therefore not possible to identify the root cause for biases in river flow with confidence, given the substantial discrepancies in the precipitation-to-runoff ratio in the models. However, the fact that the two models with lowest zonal average runoff also show the lowest river flow is indicative that the treatment of the water budget and the associated hydrological balance in the AGCMs is crucial in

capturing the magnitude of the river flow. That said, we emphasize that biases in river flow are unlikely to affect the change in frequency of the return time between the different temperature scenarios. This is also shown in our sampling uncertainty estimates derived from resampling our dataset 1000 times for the 10 largest catchments globally (See Table 6.1).

6.4.3 Magnitude of projected changes in the 100-year river flow

In contrast to the important increase in high flow occurrences, described above, we lastly find a diverse response in the change of flow magnitudes between the two temperature scenarios for the 10 largest catchments in the world (see Table 1). In catchments where we do not detect a large change in the frequency of occurrence of the historical 1-in-100 years return period flow such as the Amazon and Murray-Darling, we find a reduction of up to 5% in mean annual river flow under the 1.5°C scenario. In contrast, some mean river flows such as those at the outlets of northern catchments (Mackenzie and Ob') show important increases of up to 8% (at 2.0°C) despite quasi-constant changes in frequency of occurrence of peak flows. At the Yangtze river, apart from the increase in the frequency of occurrence of extreme river-flows as presented above, there is an important increase in the mean discharge at both, 1.5°C to 2.0°C. Also, we note that for the Mississippi and the Ganges rivers the small change in mean river flow is contrasted by an important increase in high flow frequencies. Also, we note that regarding flow magnitude, the change from 1.5°C and 2.0°C levels of warming are not as clear as those detected for high river flow frequencies. However, we note that the combined fidelity of the ensemble of our AGCMs and the river routing model to reproduce the annual cycle of the river flow, exemplified for a subset of major river catchments is limited in certain areas (See Supplementary Figure S6.5). The representation of the water budget and hydrological balance discussed in the section above may also be affecting the ability to represent changes in flow magnitudes.

Table 6.1 Consistency in projected river flow change for the four AGCMs used in this study.

Projected change (expressed as return period) of the 1-in-100-year historical flow at both scenarios and estimated change in the mean river flow (%) from ten selected major global outlets. Uncertainty due to sample size is calculated by a bootstrap method. Uncertainty for the four AGCMs was averaged. Standard deviation is calculated from our ensemble of AGCMs.

River System	Return period of historical highflow				Change in mean historical river flow (%)			
	1.5C R. period (year)	Uncertainty due to sample size	2.0C R. period (year)	Uncertainty due to sample size	1.5C		2.0 C	
					Mean	Std	Mean	Std
Amazon	108	±5	87	±3	**-4.7**	1.3	**-5.2**	2.6
Mississipi	85	±3	64	±4	**1.0**	2.4	**1.6**	5.1
Mackenzie	61	±7	49	±4	**6.3**	2.4	**8.9**	3.7
Congo	80	±6	57	±5	**-0.6**	2.2	**-0.2**	4.2
Nile	92	±7	55	±4	**-1.2**	2.2	**2.8**	3.4
Rhine	70	±8	72	±7	**2.6**	2.4	**1.3**	3.2
Danube	54	±8	63	±6	**2.0**	5.4	**-1.8**	5.1
Murray-Darling	143	±5	96	±5	**-9.0**	1.7	**-4.0**	4.8
Ganges	67	±4	41	±3	**1.7**	3.6	**5.0**	4.7
Indus	130	±6	127	±6	**-1.2**	5.1	**-0.3**	7.4
Yangtze	58	±8	26	±9	**7.4**	4.9	**8.2**	5.9
Ob'	54	±9	48	±9	**5.7**	3.2	**7.5**	5.1

6.4.4 Flow responses for alternative return periods

We note that although the four AGCMs ensemble disagree in maximum daily flow magnitudes, they are not sensitive to the choice of the return time as highlighted in Figure 6.4, where we have plotted the return times for all scenarios and models for four different rivers which are affecting a large fraction of global population. At the Yangtze as well as at the Orange outlets, we find that the difference between 1.5°C to 2.0°C remains small for a wide range of return times (Fig. 6.4a/d). As mentioned above, the four models show similar tendencies when simulating changes in return periods of high flows for the selected

regions, which suggests that our flow frequency results are indeed robust, despite biases in the magnitude of the river flow. The detected wet bias in runoff at certain latitudes in MIROC/MIROC5 reappears here, in that we find the river flow magnitude to be overestimated at the Yangtze and the Ganges (Fig 6.4a, b). Also, the difference in runoff between the two wettest and driest AGCMs is mirrored in the return time plots at the Upper Blue Nile (Fig 6.4c), where we find considerably higher river flow magnitudes between the two model subsets. In other words, the regionally-overestimated precipitation (~30% in NCC/NorESM1-HAPPI and CCCma/CanAM4) translates directly into higher mean and extreme river flows.

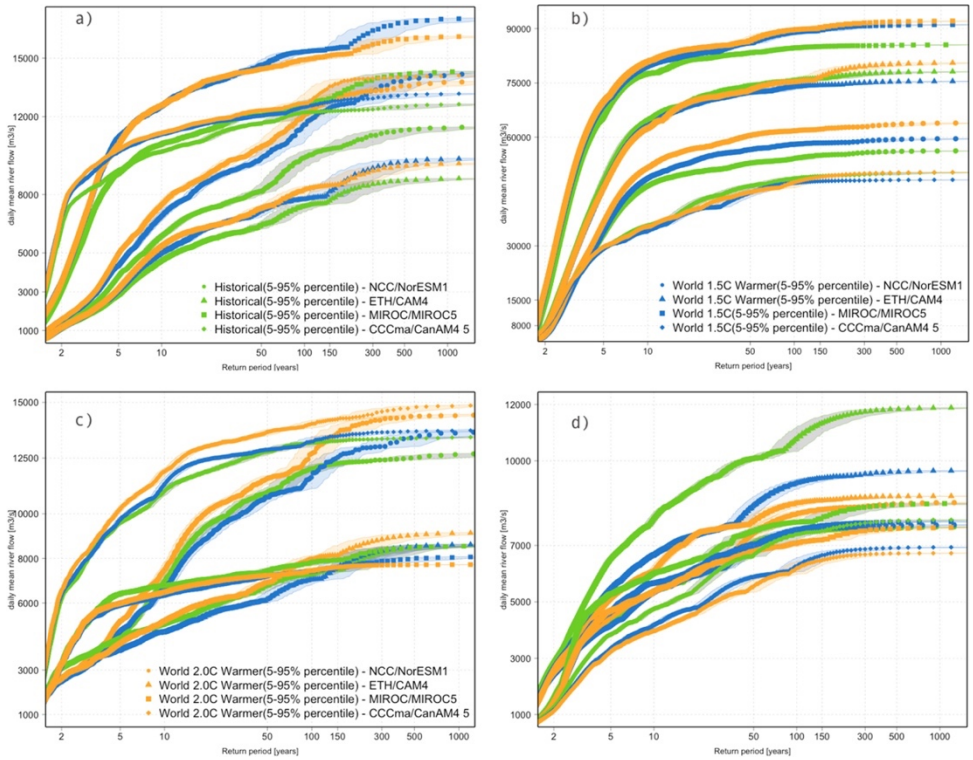

Figure 6.4 Maximum one-day river flow as simulated by the four AGCMs ensemble a) the outlet area of Yangtze River, b) outlet of the Ganges River, c) the upper Blue Nile (Ethiopian Highlands), and d) the Orange River in South Africa.

6.5 Discussion

The results shown here agree with various of the previous findings that also project shifts in runoff, river flow magnitudes and flood frequencies under representative concentration pathways in various global regions [*Hirabayashi et al*., 2013; *Stocker et al*., 2013; *Dankers et al*., 2014; *Koirala et al*., 2014; *Schewe et al*., 2014a; *Arnell and Gosling*, 2016]. For instance, our findings consistently agree with the projection of increased mean river flows and high flow frequencies for South-east Asia, Eastern Africa, and various parts of South America. Similarly, for a world 1.5 and 2.0°C warmer, Döll et al. (2018) also project increases in high flows in South and South Asia, and Central Africa. On the contrary, these studies typically suggest a general decrease in future high flows in Central-eastern Europe. On the contrary, our results project an increase in high flow frequencies in this region (relatively good multi-model consistencies found here).

Also, the non-linearity found between current conditions and the two future warming scenarios might as well be related to counterbalancing effects due to the presence of different forcing agents that vary greatly over time. In both HAPPI future scenarios, the aerosol load is reduced to approximately one third of its current levels. This leads many regions to show higher rainfall increases at 1.5ºC compared to what has been observed or simulated in similar experiments as high aerosol loads have been connected to a reduced strength of the hydrological cycle in several global regions [*Bollasina et al*., 2011]. This may be the case in the Asian monsoon region which is generally characterized with high aerosol loads and our results show an increase in high flow frequencies detected here. If the role these different drivers are playing is not appropriately analyzed, the attribution results can easily be misinterpreted. As such, it is also important to understand other region-specific features which may explain the different local flow responses between both scenarios.

Moreover, the consistent decrease in high flow frequencies found in our study for Scandinavia and South Africa has been previously estimated by Hirabayashi et al. (2013) and (Koirala et al. (2014) for the RCP8.5 scenario. Similar projections were also found by Döll et al. (2018) for the particular temperature targets agreed in Paris. Also, it is important to note that in some areas where consistently project an increase in high flow frequencies, various previous reports estimate a future decrease in mean river flow accompanied by major drought hazard at 2.0°C [*Schewe et al.*, 2014a; *Lehner et al.*, 2017]. These areas include, southern China (such as the Yangtze river), central Europe, and central South America. Thus, our findings suggest an intensification of hydrological extremes in these regions. Yet, it is important to consider the additional role that that the reduction of aerosols, described previously, may have in showing wetter futures in our estimates in these regions.

6.6 Conclusions

By using the HAPPI Protocol, which is a framework designed to reduce the influence of model sensitivity in climate outputs, we analyze the impacts of an additional half degree of warming on high river flows, as agreed in Paris in 2015. We find that historical extreme flows (represented by 1-in-100 year return periods) occur more frequently at 1.5°C, but even greater additional changes are projected for many regions at 2.0°C. These regions include most of South America, central Africa, central-western Europe, the South of the U.S. (Mississippi river area), central Asia, and Siberian catchments. We detect that in these regions, the median increase of the frequency of the current 1-in-100-year flow is once in 70–90 years at 1.5°C, and at 2.0°C this frequency increases to at least once in 50 years. Our result suggests that in these areas (with the exception of Siberia), this change is accompanied by shorter, and consequently more intense, rainy seasons. As such, committing to a 1.5°C level of warming reduces the chance of high flows in these regions. In other highly populated areas, such as South and South East Asia (south of the Yangtze

river) and the Indus river basin, the current 1-in-100-year becomes more frequent at a 1.5°C level of warming (1-in-50-year). Then the change from 1.5°C to 2.0°C is not importantly appreciable. Yet, it is important to note that reductions in atmospheric aerosol loading represented in the HAPPI experiments lead to wetter futures in the areas discussed. As such, the implications that regional-scale processes may have in our results may be worth noting in a context of global mitigation targets. Lastly, while our analysis highlights limitations concerning regional and seasonal river flow projections produced using global models, we have demonstrated that our river flow results are robust with regard to changing risks tendencies. Thus, our results may be used to inform adaptation strategies and to guide assessments of socio-economic impacts at the regional or catchment scale.

7. Vulnerability of Global Hydropower Potential under 1.5 °C and 2 °C Global Warming Targets

Homero Paltán[a]*, Raghav Pant[b], Judith Plummer Braeckman[c] & Simon Dadson[a]

[a] School of Geography and The Environment, University of Oxford, Oxford, UK

[b] Environmental Change Institute, University of Oxford, Oxford, UK

[c] Cambridge Institute for Sustainability Leadership, University of Cambridge, UK

*Paper in review, Environmental Research Letters

7.1 Abstract

The reliability of global hydropower, as a key energy source in the context of the 2015 Paris Agreement, strongly depends on its ability to cope with hydrological variability. Here we investigate the vulnerability of global Gross Hydropower Potential (GHP) to changes in variability of low flows characteristics under the climate targets agreed in Paris (global temperatures 1.5°C and 2°C warmer than pre-industrial levels). By using river flow derived from a multi-model ensemble, we find that in spite of a projected increase in global GHP, the vulnerability of the sector increases due to a future with more water shortages. We estimate that under 2.0ºC, almost a quarter of current global GHP may be vulnerable (~16.09 PWh/year). Potential losses in GHP may in turn threaten the national energy mix in Norway, Canada, Paraguay and various Asian and Sub-Saharan countries where the share of vulnerable energy may even surpass 50%.

7.2 Introduction

Hydropower production comprises approximately 16% of global electricity generation and in 2015 this source provided about 70% of the supply of renewable energy [*IEA*, 2017]. With an annual production of approximately 4,000 TWh/year, this alternative has become an increasingly attractive source of renewable energy [*Hamududu and Killingtveit*, 2012; *Bartle*, 2016]. As such, current estimates project that global installed capacity will grow at a rate of 30 GW per year showing a rapid expansion of this sector especially in the developing world [*Hoes et al.*, 2017]. Consequently, the role that this sector plays in the global energy mix is expected to increase under growing world population and economic demands [*Zarfl et al.*, 2015; *Bartle*, 2016].

The role of hydroelectric power also has gained relevance under the context of the 2015 Paris Agreement of the United Nations Framework Convention on Climate Change. Here the parties agreed to "limit the increase in global average temperature to well below 2°C above pre-industrial levels, and to pursue efforts to limit the temperature increase to 1.5°C above pre-industrial levels" [*Christoff*, 2016]. Apart from the major implications in reduction of greenhouse gas emissions that these targets represent, they also acknowledged the promotion of the access to sustainable energy. To this end, the function of the 'blue power' in the mitigation of electricity-related emissions has been widely considered and encouraged [*Berga*, 2016; *Antwi and Sedegah*, 2018]. Thus, the hydropower sector is also expected to play an important role in climate change mitigation, both directly and in balancing the production of intermittent renewables and improving grid stability [*François et al.*, 2014; *Dujardin et al.*, 2017].

The continued availability and growth of global hydropower strongly relies on its ability to cope with hydrological risks [*Blomfield and Plummer*, 2014b]. Such risks arise through

short-term variability in daily flows, long-term seasonal variability of flows, and sudden variability due to extreme flows. In order to calculate the impact of climate change on the hydropower generation, changes in hydrological variables, namely precipitation, runoff and river flow are often derived from ensemble of simulations computed from global circulation models (GCMs). At the moment, there is growing evidence that low flows have resulted in historical declines in hydropower potential at various scales [*Madani and Lund*, 2010; *Rübbelke and Vögele*, 2011; *Piman et al.*, 2013; *Gaudard et al.*, 2014; *van Vliet et al.*, 2016a] and that low flow variability has important repercussion on hydropower vulnerability at both local and regional scales [*Kuusisto*, 2004; *Loisulie*, 2010; *Harto et al.*, 2012; *Mukheibir*, 2013]. Yet, hydropower estimate at the global scale still rely on evaluating the change in future mean hydrological conditions[*Lehner et al.*, 2005; *Bartos and Chester*, 2015; *Liu et al.*, 2016]. Ignoring the possible impact of low flows and subsequent temporal water loses when projecting global changes in hydropower potential may in turn result in inadequate evaluations of the sector's vulnerability to climate change and thus, lead to important implications for power production, global economy and global energy security.

In this study we investigate the vulnerability of global gross hydropower potential to projected variability in frequency, duration, and intensity (water losses) of droughts resulting from the climate targets agreed in Paris. To address this, we use river flow simulations derived from a multi-model ensemble protocol to calculate the change in future global gross hydropower potential at 1.5°C and 2°C warming scenarios. So, we first explore the implications of the incorporation of variability in hydrological droughts in Gross Hydropower Potential (GHP) estimates. From here, we finally estimate the vulnerability of global GHP due to hydrological droughts under future climate scenarios in which global average temperatures are limited to 1.5°C and 2°C.

7.3 Methods

7.3.1 Multi-Model ensemble and River Flow Data

Here we use available river flows[*Paltan et al.*, 2018] computed under the HAPPI protocol[*Mitchell et al.*, 2017] in order to calculate changes in global gross hydropower potential between the two climate thresholds agreed in Paris. HAPPI is a multi-model project which provides data from three 10-year simulation periods with prescribed atmospheric forcing, sea-surface temperature and sea-ice coverage. The three scenarios are: 1) The reference or historical period which ranges from 2006 to 2015, 2) a future decade that is 1.5 °C warmer than pre-industrial levels, and 3) a future decade that is 2.0 °C warmer than pre-industrial levels. By using prescribed future Sea Surface Temperatures (SSTs) this framework reduces the influence of model sensitivity when simulating narrowly defined range of future temperature targets[*Mitchell et al.*, 2017].

In this study, for each scenario we use river flows routed from the output of four HAPPI AGCMS: CanAM4 (100 ensemble members); CAM4-2degree (100 ensemble members); NorESM1-HAPPI (125 ensemble members), and MIROC5 (50 ensemble members) (For details of runoff, river routing and river flow characteristics used here see Paltan et al. (2018)[*Paltan et al.*, 2018]). Each ensemble member within an experiment differs from the others in its initial weather state. So, the use of 50-125 ten-year time sliced in facts provide us with 500-1250 years of data per scenario, which in turn provides the basis for robust return-period calculations. The spatial resolution of river flows used in our study is half degree (0.5º x 0.5º). Our daily flow values do not include anthropogenic interventions such as impoundments, diversions or water abstractions.

7.3.2 Variability in Low Flows

We describe variability in low flows as changes in the frequency (number of drought events), duration (length of drought events), and intensity (cumulative water deficit) of hydrological droughts at both climate targets, when compared to its historical flow values at each grid point. Hydrological droughts are determined by following the commonly used threshold level method[*Yevjevich*, 1967; *Hisdal and Tallaksen*, 2003; *Fleig et al.*, 2006; *Van Loon and Van Lanen*, 2012; *Van Loon*, 2015a]. This technique is known for capturing and representing better the patterns and deficiencies in seasonal high-flows especially in areas with abrupt changes in river flows[*Beyene et al.*, 2014]. As such, this approach is recommended to be used in global scale studies. With this technique, a drought episode is detected when river flow values fall below a determined threshold level. So, the threshold level for any given day is calculated based on the 20th percentile (or Q80) derived from the flow duration curve of flow in the 30-day-average time window for that day of the year. Thus, this time window is moved through the daily river flow time series in order to calculate threshold values per day. The 80th percentile threshold was chosen based on that used in previous studies [*Van Loon and Van Lanen*, 2012]

Drought events are considered mutually-dependent and, consequently, they are pooled if the inter-event time is 10 days or less [*Fleig et al.*, 2006]. Next, minor droughts are eliminated if they are of 15 days duration or less. From here, the intensity measure used is the water deficit volume, which is obtained as the sum of the difference between the historical threshold level and the projected river flow at both scenarios (1.5^{o}C and 2.0^{o}C) [*Zelenhasić and Salvai*, 1987]. More details on the definitions and applications of drought definitions, the variable threshold approach and smoothing procedures used in this study can be found in Van Loon (2015)[*Van Loon*, 2015b].

Last, shifts in frequency, duration, and water deficits (intensity) are represented by the ratio of changes between the historical and the two projected scenarios, as used in previous global hydrological risk studies [*Hirabayashi et al.*, 2008]. Ratios of Change (RC), at each grid location, is given by Equation (7.1):

$$RC = \frac{Var_{Projected}}{Var_{Reference}} \text{ (Eq. 7.1)}$$

where $Var_{Projected}$ is the future state of each variable (frequency, duration, or water deficit) under 1.5ºC or 2.0ºC warming scenarios. $Var_{Reference}$ is the historical-reference state of such variable. RC > 1 indicate that the given drought indicator intensifies in a future, whereas RC<1 show a future decrease in such indicator. Ratios = 1 indicate that there is no future change in such indicator.

7.3.3 Change in Gross Hydropower Potential

The calculation of GHP was based on the approach proposed by Lehner et al. (2005), and Gross & Roppel (2012). This approach follows equation (7. 2):

$$GHP = Q * m * g * \Delta H \text{ (Eq. 7.2)}$$

Where GHP at each grid location is expressed in Watts; Q is volumetric flow rate expressed in m3/s (derived from our multi-ensemble river flow data) for such grid; m is the density of water (1000 kg/m3); g is the gravitational acceleration (9.807 m2/s), and ΔH is the elevation difference (m) calculated within each grid cell.

In our calculations, the size of each grid cell is 0.5º, to match the spatial resolution of our input streamflow time series. Elevation differences within a cell were obtained from the

GMTED2010 Global Grids DEM at 7.5-arc-seconds (~225 m) [*Danielson and Gesch*, 2011]. Thus, this finer spatial resolution permits us to calculate elevation differences found within an input grid river flow grid cell (0.5º x 0.5º). Using Eq. (7.2) we obtained global daily GHP estimates for both of the climate scenarios agreed in Paris (1.5ºC and 2.0 ºC), and for the reference period at each grid location.

7.3.4 GHP Vulnerability

Finally, the future vulnerability of GHP is estimated under both climate targets. Here vulnerability is calculated from the measures of system performance proposed by Hashimoto et al. (1982) and later applied to drought risks in water resources[*Jinno*, 1995; *Kjeldsen and Rosbjerg*, 2004; *Jain and Bhunya*, 2008]. Vulnerability is then a measure that describes how significant or severe the likely consequences of a failure may be.

In this study, a failure is denoted as the lack of capacity of a grid cell to deliver water below the drought threshold which then may compromise the theoretical GHP delivery. Hashimoto et al. (1982) and Jinno (1995) proposed a measure of vulnerability based on the likely water deficit (as the deficit water volume or intensity of drought) experienced during a drought event. In their formulation, over a time-period T with the frequency of low flow events detected as M, vulnerability is obtained by summing the probability of each failure event to be equal (1/M), and the GHP(j) that is unusable due to water deficits over these events, as shown in Equation (3). We further express the vulnerability as a fraction (or percentage) of the total GHP(T) over the overall time-period T. This is done because in order to normalize and compare the scale of vulnerability between locations:

$$Vulnerability = \left(\frac{1}{M}\sum_{j=1}^{M} GHP(j)\right)/GHP(T) \quad \text{(Eq. 7.3)}$$

7.3.5 Potential impacts of GHP vulnerability

To understand how the GHP vulnerability potentially impacts the energy production mix of countries around the world, we next estimate what percentage of total energy produced in a country is vulnerable due to the hydropower deficits that create GHP vulnerability. The process for estimating the vulnerable energy share at country scale is outlined as following. We use the Global Dams and Reservoir Dataset (GRanD) [*Lehner et al.*, 2011], selecting those dams where its main or secondary use is hydroelectricity or those with multiple use. It is assumed that the hydropower produced in a country exclusively comes from the dams in that country identified by the dataset. The dataset also gives information on the storage capacity of the reservoirs associated with dams, which is used as a proxy for dam hydropower production capacity. Since, to our understanding, there is no available global data on the actual usage as percentage of capacity for each power plant, we assume here that hydropower plants are being utilized at their total capacity. So, next the gridded GHP vulnerability information is spatially intersected with the locations of the dams. It is assumed that in a grid cell each dam's hydropower production capacity will be vulnerable in the same proportion as the GHP is vulnerable. Hence, if in a grid cell i the percentage GHP vulnerability is ΔGHP_i, and this grid cell contains $n_1, \dots, n_d$ dams with capacity $c_1, \dots, c_d$ the total amount of hydropower production that is vulnerable in the grid cell will be $\Delta GHP_i \sum_{j=1}^{d} c_j$. Consequently, the total amount of hydropower production that is vulnerable in the whole country will be $\sum_{i=1}^{N} \Delta GHP_i \sum_{j=1}^{d} c_j$, and the total percentage of the hydropower production that is vulnerable in the whole country will be $\left(\sum_{i=1}^{N} \sum_{j=1}^{d} \Delta GHP_i c_j\right) / \sum_{j=1}^{d} c_j$. As such we are able to perform a worst-case vulnerability assessment. Finally, using the World Bank's dataset on the share of electricity production from hydroelectric sources per country at 2015 [*The World Bank*, 2015] we estimate the percentage of total energy in a country that could be vulnerable. This is given by Eq.(4), where the percentage vulnerable energy production capacity in a country, ΔE_k, is the

product of the fractional vulnerable hydropower production capacity and the percentage share, p_k, of hydropower in the country k.

$$\Delta E_k = \left[\left(\sum_{i=1}^{N}\sum_{j=1}^{d}\Delta GHP_i c_j\right)/\sum_{j=1}^{d} c_j\right]p_k \text{ (Eq. 7.4)}$$

The aim of the above approach is to provide a high-level understanding of the potential implications on GHP vulnerability on energy mix at the national scale. We recognize limitations of our approach, and note that our assumptions result in a conservative assessment of hydropower vulnerability. Also, we have considered the dam sites and their production capacities to be constant in the future climate change scenarios. This is because we do not have any information on future hydropower developments for all countries in the world.

7.4. Results and discussion

7.4.1 Variability of hydrological droughts at 1.5 and 2°C warming scenarios

From an ensemble of four Atmospheric Ocean Global Circulation Models (AOGCMs, 500-1250 years of daily river flow data per scenario – See Methods), we first analyze the implications of the climate targets agreed in Paris for drought indicators: frequency, duration and intensity (water deficits) of droughts. Our results indicate that in spite of the fact that globally the frequency of droughts decreases (or does not change significantly) under a 2.0 ^{o}C warming scenario when compared with a 1.5 ^{o}C scenario, water deficits and durations of them tend to increase in most regions of the globe (Figure 7.1). Globally, the Ratio of Change (RC) of number of droughts slightly decreases on average to 0.65 at 1.5^{o}C and to 0.60 at 2.0^{o}C. This is possibly explained by the negligible change or increase in the number of days with precipitation found between the two climate scenarios in various global regions (See Supplementary Figure S7.1) including West-central North America

and Siberia. It is important to note that regions with a notable decrease in the number of rain days include the Mediterranean region, central and northern Europe, various areas in South America, and Australia. Moreover, at 1.5^{o}C the duration of droughts increases and at 2.0^{o}C drought duration increases yet further (RC from 1.26 to 1.30). Also, the water deficit resulting from drought changes only negligibly at 1.5^{o}C (RC=0.98), whereas at 2.0 ^{o}C this value increases to 1.28.

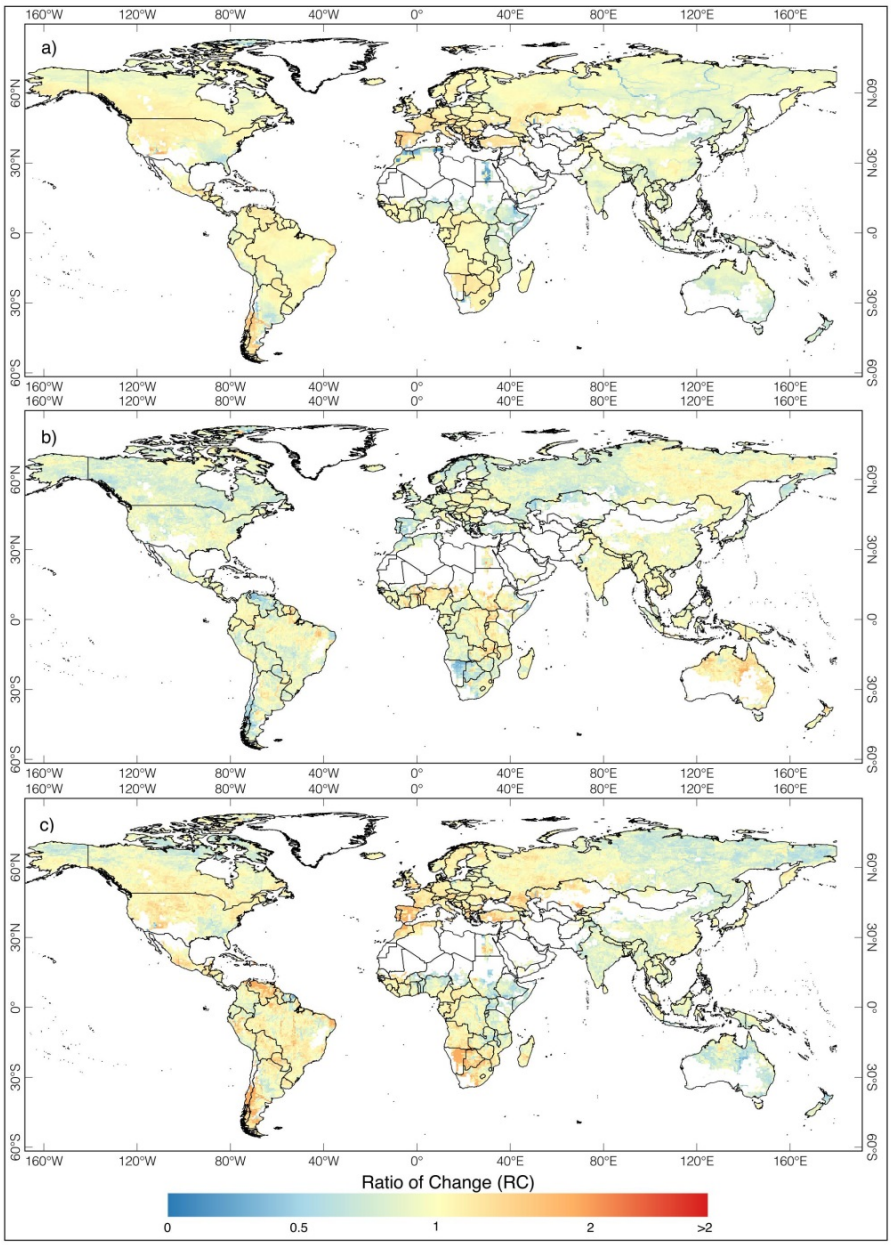

Figure 7.1 Multi-model ensemble mean of Ratio of Change (RC) of: a) water deficits b) frequency, and c) duration of droughts at 2.0 ºC, when compared to 1.5 ºC.

A ratio of change is obtained by using Equation 1 . RC > 1 indicates that the given drought indicator intensifies at 2.0 ºC when compared with the historical baseline, whereas RC < 1 means that such drought indicators weakens at such climate threshold. Ratios = 1 indicate

that there is no future change in such indicator. Grid cells with mean daily river flows < 10 m3/s were screened out.

The regions where a 2.0 ºC warming scenario would lead to fewer droughts, yet more severe and longer ones, include the U.S West Coast, central-north South America, the Iberian Peninsula, Central Europe, Southern Africa, the area surrounding the Black Sea in Western Asia, and Central China. In these areas the RC of water deficits of droughts between the two climate scenarios typically ranges 1.1 and 1.6, where the highest values are observed in the Iberian Peninsula. Moreover, in Southern Africa and the Iberian Peninsula, the duration of droughts is expected to increase by a factor of two at 2.0 ºC. Also, in North Africa, while water deficits and number of droughts decrease at 2.0 ºC when compared to a 1.5 ºC scenario, their duration importantly prolongs (RC ~2.5). These results suggest that in these regions committing to the 1.5 ºC target becomes relevant to attenuate the risks stemming from prolonged droughts.

Also, most of these regions already show the strength of these drought indicators when comparing a 1.5ºC warmer world to historical conditions (See Supplementary Figure S7.2). For example, the typical RC between the 1.5ºC and the historical scenario in South Africa ranges between 1.6 and 2.4 (for water deficits and duration of droughts). In areas such Australia or India, the more relevant shift in hydrological droughts occurs alerady when achieving the 1.5ºC target. For instance, Australia shows a decrease in the projected frequency of droughts while showing an increase in the duration and water deficits of them (water deficits RCs ~1.8 and 2.2 at 1.5 ºC and negligible at 2.0 ºC). In regions such as Southern Africa or the Iberian Peninsula, mentioned above, the RC at 1.5 ºC is typically 1.5-2.5.

Nonetheless, in other regions of the world, such as Siberia and South and East Asia, we find that by reaching a 1.5 ºC target, and then a 2.0 ºC, the frequency, duration and water

deficits of droughts decrease or do not change significantly. This may be associated with the important increase in both flow rates and high flow frequencies previously projected for these regions at 1.5 ºC which have been linked with the reduction in the aerosols load represented by the HAPPI experiment, particularly in the South and East of Asia[*Paltan et al.*, 2018]. For example, mean flow rates at the Ganges and Ob' basins are expected to increase between 5 and 7% at a 2.0ºC warming scenario. Likewise, previous studies have also detected that reaching 2.0ºC may lead to limited water availability and an increase in the number of consecutive dry days and thus intensifying drought risk in areas such as the Amazon area, South Africa, and in the Mediterranean basin [*Schleussner et al.*, 2016; *Lehner et al.*, 2017].

7.4.2 Change in Gross Hydropower Potential between 1.5°C and 2°C warming scenarios

Next, from our multi-model ensemble data we estimate that the mean global GHP is 61.40PWh/year (multi-model ensemble stdv: 16.40). This estimate falls within the ranges that recent studies have estimated between 41 and 67 PWh/year [*Bartle*, 2002; *Pokhrel et al.*, 2008; *Van Vliet et al.*, 2016; *Hoes et al.*, 2017] (Note that Zhou et al. (2015) estimated global GHP at 128 PWh/year). The difference in such estimations has been linked with the type of elevation information used, the runoff and river flow used as input, and the grid size which determines heights. Yet, in our case the relatively high values may be given by the overestimation of the flows used here which is particularly important in South Asia as a result of aerosol loads representations in the area[*Paltan et al.*, 2018]. Spatially, GHP is important in areas that traditionally have been highlighted for their hydropower potentials such as Asia or the area of the Amazon catchment (Figure 7.2a). Also, the spatial distribution of GHP does not vary significantly across the four models used in our study (see Supplementary Figure S7.3). Yet, the wettest models, MIROC5 and Can-AM4, show

major GHPs increases in areas such as South America, South Asia, or central-east Africa. For these two models, mean global GHP is 79.16 and 73.30 PWh/year respectively.

We also calculated that under both climate targets the relative global GHP increases when compared to the historical baseline (Figure 7.2b,c). In the 1.5ºC scenario, the GHP calculated from the multi-model ensemble mean is 63.24 PWh/year (increase ~2.91%) and at 2.0 ºC this value reaches 64.60 PWh/year (increase ~4.95%). This increase is similar with previous estimates that also project an increase in GHP of 2.4% and 5.3% for the RCPs 2.6 and 8.5 scenarios, correspondingly [*van Vliet et al.*, 2016b]. Yet, this trend is not globally uniform (see Figure 7.1b/c). At 1.5ºC we detect a reduction in regional GHP mainly in South America, North Africa, Southern Africa, Australia, and certain patches in the U.S. Typical decreases range between 5 and 10% with a more marked reduction in the tropics. Lastly, shifting from 1.5 to a 2.0ºC warming scenarios, apart from some slight intensifications in the patterns described, does not seem to lead to relevant discernible changes in GHP. Nonetheless, for the global estimate, these reductions in global GHP seem to be offset, by the important augment calculated in areas such as East Asia, India, Russia, or Canada.

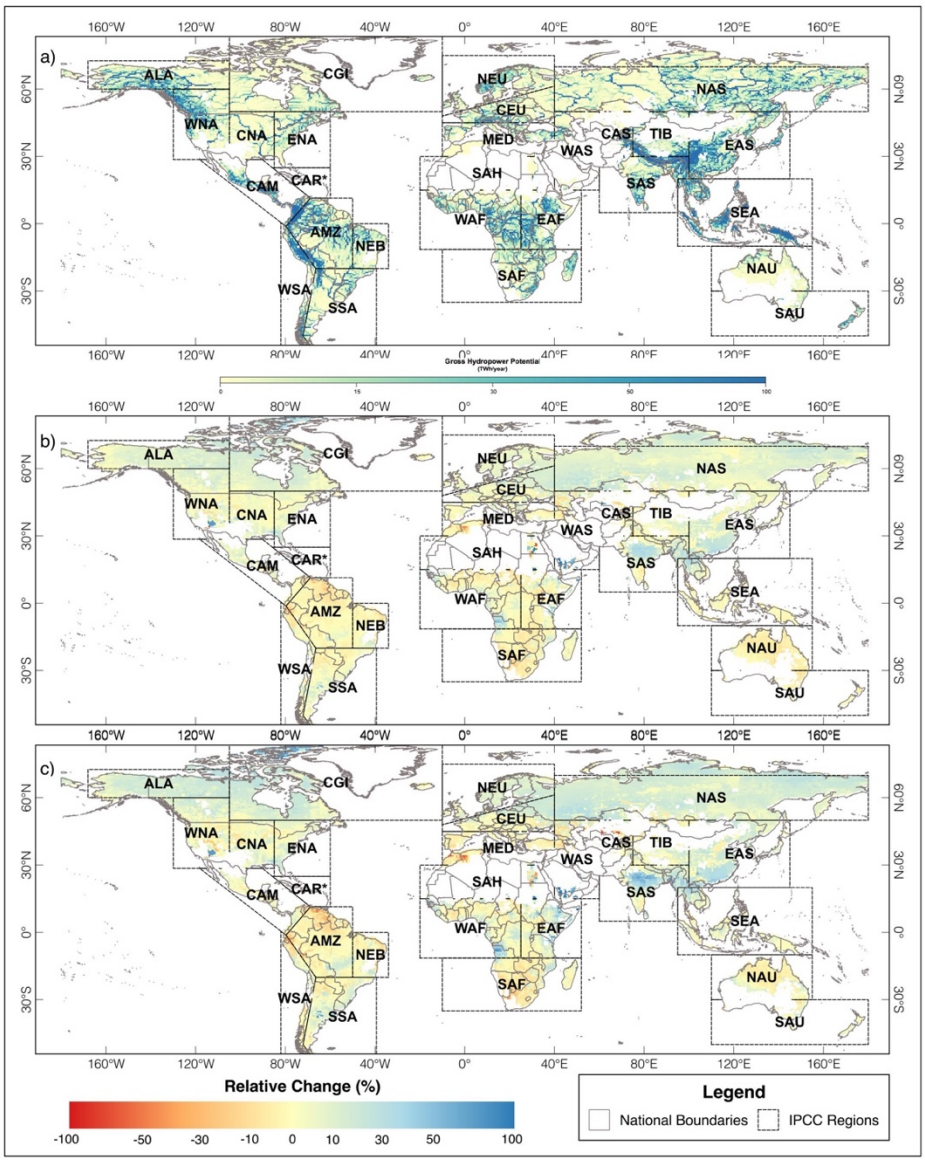

Figure 7.2 Global Gross Hydropower Potential (GHP), current situation and projected relative changes resulting from the Paris Agreement.

a) Multi-model and ensemble annual mean for four AGCMs of the current (from the baseline 2006-2016) GHP estimate, b) Relative change of historical GHP at a 1.5ºC scenario, c) Relative change of historical GHP at 2.0 ºC. Grid cells where mean daily river flows <10m3/s were screened out. The region definitions and their referential boundaries are those used by the Intergovernmental Panel on Climate Change.

Acronyms for this and other figures: Alaska/N.W. Canada (ALA), Amazon (AMZ), Central America/Mexico (CAM), Small islands regions Caribbean (CAR), Central Asia (CAS), Central Europe (CEU), Canada/Greenland/Iceland (CGI), Central North America (CNA), East Africa (EAF), East Asia (EAS), East North America (ENA), South Europe/Mediterranean (MED), North Asia (NAS), North Australia (NAU), North-East Brazil (NEB), North Europe (NEU), Southern Africa (SAF), Sahara (SAH), South Asia (SAS), South Australia/New Zealand (SAU), Southeast Asia (SEA), Southeastern South America (SSA), Tibetan Plateau (TIB), West Africa (WAF), West Asia (WAS), West North America (WNA), West Coast South America (WSA). Antarctica and Arctic and Pacific Islands are not included.

7.4.2.1 Regional GHP implications of variability in hydrological droughts

We also explore the implications of shifts in the water deficits on GHP in various global regions (Figure 7.3). Change in the water deficits is used here as our results suggest that this indicator is the most sensitive to changes in the temperature targets agreed in Paris. Also, this indicator captures the extent at which different regions of the world would suffer water losses.

The possible repercussions in GHP between the two climate targets may be importantly severe in regions such as the small islands in the Caribbean, in the Mediterranean area, Southern Africa, the Sahara, South Australia and New Zealand, Southeastern South America, West Asia, West North America, and West Coast South America. In these regions GHP slightly augments on average 1% at 1.5 ^{o}C and 3% at 2.0 ^{o}C, yet the ratio of change (RC) of water deficit increases from ~0.89 at 1.5 ^{o}C to 1.35 at 2.0^{o}C, suggesting an intensification of this indicator. Thus, in these regions, the 2.0 ^{o}C scenario may importantly constrain the apparent gains in GHP described in the section above. As such, we explore the implications of these possible water deficits in global and regional GHP estimates.

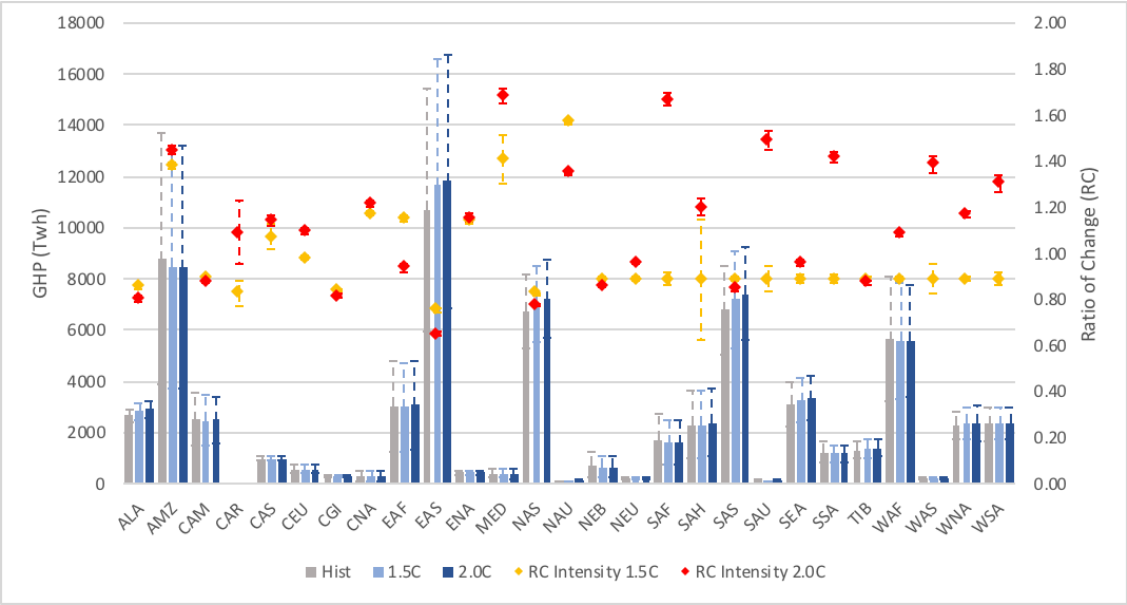

Figure 7.3 Regional Gross Hydropower Potentials (GHP) compared to shifts in Ratios of Change (RC) of water deficits at 1.5ºC and 2.0ºC warming scenarios as agreed in Paris.

The horizontal axis shows the global IPCC regions as described in Figure 7.2. The vertical axes show GHPs which represents the total sum of grid values within each region and the Ratios of Change (RCs) of Water Deficits (of each scenario compared to the historical baseline) represent regional averages. The bars indicate the 95% confidence interval. Region acronyms as figure 2.

7.4.3 Vulnerability of the hydropower sector at 1.5 and 2.0°C warmer worlds

Moreover, the share of GHP vulnerable to water losses at both temperature targets is estimated (Figure 7.4). We calculated that in average 18.40% of current global GHP (or 11.50 PWh/year) is vulnerable to hydrological droughts under 1.5ºC. At 2.0ºC global vulnerability of GHP importantly increases to 24.97% (or 16.09 PWh/year). In spite of the global increase of the GHP vulnerability at 1.5ºC, areas that significantly stand out include Alaska and North-West Canada, Central Asia; Canada, Greenland and Iceland (note that Greenland was screened out), North-East Brazil, Southern Africa, Sahara (here mostly refers to the Nile river region), and West Asia. In these regions and at this climate threshold

at least 25% of their GHP is vulnerable to water deficits. Then, in Alaska and North-West Canada, Central Asia; Canada, and West Asia the GHP vulnerable at 2.0^{o}C, notably increases an additional 5-10%. Also, at this climate target, regions such as West-North America and North Asia, the GHP vulnerability to hydrological droughts approximates 25%. Thus, existing or planned projects in these locations may be importantly constrained by variability of low flows under this climate target.

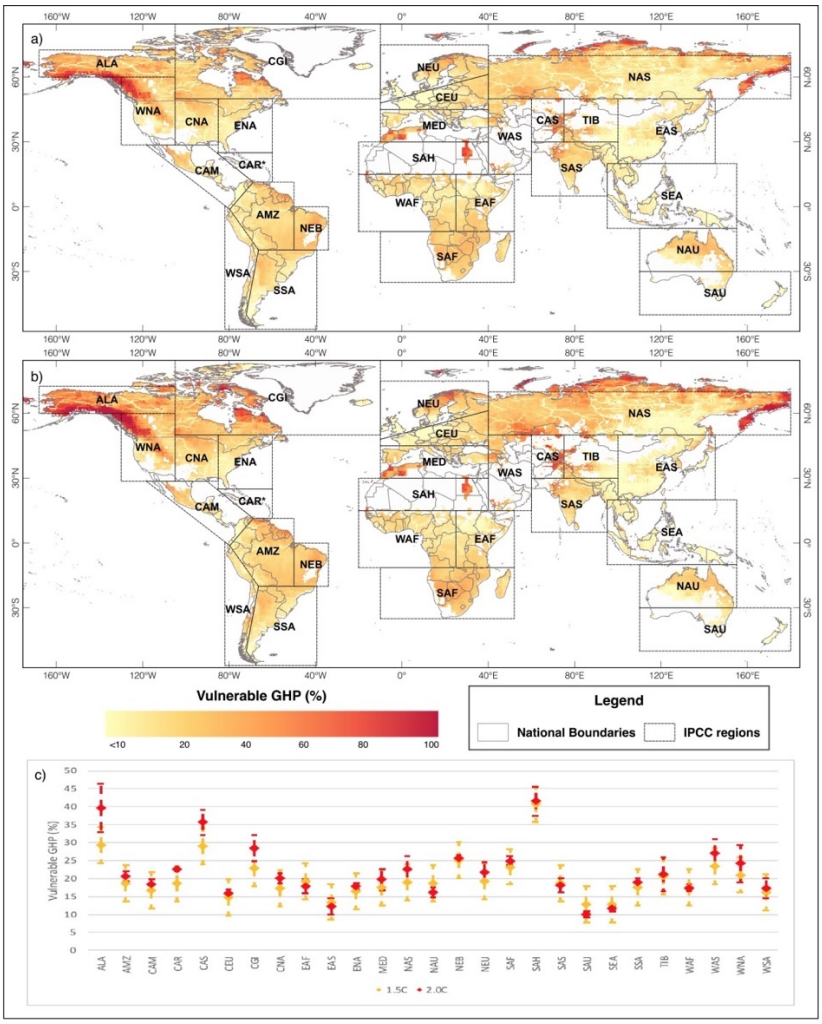

Figure 7.4 Relative Gross Hydropower Potential (GHP) vulnerable to the climate targets Agreed in Paris.

a) 1.5ºC and b) 2.0ºC scenarios; c) shows means for the IPCC regions and the bars indicate the 95% confidence interval. Grids where mean daily river flows <10m3/s were screened out. Region acronyms as figure 7.2.

7.4.3.1 Potential Implications of hydropower vulnerability in the energy mix at the country level

Lastly, our results highlight those countries that its energy production mix would be more impacted by the losses in GHP which may result from the Paris Agreement (Figure 7.5 and Figure 7.6). At 1.5ºC we note an initial impact in Canada, most of South America, Scandinavia, the Southern Africa, and various countries in central and South Asia. The most vulnerable countries are Kyrgyzstan and Tajikistan as ~40% and 50% (respectively) of their energy share may be impacted by a more vulnerable GHP. Then Sub-Saharan countries such as Namibia, Mozambique, Zambia, and the Democratic Republic of Congo show a quarter of their energy mix impacted at this climate target. Also, countries such as Nepal, Paraguay and Georgia may have about 20% of the energy mix at risk. A considerable impact is also detected in Canada, Brazil, Norway, Ethiopia, Tanzania, or Georgia (energy mix vulnerable: ~15%). These countries, apart from the important GHP share which is vulnerable to water deficits as presented in the section above, show an important contribution of hydropower generation in their national energy mix.

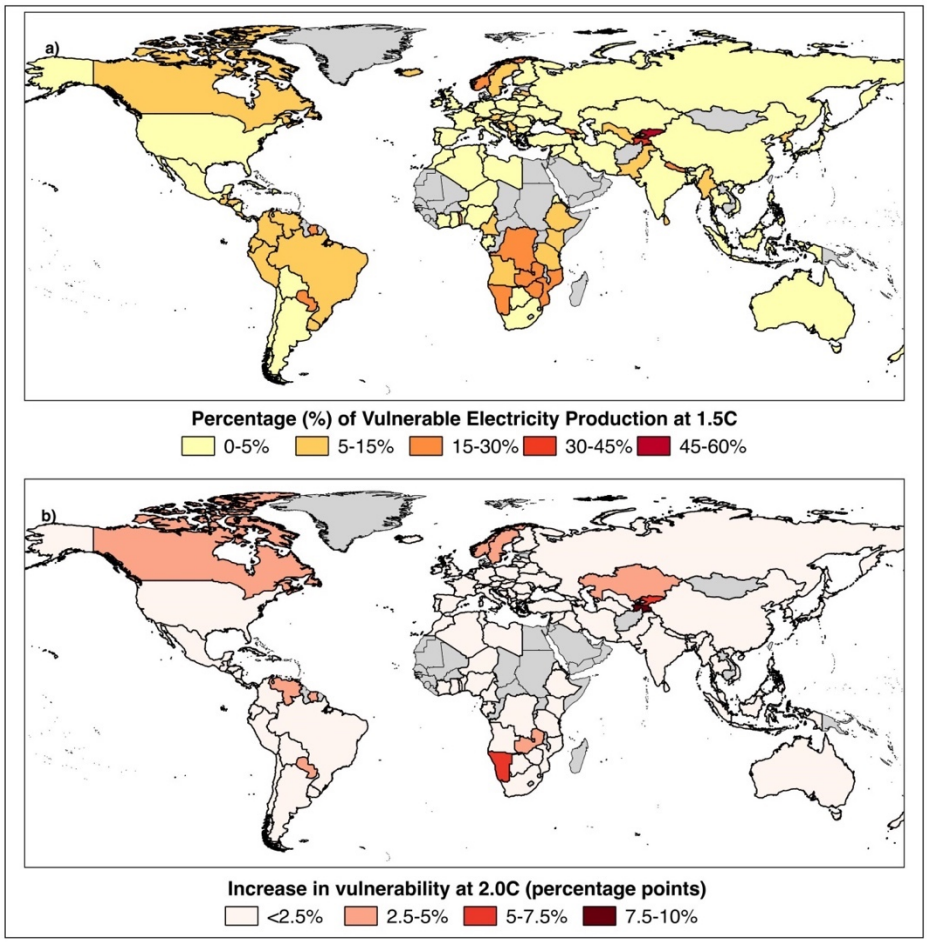

Figure 7.5 Impacts of GHP vulnerability resulting from the Paris Agreement in the global energy production mix.

a) Relative share of the total energy produced that is vulnerable to hydropower deficits under the 1.5ºC scenario; b) Increases in vulnerability (percentage points) from 1.5 to 2.0ºC. A complete list of national-scale values is presented in Supplementary Information S7.4. Countries in grey did not have values for their energy share which depends on hydropower.

While the half-degree warming typically does not lead to increases greater than 2-3%, in various countries this may importantly differ. Specially in central Asian countries such Tajikistan and Kyrgyzstan a 2.0ºC warming scenario may add almost 10 percentage points

in their total vulnerable energy mix (energy mix vulnerable: ~50% and ~60% respectively). In other Sub-Saharan countries such as Zambia and Namibia reaching 2.0ºC would lead to about 30% of their energy mix be vulnerable (showing an increase in 5 percentage points when compared to 1.5ºC). In Canada, Paraguay, Norway, Albania, and Nepal the share at risk at this climate target would be about 20%. Moreover, in countries such as Sweden, Croatia, and Venezuela the half degree warming leads to ~15% of their national energy mix be vulnerable to water deficits. As such, maintaining a 1.5 ºC level of warming becomes crucial for these listed countries.

It is important to note that apart from the mentioned Asian and Sub-Saharian countries, Kazakhstan, Morocco, Turkmenistan, Botswana, Iran, and Uzbekistan may see an important impact on their total national hydropower capacity resulted from water deficits of a world 2.0ºC (Figure 7.6).

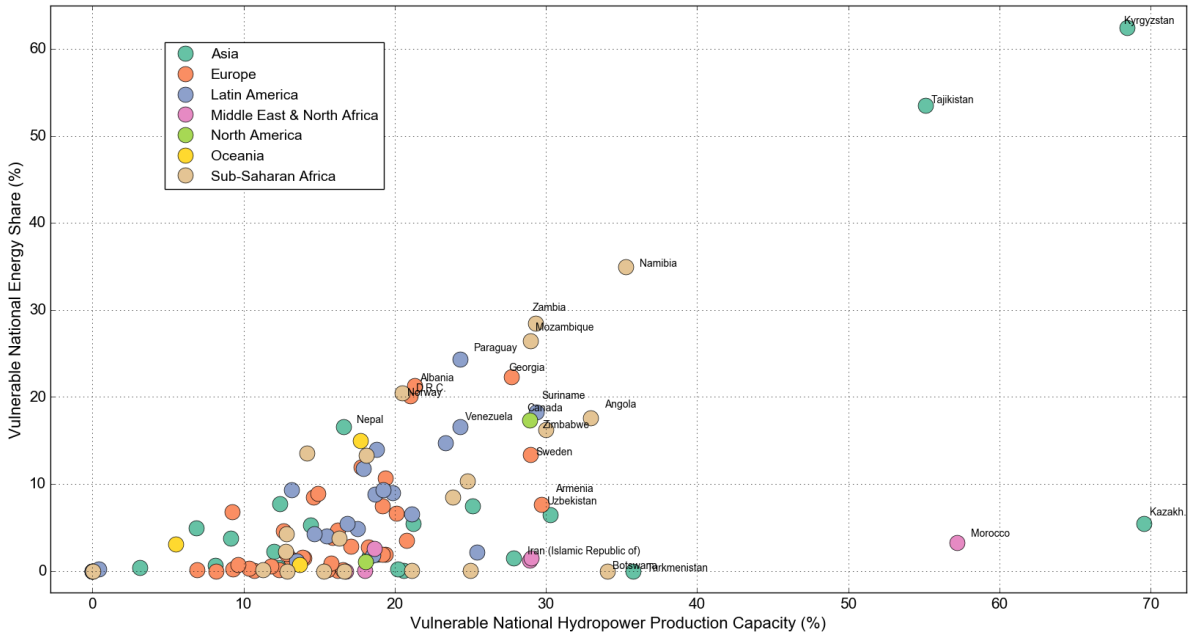

Figure 7.6 Relation of relative share (%) of the total energy that is vulnerable to hydropower deficits under 2.0ºC and relative share (%) of total vulnerable GHP capacity per country level and region.

D.R.C stands for Democratic Republic of Congo and Kazakh. for Kazakhstan. Note that various countries are missing due to the lack of information on hydropower dams and/or their energy share corresponding to hydropower (see Methods). The complete list of national-scale values is presented in Supplementary Information 4.

7.5 Conclusions

This study extends prior work by including indicators of variability of low flow in global, rather than using only the mean hydrological condition. We first show that considering only the mean hydrological state under projected climate change may lead planners to overlook the threats posed by more intense droughts which also have important repercussions for the energy mix in several countries.

We detect that mean global GHP will increase progressively under each climate target. For instance, our estimate of current GHP, 61.40 PWh/year increases by ~3% at 1.5 ºC and

by 5% at 2.0ºC (yet some reductions are observed principally in South America, North Africa, Southern Africa, and Australia). Nonetheless, despite this apparent future global GHP gains under both scenarios, the increase in water deficits between these two targets is projected to severely impact GHP. We project that shifting from 1.5ºC to 2.0ºC increases the average global intensity of droughts by about 30% (RC from 0.98 to 1.28).

As such, under 1.5ºC about 18% of global GHP is vulnerable to water losses resulting from more intense droughts and under 2.0ºC, almost a quarter of current global GHP is vulnerable (24.97%, or 16.09 PWh/year). Regions with water deficits which may lead to important losses in GHP are Alaska and North-West Canada, Central Asia, Canada, North-East Brazil, Southern Africa, Sahara (the Nile river region), and West Asia. In these areas, the performance of current, or planned hydropower projects may be importantly constrained by a future with more severe water losses.

Also, future water deficits and subsequent losses in GHP may in turn impact the energy mix in various Asian countries, most of Sub-Saharan countries, and others in Europe and Latin America such as Georgia, and Paraguay. These countries importantly rely on hydropower for a significant fraction of their electricity production and at the same time may experience more intense water deficits due to more variable droughts. Yet, committing to a 2.0 ºC level of warming, instead of 1.5ºC, importantly increases the vulnerable energy share in Canada, Norway, and Albania, in addition to the above countries. In Kyrgyzstan and Tajikistan, at 2.0ºC, the vulnerable energy share may even surpass 50%. Yet, in these estimates it is important to consider possible regional and trans-boundary water transfers which may attenuate (or intensify) these losses.

Lastly, we acknowledge that there are other technical, social, environmental or economic factors and hydropower metrics which are not considered here that may also affect the

vulnerability of the hydropower sector to future warming. Incorporating the way these wide range of factors interplay in the future vulnerability of the hydropower sector would enhance our understanding of the role of this sector to achieve the Paris targets. In particular, water shortages may affect local communities and the surrounding environment of a hydropower project and cause knock-on effects on hydropower generation, for instance if water is diverted for agriculture, industry and municipal drinking water supplies.

7.6 Acknowledgments

We acknowledge the efforts of Dr. Dann Mitchell and all those involved in the HAPPI project for making the base data of this study available and thus permitting the assessments of 1.5°C and 2.0°C climate targets.

8. Concluding Remarks

This thesis unveiled novel ways in which climate sources of variability influence the spatial and temporal heterogeneity of flows. This was done by presenting a framework which combines various physical sub-models and complementary tools that have enhanced the description of flow characteristics over large scales. So, systematically, this thesis first analyzed the role of land surface processes in flow peaks characteristics in cold regions (with traditional poor river flow representations in spite of their climatic significance). From here, the role of a critical low frequency mode of climate variability (ARs) on river flow extremes as well as land surface processes was explained. Next, the implications of international climate agreements on river flow extremes and their repercussions for hydropower systems were examined.

As such, the first case study (Chapter 3) uses WFDEI re-analysis data to perturb input parameters for JULES LSM and show that river flow peaks in snow-dominated catchments, such as the Ob', are significantly driven by the capacity of a snowpack to retain liquid water. As this driver seems to regulate the timing and the amount of snow which melts, it becomes a critical component when understanding occurrence of spring flow pulses. The second case study (Chapter 4), applied the components of the framework to examine the response of surface hydrological variables and extremes to Atmospheric Rivers, as an example of a mode of natural climatic variability. This thesis found that this form of moisture transport contributes to ~22% of total global annual runoff. In particular, this mode of variability may increase the frequency of flood and drought events (about 80%) in areas such as the West Coast of the U.S, New Zealand, the Iberian Peninsula, and South Africa, exposing about 300 million people annually.

For the next study case, the framework was adjusted to facilitate the multi-model ensemble outputs and project river flow shifts in a warmer world. The last case studies (Chapter 5 and 6) used the climate outputs from the HAPPI framework to explore the way in which achieving the climate targets agreed upon in 2015 at the COP21 in Paris would impact global river flows. By applying the components of this framework, this thesis thus drove ~500 multi-model ensemble outputs from HAPPI AOGCMs to generate global river flow time series. Further analyses found that South Asia would already be the most affected area in a world 1.5ºC which was warmer. Here, the historical 1-in-100-year flow would occur with a frequency of 1-in-25 years. Furthermore, highly populated areas such as the Yangtze river and the Upper Blue Nile, which in spite of showing only a moderate increase in high flows at 1.5°C, will see the current 100-year flood occurring approximately once every 25 years at 2.0°C. Lastly, by utilizing the river flows generated, this thesis explored the way in which the hydropower sector would be affected by variability in low flows resulting from these climatic targets. The results presented here found that the resulting intensity of future low flow variability and subsequent water losses may lead to the loss of up to 25% of global Gross Hydropower Potential. These losses may significantly compromise the electricity generation capacity in Kyrgyzstan, Tajikistan, Canada, Georgia, and the majority of South African countries.

Apart from these relevant contributions to the scientific literature and water resources managers, the framework utilized here has the potential to be applied to other similar applications that investigate physical stressors of river flows. Nonetheless, further applications should take into consideration the series of limitations that this framework contains. A first general limitation of the approach presented here is that given by the scale at which the simulations are presented (0.5^{o} x0.5^{o}). As such, various sub-grid physical processes, such as complex topographical, soil and vegetation dynamics, may be underrepresented. Thus, further studies should examine whether the utilization of new

hyper-resolution LSMs and hydrological models, would improve the large-scale analyses presented here. Similarly, an important limitation of the LSM and schemes used here is that they fail to include various types of human interventions in river flows. Most notable, the modules used in this study do not account for dams and reservoir regulations, and water transfer between catchments. They also fail to simulate agricultural dynamics and groundwater pumping. So, incorporating these characteristics in this framework would importantly enhance the description of flows examined here.

Equally, further investigation is required to address the specific limitations of each of the study cases presented here while expanding the application of the framework utilized in this project. For example, similar studies may apply the LSM used here to find the role that other land surface variables, such as soil infiltration capacity or changes in land uses, exert on river flow dynamics. Yet, as reviewed in Chapter 4, this framework fails to characterize the links between ice jams and flow peaks which are a significant source of risk not just in Arctic, but also in template regions. Further research is thus needed to incorporate state-of-the-art ice jams models into the river flow routine used here. Similarly, the incorporation of various of the recent advances in cold-regions hydrological modelling within this framework, would enhance our understanding of Arctic hydrology. For instance, examining the sensitivity of runoff and river flow to permafrost dynamics (as a major sources of carbon storages and the hydrological cycle) at regional scales would better explain the hydrological characteristics of Arctic regions and its links with the global carbon cycle. Thus, incorporating the improved permafrost representation developed by [*Chadburn et al.*, 2015] within this framework, would be a natural next step derived from Chapter 4.

At the same time, additional research is needed to analyse the role of other sources of natural climate variability in river flow and the occurrence of extremes by applying this framework and the techniques utilized in Chapter 5. For instance, the influence of high-frequency events such as Low Level Jets in terrestrial hydrology still needs to be better understood. Yet, it is important to consider the sensitivity of the results presented in this chapter to the technique developed to detect ARs. Among other conditions, the detection algorithm presented by *Guan and Waliser*, [2015a], which is used in this thesis, thresholds 6-hourly fields of ERA-Interim integrated water vapor transport (IVT) based on the seasonal 85th percentile per each global grid cell and a minimum value of 100 kgm^{-1}s^{-1} while also fulfilling a geometry requirement of both, a feature length of over 2000km and a length/width ratio >2. So, moving away from these thresholds is likely to also change the global hydrological extremes results presented here. As such, further research is required to examine the sensitivity of the global results presented here to these criteria. Also, the potential of the framework used in this project, along with the disturbed parameter technique applied, could be expanded by investigating the relative contribution of large-scale modes of variability, such as PDO or MJO, in surface hydrological variables and surface hydrological risks.

Moreover, the findings of Chapter 6 could be expanded by analyzing the potential population, infrastructure assets, human dynamics, and economic fluxes exposed to high flows resulting from the Paris Agreement. Yet, future studies of this type should take into consideration the effect of the reduced aerosol load (to about 1/3 of its current levels, as configured by the HAPPI protocol), in the hydrological cycle. Reducing the aerosol load (namely organic and black Carbon and sulfuric and nitric acids) is thought to lead to a more intense hydrological cycle in various global regions. In particular, the Asian monsoon region with current high aerosol loads, as configured by HAPPI, projects a higher increase in rainfall when compared to similar experiments. Thus, further hydrological

assessments which utilize the HAPPI experiment, or the results of this chapter, should address this source of uncertainty.

Moreover, as Chapter 7 presents a global overview of this Agreement's influence on global hydropower capacity, further studies are needed to refine the implications of these findings at finer scales. As such, other system performance metrics, such as resilience, robustness and reliability, would need to be included to explore further repercussions of flow variability in the energy sector. Similarly, the flows and data generated in these case studies could enrich further evaluations of the possible consequences of the climate targets agreed to in the Paris Agreement in sectors such as agriculture and food, health, water supply, transport, or in more sophisticated energy-electricity applications. This would require the incorporation to this framework of other sub-models which characterize such sectors. Yet, such further studies require to address the lack of representation of storage in the river flow dataset used in this chapter. Incorporating storage dynamics in the hydropower potential model is likely to attenuate the impacts of drought intensities found in this chapter. Similarly, it is important to consider the sensitivity of these results to the drought threshold utilized here (Q80 flow). Drought thresholds are derived from percentiles of the flow duration curve, per each grid cell. For perennial rivers the threshold typically ranges from the Q70 to the Q95 flow[*Hisdal and Tallaksen*, 2003; *Andreadis and Lettenmaier*, 2006; *Fleig et al.*, 2006; *Wong et al.*, 2011; *Van Loon*, 2015b]. Thus, further assessments require to evaluate the natural effect of selecting a different threshold in the estimated drought characteristics presented here.

Altogether, the findings presented in this thesis should be taken as initial evaluations which enhance our understanding of the relationship between climate, surface water, and in consequence, global water security. Thus, the outputs and techniques presented here have

the potential, not just to examine similar scientific questions, but also to be part of further efforts to build resilient measurements in a changing world.

9. Supplementary Information

This section presents the supplementary information which support the work published and submitted in Chapters 4, 5, 6, and 7.

Supplementary Table S4.1 Validation sites used for river discharge in the Ob' river.

Validation Site	Code	Latitude	Longitude	Distance to outlet (m)	Altitude (masl)	Years of Record since 1979
Ob At Salekhard	**11801**	66.63	66.60	287	46	21
Irtish At Omsk	**11048**	55.02	73.30	1824	93	21
Irtish At Tobol'sk	**11056**	58.2	68.23	637	31	21
Irtish At Khanty-Mansiysk	**11061**	60.97	69.07	20	30	18
Severnaya Sosva At Igrim	**11545**	63.18	64.40	147	9	21
Ishim At Vikulovo	**11414**	56.82	70.63	215	56	21
Tobol At Korkino	**12554**	56.08	65.92	559	66	20
Severnaya Sosva At Sosva	**11542**	63.65	62.10	324	23	21
Ursul At Onguday	**10100**	50.73	86.17	32	851	20
Tom' At Kemerovo	**10246**	55.38	86.05	273	141	13
Ob At Prokhorkino	**10023**	59.52	79.47	2024	41	16
Ob At Kolpashevo	**10021**	58.3	82.88	2422	56	20

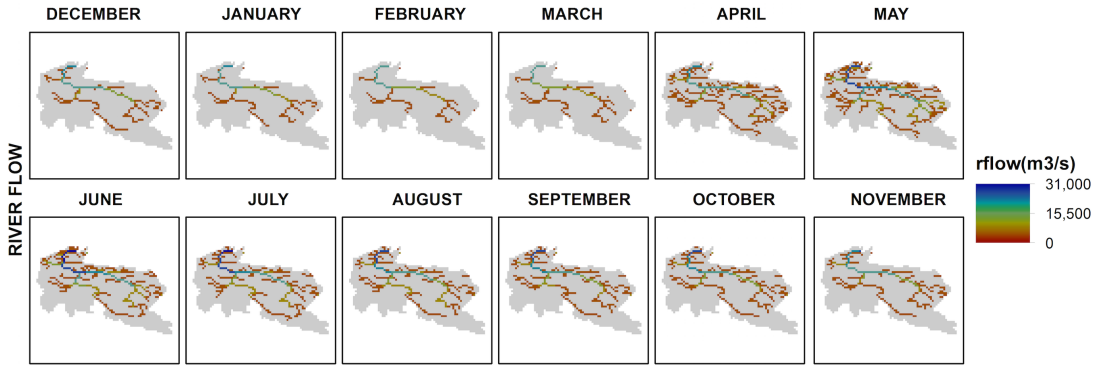

Supplementary Figure S4.1 River flow as simulated by JULES when using the multi-layer model. Monthly averaged values 1979 – 2011.

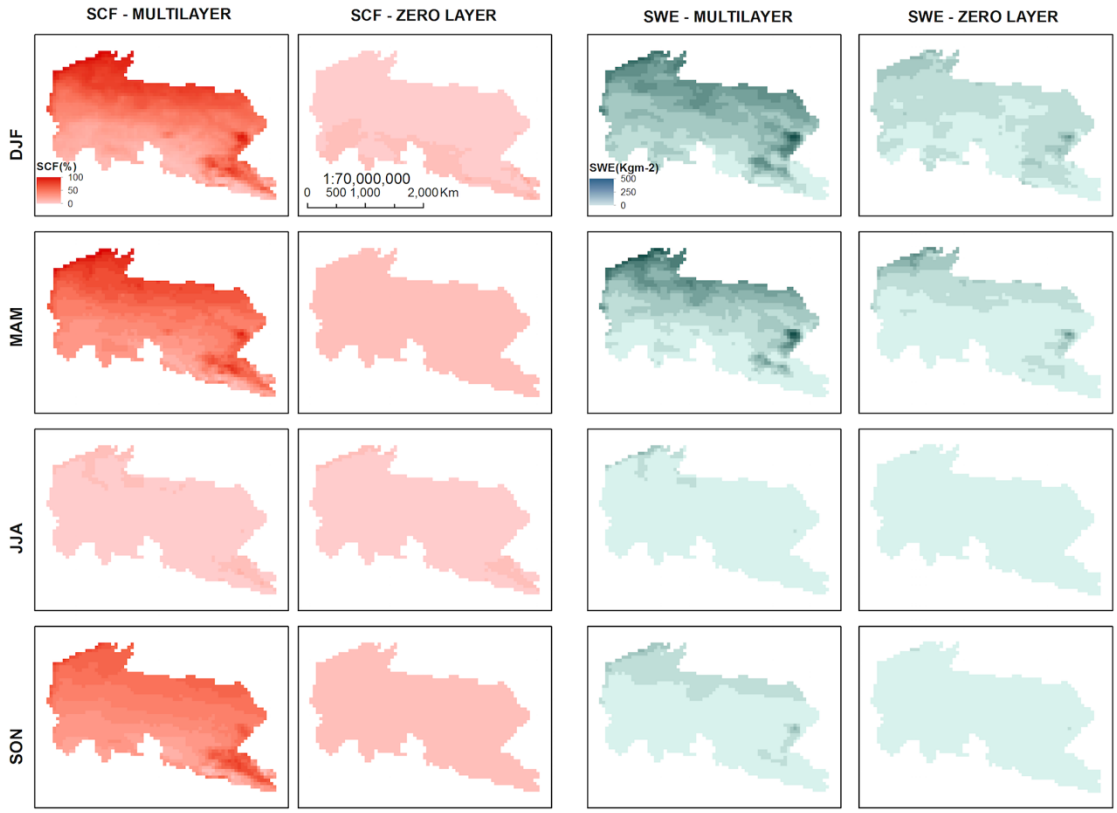

Supplementary Figure S4.2 Comparison of simulated seasonal Snow Cover Fraction (SCF) and Snow Water Equivalent (SWE) when two snow models are used. Seasonal averages are plotted for winter (DJF), spring (MAM), summer (JJA) and autumn (SON), for the period 1979 – 2011.

During early spring when SWE values peak, areas with snow masses of about 150 kg m^{-2} are typically found in this part of the basin. However, in spite of the significant snow extent observed here, total snow masses are not as great here as those found in the Upper Ob' sub basin, where terrain is characterised by mountains. By early March snow accumulated here typically exceeds 250 kg m^{-2}. Conversely, the third identified area corresponds to the sub-basins outside the main Ob' channel (Upper Irtysh, Ishim, Tobol and Lower Irtysh sub basins) that show relatively low values of SWE (not greater than 50 kg m^{-2}).

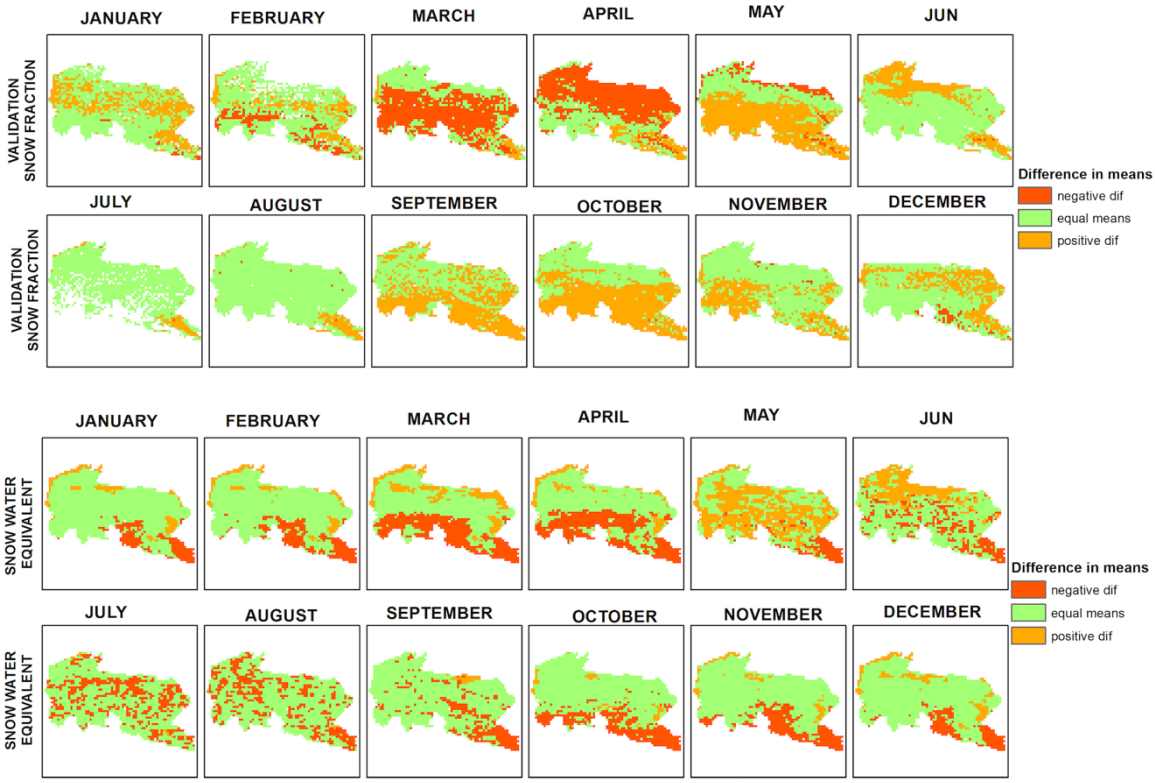

Supplementary Figure S4.3 Difference of means (two-tailed t-test $p \leq 0.05$) between simulated (JULES-multi-layer snow model) and observed (satellite derived) SCF and SWE values. Green areas represent areas with no difference in means which suggests correct representations by our multi-layer.

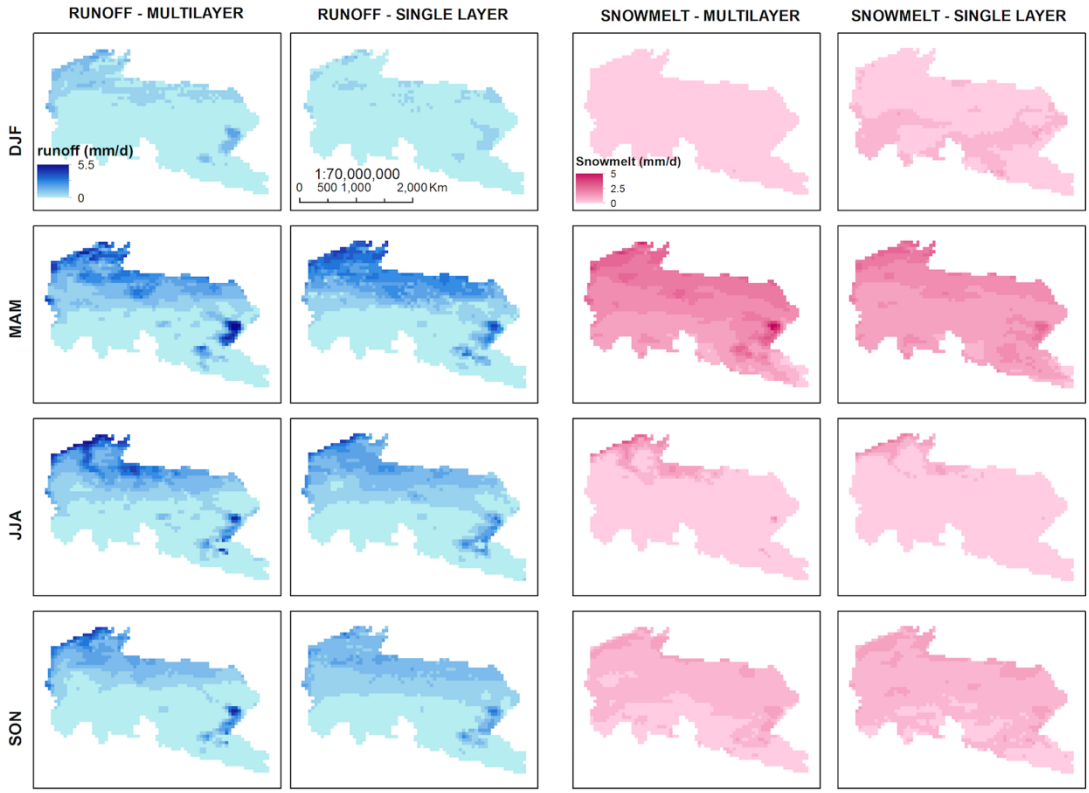

Supplementary Figure S4.4 Comparison of simulated seasonal runoff and snowmelt when two snow models are used. Seasonal averages are plotted, winter (DJF), spring (MAM), summer (JJA) and autumn (SON), for the period 1979 – 2011.

The areas of the Ob' with the greatest SWE values generate snowmelt that typically produces runoff values of over 3.5 mm d^{-1} during spring. In the other parts of the sub basin (and in the Upper Ob' as well) snow accumulates over an extensive area, however total snow masses are not as great as those found in the areas near the tributaries. At their peak during April, snowmelt values are typically over 60 m^3 s^{-1} and runoff generated exceeds 1.40 mm d^{-1}. As most of the main Ob' channel flows through this part of the basin, runoff generated here exerts a strong influence on the main river flow. In the Upper Irtysh, Ishim, Tobol and Lower Irtysh sub basins sub basins, where snow accumulated in April and May

is small, leads to a rapid thaw of the ground as spring onsets. Runoff generated here does not exceed 5 mm d^{-1}. Such runoff contributes to river flow variability in the Tobol, Ishim and Irtysh tributaries).

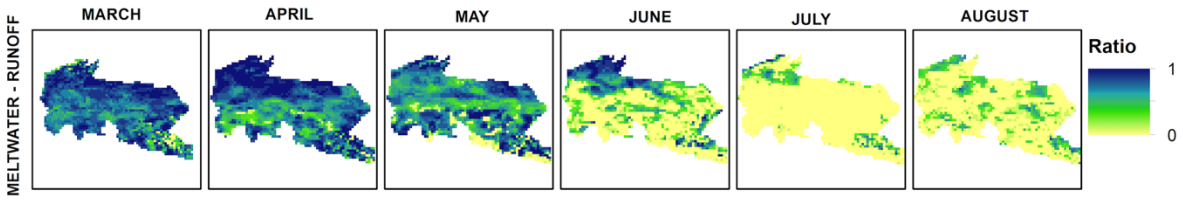

Supplementary Figure 4.5 Ratio between meltwater from the snowpack and runoff for the melting period (March – August). Monthly averaged simulated values between 1979-2011 Blank spaces show areas with no data due to clouds or errors in the satellite.

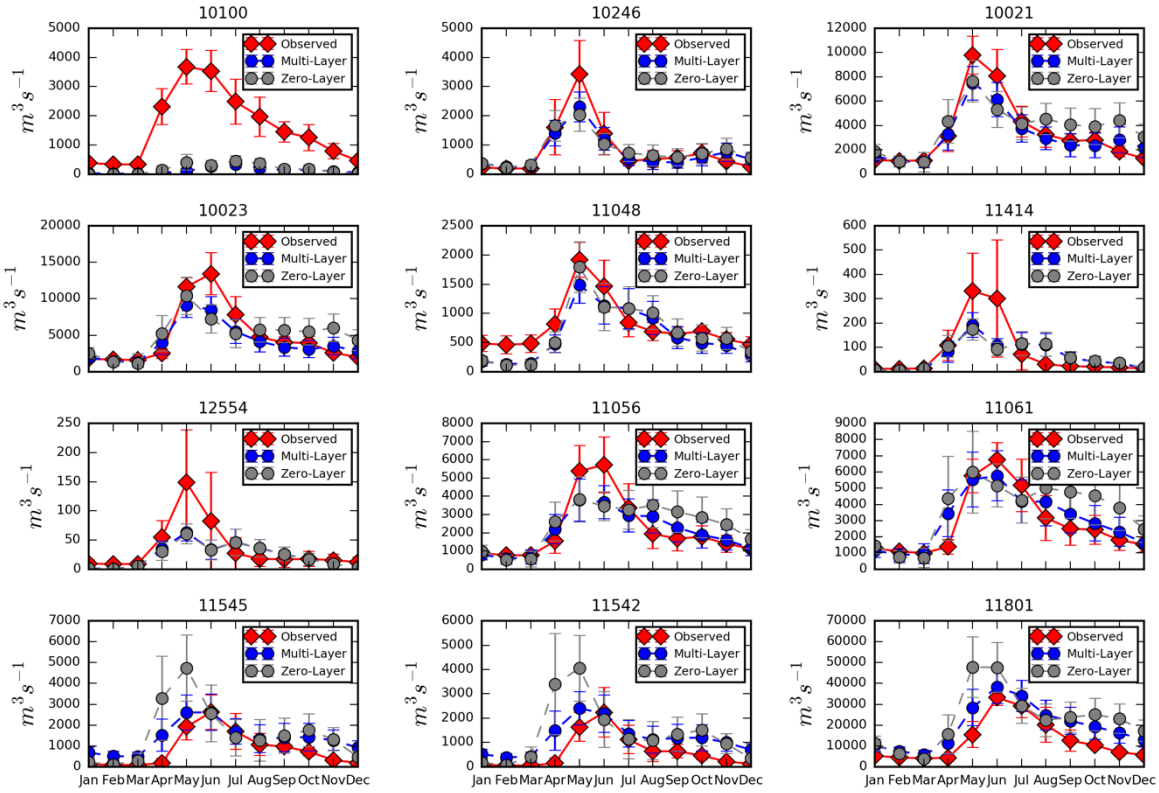

Supplementary Figure S4.6 Hydrographs showing averaged river flow monthly values for the period 1979-2011. Observed discharge vs simulated discharge of the multi-layer and zero-layer snow modules

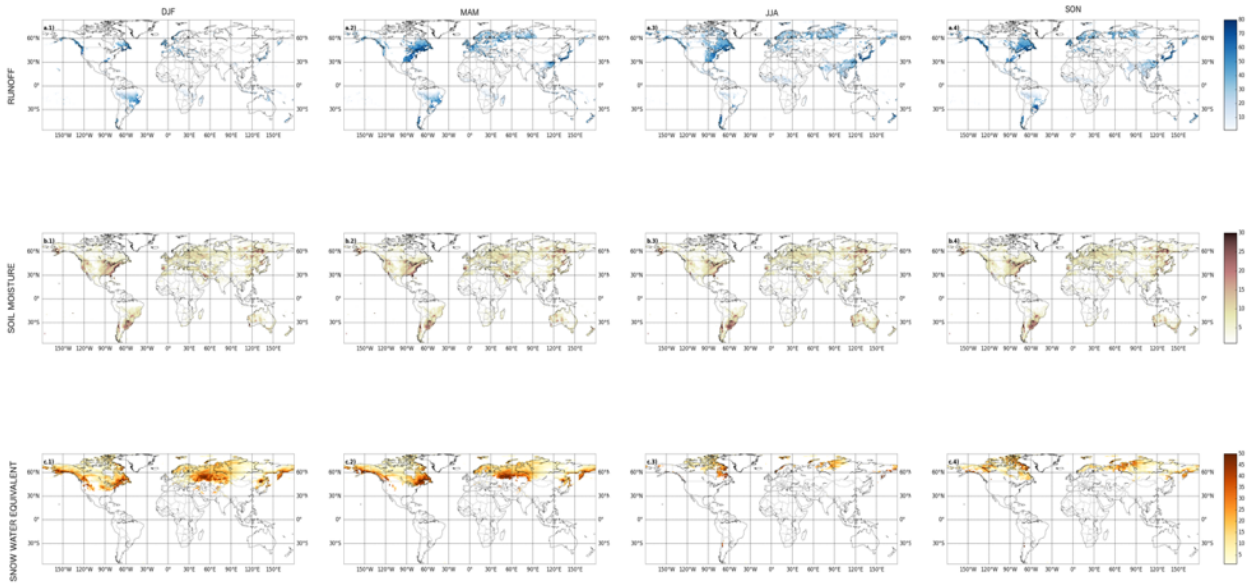

Figure S5.1. Global seasonal contribution of ARs to hydrological land surface variables runoff, total soil moisture content and snow water equivalent. DJF(December, January, and February), MAM(March, April, March), JJA, (June, July, August), SON (September, October, November).

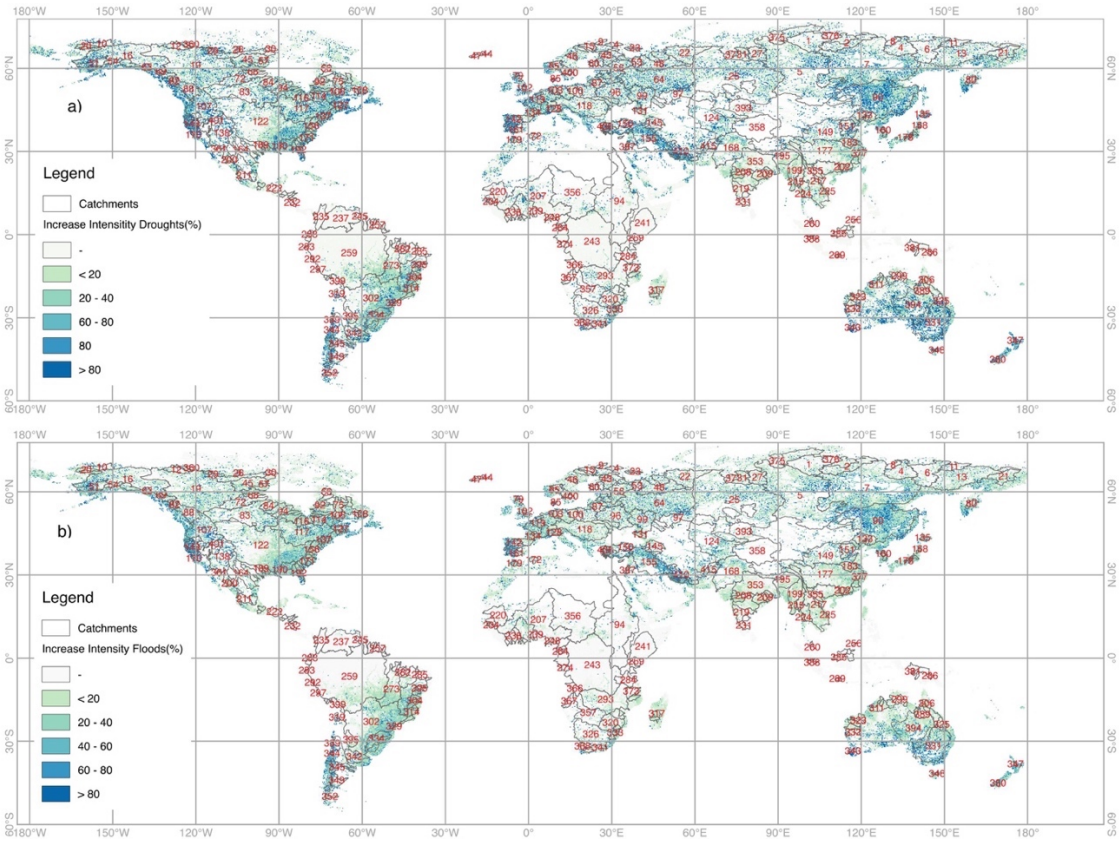

Figure S5.2 Contribution (%) of ARs to extreme flows: a) Low flows and b) High flows. Low flow is defined here as the Q90 flow, so this is the flow that is expected to be equaled or exceed 90% of the time. High flow is defined here as the Q10 flow, so this is the flow that is expected to be equaled or exceeded 10% of the time. Mean annual contribution (%) to flows for the period 1979-2010.

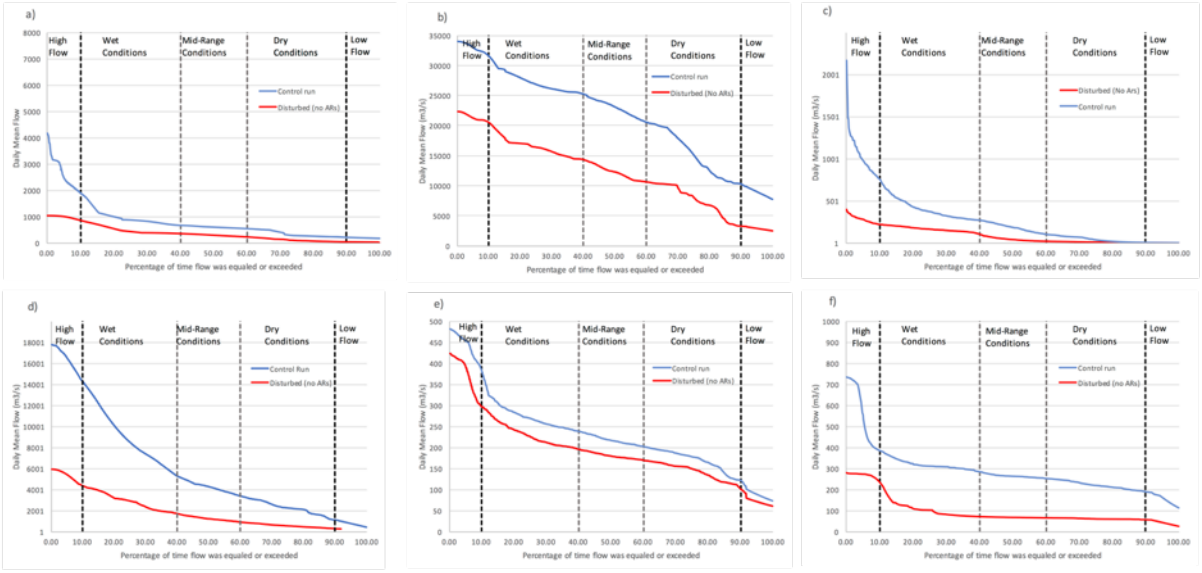

Figure S5.3 Flow Duration Curves calculated at the outlets of the following catchments: a) Sacramento River (Central Valley, California) b) Parana (Brazil) c) Duoro (Iberian Peninsula) d) Amur (China), e) Orange (South Africa), f) Murray-Darling (Australia). Daily mean values 1979-2010.

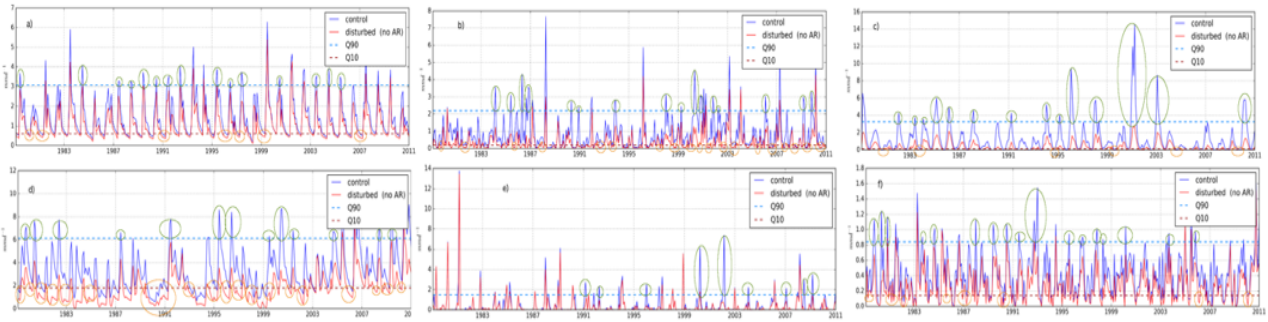

Figure S5.4 Role of ARs in the occurrence of extreme hydrology in 6 representative catchments: a) Sacramento (California), b) Parana, c) Douro, d) Amur, e) Orange (South Africa), f) Murray-Darling. Time series show monthly means of runoff and Q10 and Q90 values as thresholds. Green ellipses show events where monthly aggregates runoff exceeded the Q10 threshold in the control simulation yet this peak is not observed in our perturbed simulation. Thus, these are historical high flow episodes attributed to ARs. Similarly, orange ellipses show those events where low flow episodes occurs when ARs are not presents. In this case, ARs broke this hydrological drought conditions and thus increased the time lapse (and frequency) between low flow periods.

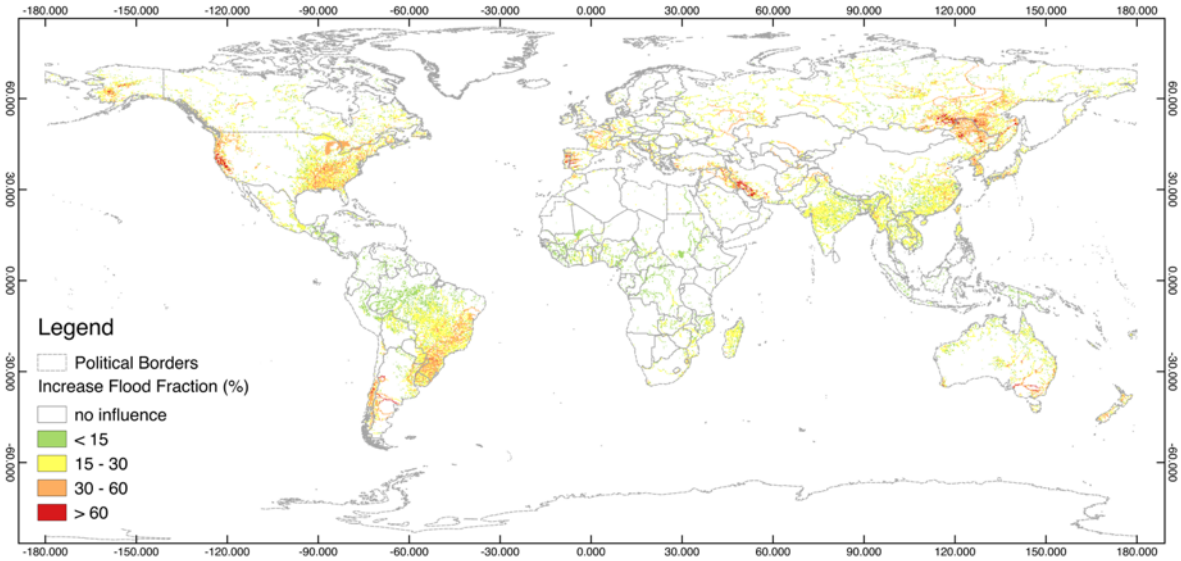

Figure S5.5. Map of contribution of ARs in the increase in flood fraction (for the 100-year simulated flood).

Table S5.1. Contribution (%) of ARs to extreme flows to global catchments.

< This table can be accessed electronically on:
https://agupubs.onlinelibrary.wiley.com/doi/abs/10.1002/2017GL074882 >

S6.1 The HAPPI Protocol

Since current intermodel-comparison exercises such as CMIP5 use radiative forcing protocols to project future temperature changes, which naturally leads to a very large range of possible future temperatures as a function of model sensitivity, the HAPPI experiment is designed to simulate specified temperature targets as precisely as possible. In accordance with the Paris agreement, two targets have been defined: 1.5°C and 2.0°C warmer than pre-industrial (1861–1880) conditions. For both targets, a set of 50-100 member ensembles simulating future conditions over a period of ten years has been simulated with a number of AGCMs. In order to estimate the associated climate impacts since pre-industrial times as well as compared to current conditions, two more experiments with the same ensemble size, one representative for the 2006-2015 period (actual experiment, in this study called historical scenario) and another one representative for the 1861-1880 period (natural experiment).

All experiments use an AMIP-style framework where boundary conditions over the ocean are prescribed by observed or modelled SSTs and sea ice. As for fully-coupled model experiments, radiative forcing is prescribed in accordance with the expected temperature outcome based on the CMIP5 mulit-model-means as described below. Ten year simulation periods are chosen for past, present and future as they provide sufficient material for some analysis of multi-year events, such as droughts. Each simulation within an experiment differs from the others in its initial weather state. So, if 100 ten-year time slices from a AGCM are used, it really provides 1000 years of data per experiment.

For the actual experiment, the 2006-2015 decade is chosen because it is our most recently observed period, but also because it contains a range of different SST patterns over the decade, allowing for an assessment of how the ocean conditions vary on inter-annual timescales, including El Nino and La Nina events. For the natural experiment, delta SSTs

taken from CMIP5 actual (historical) and natural experiments (10 year monthly means of the 1996-2005 decade) are subtracted from the OSTIA SSTs [*Donlon et al.*, 1998] to simulate counterfactual conditions. Past sea ice conditions as well as radiative forcings are taken from CMIP5 natural experiments directly (1996-2005).

Based on the temperature evolution over land and ocean, it is possible to estimate the required SST warming to achieve 1.5°C or 2.0°C warming for the globe as a whole. By chance, the multi-model-mean across CMIP5 GCMs under the RCP2.6 forcing scenario results in a global average temperature response at 1.55°C relative to pre-industrial levels (2091-2100 relative to 1861-1880), which is why for the HAPPI 1.5°C experiment, delta SSTs (that are added onto OSTIA SSTs as before for the natural experiment) from CMIP5 actual (1996-2005) and RCP2.6 (2091-2100) are used. So are future sea ice conditions and radiative forcings.

For the HAPPI 2.0°C experiments, no analogous CMIP5 simulations are available. The RCP scenario resulting in the second coolest temperatures by the end of the 21st century is RCP4.5, which reaches ~2.5°C relative to pre-industrial levels by the end of the 21st century. To calculate the future SST and sea ice conditions of a 2.0°C world we therefore take a weighted sum of the two RCP scenarios, W1 × RCP2.6 + W2 × RCP4.5. The weights are calculated such that the global-mean temperature response is 2.05°C (i.e. exactly half a degree above the 1.55°C response from the 1.5°C experiment), and results in W1 = 0.41 and W2 = 0.59. These weights are used to calculate the SSTs and sea ice coverage using the same methodology as in the 1.5°C experiment. The same weighting is used for the radiative forcing applied in the experiment. More details on the experimental setup can be found in [*Mitchell et al.*, 2017].

Following this scheme, we obtained the historical, and the future experiments for 4 AGCMs which met our requirements of either having produced runoff, or having sufficient atmospheric variables to compute it for the three scenarios. Thus, NCC/NorESM1-HAPPI model contains 125 ensemble members and ETH/CAM4 contains 500 ensemble members for each scenario; MIROC/MIROC5 contains 50 complete time slices for the historical experiment, and 100 slices for both futures, and CCCma/CanAM4 contains 100 ensemble members each scenario.

Also, as far as the effect of other forcing factors driving change, here we briefly discuss the counterbalancing nature of increased levels of anthropogenic aerosol levels (namely Organic and Black Carbon, BC and OC accordingly, as well as Sulfuric and Nitric acids, SO_2 and NO_3 correspondingly).

While OC, SO_2 and NO_3 hampers surface warming (by reflecting Short Wave radiation), BC warms upper levels of the atmosphere (absorption). Both effects lead to a reduced strength of the hydrological cycle, particularly in the Asian monsoon region with high aerosol loads (Bollasina et al. 2011). Since the aerosol load is reduced to approximately 1/3 of its current levels in both future HAPPI scenarios, many regions are going to see higher rainfall increases at 1.5ºC compared to what has been observed or simulated until now. Since HAPPI does not provide GHG-only experiments, unfortunately we are unable to disentangle potential thermodynamic and dynamic responses due to either GHGs or anthropogenic aerosols at this point in time.

S 6.2 Change in historical 100-year return period for AGCMs used here

This supplementary Figure illustrates the multi-ensemble median return period for future river flow for each of the AGCMs used in this study, shown in Fig.1 in the manuscript.

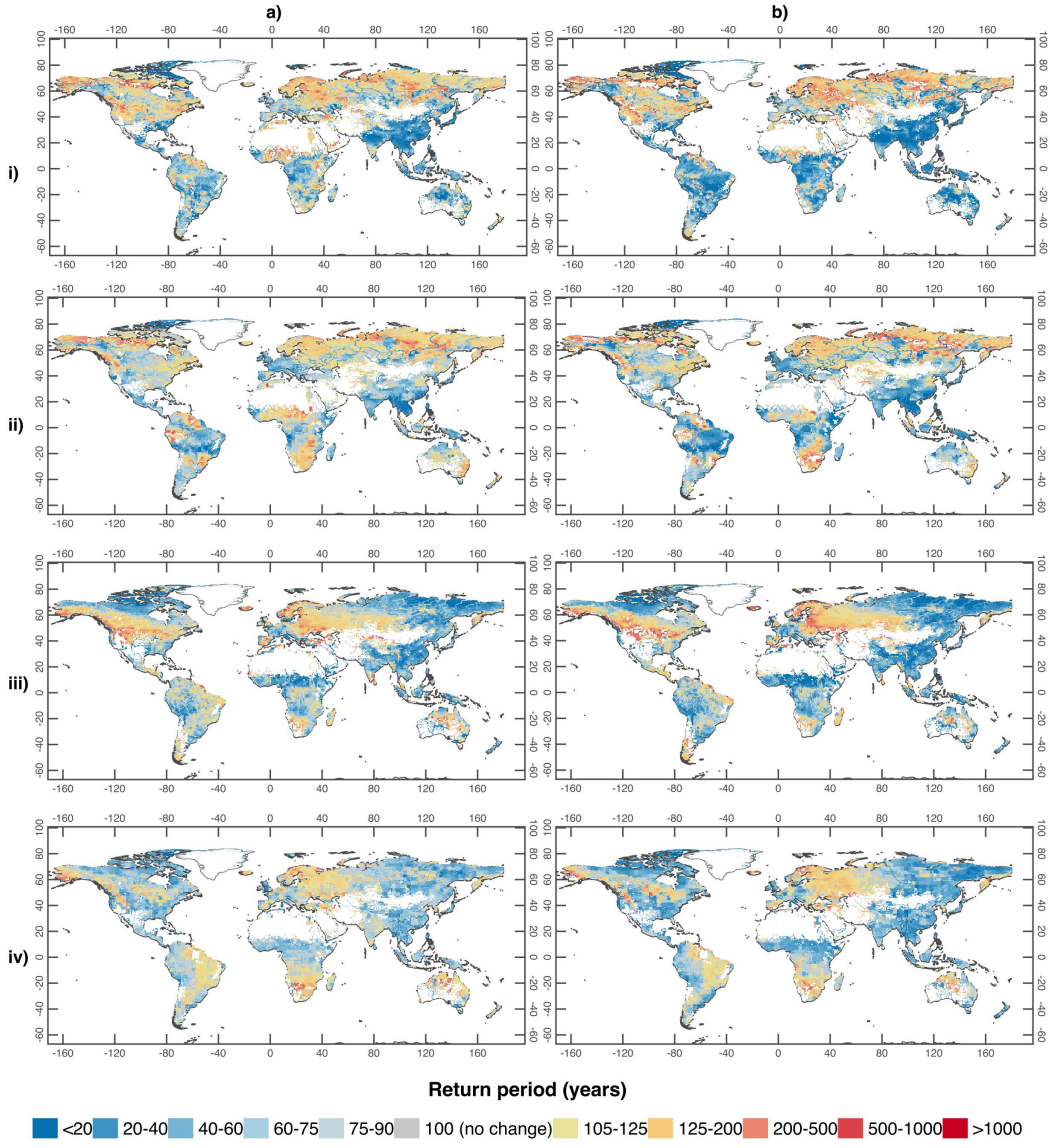

Figure SF 6.1. Multi-ensemble median return period (years) for future river flow corresponding to the historical 100-year flow. a) World 1.5°C warmer b) World 2C

warmer. AGCMs used in this study: i) NCC/NorESM1-HAPPI ii) ETH/CAM4-2degree iii) MIROC/MIROC5 iv) CCCma/CanAM4. Grids with where the historical averaged annual flow is $<1 m^3/s$ were removed.

Precipitation

Daily precipitation values were obtained from each of the AGCMs used in this study. First, here we present the percent change in precipitation amounts between the two scenarios and the historical period.

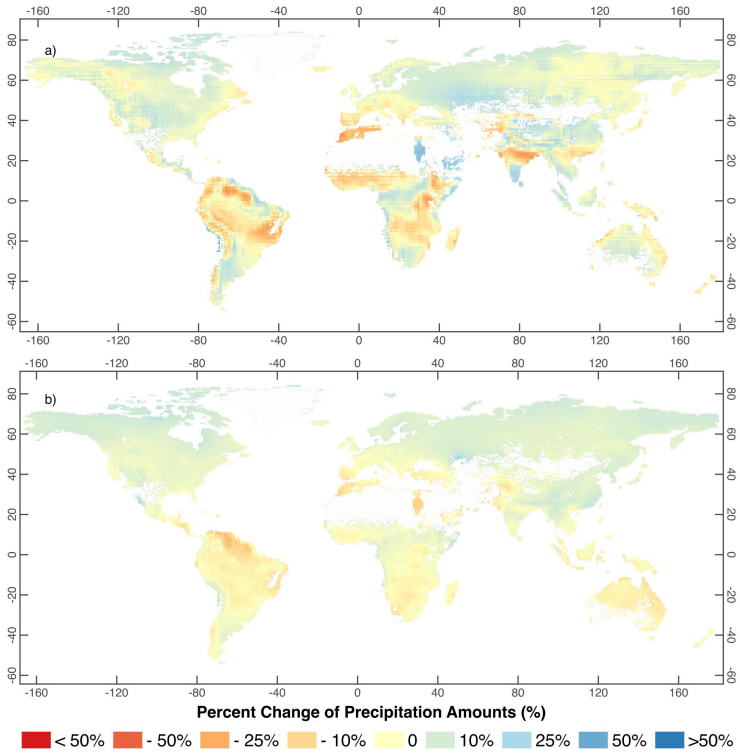

Figure SF S6.2. Multi-model average of percent change of annual precipitation amounts between a) A world 1.5C warmer, b) 2.0C warmer and the historical period (2006-2015).

Also, their mean average was compared against GPCC data [*Schneider et al.*, 2016]. The latitude-contribution for the historical base periods are shown below:

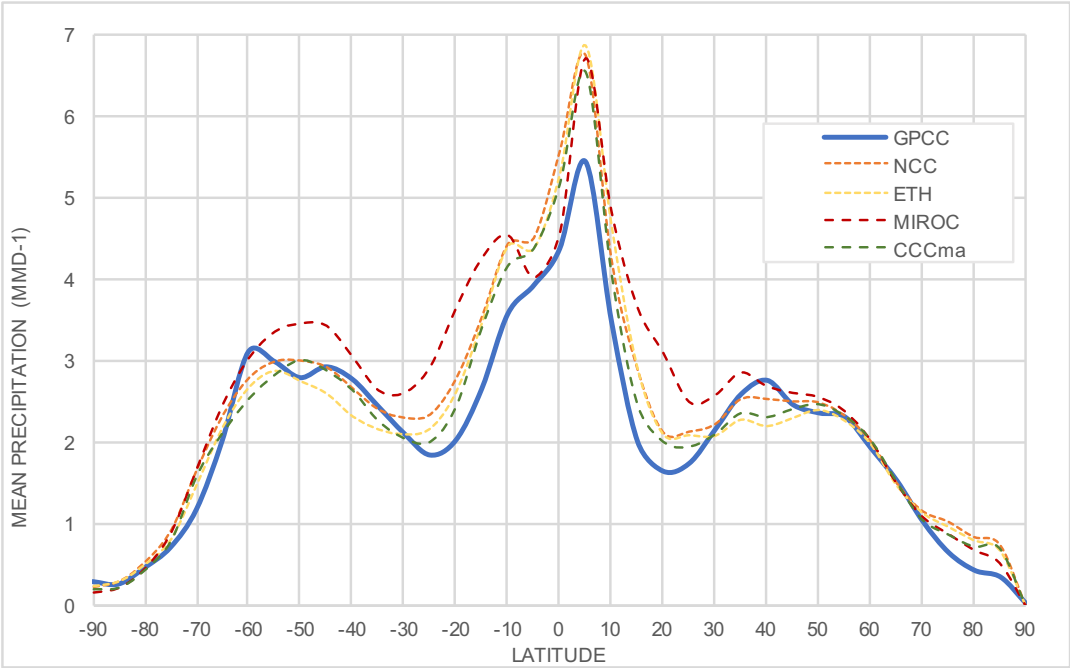

Figure SF S6.3. Multi-annual averaged global water precipitation (mm/day) calculated from the historical runs and compared against GPCC data. a) NCC/NorESM1-HAPPI b) ETH/CAM4-2degree and c) MIROC/MIROC5 d) CCCma/CanAM4.

Precipitation generated by the four AGCMs is principally overestimated in the tropics. This overestimation persists in temperate regions and is more severe for MIROC. Also, ETH/CAM4-2degree underestimates precipitation in temperate regions (between 30N? and 50N and S). Similarly, this overestimation is found for CCCma/CanAM4 between 30 and 50N. Precipitation is generally well represented by the four AGCMs in polar regions.

Biases may exist in the climatic variables represented by these AGCMs and thus in the runoff derived (either provided directly from the AGCMs or from our estimations).

Nevertheless, it has been understood that the change in extremes from long return periods, such as high flows, could be reasonably represented without correcting for bias [*Hirabayashi et al.*, 2013]. Also, it is important to highlight that bias corrections may not necessarily increase the estimation of future shifts in flood frequency.

Runoff

The runoffs, which were either obtained as a direct output AGCMs (NCC/NorESM1-HAPPI and CCCma/CanAM4), or calculated in thus study (MIROC/MIROC5 and CCCma/CanAM4) were compared against a reference observed runoff. The reference runoff was obtained from the Global Runoff Data Centre (GRDC) [*Fekete et al.*, 2002]. The values are global means from the global datasets available. We have used these runoff composites in order to make best use of the globally-available validation data. Unfortunately, there are no globally available data which can be used to validate calculations of river flow extremes at all locations. In consequence, in our paper we focus on changes in extremes rather than absolute magnitudes.

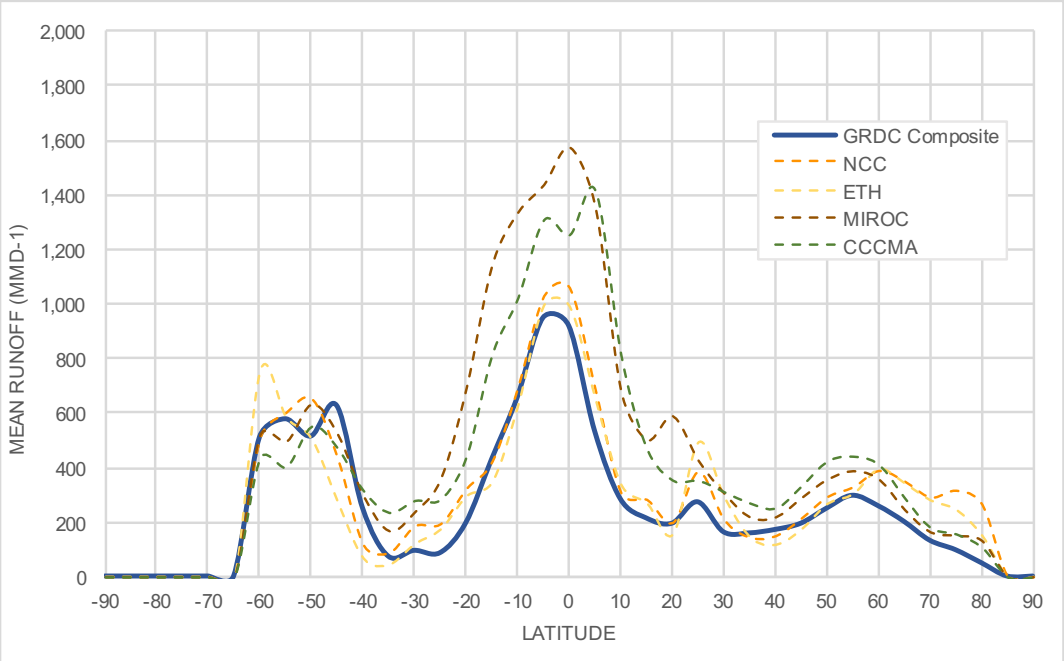

Figure SF S6.4. Multi-model daily mean global runoff compared to runoff observed by GRDC. NorESM1: NCC/NorESM1-HAPPI, CAM4: ETH/CAM4-2degree, MIROC5: MIROC/MIROC5, CanAM4: CCCma/CanAM4.

Runoff generated from NCC/NorESM1-HAPPI and ETH/CAM4-2degree show a fair agreement with observed data in tropical areas. Then most important disagreements of these two AGCMs are found in temperate regions of the northern hemisphere (between latitude 20N and 40N), and particularly at northern high latitudes (>60ºN). Also, overestimations in runoff are found at high latitudes. MIROC5 and CanAM4, on the other hand, tend to overestimate global runoff especially in tropical regions. In northern temperate areas, the overestimation persists, especially for MIROC/MIROC5. Yet these two AGCMs seem to perform better at northern high latitudes. Lastly, at southern latitudes (<40ºS), the four AGCMs show an adequate representation of runoff apart from ETH/CAM4-2degree.

River Flow

Prior to using AGCMs to inform future high flow impacts, model validations must be performed. In this analysis, daily river flow values from the historical-reference period (2006-2016) were averaged into monthly means for all AGCMs. We then compared these values against observed data as provided by GRDC [*Fekete et al.*, 2002]. Due to limited outlet data availability, five rivers representative of the main continents (see SF6.3 below) were chosen for this validation.

We detect that the performance of the four AGCMs is not homogenous across the analysed catchments. For instance, the four models satisfactorily show the seasonal variations in the Amazon (SF3a); yet MIROC/MIROC5 overestimates flow magnitudes throughout the year. Although the four models estimate the high-flow season in the Ganges (SF3d), the peak flow generally seems to be delayed by one month. MIROC/MIROC5, and to a lesser extent CanAM4: CCCma/CanAM4 overestimate flow magnitudes of the Ganges. For the Rhine (SF3b), these two models capture parts of the inter-annual variation whereas NCC/NorESM1-HAPPI and CAM4: ETH/CAM4-2degree show a strong seasonality that cannot be confirmed in the observed data. For the Amur river (SF6.3d), we find that the AGCMs generally capture the seasonal variations, yet this is delayed, and in the case of MIROC/MIROC5 and CanAM4 the high flow seasons is overestimated. In the Congo (SF3c) we find that the four AGCMs perform poorly.

Thus, further research should explore the role of each of the precipitation and runoff biases in river flow simulations. Moreover, these estimations may be improved by assessing the role of anthropogenic river flow interventions such as reservoir operation or water extractions in influencing model performance.

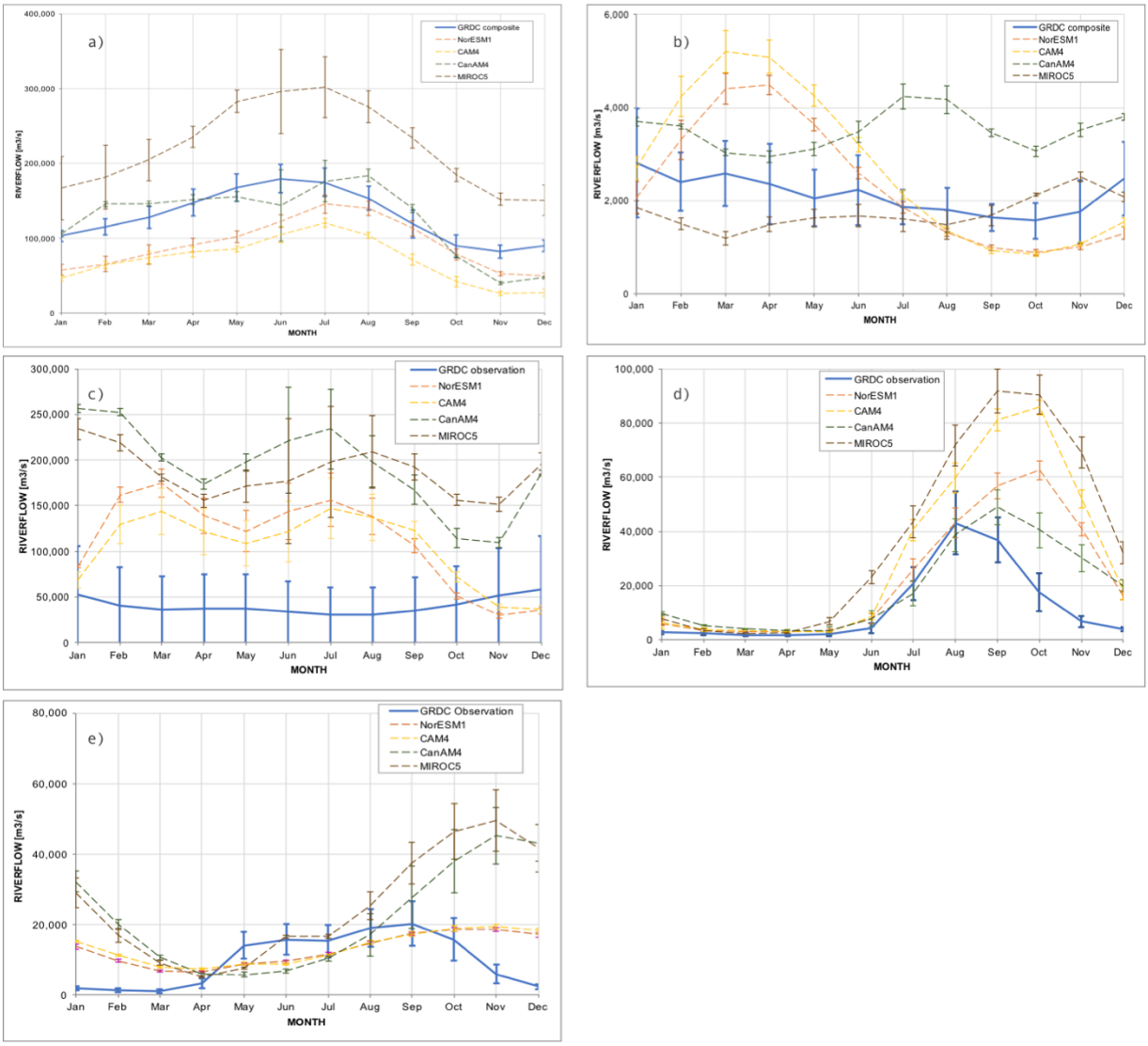

Figure SF S6.5. Monthly mean river flow (2006-2016) calculated from the 4 AGCMs used in this study and compared to observed river flow as provided by GRDC from different catchments. a) Amazon, b) Rhine, c) Congo, d) Ganges, e) Amur. NorESM1: NCC/NorESM1-HAPPI, CAM4: ETH/CAM4-2degree, MIROC5: MIROC/MIROC5, CanAM4: CCCma/CanAM4.

Supplementary Figure 7.1

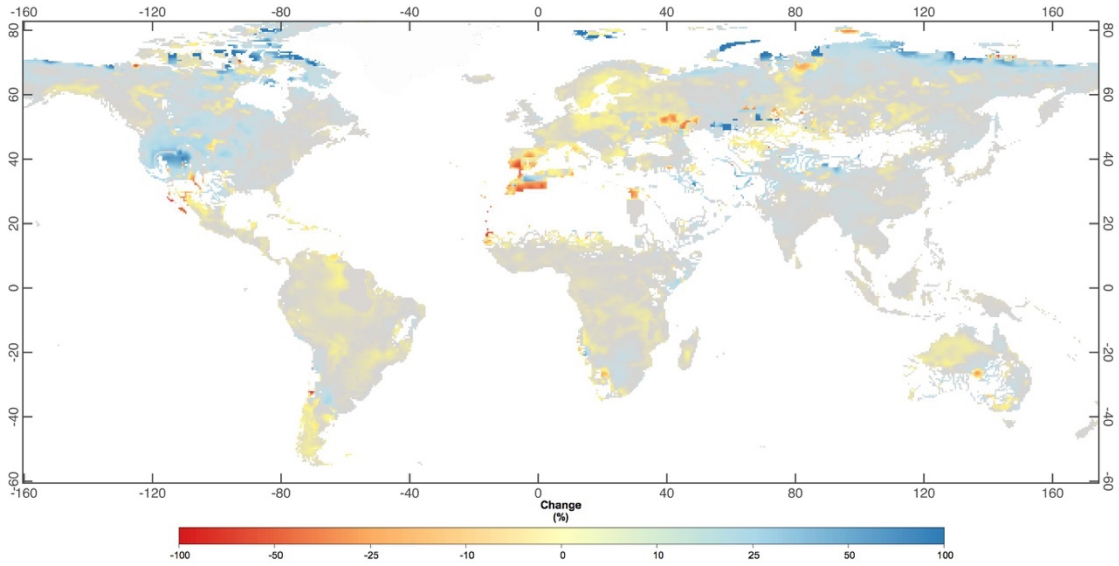

Figure S7.1 Multi-model median change (%) in the number of days with precipitation between the 1.5 °C and 2.0 °C scenario. We define a day with precipitation as that where estimated daily precipitation is greater than 2 mm/day. This threshold is selected as it adequately describes the range of global light precipitation (0.1 – 5mm/day) (Qiaohong et al. 2017).

Supplementary Figure S7.2

Change in droughts characteristics of worlds 1.5 ºC and 2.0 ºC warmer (when compared to the historical).

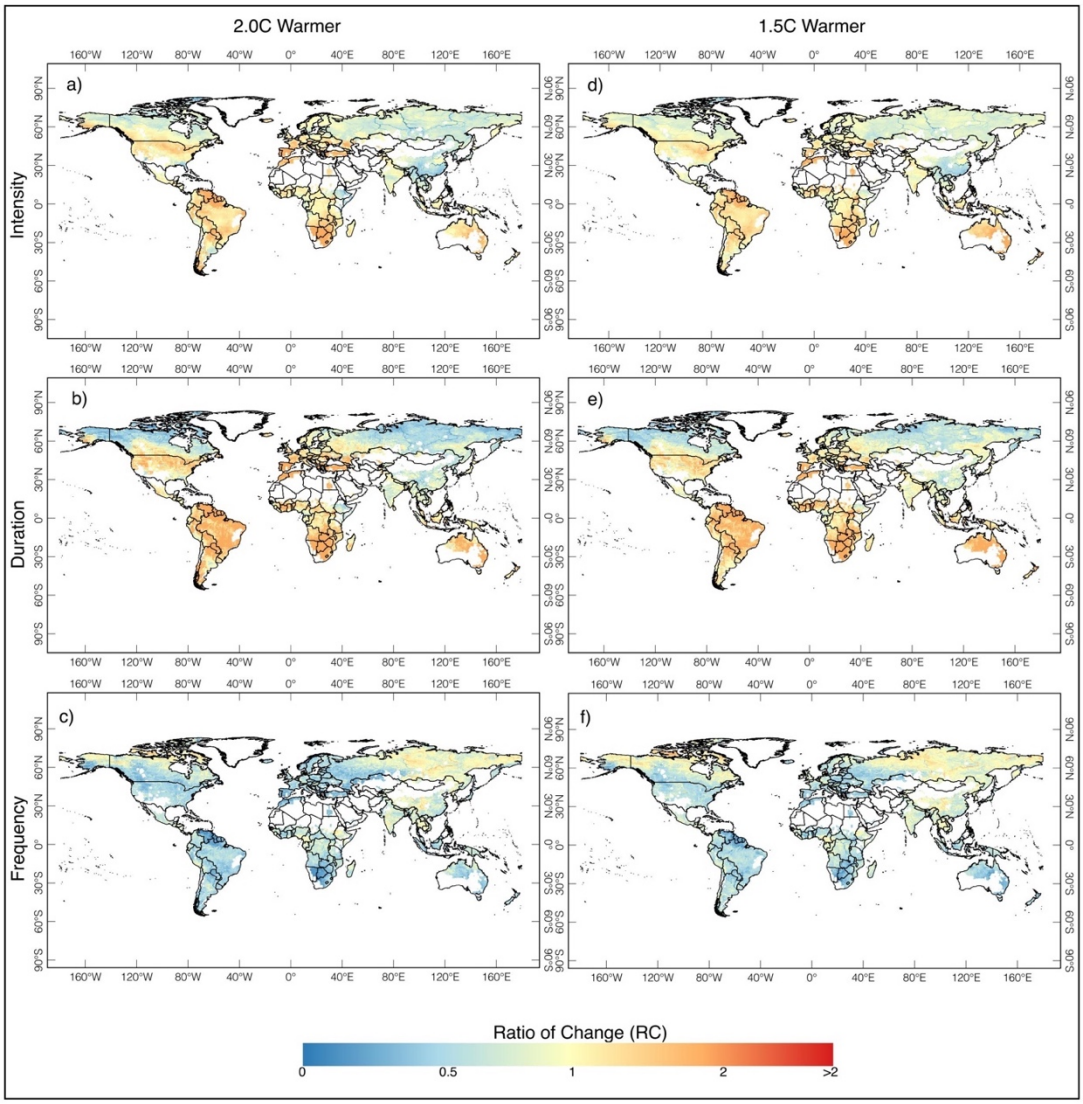

Figure S7.2 Multi-model ensemble mean of Ratio of Change (RC) of: intensity, frequency, and duration of droughts at worlds 2.0 ºC and 1.5 ºC warmer ones when compared to their

historical baseline (2006-2016). A ratio of change is obtained by following Equation 1. RC > 1 indicate that the given drought indicator intensifies at 2.0 oC whereas RC<1 means that such indicators smooths at such climate threshold. Ratios = 1 indicate that there is no future change in such indicator

Supplementary S7.3

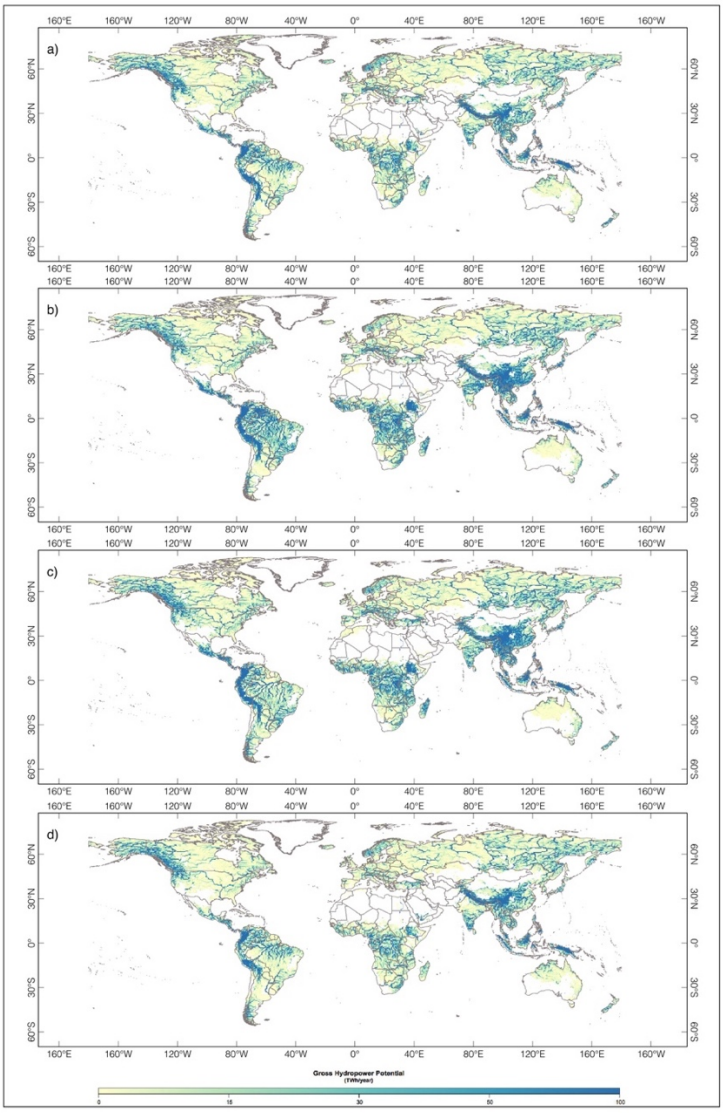

Figure S7.3 Multi-ensemble mean of Current Gross Hydropower Potential (GHP), from the baseline 2006-2016: a) Model NorESM1-HAPPI, b) Model MIROC5, c) Model Can-AM4 and d) Model CAM4-2degree

10. References

Abdulla, F. A., and D. P. Lettenmaier (1997), Development of regional parameter estimation equations for a macroscale hydrologic model, *J. Hydrol.*, *197*(1), 230–257, doi:https://doi.org/10.1016/S0022-1694(96)03262-3.

Adam, J. C., A. F. Hamlet, and D. P. Lettenmaier (2009), Implications of global climate change for snowmelt hydrology in the twenty-first century, *Hydrol. Process.*, *23*(MARCH 2009), 962–982, doi:10.1002/hyp.7201.

Adegoke, J. O., R. A. Pielke Sr, J. Eastman, R. Mahmood, and K. G. Hubbard (2003), Impact of irrigation on midsummer surface fluxes and temperature under dry synoptic conditions: A regional atmospheric model study of the US High Plains, *Mon. Weather Rev.*, *131*(3), 556–564.

Ajayamohan, R. D., and A. Rao (2008), Indian Ocean Dipole Modulates the Number of Extreme Rainfall Events over India in a Warming Environment, *J. Meteorol. Soc. Japan*, *86*(1), 245–252, doi:10.2151/jmsj.86.245.

Akbari, G., and B. Firoozi (2010), Implicit and explicit numerical solution of Saint-Venant equations for simulating flood wave in natural rivers, in *5th National Congress on Civil Engineering*, Feridowsi University of Mashhad Iran.

Alcamo, J., P. Döll, F. Kaspar, and S. Siebert (1997), Global change and global scenarios of water use and availability: an application of WaterGAP 1.0, *Cent. Environ. Syst. Res. (CESR), Univ. Kassel, Ger.*, *1720*.

Alexander, M. A., J. D. Scott, D. Swales, M. Hughes, K. Mahoney, and C. A. Smith (2015), Moisture Pathways into the U.S. Intermountain West Associated with Heavy Winter Precipitation Events, *J. Hydrometeorol.*, *16*(3), 1184–1206, doi:10.1175/JHM-D-14-0139.1.

Alfieri, L., P. Salamon, A. Bianchi, J. Neal, P. Bates, and L. Feyen (2014), Advances in pan- European flood hazard mapping, *Hydrol. Process.*, *28*(13), 4067–4077,

doi:10.1002/hyp.9947.

Alfieri, L., B. Bisselink, F. Dottori, G. Naumann, A. de Roo, P. Salamon, K. Wyser, and L. Feyen (2017), Global projections of river flood risk in a warmer world, *Earth's Futur.*, *5*(2), 171–182, doi:10.1002/2016EF000485.

Allen, M. R., and W. J. Ingram (2002), Constraints on future changes in climate and the hydrologic cycle, *Nature*, *419*(6903), 224–232.

Alsdorf, D., S.-C. Han, P. Bates, and J. Melack (2010), Seasonal water storage on the Amazon floodplain measured from satellites, *Remote Sens. Environ.*, *114*(11), 2448–2456.

Alsdorf, D. E., and D. P. Lettenmaier (2003), Tracking Fresh Water from Space, *Science (80-.).*, *301*(5639), 1491 LP-1494.

Andreadis, K. M., and D. P. Lettenmaier (2006), Assimilating remotely sensed snow observations into a macroscale hydrology model, *Adv. Water Resour.*, *29*(6), 872–886, doi:10.1016/j.advwatres.2005.08.004.

Antwi, M., and D. D. Sedegah (2018), Climate Change and Societal Change—Impact on Hydropower Energy Generation, in *Sustainable Hydropower in West Africa*, pp. 63–73, Elsevier.

Arnell, N. W. (1999), Climate change and global water resources, *Glob. Environ. Chang.*, *9*, S31–S49.

Arnell, N. W., and S. N. Gosling (2016), The impacts of climate change on river flood risk at the global scale, *Clim. Change*, *134*(3), 387–401, doi:10.1007/s10584-014-1084-5.

Arnell, N. W., and B. Lloyd-Hughes (2014), The global-scale impacts of climate change on water resources and flooding under new climate and socio-economic scenarios, *Clim. Change*, *122*(1–2), 127–140, doi:10.1007/s10584-013-0948-4.

Arnold, J. G., J. R. Williams, and D. R. Maidment (1995), Continuous-time water and sediment-routing model for large basins, *J. Hydraul. Eng.*, *121*(2), 171–183.

Arora, V. K., and G. J. Boer (1999), A variable velocity flow routing algorithm for GCMs, *J. Geophys. Res. Atmos.*, *104*(D24), 30965–30979.

Arritt, R. W., T. D. Rink, M. Segal, D. P. Todey, C. A. Clark, M. J. Mitchell, and K. M. Labas (1997), The Great Plains low-level jet during the warm season of 1993, *Mon. Weather Rev.*, *125*(9), 2176–2192.

Ashok, K., Z. Guan, and T. Yamagata (2001), Impact of the Indian Ocean dipole on the relationship between the Indian monsoon rainfall and ENSO, *Geophys. Res. Lett.*, *28*(23), 4499–4502.

Ashok, K., Z. Guan, and T. Yamagata (2003), Influence of the Indian Ocean Dipole on the Australian winter rainfall, *Geophys. Res. Lett.*, *30*(15).

Di Baldassarre, G., and S. Uhlenbrook (2012), Is the current flood of data enough? A treatise on research needs for the improvement of flood modelling, *Hydrol. Process.*, *26*(1), 153–158, doi:10.1002/hyp.8226.

Balmaseda, M. A., K. E. Trenberth, and E. Källén (2013), Distinctive climate signals in reanalysis of global ocean heat content, *Geophys. Res. Lett.*, *40*(9), 1754–1759.

Barnett, T. P., J. C. Adam, and D. P. Lettenmaier (2005), Potential impacts of a warming climate on water availability in snow-dominated regions, *Nature*, *438*(7066), 303–309, doi:10.1038/nature04141.

Bartle, A. (2002), Hydropower potential and development activities, *Energy Policy*, *30*(14), 1231–1239.

Bartle, A. (2016), *World Atlas & Industry Guide 2016*, Aqua-Media International.

Bartos, M. D., and M. V Chester (2015), Impacts of climate change on electric power supply in the Western United States, *Nat. Clim. Chang.*, *5*(8), 748.

Bates, P. D., M. S. Horritt, and T. J. Fewtrell (2010), A simple inertial formulation of the shallow water equations for efficient two-dimensional flood inundation modelling, *J. Hydrol.*, *387*(1–2), 33–45.

Becker, A., P. Finger, A. Meyer-Christoffer, B. Rudolf, and M. Ziese (2011), GPCC full

data reanalysis version 7.0 at 0.5: Monthly land-surface precipitation from rain-gauges built on GTS-based and historic data,

Becker, M., W. LLovel, A. Cazenave, A. Güntner, and J.-F. Crétaux (2010), Recent hydrological behavior of the East African great lakes region inferred from GRACE, satellite altimetry and rainfall observations, *Comptes Rendus Geosci.*, *342*(3), 223–233, doi:https://doi.org/10.1016/j.crte.2009.12.010.

Beek, L. P. H., T. Eikelboom, M. T. H. Vliet, and M. F. P. Bierkens (2012), A physically based model of global freshwater surface temperature, *Water Resour. Res.*, *48*(9).

Van Beek, L. P. H., and M. F. P. Bierkens (2009), The Global Hydrological Model PCR-GLOBWB: Conceptualization, Parameterization and Verification, Report Department of Physical Geography, Utrecht University, Utrecht, The Netherlands, *vanbeek. geo. uu. nl/suppinfo/vanbeekbierkens2009. pdf (last access 6 May 2014)*.

Beighley, R. E., K. G. Eggert, T. Dunne, Y. He, V. Gummadi, and K. L. Verdin (2009), Simulating hydrologic and hydraulic processes throughout the Amazon River Basin, *Hydrol. Process. An Int. J.*, *23*(8), 1221–1235.

Bell, V. a., a. L. Kay, R. G. Jones, and R. J. Moore (2007), Development of a high resolution grid-based river flow model for use with regional climate model output, *Hydrol. Earth Syst. Sci.*, *11*(1), 532–549, doi:10.5194/hess-11-532-2007.

Bell, V. A., and R. J. Moore (1998), A grid-based distributed flood forecasting model for use with weather radar data: Part 2. Case studies, *Hydrol. Earth Syst. Sci.*, *2*(2/3), 283–298, doi:10.5194/hess-2-283-1998.

Beltaos, S. (1995), *River ice jams*, Water Resources Publication.

Beltaos, S. (2008), Progress in the study and management of river ice jams, *Cold Reg. Sci. Technol.*, *51*(1), 2–19, doi:https://doi.org/10.1016/j.coldregions.2007.09.001.

Beltaos, S. (2010), Internal strength properties of river ice jams, *Cold Reg. Sci. Technol.*, *62*(2–3), 83–91.

Benton, G. S., and M. A. Estoque (1954), Water-vapor transfer over the North American

continent, *J. Meteorol.*, *11*(6), 462–477.

Berga, L. (2016), The role of hydropower in climate change mitigation and adaptation: a review, *Engineering*, *2*(3), 313–318.

Best, M. J. et al. (2011), The Joint UK Land Environment Simulator (JULES), model description. Part 1: Energy and water fluxes, *Geosci. Model Dev.*, *4*, 677–699, doi:10.5194/gmdd-4-641-2011.

Bettin, G., and A. Zazzaro (2018), The impact of natural disasters on remittances to low- and middle-income countries, *J. Dev. Stud.*, *54*(3), 481–500.

Beven, K. J. (2011), *Rainfall-runoff modelling: the primer*, John Wiley & Sons.

Beven, K. J., and H. L. Cloke (2012), Comment on "Hyperresolution global land surface modeling: Meeting a grand challenge for monitoring Earth's terrestrial water" by Eric F. Wood et al., *Water Resour. Res.*, *48*(1).

Beven, K. J., and M. J. Kirby (1979), A physically based, variable contributing area model of basin hydrology / Un modèle à base physique de zone d'appel variable de l'hydrologie du bassin versant, *Hydrol. Sci. Bull.*, *24*(1), 43–69, doi:10.1080/02626667909491834.

Beyene, B. S., A. F. Van Loon, H. A. J. Van Lanen, and P. Torfs (2014), Investigation of variable threshold level approaches for hydrological drought identification, *Hydrol. Earth Syst. Sci. Discuss.*, *11*(11), 12765–12797.

Bierkens, M. F., I. de Graaf, Y. Wada, N. Wanders, and L. P. Van Beek (2017), Modelling water use in global hydrological models: review, challenges and directions, in *AGU Fall Meeting Abstracts*.

Bierkens, M. F. P. (2015), Global hydrology 2015: State, trends, and directions, *Water Resour. Res.*, *51*(7), 4923–4947.

Bierkens, M. F. P., V. A. Bell, P. Burek, N. Chaney, L. E. Condon, C. H. David, A. de Roo, P. Döll, N. Drost, and J. S. Famiglietti (2015), Hyper-resolution global hydrological modelling: what is next? "Everywhere and locally relevant," *Hydrol.*

Process., *29*(2), 310–320.

Bintanja, R., and F. M. Selten (2014), Future increases in Arctic precipitation linked to local evaporation and sea-ice retreat., *Nature*, *509*(7501), 479–82, doi:10.1038/nature13259.

Bjerklie, D. M., S. L. Dingman, C. J. Vorosmarty, C. H. Bolster, and R. G. Congalton (2003), Evaluating the potential for measuring river discharge from space, *J. Hydrol.*, *278*(1–4), 17–38.

Black, E. (2005), The relationship between Indian Ocean sea–surface temperature and East African rainfall, *Philos. Trans. R. Soc. London A Math. Phys. Eng. Sci.*, *363*(1826), 43–47.

Blackbourn, D. (2011), *The conquest of nature: water, landscape, and the making of modern Germany*, Random House.

Blackburn, J., and F. Hicks (2003), Suitability of dynamic modeling for flood forecasting during ice jam release surge events, *J. Cold Reg. Eng.*, *17*(1), 18–36.

Blomfield, A., and J. Plummer (2014a), The allocation and documentation of hydrological risk H, , (November).

Blomfield, A., and J. Plummer (2014b), The allocation and documentation of hydrological risk H,

Blöschl, G., S. Ardoin-Bardin, M. Bonell, M. Dorninger, D. Goodrich, D. Gutknecht, D. Matamoros, B. Merz, P. Shand, and J. Szolgay (2007), At what scales do climate variability and land cover change impact on flooding and low flows?, *Hydrol. Process.*, *21*(9), 1241–1247, doi:10.1002/hyp.6669.

Blyth, E., M. Best, P. Cox, R. Essery, O. Boucher, R. Harding, C. Prentice, P. L. Vidale, and I. Woodward (2006a), JULES: a new community land surface model, *Glob. Chang. NewsLette*, (66), 9–11.

Blyth, E., M. Best, P. Cox, R. Essery, O. Boucher, R. Harding, C. Prentice, P. L. Vidale, and I. Woodward (2006b), JULES: a new community land surface model, *Glob.*

Chang. Newsl., *66*, 9–13.

Blyth, E., D. B. Clark, R. Ellis, C. Huntingford, S. Los, M. Pryor, M. Best, and S. Sitch (2011), A comprehensive set of benchmark tests for a land surface model of simultaneous fluxes of water and carbon at both the global and seasonal scale, *Geosci. Model Dev.*, *4*(2), 255–269, doi:10.5194/gmd-4-255-2011.

Bollasina, M. A., Y. Ming, and V. Ramaswamy (2011), Anthropogenic Aerosols and the Weakening of the South Asian Summer Monsoon, *Science (80-.).*, *334*(6055), 502 LP-505.

Bonan, G. B. (2008), Forests and climate change: forcings, feedbacks, and the climate benefits of forests, *Science (80-.).*, *320*(5882), 1444–1449.

Bond, N. A., and G. A. Vecchi (2003), The influence of the Madden–Julian oscillation on precipitation in Oregon and Washington, *Weather Forecast.*, *18*(4), 600–613.

Botter, G., and A. Rinaldo (2003), Scale effect on geomorphologic and kinematic dispersion, *Water Resour. Res.*, *39*(10).

Boucher, O., and M. Best (2010), *THE WATCH FORCING DATA 1958-2001: A METEOROLOGICAL FORCING DATASET FOR LAND SURFACE-AND HYDROLOGICAL-MODELS.*, WATCH technical report.

Boucher, O., G. Myhre, and A. Myhre (2004), Direct human influence of irrigation on atmospheric water vapour and climate, *Clim. Dyn.*, *22*(6–7), 597–603.

Branstetter, M. L., and D. J. Erickson (2003), Continental runoff dynamics in the Community Climate System Model 2 (CCSM2) control simulation, *J. Geophys. Res. Atmos.*, *108*(D17).

Brekke, L. D., E. P. Maurer, J. D. Anderson, M. D. Dettinger, E. S. Townsley, A. Harrison, and T. Pruitt (2009), Assessing reservoir operations risk under climate change, *Water Resour. Res.*, *45*(4), n/a--n/a, doi:10.1029/2008WR006941.

Brun, E., V. Vionnet, A. Boone, B. Decharme, Y. Peings, R. Valette, F. Karbou, and S. Morin (2012), Simulation of northern Eurasian local snow depth, mass and density

using a detailed snowpack model and meteorological reanalysis, *J. Hydrometeorol.*, 120914092949009, doi:10.1175/JHM-D-12-012.1.

Burke, E. J., R. Dankers, C. D. Jones, and A. J. Wiltshire (2013), A retrospective analysis of pan Arctic permafrost using the JULES land surface model, *Clim. Dyn.*, *41*(3–4), 1025–1038, doi:10.1007/s00382-012-1648-x.

Cai, M. (2005), Dynamical amplification of polar warming, *Geophys. Res. Lett.*, *32*(22), 1–5, doi:10.1029/2005GL024481.

Cai, W., and P. Rensch (2012), The 2011 southeast Queensland extreme summer rainfall: a confirmation of a negative Pacific Decadal Oscillation phase?, *Geophys. Res. Lett.*, *39*(8).

Cao, L., W. Dong, Y. Xu, Y. Zhang, and M. Sparrow (2007), Validating the runoff from the PRECIS model using a large-scale routing model, *Adv. Atmos. Sci.*, *24*(5), 855–862.

Center for International Earth Science Information Network - CIESIN - Columbia University (2016), Gridded Population of the World, Version 4 (GPWv4): Population Density Adjusted to Match 2015 Revision UN WPP Country Totals,

Chadburn, S., E. Burke, R. Essery, J. Boike, M. Langer, M. Heikenfeld, P. Cox, and P. Friedlingstein (2015), An improved representation of physical permafrost dynamics in the JULES land surface model, *Geosci. Model Dev. Discuss.*, *8*(1), 715–759, doi:10.5194/gmdd-8-715-2015.

Chan, S. C., S. K. Behera, and T. Yamagata (2008), Indian Ocean dipole influence on South American rainfall, *Geophys. Res. Lett.*, *35*(14).

Chao, B. F., Y. H. Wu, and Y. S. Li (2008), Impact of artificial reservoir water impoundment on global sea level, *Science (80-.).*, *320*(5873), 212–214.

Charlson, R. J., S. E. Schwartz, J. M. Hales, R. D. Cess, J. J. A. Coakley, J. E. Hansen, and D. J. Hofmann (1992), Climate forcing by anthropogenic aerosols, *Science (80-.).*, *255*(5043), 423–430.

Cherchi, A., and A. Navarra (2013), Influence of ENSO and of the Indian Ocean Dipole on the Indian summer monsoon variability, *Clim. Dyn.*, *41*(1), 81–103, doi:10.1007/s00382-012-1602-y.

Chiew, F. H. S., and T. A. McMAHON (2002), Global ENSO-streamflow teleconnection, streamflow forecasting and interannual variability, *Hydrol. Sci. J.*, *47*(3), 505–522.

Christoff, P. (2016), The promissory note: COP 21 and the Paris Climate Agreement, *Env. Polit.*, *25*(5), 765–787.

Clark, D. B., and N. Gedney (2008), Representing the effects of subgrid variability of soil moisture on runoff generation in a land surface model, *J. Geophys. Res.*, *113*(D10), D10111, doi:10.1029/2007JD008940.

Clark, M. P., R. L. Wilby, E. D. Gutmann, J. A. Vano, S. Gangopadhyay, A. W. Wood, H. J. Fowler, C. Prudhomme, J. R. Arnold, and L. D. Brekke (2016a), Characterizing uncertainty of the hydrologic impacts of climate change, *Curr. Clim. Chang. Reports*, *2*(2), 55–64.

Clark, M. P., R. L. Wilby, E. D. Gutmann, J. A. Vano, S. Gangopadhyay, A. W. Wood, H. J. Fowler, C. Prudhomme, J. R. Arnold, and L. D. Brekke (2016b), Characterizing Uncertainty of the Hydrologic Impacts of Climate Change, *Curr. Clim. Chang. Reports*, *2*(2), 55–64, doi:10.1007/s40641-016-0034-x.

Coe, M. T. (1998), A linked global model of terrestrial hydrologic processes: Simulation of modern rivers, lakes, and wetlands, *J. Geophys. Res. Atmos.*, *103*(D8), 8885–8899.

Cohen, J., and D. Entekhabi (1999), Eurasian snow cover variability and northern hemisphere climate predictability, *Geophys. Res. Lett.*, *26*(3), 345–348, doi:10.1029/1998GL900321.

Cohen, J., and D. Rind (1991), The Effect of Snow Cover on the Climate, *J. Clim.*, *4*(7), 689–706, doi:10.1175/1520-0442(1991)004<0689:TEOSCO>2.0.CO;2.

Collins, M., S.-I. An, W. Cai, A. Ganachaud, E. Guilyardi, F.-F. Jin, M. Jochum, M. Lengaigne, S. Power, and A. Timmermann (2010), The impact of global warming on

the tropical Pacific Ocean and El Niño, *Nat. Geosci.*, *3*(6), 391.

Collins, M. et al. (2013), Long-term Climate Change: Projections, Commitments and Irreversibility, in *Climate Change 2013: The Physical Science Basis. Contribution of Working Group I to the Fifth Assessment Report of the Intergovernmental Panel on Climate Change*, Cambridge University Press, Cambridge, United Kingdom and New York, NY, USA.

Cook, C., C. J. C. Reason, and B. C. Hewitson (2004), Wet and dry spells within particularly wet and dry summers in the South African summer rainfall region, *Clim. Res.*, *26*(1), 17–31.

Corobov, R. M. (2001), Downscaling of the Global Climate Change Projections: Some Approaches, *Detect. Model. Reg. Clim. Chang.*, 491–499, doi:10.1007/978-3-662-04313-4_41.

Cosby, B. J., G. M. Hornberger, R. B. Clapp, and T. R. Ginn (1984), A Statistical Exploration of the Relationships of Soil Moisture Characteristics to the Physical Properties of Soils, *Water Resour. Res.*, *20*(6), 682–690, doi:10.1029/WR020i006p00682.

Cubasch, U., and R. Voss (2000), The influence of total solar irradiance on climate, *Space Sci. Rev.*, *94*(1–2), 185–198.

Cullen, H. M., and P. B. Demenocal (2000), North Atlantic influence on Tigris–Euphrates streamflow, *Int. J. Climatol. A J. R. Meteorol. Soc.*, *20*(8), 853–863.

Curtis, S. (2008), The Atlantic multidecadal oscillation and extreme daily precipitation over the US and Mexico during the hurricane season, *Clim. Dyn.*, *30*(4), 343–351, doi:10.1007/s00382-007-0295-0.

Dacre, H. F., P. a. Clark, O. Martinez-Alvarado, M. a. Stringer, and D. a. Lavers (2015), How Do Atmospheric Rivers Form?, *Bull. Am. Meteorol. Soc.*, *96*(8), 1243–1255, doi:10.1175/BAMS-D-14-00031.1.

Dadson, S. J., V. a. Bell, and R. G. Jones (2011), Evaluation of a grid-based river flow

model configured for use in a regional climate model, *J. Hydrol.*, *411*(3–4), 238–250, doi:10.1016/j.jhydrol.2011.10.002.

Danielson, J. J., and D. B. Gesch (2011), *Global multi-resolution terrain elevation data 2010 (GMTED2010)*, US Geological Survey.

Dankers, R., and L. Feyen (2008), Climate change impact on flood hazard in Europe: An assessment based on high-resolution climate simulations, *J. Geophys. Res. Atmos.*, *113*(19), 1–17, doi:10.1029/2007JD009719.

Dankers, R., and L. Feyen (2009), Climate change impact on flood hazard in Europe: an assessment based on high-resolution climate simulations, *J. Geophys. Res.*, *113*(D19105).

Dankers, R., E. J. Burke, and J. Price (2011), Simulation of permafrost and seasonal thaw depth in the JULES land surface scheme, *Cryosph. Discuss.*, *5*(2), 1263–1309, doi:10.5194/tcd-5-1263-2011.

Dankers, R. et al. (2014), First look at changes in flood hazard in the Inter-Sectoral Impact Model Intercomparison Project ensemble, *Proc. Natl. Acad. Sci.*, *111*(9), 3257–3261, doi:10.1073/pnas.1302078110.

Davies, H. N., and V. a Bell (2009), Assessment of methods for extracting low-resolution river networks from high-resolution digital data, *Hydrol. Sci. Journal-Journal Des Sci. Hydrol.*, *54*(1), 17–28, doi:10.1623/hysj.54.1.17.

Decharme, B., R. Alkama, H. Douville, M. Becker, and A. Cazenave (2010), Global evaluation of the ISBA-TRIP continental hydrological system. Part II: Uncertainties in river routing simulation related to flow velocity and groundwater storage, *J. Hydrometeorol.*, *11*(3), 601–617.

Decker, M., M. A. Brunke, Z. Wang, K. Sakaguchi, X. Zeng, and M. G. Bosilovich (2011), Evaluation of the Reanalysis Products from GSFC, NCEP, and ECMWF Using Flux Tower Observations, *J. Clim.*, *25*(6), 1916–1944, doi:10.1175/JCLI-D-11-00004.1.

Dee, D. P., S. M. Uppala, A. J. Simmons, P. Berrisford, P. Poli, S. Kobayashi, U. Andrae,

M. A. Balmaseda, G. Balsamo, and d P. Bauer (2011), The ERA-Interim reanalysis: Configuration and performance of the data assimilation system, *Q. J. R. Meteorol. Soc.*, *137*(656), 553–597.

Dell, M., B. F. Jones, and B. A. Olken (2014), What do we learn from the weather? The new climate-economy literature, *J. Econ. Lit.*, *52*(3), 740–798.

Deser, C., A. Phillips, V. Bourdette, and H. Teng (2012), Uncertainty in climate change projections: the role of internal variability, *Clim. Dyn.*, *38*(3–4), 527–546.

Dettinger, M. (2011a), Climate change, atmospheric rivers, and floods in California - a multimodel analysis of storm frequency and magnitude changes, *J. Am. Water Resour. Assoc.*, *47*(3), 514–523, doi:10.1111/j.1752-1688.2011.00546.x.

Dettinger, M. (2011b), Climate Change , Atmospheric Rivers , and Floods in California – a Multimodel Analysis of Storm Frequency and Magnitude Changes 1, , *47*(3), 514–523, doi:10.1111/j.1752-1688.2011.00546.x.

Dettinger, M., and D. R. Cayan (2014), Drought and the California Delta—A Matter of Extremes, *San Fr. Estuary Watershed Sci.* , *12*(2).

Dettinger, M. D. (2013), Atmospheric Rivers as Drought Busters on the U.S. West Coast, *J. Hydrometeorol.*, *14*(6), 1721–1732, doi:10.1175/JHM-D-13-02.1.

Dettinger, M. D., and H. F. Diaz (2000), Global characteristics of stream flow seasonality and variability, *J. Hydrometeorol.*, *1*(4), 289–310.

Dijkstra, H. A., L. Te Raa, M. Schmeits, and J. Gerrits (2006), On the physics of the Atlantic multidecadal oscillation, *Ocean Dyn.*, *56*(1), 36–50.

Dima, M., and G. Lohmann (2007), A hemispheric mechanism for the Atlantic Multidecadal Oscillation, *J. Clim.*, *20*(11), 2706–2719.

Dirmeyer, P. A., and J. L. Kinter (2009), The "Maya Express": Floods in the U.S. Midwest, *Eos, Trans. Am. Geophys. Union*, *90*(12), 101–102, doi:10.1029/2009EO120001.

Döll, P., H. Douville, A. Güntner, H. Müller Schmied, and Y. Wada (2016), Modelling Freshwater Resources at the Global Scale: Challenges and Prospects, *Surv. Geophys.*,

37(2), 195–221, doi:10.1007/s10712-015-9343-1.

Döll, P., T. Trautmann, D. Gerten, H. M. Schmied, S. Ostberg, F. Saaed, and C.-F. Schleussner (2018), Risks for the global freshwater system at 1.5° C and 2° C global warming, *Environ. Res. Lett.*, *13*(4), 44038.

Donlon, C. J., M. Martin, J. Stark, J. Roberts-Jones, E. Fiedler, and W. Wimmer (1998), The Operational Sea Surface Temperature and Sea Ice Analysis (OSTIA) system, *Remote Sens. Environ.*, *116*(Supplement C), 140–158, doi:https://doi.org/10.1016/j.rse.2010.10.017.

Dujardin, J., A. Kahl, B. Kruyt, S. Bartlett, and M. Lehning (2017), Interplay between photovoltaic, wind energy and storage hydropower in a fully renewable Switzerland, *Energy*, *135*, 513–525.

Dutra, E., G. Balsamo, P. Viterbo, P. M. A. Miranda, A. Beljaars, C. Schär, and K. Elder (2010), An Improved Snow Scheme for the ECMWF Land Surface Model: Description and Offline Validation, *J. Hydrometeorol.*, *11*(4), 899–916, doi:10.1175/2010JHM1249.1.

Dutra, E., P. Viterbo, P. Miranda, and G. Balsamo (2012), Complexity of Snow Schemes in a Climate Model and Its Impact on Surface Energy and Hydrology, *J. Hydrometeorol.*, *13*, 521–538, doi:10.1175/JHM-D-11-072.1.

Emerton, R., H. L. Cloke, E. M. Stephens, E. Zsoter, S. J. Woolnough, and F. Pappenberger (2017), Complex picture for likelihood of ENSO-driven flood hazard, *Nat. Commun.*, *8*, 14796.

Enfield, D. B., A. M. Mestas-Nuñez, and P. J. Trimble (2001), The Atlantic multidecadal oscillation and its relation to rainfall and river flows in the continental US, *Geophys. Res. Lett.*, *28*(10), 2077–2080.

Essery, R., and D. B. Clark (2003), Developments in the MOSES 2 land-surface model for PILPS 2e, *Glob. Planet. Change*, *38*(1), 161–164, doi:https://doi.org/10.1016/S0921-8181(03)00026-2.

Essery, R., N. Rutter, J. Pomeroy, R. Baxter, M. Stahli, D. Gustafsson, A. Barr, P. Bartlett, and K. Elder (2006), SNOWMIP2: An Evaluation of Forest snow Process simulations, *Bull. Am. Meteorol. Soc.*, (90), 1120–1135.

Ettema, R., G. Kirkil, and S. Daly (2009), Frazil ice concerns for channels, pump-lines, penstocks, siphons, and tunnels in mountainous regions, *Cold Reg. Sci. Technol.*, *55*(2), 202–211.

Falkenmark, M. (1997), Meeting water requirements of an expanding world population, *Philos. Trans. R. Soc. B Biol. Sci.*, *352*(1356), 929–936.

Falter, D., K. Schröter, N. V. Dung, S. Vorogushyn, H. Kreibich, Y. Hundecha, H. Apel, and B. Merz (2015), Spatially coherent flood risk assessment based on long-term continuous simulation with a coupled model chain, *J. Hydrol.*, *524*, 182–193.

Falter, D., N. V Dung, S. Vorogushyn, K. Schröter, Y. Hundecha, H. Kreibich, H. Apel, F. Theisselmann, and B. Merz (2016), Continuous, large-scale simulation model for flood risk assessments: proof-of-concept, *J. Flood Risk Manag.*, *9*(1), 3–21.

Fekete, B., C. Vörösmarty, and G. W. (2002), *Global composite runoff fields on observed river discharge and simulated water balances / Water System Analysis Group,University of New Hampshire, and Global Runoff Data Centre.*, Koblenz, Germany.

Fekete, B. M., C. J. Vörösmarty, and W. Grabs (1999), Global, composite runoff fields based on observed river discharge and simulated water balances,

Fekete, B. M., J. J. Gibson, P. Aggarwal, and C. J. Vörösmarty (2006), Application of isotope tracers in continental scale hydrological modeling, *J. Hydrol.*, *330*(3–4), 444–456.

Fekete, B. M., U. Looser, A. Pietroniro, and R. D. Robarts (2012), Rationale for Monitoring Discharge on the Ground, *J. Hydrometeorol.*, *13*(6), 1977–1986, doi:10.1175/JHM-D-11-0126.1.

Feng, S., and Q. Hu (2008), How the North Atlantic Multidecadal Oscillation may have

influenced the Indian summer monsoon during the past two millennia, *Geophys. Res. Lett.*, *35*(1).

Ferguson, R. I. (1999), Snowmelt runoff models, *Prog. Phys. Geogr.*, *23*(1999), 205–227, doi:10.1191/030913399672720559.

Fischer, G., F. Nachtergaele, S. Prieler, H. T. van Velthuizen, L. Verelst, and D. Wiberg (2012), *Global Agro-ecological Zones Assessment for Agriculture (GAEZ 2008)*.

Fleig, A. K., L. M. Tallaksen, H. Hisdal, and S. Demuth (2006), A global evaluation of streamflow drought characteristics, *Hydrol. Earth Syst. Sci. Discuss.*, *10*(4), 535–552.

Forster, P., V. Ramaswamy, P. Artaxo, T. Berntsen, R. Betts, D. W. Fahey, J. Haywood, J. Lean, D. C. Lowe, and G. Myhre (2007), Changes in atmospheric constituents and in radiative forcing. Chapter 2, in *Climate Change 2007. The Physical Science Basis*.

François, B., M. Borga, S. Anquetin, J. D. Creutin, K. Engeland, A. C. Favre, B. Hingray, M. H. Ramos, D. Raynaud, and B. Renard (2014), Integrating hydropower and intermittent climate-related renewable energies: a call for hydrology, *Hydrol. Process.*, *28*(21), 5465–5468.

Fread, D. L. (1973), Technique for implicit dynamic routing in rivers with tributaries, *Water Resour. Res.*, *9*(4), 918–926.

Gash, J. H. C. (1979), An analytical model of rainfall interception by forests, *Q. J. R. Meteorol. Soc.*, *105*(443), 43–55, doi:10.1002/qj.49710544304.

Gaudard, L., F. Romerio, F. Dalla Valle, R. Gorret, S. Maran, G. Ravazzani, M. Stoffel, and M. Volonterio (2014), Climate change impacts on hydropower in the Swiss and Italian Alps, *Sci. Total Environ.*, *493*, 1211–1221, doi:https://doi.org/10.1016/j.scitotenv.2013.10.012.

Gaur, A., and S. P. Simonovic (2015), Towards reducing climate change impact assessment process uncertainty, *Environ. Process.*, *2*(2), 275–290.

Gedney, N., and P. M. Cox (2003), The Sensitivity of Global Climate Model Simulations to the Representation of Soil Moisture Heterogeneity, *J. Hydrometeorol.*, *4*(6), 1265–

1275, doi:10.1175/1525-7541(2003)004<1265:TSOGCM>2.0.CO;2.

Van Genuchten, M. T. (1980), A closed-form equation for predicting the hydraulic conductivity of unsaturated soils 1, *Soil Sci. Soc. Am. J.*, *44*(5), 892–898.

Gershunov, A., and T. P. Barnett (1998), Interdecadal modulation of ENSO teleconnections, *Bull. Am. Meteorol. Soc.*, *79*(12), 2715–2725.

Ghanbarian-Alavijeh, B., a. Liaghat, G.-H. Huang, and M. T. Van Genuchten (2010), Estimation of the van Genuchten Soil Water Retention Properties from Soil Textural Data, *Pedosphere*, *20*(4), 456–465, doi:10.1016/S1002-0160(10)60035-5.

Ghizzoni, T., G. Roth, and R. Rudari (2012), Multisite flooding hazard assessment in the Upper Mississippi River, *J. Hydrol.*, *412*, 101–113.

Gimeno, L., R. Nieto, M. Vazquez, and D. a. Lavers (2014), Atmospheric rivers: a mini-review, *Front. Earth Sci.*, *2*(March), 1–6, doi:10.3389/feart.2014.00002.

Gimeno, L., F. Dominguez, R. Nieto, R. Trigo, A. Drumond, C. J. C. Reason, A. S. Taschetto, A. M. Ramos, R. Kumar, and J. Marengo (2016), Major Mechanisms of Atmospheric Moisture Transport and Their Role in Extreme Precipitation Events, *Annu. Rev. Environ. Resour.*, *41*(1), 117–141, doi:10.1146/annurev-environ-110615-085558.

Giorgi, F., B. Hewitson, J. Christensen, M. Hulme, H. Von Storch, P. Whetton, R. Jones, L. Mearns, C. Fu, and R. Arritt (2001), Regional climate information—evaluation and projections,

Giorgi, F., C. Jones, and G. R. Asrar (2009), Addressing climate information needs at the regional level: the CORDEX framework, *Bull. - World Meteorol. Organ.*, *58*(3), 175–183.

Gleick, P. H. (1989), Climate change, hydrology, and water resources, *Rev. Geophys.*, *27*(3), 329, doi:10.1029/RG027i003p00329.

Gleick, P. H. (2014), Water, drought, climate change, and conflict in Syria, *Weather. Clim. Soc.*, *6*(3), 331–340.

Global Runoff Data Centre (2007), Major River Basins of the World,

Goldenberg, S. B., C. W. Landsea, A. M. Mestas-Nuñez, and W. M. Gray (2001), The recent increase in Atlantic hurricane activity: Causes and implications, *Science (80-.).*, *293*(5529), 474–479.

Goodrich, G. B. (2007), Influence of the Pacific decadal oscillation on winter precipitation and drought during years of neutral ENSO in the western United States, *Weather Forecast.*, *22*(1), 116–124.

Goteti, G., J. S. Famiglietti, and K. Asante (2008), A Catchment-Based Hydrologic and Routing Modeling System with explicit river channels, *J. Geophys. Res. Atmos.*, *113*(D14).

Graham, L. P., J. Andréasson, and B. Carlsson (2007), Assessing climate change impacts on hydrology from an ensemble of regional climate models , model scales and linking methods – a case study on the Lule River basin, , 293–307, doi:10.1007/s10584-006-9215-2.

Grey, D., and C. W. Sadoff (2007), Sink or Swim? Water security for growth and development, *Water Policy*, *9*(6), 545–571, doi:10.2166/wp.2007.021.

Grey, D., D. Garrick, D. Blackmore, J. Kelman, M. Muller, and C. Sadoff (2013), Water security in one blue planet: twenty-first century policy challenges for science, *Philos. Trans. R. Soc. A Math. Eng. Sci.*, *371*(2002), 20120406, doi:10.1098/rsta.2012.0406.

Grippa, M., L. Kergoat, T. Le Toan, N. M. Mognard, N. Delbart, J. L'Hermitte, and S. M. Vicente-Serrano (2005), The impact of snow depth and snowmelt on the vegetation variability over central Siberia - art. no. L21412, *Geophys. Res. Lett.*, *32*(21), 21412, doi:10.1029/2005GL024286.

Gross, C. A., and T. A. Roppel (2012), *Fundamentals of electrical engineering*, CRC press.

Grotch, S. L., and M. C. MacCracken (1991), The Use of General Circulation Models to Predict Regional Climatic Change, *J. Clim.*, *4*(3), 286–303, doi:10.1175/1520-

0442(1991)004<0286:TUOGCM>2.0.CO;2.

Guan, B., and D. E. Waliser (2015a), Detection of atmospheric rivers: Evaluation and application of an algorithm for global studies, *J. Geophys. Res. Atmos.*, *120*(24), 12514–12535, doi:10.1002/2015JD024257.

Guan, B., and D. E. Waliser (2015b), Detection of Atmospheric Rivers: Evaluation and Application of an Algorithm for Global Studies, *J. Geophys. Res. Atmos.*, *120*(24), 12514–12535, doi:10.1002/2015JD024257.

Guan, B., N. P. Molotch, D. E. Waliser, E. J. Fetzer, and P. J. Neiman (2013), The 2010/2011 snow season in California's Sierra Nevada: Role of atmospheric rivers and modes of large-scale variability, *Water Resour. Res.*, *49*(10), 6731–6743, doi:10.1002/wrcr.20537.

Gumbel, E. J. (1941), The Return Period of Flood Flows, , 163–190, doi:10.1214/aoms/1177731747.

Gupta, H., S. Sorooshian, and P. Yapo (1999), Status of Automatic Calibration for Hydrologic Models: Comparison with Multilevel Expert Calibration, *J. Hydrol. Eng.*, *4*(2), 135–143, doi:10.1061/(ASCE)1084-0699(1999)4:2(135).

Gupta, H. V, T. Wagener, and Y. Liu (2008), Reconciling theory with observations: elements of a diagnostic approach to model evaluation, *Hydrol. Process.*, *22*(18), 3802–3813.

Gutmann, E., T. Pruitt, M. P. Clark, L. Brekke, J. R. Arnold, D. A. Raff, and R. M. Rasmussen (2014), An intercomparison of statistical downscaling methods used for water resource assessments in the United States, *Water Resour. Res.*, *50*(9), 7167–7186.

Haberlandt, U., and I. Radtke (2014), Hydrological model calibration for derived flood frequency analysis using stochastic rainfall and probability distributions of peak flows, *Hydrol. Earth Syst. Sci. 18 (2014), Nr. 1*, *18*(1), 353–365.

Hall, D. K., G. A. Riggs, and V. V. Salomonson (2006), *MODIS/Terra Snow Cover*

Monthly L3 Global 0.05Deg CMG V005, Boulder, CO, USA.

Hall, J. W., D. Grey, D. Garrick, F. Fung, C. Brown, S. J. Dadson, and C. W. Sadoff (2014), Coping with the curse of freshwater variability, *Science (80-.).*, *346*(6208), 429–430, doi:10.1126/science.1257890.

Halverson, J. B. (2018), The Costliest Hurricane Season in U.S. History, *Weatherwise*, *71*(2), 20–27, doi:10.1080/00431672.2018.1416862.

Hamududu, B., and A. Killingtveit (2012), Assessing climate change impacts on global hydropower, *Energies*, *5*(2), 305–322.

Hanasaki, N., S. Kanae, T. Oki, K. Masuda, K. Motoya, N. Shirakawa, Y. Shen, and K. Tanaka (2008), An integrated model for the assessment of global water resources– Part 1: Model description and input meteorological forcing, *Hydrol. Earth Syst. Sci.*, *12*(4), 1007–1025.

Hancock, S., R. Baxter, J. Evans, and B. Huntley (2013), Evaluating global snow water equivalent products for testing land surface models, *Remote Sens. Environ.*, *128*, 107–117, doi:Doi 10.1016/J.Rse.2012.10.004.

Hannah, D. M., S. Demuth, H. A. J. van Lanen, U. Looser, C. Prudhomme, G. Rees, K. Stahl, and L. M. Tallaksen (2011), Large-scale river flow archives: importance, current status and future needs, *Hydrol. Process.*, *25*(7), 1191–1200.

Hartmann, D. L., A. M. G. K. Tank, and M. Rusticucci (2013), IPCC Fifth Assessment Report, Climatie Change 2013: The Physical Science Basis, *IPCC*, *AR5*, 31–39.

Harto, C. B., Y. E. Yan, Y. K. Demissie, D. Elcock, V. C. Tidwell, K. Hallett, J. Macknick, M. S. Wigmosta, and T. K. Tesfa (2012), *Analysis of drought impacts on electricity production in the Western and Texas interconnections of the United States.*, Argonne National Laboratory (ANL).

Hashimoto, T., J. R. Stedinger, and D. P. Loucks (1982), Reliability, resiliency, and vulnerability criteria for water resource system performance evaluation, *Water Resour. Res.*, *18*(1), 14–20.

Hashizume, M., T. Terao, and N. Minakawa (2009), The Indian Ocean Dipole and malaria risk in the highlands of western Kenya, *Proc. Natl. Acad. Sci.*, *106*(6), 1857–1862.

Hashizume, M., A. S. G. Faruque, T. Terao, M. Yunus, K. Streatfield, T. Yamamoto, and K. Moji (2011), The Indian Ocean dipole and cholera incidence in Bangladesh: a time-series analysis, *Environ. Health Perspect.*, *119*(2), 239.

Hay, L. E., R. L. Wilby, and G. H. Leavesley (2000), A COMPARISON OF DELTA CHANGE AND DOWNSCALED GCM SCENARIOS FOR THREE MOUNTAINOUS BASINS IN THE UNITED STATES1, *JAWRA J. Am. Water Resour. Assoc.*, *36*(2), 387–397, doi:10.1111/j.1752-1688.2000.tb04276.x.

Heal, G., and A. Millner (2014), Reflections: Uncertainty and decision making in climate change economics, *Rev. Environ. Econ. Policy*, *8*(1), 120–137.

Healy, D., and F. Hicks (1999), Comparison of ICEJAM and RIVJAM ice jam profile models, *J. cold Reg. Eng.*, *13*(4), 180–198.

Held, I. M., and B. J. Soden (2006), Robust Responses of the Hydrological Cycle to Global Warming, *J. Clim.*, *19*(21), 5686–5699, doi:10.1175/JCLI3990.1.

Hicks, F. (2009), An overview of river ice problems: CRIPE07 guest editorial,

Hirabayashi, Y., S. Kanae, S. Emori, T. Oki, and M. Kimoto (2008), Global projections of changing risks of floods and droughts in a changing climate, *Hydrol. Sci. J.*, *53*(4), 754–772, doi:10.1623/hysj.53.4.754.

Hirabayashi, Y., R. Mahendran, S. Koirala, L. Konoshima, D. Yamazaki, S. Watanabe, H. Kim, and S. Kanae (2013), Global flood risk under climate change, *Nat. Clim. Chang.*, *3*(9), 816–821, doi:10.1038/nclimate1911.

Hisdal, H., and L. M. Tallaksen (2003), Estimation of regional meteorological and hydrological drought characteristics: a case study for Denmark, *J. Hydrol.*, *281*(3), 230–247.

Hock, R. (2003), Temperature index melt modelling in mountain areas, *J. Hydrol.*, *282*(1), 104–115, doi:https://doi.org/10.1016/S0022-1694(03)00257-9.

Hoekstra, A. Y. (2014), Water scarcity challenges to business, *Nat. Clim. Chang.*, *4*(5), 318.

Hoes, O. A. C., L. J. J. Meijer, R. J. Van Der Ent, and N. C. Van De Giesen (2017), Systematic high-resolution assessment of global hydropower potential, *PLoS One*, *12*(2), e0171844.

Horii, T., H. Hase, I. Ueki, and Y. Masumoto (2008), Oceanic precondition and evolution of the 2006 Indian Ocean dipole, *Geophys. Res. Lett.*, *35*(3).

Hosking, J. R. M., and J. R. Wallis (2005), *Regional frequency analysis: an approach based on L-moments*, Cambridge University Press.

Houghton, J. T., B. A. Callander, and S. K. Varney (1992), *Climate change 1992*, Cambridge University Press.

Hsiang, S. M., and K. C. Meng (2015), Tropical economics, *Am. Econ. Rev.*, *105*(5), 257–261.

Huang, J., H. Yu, X. Guan, G. Wang, and R. Guo (2016), Accelerated dryland expansion under climate change, *Nat. Clim. Chang.*, *6*(2), 166.

Hui, Y., and L. Chongyin (2003), The relation between atmospheric intraseasonal oscillation and summer severe flood and drought in the Changjiang—Huaihe River Basin, *Adv. Atmos. Sci.*, *20*(4), 540–553.

Hulme, M. (2016), 1.5 °C and climate research after the Paris Agreement, *Nat. Clim. Chang.*, *6*(3), 222–224, doi:10.1038/nclimate2939.

Hurrell, J. W. (1995), Decadal trends in the North Atlantic Oscillation: regional temperatures and precipitation, *Science (80-.).*, *269*(5224), 676–679.

Hurrell, J. W., and C. Deser (2010), North Atlantic climate variability: the role of the North Atlantic Oscillation, *J. Mar. Syst.*, *79*(3–4), 231–244.

Hurrell, J. W., Y. Kushnir, and M. Visbeck (2001), The North Atlantic Oscillation, *Science (80-.).*, *291*(5504), 603 LP-605.

IEA (2017), *World Energy Outlook 2017*, International Energy Agency.

Internal Displacement Monitoring Centre (IDMC) (2017), *Global Report on Internal Displacement*, Geneva.

Jain, S. K., and P. K. Bhunya (2008), Reliability, resilience and vulnerability of a multipurpose storage reservoir/Confiance, résilience et vulnérabilité d'un barrage multi-objectifs, *Hydrol. Sci. J.*, *53*(2), 434–447.

Jinno, K. (1995), Risk assessment of a water supply system during drought, *Int. J. Water Resour. Dev.*, *11*(2), 185–204.

Jones, C., D. E. Waliser, K. M. Lau, and W. Stern (2004), Global occurrences of extreme precipitation and the Madden–Julian oscillation: Observations and predictability, *J. Clim.*, *17*(23), 4575–4589.

Jongman, B., S. Hochrainer-stigler, L. Feyen, J. C. J. H. Aerts, R. Mechler, W. J. W. Botzen, L. M. Bouwer, G. Pflug, R. Rojas, and P. J. Ward (2014), Increasing stress on disaster-risk finance due to large floods, , *4*(5), 1–5, doi:10.1038/NCLIMATE2124.

Joseph, P. V, and A. Simon (2005), Weakening trend of the southwest monsoon current through peninsular India from 1950 to the present, *Curr. Sci.*, 687–694.

Kay, J. E., C. Deser, A. Phillips, A. Mai, C. Hannay, G. Strand, J. M. Arblaster, S. C. Bates, G. Danabasoglu, and J. Edwards (2015), The Community Earth System Model (CESM) large ensemble project: A community resource for studying climate change in the presence of internal climate variability, *Bull. Am. Meteorol. Soc.*, *96*(8), 1333–1349.

Keef, C., J. A. Tawn, and R. Lamb (2013), Estimating the probability of widespread flood events, *Environmetrics*, *24*(1), 13–21.

Kennett, D. J., S. F. M. Breitenbach, V. V Aquino, Y. Asmerom, J. Awe, J. U. L. Baldini, P. Bartlein, B. J. Culleton, C. Ebert, and C. Jazwa (2012), Development and disintegration of Maya political systems in response to climate change, *Science (80-.).*, *338*(6108), 788–791.

Kenyon, J., and G. C. Hegerl (2010a), Influence of modes of climate variability on global precipitation extremes, *J. Clim.*, *23*(23), 6248–6262, doi:10.1175/2010JCLI3617.1.

Kenyon, J., and G. C. Hegerl (2010b), Influence of Modes of Climate Variability on Global Precipitation Extremes, *J. Clim.*, *23*(23), 6248–6262, doi:10.1175/2010JCLI3617.1.

Kharin, V. V, F. W. Zwiers, X. Zhang, and M. Wehner (2013), Changes in temperature and precipitation extremes in the CMIP5 ensemble, *Clim. Change*, *119*(2), 345–357.

Kjeldsen, T. R., and D. Rosbjerg (2004), Choice of reliability, resilience and vulnerability estimators for risk assessments of water resources systems/Choix d'estimateurs de fiabilité, de résilience et de vulnérabilité pour les analyses de risque de systèmes de ressources en eau, *Hydrol. Sci. J.*, *49*(5).

Koirala, S., Y. Hirabayashi, R. Mahendran, and S. Kanae (2014), Global assessment of agreement among stream flow projections using CMIP5 model outputs, *Environ. Res. Lett.*, *9*(6), 64017, doi:10.1088/1748-9326/9/6/064017.

Kollet, S. J., R. M. Maxwell, C. S. Woodward, S. Smith, J. Vanderborght, H. Vereecken, and C. Simmer (2010), Proof of concept of regional scale hydrologic simulations at hydrologic resolution utilizing massively parallel computer resources, *Water Resour. Res.*, *46*(4).

Krakauer, N. Y., H. Li, and Y. Fan (2014), Groundwater flow across spatial scales: Importance for climate modeling, *Environ. Res. Lett.*, *9*(3), 34003.

Krinner, G., N. Viovy, N. de Noblet-Ducoudré, J. Ogée, J. Polcher, P. Friedlingstein, P. Ciais, S. Sitch, and I. C. Prentice (2005), A dynamic global vegetation model for studies of the coupled atmosphere-biosphere system, *Global Biogeochem. Cycles*, *19*(1).

Kummu, M., D. Gerten, J. Heinke, M. Konzmann, and O. Varis (2014), Climate-driven interannual variability of water scarcity in food production potential: a global analysis, *Hydrol. Earth Syst. Sci.*, *18*(2), 447–461.

Kuusisto, E. (2004), Droughts in Finland–past, present and future, *Hydrol. Days*, *2004*,

143–147.

Lal, A. M. W., and H. T. Shen (1991), Mathematical model for river ice processes, *J. Hydraul. Eng.*, *117*(7), 851–867.

Lamb, R., C. Keef, J. Tawn, S. Laeger, I. Meadowcroft, S. Surendran, P. Dunning, and C. Batstone (2010), A new method to assess the risk of local and widespread flooding on rivers and coasts, *J. Flood Risk Manag.*, *3*(4), 323–336.

Lambert, S. J., and G. J. Boer (2001), CMIP1 evaluation and intercomparison of coupled climate models, *Clim. Dyn.*, *17*(2–3), 83–106.

Lavers, D. a, R. P. Allan, G. Villarini, B. Lloyd-Hughes, D. J. Brayshaw, and A. J. Wade (2013), Future changes in atmospheric rivers and their implications for winter flooding in Britain, *Environ. Res. Lett.*, *8*, 34010, doi:10.1088/1748-9326/8/3/034010.

Lavers, D. a., and G. Villarini (2015a), The contribution of atmospheric rivers to precipitation in Europe and the United States, *J. Hydrol.*, *522*, 382–390, doi:10.1016/j.jhydrol.2014.12.010.

Lavers, D. A., and G. Villarini (2013), Atmospheric Rivers and Flooding over the Central United States, *J. Clim.*, *26*(20), 7829–7836, doi:10.1175/JCLI-D-13-00212.1.

Lavers, D. A., and G. Villarini (2015b), The contribution of atmospheric rivers to precipitation in Europe and the United States, *J. Hydrol.*, *522*, 382–390, doi:10.1016/j.jhydrol.2014.12.010.

Lawston, P. M., J. A. Santanello Jr, B. F. Zaitchik, and M. Rodell (2015), Impact of irrigation methods on land surface model spinup and initialization of WRF forecasts, *J. Hydrometeorol.*, *16*(3), 1135–1154.

Lean, J., J. Beer, and R. Bradley (1995), Reconstruction of solar irradiance since 1610: Implications for climate change, *Geophys. Res. Lett.*, *22*(23), 3195–3198.

Lean, J. L. (2010), Cycles and trends in solar irradiance and climate, *Wiley Interdiscip. Rev. Clim. Chang.*, *1*(1), 111–122.

LeGrande, A. N., and K. J. Anchukaitis (2015), Volcanic eruptions and climate, *PAGES Newsl.*, *23*, 46–47.

Lehner, B., and G. Grill (2013), Global river hydrography and network routing: baseline data and new approaches to study the world's large river systems, *Hydrol. Process.*, *27*(15), 2171–2186.

Lehner, B., G. Czisch, and S. Vassolo (2005), The impact of global change on the hydropower potential of Europe: a model-based analysis, *Energy Policy*, *33*(7), 839–855.

Lehner, B., K. Verdin, and A. Jarvis (2008), New global hydrography derived from spaceborne elevation data, *Eos, Trans. Am. Geophys. Union*, *89*(10), 93–94, doi:10.1029/2008EO100001.

Lehner, B., C. R. Liermann, C. Revenga, C. Vörösmarty, B. Fekete, P. Crouzet, P. Döll, M. Endejan, K. Frenken, and J. Magome (2011), Global reservoir and dam (grand) database, *NASA Socioecon. Data Appl. Cent. Tech. Doc.(ver. 1.1).[Available online http//sedac. ciesin. columbia. edu/data/collection/grand-v1.]*.

Lehner, F., S. Coats, T. F. Stocker, A. G. Pendergrass, B. M. Sanderson, C. C. Raible, and J. E. Smerdon (2017), Projected drought risk in 1.5°C and 2°C warmer climates, *Geophys. Res. Lett.*, (44), n/a--n/a, doi:10.1002/2017GL074117.

Lennart, B., H. Stefan, and H. K. I. (2004), Can climate trends be calculated from reanalysis data?, *J. Geophys. Res. Atmos.*, *109*(D11), doi:10.1029/2004JD004536.

Li, H., and M. Sivapalan (2011), Effect of spatial heterogeneity of runoff generation mechanisms on the scaling behavior of event runoff responses in a natural river basin, *Water Resour. Res.*, *47*(3).

Li, H., M. S. Wigmosta, H. Wu, M. Huang, Y. Ke, A. M. Coleman, and L. R. Leung (2013), A Physically Based Runoff Routing Model for Land Surface and Earth System Models, *J. Hydrometeorol.*, *14*(3), 808–828, doi:10.1175/JHM-D-12-015.1.

Li, L., Y. Wang, Q. Yu, B. Pak, D. Eamus, J. Yan, E. Gorsel, and I. T. Baker (2012),

Improving the responses of the Australian community land surface model (CABLE) to seasonal drought, *J. Geophys. Res. Biogeosciences*, *117*(G4).

Li, T. (2014), Recent advance in understanding the dynamics of the Madden-Julian oscillation, *J. Meteorol. Res.*, *28*(1), 1–33.

Lin, J.-L. (2007), The double-ITCZ problem in IPCC AR4 coupled GCMs: Ocean–atmosphere feedback analysis, *J. Clim.*, *20*(18), 4497–4525.

Lindenschmidt, K., A. Das, P. Rokaya, and T. Chu (2016), Ice-jam flood risk assessment and mapping, *Hydrol. Process.*, *30*(21), 3754–3769.

Lindsay, R., M. Wensnahan, A. Schweiger, and J. Zhang (2014), Evaluation of Seven Different Atmospheric Reanalysis Products in the Arctic, *J. Clim.*, *27*(7), 2588–2606, doi:10.1175/JCLI-D-13-00014.1.

Liu, L., H. Li, and H. T. Shen (2006), A two-dimensional comprehensive river ice model, in *Proceedings of the 18th IAHR Symposium on River Ice, Sapporo, Japan*.

Liu, X. C., Q. H. Tang, N. Voisin, and H. J. Cui (2016), Projected impacts of climate change on hydropower potential in China,

De Loe, R. C., and R. D. Kreutzwiser (2000), Climate variability, climate change and water resource management in the Great Lakes, *Clim. Change*, *45*, 163–179, doi:10.1023/A:1005649219332.

Lohmann, D., E. Raschke, B. Nijssen, and D. P. Lettenmaier (1998), Regional scale hydrology: I. Formulation of the VIC-2L model coupled to a routing model, *Hydrol. Sci. J.*, *43*(1), 131–141.

Lohmann, D. A. G., R. NOLTE-HOLUBE, and E. Raschke (1996), A large-scale horizontal routing model to be coupled to land surface parametrization schemes, *Tellus A*, *48*(5), 708–721.

Loisulie, S. (2010), Vulnerability of Tanzania hydropower production to extreme weather events, in *the Joint ICTP-IAEA Workshop on Vulnerability of Energy Systems to Climate Change and Extreme Events*.

Van Loon, A. F. (2015a), Hydrological drought explained, *WIREs Water*, *2:359–392*(August), doi:10.1002/wat2.1085.

Van Loon, A. F. (2015b), Hydrological drought explained, *Wiley Interdiscip. Rev. Water*, *2*(4), 359–392.

Van Loon, A. F., and H. A. J. Van Lanen (2012), A process-based typology of hydrological drought, *Hydrol. Earth Syst. Sci.*, *16*(7), 1915.

Lorenz, C., and H. Kunstmann (2012), The hydrological cycle in three state-of-the-art reanalyses: Intercomparison and performance analysis, *J. Hydrometeorol.*, *13*(5), 1397–1420.

Lowe, D. C., and N. Zealand (2007), Changes in Atmospheric Constituents and in Radiative Forcing, *Change*, *30*(22), 129–234, doi:10.1103/PhysRevB.77.220407.

Lü, J., J. Ju, J. Ren, and W. Gan (2012), The influence of the Madden-Julian Oscillation activity anomalies on Yunnan's extreme drought of 2009–2010, *Sci. China Earth Sci.*, *55*(1), 98–112.

Lu, R., B. Dong, and H. Ding (2006), Impact of the Atlantic Multidecadal Oscillation on the Asian summer monsoon, *Geophys. Res. Lett.*, *33*(24).

Lucas-Picher, P., V. K. Arora, D. Caya, and R. Laprise (2003), Implementation of a large-scale variable velocity river flow routing algorithm in the Canadian Regional Climate Model (CRCM), *Atmosphere-ocean*, *41*(2), 139–153.

Ludwig, F., E. van Slobbe, and W. Cofino (2014), Climate change adaptation and Integrated Water Resource Management in the water sector, *J. Hydrol.*, *518*(PB), 235–242, doi:10.1016/j.jhydrol.2013.08.010.

Lyon, S. W., F. Dominguez, D. J. Gochis, N. A. Brunsell, C. L. Castro, F. K. Chow, Y. Fan, D. Fuka, Y. Hong, and P. A. Kucera (2008), Coupling terrestrial and atmospheric water dynamics to improve prediction in a changing environment, *Bull. Am. Meteorol. Soc.*, *89*(9), 1275–1279.

Ma, Z., and C. Fu (2007), Global aridification in the second half of the 20th century and

its relationship to large-scale climate background, *Sci. China Ser. D Earth Sci.*, *50*(5), 776–788.

MacKellar, N. C., S. J. Dadson, M. New, and P. Wolski (2013), Evaluation of the JULES land surface model in simulating catchment hydrology in Southern Africa, *Hydrol. Earth Syst. Sci. Discuss.*, *10*(8), 11093–11128, doi:10.5194/hessd-10-11093-2013.

Madani, K., and J. R. Lund (2010), Estimated impacts of climate warming on California's high-elevation hydropower, *Clim. Change*, *102*(3), 521–538, doi:10.1007/s10584-009-9750-8.

Manatsa, D., B. Chipindu, and S. K. Behera (2012), Shifts in IOD and their impacts on association with East Africa rainfall, *Theor. Appl. Climatol.*, *110*(1), 115–128, doi:10.1007/s00704-012-0610-5.

Mantua, N. J., and S. R. Hare (2002), The Pacific decadal oscillation, *J. Oceanogr.*, *58*(1), 35–44.

Marchant, R., C. Mumbi, S. Behera, and T. Yamagata (2007), The Indian Ocean dipole–the unsung driver of climatic variability in East Africa, *Afr. J. Ecol.*, *45*(1), 4–16.

Marengo, J. A., W. R. Soares, C. Saulo, and M. Nicolini (2004), Climatology of the low-level jet east of the Andes as derived from the NCEP–NCAR reanalyses: Characteristics and temporal variability,

Marthews, T. R., S. J. Dadson, B. Lehner, S. Abele, and N. Gedney (2015a), High-resolution global topographic index values for use in large-scale hydrological modelling, *Hydrol. Earth Syst. Sci.*, *19*(1), 91–104, doi:10.5194/hess-19-91-2015.

Marthews, T. R., S. J. Dadson, B. Lehner, S. Abele, and N. Gedney (2015b), High-resolution global topographic index values for use in large-scale hydrological modelling, *Hydrol. Earth Syst. Sci.*, *19*(1), 91–104, doi:doi:10.5194/hess-19-91-2015.

Martinez, J. A., and F. Dominguez (2014), Sources of atmospheric moisture for the La Plata River basin, *J. Clim.*, *27*(17), 6737–6753.

Maslin, M., and P. Austin (2012), Uncertainty: Climate models at their limit?, *Nature*, *486*(7402), 183.

Mateo, C. M. R., D. Yamazaki, H. Kim, A. Champathong, J. Vaze, and T. Oki (2017), Impacts of spatial resolution and representation of flow connectivity on large-scale simulation of floods, *Hydrol. Earth Syst. Sci.*, *21*(10), 5143.

Materia, S., P. A. Dirmeyer, Z. Guo, A. Alessandri, and A. Navarra (2009), The Sensitivity of Simulated River Discharge to Land Surface Representation and Meteorological Forcings, *J. Hydrometeorol.*, *11*(2), 334–351, doi:10.1175/2009JHM1162.1.

Matthews, A. J. (2000), Propagation mechanisms for the Madden-Julian Oscillation, *Q. J. R. Meteorol. Soc.*, *126*(569), 2637–2651.

Maurer, E. P., and H. G. Hidalgo (2008), Utility of daily vs. monthly large-scale climate data: an intercomparison of two statistical downscaling methods,

Maxwell, R. M., and N. L. Miller (2005), Development of a coupled land surface and groundwater model, *J. Hydrometeorol.*, *6*(3), 233–247.

McCabe, G. J., and M. A. Palecki (2006), Multidecadal climate variability of global lands and oceans, *Int. J. Climatol.*, *26*(7), 849–865, doi:10.1002/joc.1289.

McMillan, H. K., and J. Brasington (2008), End-to-end flood risk assessment: A coupled model cascade with uncertainty estimation, *Water Resour. Res.*, *44*(3).

McPhaden, M. J., S. E. Zebiak, and M. H. Glantz (2006), ENSO as an integrating concept in earth science, *Science (80-.).*, *314*(5806), 1740–1745.

Mearns, L. O., S. Sain, L. R. Leung, M. S. Bukovsky, S. McGinnis, S. Biner, D. Caya, R. W. Arritt, W. Gutowski, and E. Takle (2013), Climate change projections of the North American regional climate change assessment program (NARCCAP), *Clim. Change*, *120*(4), 965–975.

Menon, S., J. Hansen, L. Nazarenko, and Y. Luo (2002), Climate effects of black carbon aerosols in China and India, *Science (80-.).*, *297*(5590), 2250–2253.

Mestas-Nuñez, A. M., and D. B. Enfield (1999), Rotated global modes of non-ENSO sea

surface temperature variability, *J. Clim.*, *12*(9), 2734–2746, doi:10.1175/1520-0442(1999)012<2734:RGMONE>2.0.CO;2.

Miller, J. R., G. L. Russell, and G. Caliri (1994), Continental-scale river flow in climate models, *J. Clim.*, *7*(6), 914–928, doi:10.1175/1520-0442(1994)007<0914:CSRFIC>2.0.CO;2.

Milly, P. C. D., R. T. Wetherald, K. a Dunne, and T. L. Delworth (2002), Increasing risk of great floods in a changing climate., *Nature*, *415*(6871), 514–517, doi:10.1038/415514a.

Min, S.-K., X. Zhang, and F. Zwiers (2008), Human-induced Arctic moistening., *Science*, *320*(2008), 518–520, doi:10.1126/science.1153468.

Mitchell, D., R. James, P. M. Forster, R. A. Betts, H. Shiogama, and M. Allen (2016), Realizing the impacts of a 1.5 °C warmer world, *Nat. Clim. Chang.*, *6*(8), 735–737, doi:10.1038/nclimate3055.

Mitchell, D. et al. (2017), Half a degree additional warming , prognosis and projected impacts (HAPPI): background and experimental design, , 571–583, doi:10.5194/gmd-10-571-2017.

Mithen, S. (2012), *Thirst: For Water and Power in the Ancient World*, Harvard University Press.

Mo, K. C., J. Nogues-Paegle, and J. Paegle (1995), Physical mechanisms of the 1993 summer floods, *J. Atmos. Sci.*, *52*(7), 879–895.

de Moel, H., B. Jongman, H. Kreibich, B. Merz, E. Penning-Rowsell, and P. J. Ward (2015), Flood risk assessments at different spatial scales, *Mitig. Adapt. Strateg. Glob. Chang.*, *20*(6), 865–890, doi:10.1007/s11027-015-9654-z.

Monteith, J. L. (1965), *Evaporation and the Environment in the State and Movement of Water in Living Organisms*, Cambridge.

Moore, R. J., V. A. Bell, R. M. Austin, and R. J. Harding (1999), Methods for snowmelt forecasting in upland Britain, *Hydrol. Earth Syst. Sci. Discuss.*, *3*(2), 233–246.

Moriasi, D. N., J. G. Arnold, M. W. Van Liew, R. L. Binger, R. D. Harmel, and T. L. Veith (2007), Model evaluation guidelines for systematic quantification of accuracy in watershed simulations, *Trans. ASABE*, *50*(3), 885–900, doi:10.13031/2013.23153.

Morse, B., and F. Hicks (2005), Advances in river ice hydrology 1999–2003, *Hydrol. Process. An Int. J.*, *19*(1), 247–263.

Moussa, R., and C. Bocquillon (1996), Criteria for the choice of flood-routing methods in natural channels, *J. Hydrol.*, *186*(1–4), 1–30.

Mukheibir, P. (2013), Potential consequences of projected climate change impacts on hydroelectricity generation, *Clim. Change*, *121*(1), 67–78.

Murphy, J. M., D. M. H. Sexton, D. N. Barnett, G. S. Jones, M. J. Webb, M. Collins, and D. A. Stainforth (2004), Quantification of modelling uncertainties in a large ensemble of climate change simulations, *Nature*, *430*(7001), 768.

Nazemosadat, M. J., and H. Ghaedamini (2010), On the relationships between the Madden–Julian oscillation and precipitation variability in southern Iran and the Arabian Peninsula: Atmospheric circulation analysis, *J. Clim.*, *23*(4), 887–904.

Neelin, J. D., D. S. Battisti, A. C. Hirst, F. Jin, Y. Wakata, T. Yamagata, and A. E (1998), ENSO theory, *J. Geophys. Res. Ocean.*, *103*(C7), 14261–14290, doi:10.1029/97JC03424.

Negin, A., D. D. A., and S. M. J. (2015), Sustainability Review of Water-Supply Options in the Los Angeles Region, *J. Water Resour. Plan. Manag.*, *141*(12), A4015005, doi:10.1061/(ASCE)WR.1943-5452.0000541.

Neiman, P. J., L. J. Schick, F. M. Ralph, M. Hughes, and G. a. Wick (2011), Flooding in Western Washington: The Connection to Atmospheric Rivers*, *J. Hydrometeorol.*, *12*(6), 1337–1358, doi:10.1175/2011JHM1358.1.

New, M., M. Hulme, and P. Jones (2000), Representing twentieth-century space–time climate variability. Part II: Development of 1901–96 monthly grids of terrestrial surface climate, *J. Clim.*, *13*(13), 2217–2238.

Newman, M., M. A. Alexander, T. R. Ault, K. M. Cobb, C. Deser, E. Di Lorenzo, N. J. Mantua, A. J. Miller, S. Minobe, and H. Nakamura (2016), The Pacific decadal oscillation, revisited, *J. Clim.*, *29*(12), 4399–4427.

Nguyen, D. D. (2012), Water Body Extraction From Multi Spectral Image By Spectral Pattern Analysis, *ISPRS - Int. Arch. Photogramm. Remote Sens. Spat. Inf. Sci.*, *XXXIX-B8*(September), 181–186, doi:10.5194/isprsarchives-XXXIX-B8-181-2012.

Nigam, S., M. Barlow, and E. H. Berbery (1999), Analysis links Pacific decadal variability to drought and streamflow in United States, *EOS, Trans. Am. Geophys. Union*, *80*(51), 621–625.

Nijssen, B., G. M. O'Donnell, A. F. Hamlet, and D. P. Lettenmaier (2001a), Hydrologic Sensitivity of Global Rivers to Climate Change, *Clim. Change*, *50*(1), 143–175, doi:10.1023/A:1010616428763.

Nijssen, B., G. M. O'Donnell, D. P. Lettenmaier, D. Lohmann, and E. F. Wood (2001b), Predicting the discharge of global rivers, *J. Clim.*, *14*(15), 3307–3323.

Niu, G.-Y. et al. (2011), The community Noah land surface model with multiparameterization options (Noah-MP): 1. Model description and evaluation with local-scale measurements, *J. Geophys. Res. Atmos.*, *116*(D12), n/a--n/a, doi:10.1029/2010JD015139.

Nordhaus, W. D. (2007), A review of the Stern review on the economics of climate change, *J. Econ. Lit.*, *45*(3), 686–702.

Okazaki, A. (2012), Changes in Flood Risk under Global Warming Estimated Using MIROC5 and the Discharge Probability Index, , (August), doi:10.2151/jmsj.2012-405.

Oki, T., and Y. C. Sud (1998), Design of Total Runoff Integrating Pathways (TRIP)—A global river channel network, *Earth Interact.*, *2*(1), 1–37.

Oki, T., Y. Agata, S. Kanae, T. Saruhashi, D. Yang, and K. Musiake (2001), Global assessment of current water resources using total runoff integrating pathways,

Hydrol. Sci. J., *46*(6), 983–995.

Olivera, F., and R. Raina (2003), Development of large scale gridded river networks from vector stream data, *J. Am. Water Resour. Assoc.*, *39*(5), 1235–1248, doi:10.1111/j.1752-1688.2003.tb03705.x.

Overpeck, J. T., G. A. Meehl, S. Bony, and D. R. Easterling (2011), Climate data challenges in the 21st century, *Science (80-.).*, *331*(6018), 700–702.

Paltan, H., M. Allen, K. Haustein, L. Fuldauer, and S. Dadson (2018), Global implications of 1.5 °C and 2 °C warmer worlds on extreme river flows, *Environ. Res. Lett.*

Parajka, J., S. Dadson, T. Lafon, and R. Essery (2010), Evaluation of snow cover and depth simulated by a land surface model using detailed regional snow observations from Austria, *J. Geophys. Res.*, *115*(D24), D24117, doi:10.1029/2010JD014086.

Paz, A. R. Da, W. Collischonn, A. Risso, and C. A. B. Mendes (2008), Errors in river lengths derived from raster digital elevation models, *Comput. Geosci.*, *34*(11), 1584–1596, doi:10.1016/j.cageo.2007.10.009.

Peduzzi, P., H. Dao, C. Herold, and F. Mouton (2009), Assessing global exposure and vulnerability towards natural hazards: the Disaster Risk Index, *Nat. Hazards Earth Syst. Sci.*, *9*(4), 1149–1159, doi:10.5194/nhess-9-1149-2009.

Pervez, M. S., and G. M. Henebry (2015), Spatial and seasonal responses of precipitation in the Ganges and Brahmaputra river basins to ENSO and Indian Ocean dipole modes: implications for flooding and drought, *Nat. Hazards Earth Syst. Sci.*, *15*(1), 147.

Pfeffer, W. T. (2007), Glaciers Dominate Eustatic Sea-Level Rise in the 21st Century, , (September 2015), 1064–1068, doi:10.1126/science.1143906.

Pielke Jr, R. A., and C. N. Landsea (1999), La nina, el nino and atlantic hurricane damages in the united states, *Bull. Am. Meteorol. Soc.*, *80*(10), 2027–2033.

Pierce, D. W., T. P. Barnett, B. D. Santer, and P. J. Gleckler (2009), Selecting global climate models for regional climate change studies, *Proc. Natl. Acad. Sci.*, *106*(21),

8441 LP-8446.

Piman, T., T. Cochrane, E. Arias, A. Green, and D. Dat (2013), Assessment of Flow Changes from Hydropower Development and Operations in Sekong, Sesan, and Srepok Rivers of the Mekong Basin, *J. Water Resour. Plan. Manag.*, *139*(6), 723–732, doi:10.1061/(ASCE)WR.1943-5452.0000286.

Pincus, R., C. P. Batstone, R. J. P. Hofmann, K. E. Taylor, and P. J. Glecker (2008), Evaluating the present-day simulation of clouds, precipitation, and radiation in climate models, *J. Geophys. Res. Atmos.*, *113*(D14).

Pitman, A. J. (2003), The evolution of, and revolution in, land surface schemes designed for climate models, *Int. J. Climatol.*, *23*, 479–510, doi:10.1002/joc.893.

Pokhrel, Y. N., T. Oki, and S. Kanae (2008), A grid based assessment of global theoretical hydropower potential, *Proc. Hydraul. Eng.*, *52*, 7–12.

Pokhrel, Y. N., N. Hanasaki, Y. Wada, and H. Kim (2016), Recent progresses in incorporating human land–water management into global land surface models toward their integration into Earth system models, *Wiley Interdiscip. Rev. Water*, *3*(4), 548–574.

Poveda, G., and O. J. Mesa (1999), The superficial jet stream of west (of Choco) and other two jet streams in Colombia: Climatology and variability during the phases of the Enso, *Rev. la Acad. Colomb. Ciencias Exactas, Fis. y Nat.*, *23*(89), 517–528.

Poveda, G., L. Jaramillo, and L. F. Vallejo (2014), Seasonal precipitation patterns along pathways of South American low-level jets and aerial rivers, *Water Resour. Res.*, *50*(1), 98–118.

Powell, T. L., D. R. Galbraith, B. O. Christoffersen, A. Harper, H. M. A. Imbuzeiro, L. Rowland, S. Almeida, P. M. Brando, A. C. L. da Costa, and M. H. Costa (2013), Confronting model predictions of carbon fluxes with measurements of Amazon forests subjected to experimental drought, *New Phytol.*, *200*(2), 350–365.

Prowse, T. D., and S. Beltaos (2002), Climatic control of river-ice hydrology: a review,

Hydrol. Process., *16*(4), 805–822.

Prowse, T. D., F. J. Wrona, J. D. Reist, J. J. Gibson, J. E. Hobbie, L. M. J. Lévesque, W. F. Vincent, and L. M. J. Le (2006), Climate Change Effects on Hydroecology of Arctic Freshwater Ecosystems, , *35*(7), 347–358.

Prudhomme, C., N. Reynard, and S. Crooks (2002), Downscaling of global climate models for flood frequency analysis: where are we now?, *Hydrol. Process.*, *16*(6), 1137–1150.

Prudhomme, C., S. Parry, J. Hannaford, D. B. Clark, S. Hagemann, and F. Voss (2011), How well do large-scale models reproduce regional hydrological extremes in Europe?, *J. Hydrometeorol.*, *12*(6), 1181–1204.

Prudhomme, C. et al. (2014), Hydrological droughts in the 21st century, hotspots and uncertainties from a global multimodel ensemble experiment., *Proc. Natl. Acad. Sci. U. S. A.*, *111*(9), 3262–3267, doi:10.1073/pnas.1222473110.

Pu, B., and K. H. Cook (2012), Role of the West African westerly jet in Sahel rainfall variations, *J. Clim.*, *25*(8), 2880–2896.

Qian, T., A. Dai, K. E. Trenberth, and K. W. Oleson (2006), Simulation of Global Land Surface Conditions from 1948 to 2004. Part I: Forcing Data and Evaluations, *J. Hydrometeorol.*, *7*(5), 953–975, doi:10.1175/JHM540.1.

Qiaohong, S., M. Chiyuan, D. Qingyun, A. Hamed, S. Soroosh, and H. Kuo-Lin (2017), A Review of Global Precipitation Data Sets: Data Sources, Estimation, and Intercomparisons, *Rev. Geophys.*, *56*(1), 79–107, doi:10.1002/2017RG000574.

Rahmstorf, S., A. Cazenave, J. A. Church, J. E. Hansen, R. F. Keeling, D. E. Parker, and R. C. J. Somerville (2007), Recent climate observations compared to projections, *Science (80-.).*, *316*(5825), 709.

Rajeevan, M., J. Bhate, and A. K. Jaswal (2008), Analysis of variability and trends of extreme rainfall events over India using 104 years of gridded daily rainfall data, *Geophys. Res. Lett.*, *35*(18).

Ralph, F. M., and M. D. Dettinger (2011), Storms, floods, and the science of atmospheric rivers, *Eos (Washington. DC).*, *92*(32), 265–266, doi:10.1029/2011EO320001.

Ralph, F. M., P. J. Neiman, G. A. Wick, S. I. Gutman, M. D. Dettinger, D. R. Cayan, and A. B. White (2006), Flooding on California ' s Russian River : Role of atmospheric rivers, , *33*, 2–6, doi:10.1029/2006GL026689.

Ralph, F. M., T. Coleman, P. J. Neiman, R. J. Zamora, and M. D. Dettinger (2012), Observed impacts of duration and seasonality of atmospheric-river landfalls on soil moisture and runoff in coastal northern California, *J. Hydrometeorol.*, (2004), 121026084711009, doi:10.1175/JHM-D-12-076.1.

Ramanathan, V., P. J. Crutzen, J. T. Kiehl, and D. Rosenfeld (2001), Aerosols, climate, and the hydrological cycle, *Science (80-.).*, *294*(5549), 2119–2124.

Ramos, A. M., R. Tomé, R. M. Trigo, M. L. R. Liberato, and J. G. Pinto (2016), Projected changes in atmospheric rivers affecting Europe in CMIP5 models, *Geophys. Res. Lett.*, *43*(17), 9315–9323, doi:10.1002/2016GL070634.

Randall, D. A. et al. (2007), Cilmate Models and Their Evaluation, in *Climate Change 2007: The Physical Science Basis. Contribution of Working Group I to the Fourth Assessment Report of the Intergovernmental Panel on Climate Change*, edited by S. Solomon, D. Qin, M. Manning, Z. Chen, M. Marquis, K. B. Averyt, M. Tignor, and H. L. Miller, Cambridge University Press, Cambridge, United Kingdom and New York, NY, USA.

Randalls, S. (2010), History of the 2 C climate target, *Wiley Interdiscip. Rev. Clim. Chang.*, *1*(4), 598–605.

Rango, A., and J. Martinec (2007), Revisiting the degree day-method for snowmleat computations, *JAWRA J. Am. Water Resour. Assoc.*, *31*(4), 657–669, doi:10.1111/j.1752-1688.1995.tb03392.x.

Rango, a. (1993), II. Snow hydrology processes and remote sensing, *Hydrol. Process.*, *7*(2), 121–138, doi:10.1002/hyp.3360070204.

Rao, S. A., H. S. Chaudhari, S. Pokhrel, and B. N. Goswami (2010), Unusual central Indian drought of summer monsoon 2008: role of southern tropical Indian Ocean warming, *J. Clim.*, *23*(19), 5163–5174.

Reason, C. J. C. (2001), Subtropical Indian Ocean SST dipole events and southern African rainfall, *Geophys. Res. Lett.*, *28*(11), 2225–2227.

Renofalt, B., R. Jansson, and C. Nilsson (2010), Effects of hydropower generation and opportunities for environmental flow management in Swedish riverine ecosystems, *Freshw. Biol.*, *55*(1), 49–67.

Rienecker, M. M., M. J. Suarez, R. Gelaro, R. Todling, J. Bacmeister, E. Liu, M. G. Bosilovich, S. D. Schubert, L. Takacs, and G.-K. Kim (2011), MERRA: NASA's modern-era retrospective analysis for research and applications, *J. Clim.*, *24*(14), 3624–3648.

Robock, A. (2000), Volcanic eruptions and climate, *Rev. Geophys.*, *38*(2), 191–219.

Rockström, J., W. Steffen, K. Noone, Å. Persson, F. S. Chapin III, E. F. Lambin, T. M. Lenton, M. Scheffer, C. Folke, and H. J. Schellnhuber (2009), A safe operating space for humanity, *Nature*, *461*(7263), 472.

Rodda, H. J. E. (2001), The development of a stochastic rainfall model for UK flood modelling, *Int. Kommission für die Hydrol. des Rheingebietes*, 107.

Rogelj, J., M. Den Elzen, N. Höhne, T. Fransen, H. Fekete, H. Winkler, R. Schaeffer, F. Sha, K. Riahi, and M. Meinshausen (2016a), Paris Agreement climate proposals need a boost to keep warming well below 2 C, *Nature*, *534*(7609), 631.

Rogelj, J., M. Den Elzen, T. Fransen, H. Fekete, H. Winkler, R. Schaeffer, F. Sha, K. Riahi, and M. Meinshausen (2016b), Perspective : Paris Agreement climate proposals need boost to keep warming well below 2 ° C, *Nat. Clim. Chang.*, *534*(June), 631–639, doi:10.1038/nature18307.

De Roo, A. P. J., C. G. Wesseling, and W. P. A. Van Deursen (2000), Physically based river basin modelling within a GIS: the LISFLOOD model, *Hydrol. Process.*, *14*(11-

12), 1981–1992.

Rübbelke, D., and S. Vögele (2011), Impacts of climate change on European critical infrastructures: the case of the power sector, *Environ. Sci. Policy*, *14*(1), 53–63.

Ruiter, A. (2012), Delta-change approach for CMIP5 GCMs. Internship Report, , 36.

Rummukainen, M. (2009), State-of-the-art with regional climate models, *Wiley Interdiscip. Rev. Clim. Chang.*, *1*(1), 82–96, doi:10.1002/wcc.8.

Rummukainen, M. (2010), State-of-the-art with regional climate models, *Wiley Interdiscip. Rev. Chang.*, *1*(1), 82–96, doi:10.1002/wcc.008.

Rutz, J. J., W. J. Steenburgh, and F. M. Ralph (2015), The Inland Penetration of Atmospheric Rivers over Western North America: A Lagrangian Analysis, *Mon. Weather Rev.*, *143*(5), 1924–1944, doi:10.1175/MWR-D-14-00288.1.

Saji, N. H., and T. Yamagata (2003), Possible impacts of Indian Ocean dipole mode events on global climate, *Clim. Res.*, *25*(2), 151–169.

Saji, N. H., B. N. Goswami, P. N. Vinayachandran, and T. Yamagata (1999), A dipole mode in the tropical Indian Ocean, *Nature*, *401*(6751), 360.

Sakai, D., H. Itoh, and S. Yukimoto (2009), Changes in the interannual surface air temperature variability in the Northern Hemisphere in response to global warming, *J. Meteorol. Soc. Japan. Ser. II*, *87*(4), 721–737.

Schellnhuber, H. J., S. Rahmstorf, and R. Winkelmann (2016), Why the right climate target was agreed in Paris, *Nat. Clim. Chang.*, *6*(7), 649–653, doi:10.1038/nclimate3013.

Schewe, J. et al. (2014a), Multimodel assessment of water scarcity under climate change, *Proc. Natl. Acad. Sci.*, *111*(9), 3245 LP-3250.

Schewe, J. et al. (2014b), Multimodel assessment of water scarcity under climate change., *Proc. Natl. Acad. Sci. U. S. A.*, *111*(9), 3245–50, doi:10.1073/pnas.1222460110.

Schleussner, C.-F. et al. (2016), Differential climate impacts for policy-relevant limits to global warming: the case of 1.5 °C and 2 °C, *Earth Syst. Dynam.*, *7*(2), 327–351,

doi:10.5194/esd-7-327-2016.

Schneider, U., M. Ziese, A. Meyer-Christoffer, P. Finger, E. Rustemeier, and A. Becker (2016), The new portfolio of global precipitation data products of the Global Precipitation Climatology Centre suitable to assess and quantify the global water cycle and resources, *Proc. IAHS*, *374*, 29–34, doi:10.5194/piahs-374-29-2016.

Schott, F. A., S. Xie, and J. P. McCreary (2009), Indian Ocean circulation and climate variability, *Rev. Geophys.*, *47*(1).

Sellers, P. J., J. A. Berry, G. J. Collatz, C. B. Field, and F. G. Hall (1992), Canopy reflectance, photosynthesis, and transpiration. III. A reanalysis using improved leaf models and a new canopy integration scheme., *Remote Sens. Environ.*, *42*(3), 187–216.

Semenov, M. A., and P. Stratonovitch (2010), Use of multi-model ensembles from global climate models for assessment of climate change impacts, *Clim. Res.*, *41*(1), 1–14.

Seneviratne, S. I., T. Corti, E. L. Davin, M. Hirschi, E. B. Jaeger, I. Lehner, B. Orlowsky, and A. J. Teuling (2010), Investigating soil moisture–climate interactions in a changing climate: A review, *Earth-Science Rev.*, *99*(3–4), 125–161, doi:http://dx.doi.org/10.1016/j.earscirev.2010.02.004.

Serreze, M. C. (2010), Understanding recent climate change., *Conserv. Biol.*, *24*(1), 10–17, doi:10.1111/j.1523-1739.2009.01408.x.

Serreze, M. C., D. H. Bromwich, M. P. Clark, A. J. Etringer, T. Zhang, and R. Lammers (2002), Large-scale hydro-climatology of the terrestrial Arctic drainage system, *J. Geophys. Res.*, *108*, doi:10.1029/2001JD000919.

Shao, X., S. Li, N. Liu, and J. Song (2018), The Madden–Julian oscillation during the 2016 summer and its possible impact on rainfall in China, *Int. J. Climatol.*, *38*(5), 2575–2589.

She, Y., and F. Hicks (2006), Modeling ice jam release waves with consideration for ice effects, *Cold Reg. Sci. Technol.*, *45*(3), 137–147.

Sheffield, J., and E. F. Wood (2011), *Drought: Past Problems and Future Scenarios*, Earthscan.

Shelton, M. (2009), *Hydroclimatology: Perspectives and Applications*, 1st ed., Cambridge University Press, New York, NY, USA.

Shen, H. T. (2010), Mathematical modeling of river ice processes, *Cold Reg. Sci. Technol.*, *62*(1), 3–13.

Shen, H. T., D. S. Wang, and A. M. W. Lal (1995), Numerical simulation of river ice processes, *J. Cold Reg. Eng.*, *9*(3), 107–118.

Shen, H. T., J. Su, and L. Liu (2000), SPH simulation of river ice dynamics, *J. Comput. Phys.*, *165*(2), 752–770.

Shiklomanov, I. A., A. I. Shiklomanov, R. B. Lammers, B. J. Peterson, and C. J. Vorosmarty (2000), The Dynamics of River Water Inflow to the Arctic Ocean, in *The Freshwater Budget of the Arctic Ocean SE - 13*, vol. 70, edited by E. Lewis, E. P. Jones, P. Lemke, T. Prowse, and P. Wadhams, pp. 281–296, Springer Netherlands.

Shimizu, M. H., T. Ambrizzi, and B. Liebmann (2017), Extreme precipitation events and their relationship with ENSO and MJO phases over northern South America, *Int. J. Climatol.*, *37*(6), 2977–2989.

Shindell, D., and G. Faluvegi (2009), Climate response to regional radiative forcing during the twentieth century, *Nat. Geosci.*, *2*(4), 294.

Shindell, D. T., G. A. Schmidt, R. L. Miller, and M. E. Mann (2003), Volcanic and solar forcing of climate change during the preindustrial era, *J. Clim.*, *16*(24), 4094–4107.

Shinoda, T., and W. Han (2005), Influence of the Indian Ocean dipole on atmospheric subseasonal variability, *J. Clim.*, *18*(18), 3891–3909.

Shorthouse, C. A., and N. W. Arnell (1997), Spatial and temporal variability in European river flows and the North Atlantic Oscillation, *IAHS Publ.*, *246*, 77–85.

Sigl, M., M. Winstrup, J. R. McConnell, K. C. Welten, G. Plunkett, F. Ludlow, U. Büntgen, M. Caffee, N. Chellman, and D. Dahl-Jensen (2015), Timing and climate

forcing of volcanic eruptions for the past 2,500 years, *Nature*, *523*(7562), 543.

Sillmann, J., V. V Kharin, F. W. Zwiers, X. Zhang, and D. Bronaugh (2013), Climate extremes indices in the CMIP5 multimodel ensemble: Part 2. Future climate projections, *J. Geophys. Res. Atmos.*, *118*(6), 2473–2493.

Simonovic, S. P. (2017), Bringing Future Climatic Change into Water Resources Management Practice Today, *Water Resour. Manag.*, *31*(10), 2933–2950, doi:10.1007/s11269-017-1704-8.

Sivapalan, M., G. Blöschl, L. Zhang, and R. Vertessy (2003), Downward approach to hydrological prediction, *Hydrol. Process.*, *17*(11), 2101–2111.

Slingo, M. J., R. D, S. K, and Nortley (2006), On the predictability of the interannual behaviour of the Madden-Julian oscillation and its relationship with el Niño, *Q. J. R. Meteorol. Soc.*, *125*(554), 583–609, doi:10.1002/qj.49712555411.

Smith, S. C., and D. Ubilava (2017), The El Niño Southern Oscillation and economic growth in the developing world, *Glob. Environ. Chang.*, *45*, 151–164.

Soden, B. J., and I. M. Held (2006), An assessment of climate feedbacks in coupled ocean–atmosphere models, *J. Clim.*, *19*(14), 3354–3360.

Solomon, S. (2007), *Climate change 2007-the physical science basis: Working group I contribution to the fourth assessment report of the IPCC*, Cambridge university press.

Sophocleous, M. (2002), Interactions between groundwater and surface water: the state of the science, *Hydrogeol. J.*, *10*(1), 52–67.

Sossa, A., B. Liebmann, I. Bladé, D. Allured, H. H. Hendon, P. Peterson, and A. Hoell (2017), Statistical connection between the Madden–Julian oscillation and large daily precipitation events in West Africa, *J. Clim.*, *30*(6), 1999–2010.

Sperna Weiland, F. C. (2011), Hydrological impacts of climate change: interpretation of uncertainties introduced by global models of climate and hydrology,

Stacke, T., and S. Hagemann (2012), Development and evaluation of a global dynamical wetlands extent scheme, *Hydrol. Earth Syst. Sci.*, *16*(8), 2915–2933,

doi:10.5194/hess-16-2915-2012.

Stainforth, D. a et al. (2005), Uncertainty in predictions of the climate response to rising levels of greenhouse gases., *Nature*, *433*(7024), 403–406, doi:10.1038/nature03301.

Stainforth, D. A., M. R. Allen, E. R. Tredger, and L. A. Smith (2007), Confidence, uncertainty and decision-support relevance in climate predictions, *Philos. Trans. R. Soc. London A Math. Phys. Eng. Sci.*, *365*(1857), 2145–2161.

Stensrud, D. J. (1996), Importance of low-level jets to climate: A review, *J. Clim.*, *9*(8), 1698–1711.

Stocker, T. F., D. Qin, G.-K. Plattner, L. V Alexander, S. K. Allen, N. L. Bindoff, F.-M. Bréon, J. A. Church, U. Cubasch, and S. Emori (2013), Technical summary, in *Climate change 2013: the physical science basis. Contribution of Working Group I to the Fifth Assessment Report of the Intergovernmental Panel on Climate Change*, pp. 33–115, Cambridge University Press.

Stohl, A., and P. James (2004), A Lagrangian analysis of the atmospheric branch of the global water cycle. Part I: Method description, validation, and demonstration for the August 2002 flooding in central Europe, *J. Hydrometeorol.*, *5*(4), 656–678.

von Storch, H., and F. W. Zwiers (1999), *Statistical Analysis in Climate Research*, 1st ed., Cambridge University Press, Cambridge, United Kingdom.

Sturm, M. (2015), White water: fifty years of snow research in WRR and the outlook for the future, *Water Resour. Res.*, *51*, 4948–4965, doi:10.1002/2015WR017242.Received.

Sultana, R., K.-L. Hsu, J. Li, and S. Sorooshian (2014), Evaluating the Utah Energy Balance (UEB) snow model in the Noah land-surface model, *Hydrol. Earth Syst. Sci.*, *18*(9), 3553–3570, doi:10.5194/hess-18-3553-2014.

Sun, C. (2004), A methodology for snow data assimilation in a land surface model, *J. Geophys. Res.*, *109*(D8), D08108, doi:10.1029/2003JD003765.

Sun, F., M. L. Roderick, and G. D. Farquhar (2012), Changes in the variability of global

land precipitation, *Geophys. Res. Lett.*, *39*(19).

Swapna, P., and M. R. RameshKumar (2002), Role of low level flow on the summer monsoon rainfall over the Indian subcontinent during two contrasting monsoon years,

Tallaksen, L. M., and K. Stahl (2014), Spatial and temporal patterns of large-scale droughts in Europe: Model dispersion and performance, *Geophys. Res. Lett.*, *41*(2), 429–434.

Taylor, K. E., R. J. Stouffer, and G. A. Meehl (2012), An overview of CMIP5 and the experiment design, *Bull. Am. Meteorol. Soc.*, *93*(4), 485–498.

Tebaldi, C. et al. (2007), The use of the multi-model ensemble in probabilistic climate projections., *Philos. Trans. A. Math. Phys. Eng. Sci.*, *365*(1857), 2053–75, doi:10.1098/rsta.2007.2076.

Tedesco, M., R. Kelly, J. L. Foester, and A. T. C. Chang. (2004), *AMSR-E/Aqua Daily L3 Global Snow Water Equivalent EASE-Grids. Version 2.*, Boulder, CO, USA.

Teng, J., J. Vaze, F. H. S. Chiew, B. Wang, and J.-M. Perraud (2012), Estimating the relative uncertainties sourced from GCMs and hydrological models in modeling climate change impact on runoff, *J. Hydrometeorol.*, *13*(1), 122–139.

Teutschbein, C., and J. Seibert (2012), Bias correction of regional climate model simulations for hydrological climate-change impact studies: Review and evaluation of different methods, *J. Hydrol.*, *456–457*, 12–29, doi:10.1016/j.jhydrol.2012.05.052.

The World Bank (2015), Electricity production from hydroelectric sources, Available from: https://data.worldbank.org/indicator/EG.ELC.HYRO.ZS

Thieken, A. H., H. Apel, and B. Merz (2015), Assessing the probability of large-scale flood loss events: a case study for the river Rhine, Germany, *J. Flood Risk Manag.*, *8*(3), 247–262.

Todini, E. (1988), Rainfall-runoff modeling — Past, present and future, *J. Hydrol.*, *100*(1), 341–352, doi:https://doi.org/10.1016/0022-1694(88)90191-6.

Tokinaga, H., and Y. Tanimoto (2004), Seasonal transition of SST anomalies in the

tropical Indian Ocean during El Niño and Indian Ocean dipole years, *J. Meteorol. Soc. Japan. Ser. II*, *82*(4), 1007–1018.

Tong, J., and I. Velicogna (2010), A comparison of AMSR-E/Aqua snow products with in situ observations and MODIS snow cover products in the Mackenzie River Basin, Canada, *Remote Sens.*, *2*(10), 2313–2322, doi:10.3390/rs2102313.

Trenberth, K. E. (2005), The Impact of Climate Change and Variability on Heavy Precipitation, Floods, and Droughts, *Encycl. Hydrol. Sci.*, 1–11, doi:10.1002/0470848944.hsa211.

Trenberth, K. E. (2011), Changes in precipitation with climate change, *Clim. Res.*, *47*(1/2), 123–138.

Trigo, R. M., D. Pozo-Vázquez, T. J. Osborn, Y. Castro-Díez, S. Gámiz-Fortis, and M. J. Esteban-Parra (2004), North Atlantic Oscillation influence on precipitation, river flow and water resources in the Iberian Peninsula, *Int. J. Climatol.*, *24*(8), 925–944.

Ukkola, A. M., and I. C. Prentice (2013), A worldwide analysis of trends in water-balance evapotranspiration, , 4177–4187, doi:10.5194/hess-17-4177-2013.

Ukkola, A. M., A. J. Pitman, M. Decker, M. G. De Kauwe, G. Abramowitz, J. Kala, and Y.-P. Wang (2016), Modelling evapotranspiration during precipitation deficits: identifying critical processes in a land surface model, *Hydrol. Earth Syst. Sci.*, *20*(6), 2403–2419.

Ummenhofer, C., M. England, P. McIntosh, G. Meyers, M. Pook, J. Risbey, A. Gupta, and A. Taschetto (2009), What causes southeast Australia's worst droughts?, *Geophys. Res. Lett.*, *36*(4), doi:10.1029/2008GL036801.

Vavrus, S. (2007), The role of terrestrial snow cover in the climate system, *Clim. Dyn.*, *29*(January), 73–88, doi:10.1007/s00382-007-0226-0.

Vera, C., J. Baez, M. Douglas, C. B. Emmanuel, J. Marengo, J. Meitin, M. Nicolini, J. Nogues-Paegle, J. Paegle, and O. Penalba (2006), The South American low-level jet experiment, *Bull. Am. Meteorol. Soc.*, *87*(1), 63–77.

Viale, M., and M. N. Nuñez (2011), Climatology of winter orographic precipitation over the subtropical central Andes and associated synoptic and regional characteristics, *J. Hydrometeorol.*, *12*(4), 481–507, doi:10.1175/2010JHM1284.1.

Viles, H. A., and A. S. Goudie (2003), Interannual, decadal and multidecadal scale climatic variability and geomorphology, *Earth-Science Rev.*, *61*(1–2), 105–131, doi:10.1016/S0012-8252(02)00113-7.

Vinayachandran, P. N., P. A. Francis, and S. A. Rao (2009), Indian Ocean dipole: processes and impacts, *Curr. trends Sci.*, 569–589.

Visbeck, M. H., J. W. Hurrell, L. Polvani, and H. M. Cullen (2001), The North Atlantic Oscillation: past, present, and future, *Proc. Natl. Acad. Sci.*, *98*(23), 12876–12877.

van Vliet, M. T. H., J. Sheffield, D. Wiberg, and E. F. Wood (2016a), Impacts of recent drought and warm years on water resources and electricity supply worldwide, *Environ. Res. Lett.*, *11*(12), 124021.

van Vliet, M. T. H., D. Wiberg, S. Leduc, and K. Riahi (2016b), Power-generation system vulnerability and adaptation to changes in climate and water resources, *Nat. Clim. Chang.*, *6*(January), 375–380, doi:10.1038/nclimate2903.

Van Vliet, M. T. H., L. P. H. van Beek, S. Eisner, M. Flörke, Y. Wada, and M. F. P. Bierkens (2016), Multi-model assessment of global hydropower and cooling water discharge potential under climate change, *Glob. Environ. Chang.*, *40*, 156–170.

Vorogushyn, S., P. D. Bates, K. de Bruijn, A. Castellarin, H. Kreibich, S. Priest, K. Schröter, S. Bagli, G. Blöschl, and A. Domeneghetti (2018), Evolutionary leap in large-scale flood risk assessment needed, *Wiley Interdiscip. Rev. Water*, *5*(2), e1266.

Vörösmarty, C. J., and B. Moore (1991), Modeling basin-scale hydrology in support of physical climate and global biogeochemical studies: An example using the Zambezi River, *Surv. Geophys.*, *12*(1–3), 271–311.

Vörösmarty, C. J., C. A. Federer, and A. L. Schloss (1998), Potential evaporation functions compared on US watersheds: Possible implications for global-scale water balance

and terrestrial ecosystem modeling, *J. Hydrol.*, *207*(3–4), 147–169.

Vörösmarty, C. J. et al. (2010), Global threats to human water security and river biodiversity., *Nature*, *467*(7315), 555–561, doi:10.1038/nature09549.

van Vuuren, D. P. et al. (2011), The representative concentration pathways: an overview, *Clim. Change*, *109*(1), 5, doi:10.1007/s10584-011-0148-z.

Wagener, T., M. Sivapalan, P. A. Troch, B. L. McGlynn, C. J. Harman, H. V Gupta, P. Kumar, P. S. C. Rao, N. B. Basu, and J. S. Wilson (2010), The future of hydrology: An evolving science for a changing world, *Water Resour. Res.*, *46*(5).

Wake, B. (2013), Flooding costs, *Nat. Publ. Gr.*, *3*(9), 778, doi:10.1038/nclimate1997.

Waliser, D., and B. Guan (2017), Extreme winds and precipitation during landfall of atmospheric rivers, *Nat. Geosci*, *advance on*.

Walter, R. C., and D. J. Merritts (2008), Natural streams and the legacy of water-powered mills, *Science (80-.).*, *319*(5861), 299–304.

Wang, C. (2004), ENSO, Atlantic climate variability, and the Walker and Hadley circulations, in *The Hadley circulation: present, past and future*, pp. 173–202, Springer.

Wania, R. et al. (2013), Present state of global wetland extent and wetland methane modelling: methodology of a model inter-comparison project (WETCHIMP), *Geosci. Model Dev.*, *6*(3), 617–641, doi:10.5194/gmd-6-617-2013.

Wanner, H., S. Brönnimann, C. Casty, D. Gyalistras, J. Luterbacher, C. Schmutz, D. B. Stephenson, and E. Xoplaki (2001), North Atlantic Oscillation–concepts and studies, *Surv. Geophys.*, *22*(4), 321–381.

Ward, P., B. Jongman, F. Weiland, B. Bouwman, R. van Beek, M. Bierkens, W. Ligtvoet, and H. Winsemius (2013), Assessing flood risk at the global scale: model setup, results, and sensitivity, *Environ. Res. Lett.*, *8*(4), 44019.

Ward, P. J., S. Eisner, M. Flörke, M. D. Dettinger, and M. Kummu (2014), Annual flood sensitivities to El Niño–Southern Oscillation at the global scale, *Hydrol. Earth Syst.*

Sci., *18*(1), 47–66.

Ward, P. J., M. Kummu, and U. Lall (2016), Flood frequencies and durations and their response to El Niño Southern Oscillation: Global analysis, *J. Hydrol.*, *539*, 358–378, doi:https://doi.org/10.1016/j.jhydrol.2016.05.045.

Weedon, G. P., S. Gomes, P. Viterbo, W. J. Shuttleworth, E. Blyth, H. Österle, J. C. Adam, N. Bellouin, O. Boucher, and M. Best (2011), Creation of the WATCH Forcing Data and Its Use to Assess Global and Regional Reference Crop Evaporation over Land during the Twentieth Century, *J. Hydrometeorol.*, *12*(5), 823–848, doi:10.1175/2011JHM1369.1.

Weedon, G. P., G. Balsamo, N. Bellouin, S. Gomes, M. J. Best, and P. Viterbo (2014), The WFDEI meteorological forcing data set: WATCH Forcing Data methodology applied to ERA-Interim reanalysis data, *Water Resour. Res.*, *50*(9), 7505–7514, doi:10.1002/2014WR015638.

Weisheimer, a (2009), Decadal Variability: processes, predictability and prediction,

Weiss, M. I. (2015), A perfect storm: the causes and consequences of severe water scarcity, institutional breakdown and conflict in Yemen, *Water Int.*, *40*(2), 251–272, doi:10.1080/02508060.2015.1004898.

Whitehead, P. G., E. J. Wilson, D. Butterfield, and K. Seed (1998), A semi distributed nitrogen model for multiple source assessments in catchments (INCA): Part II—Application to large river basins in south Wales and eastern England, *Sci. Total Env.*, 210–211.

Whitfield, P. H., R. D. Moore, S. W. Fleming, and A. Zawadzki (2010), Pacific Decadal Oscillation and the hydroclimatology of western Canada—Review and prospects, *Can. Water Resour. J.*, *35*(1), 1–28.

Wick, G. A., P. J. Neiman, F. M. Ralph, and T. M. Hamill (2013), Evaluation of Forecasts of the Water Vapor Signature of Atmospheric Rivers in Operational Numerical Weather Prediction Models, *Weather Forecast.*, *28*(6), 1337–1352,

doi:10.1175/WAF-D-13-00025.1.

Wicks, J. M., C. Hu, M. Scott, L. Chen, and X. Cheng (2013), A broad scale model for flood simulation in the Taihu Basin, China, *J. Flood Risk Manag.*, *6*(1), 33–41.

Wilby, R. L., and C. W. Dawson (2013), The Statistical DownScaling Model: insights from one decade of application, *Int. J. Climatol.*, *33*(7), 1707–1719, doi:10.1002/joc.3544.

Wilby, R. L., and T. M. L. Wigley (1997), Downscaling general circulation model output: a review of methods and limitations, *Prog. Phys. Geogr.*, *21*(4), 530–548.

Wilby, R. L., C. W. Dawson, and E. M. Barrow (2002), SDSM—a decision support tool for the assessment of regional climate change impacts, *Environ. Model. Softw.*, *17*(2), 145–157.

Winsemius, H. C. et al. (2015), Global drivers of future river flood risk, , *6*, 381.

Wiscombe, W. J., and S. G. Warren (1980), A model for the spectral albedo of snow. I: Pure snow, *J. Atmos. Sci.*, *37*(12), 2712–2733.

Wisser, D., S. Frolking, E. M. Douglas, B. M. Fekete, A. H. Schumann, and C. J. Vörösmarty (2010), The significance of local water resources captured in small reservoirs for crop production–A global-scale analysis, *J. Hydrol.*, *384*(3–4), 264–275.

Wolock, D. M., and G. J. McCabe (1999), Estimates of Runoff Using Water-Balance and Atmospheric General Circulation Models, *JAWRA J. Am. Water Resour. Assoc.*, *35*(6), 1341–1350.

Wong, W. K., S. Beldring, T. Engen-Skaugen, I. Haddeland, and H. Hisdal (2011), Climate change effects on spatiotemporal patterns of hydroclimatological summer droughts in Norway, *J. Hydrometeorol.*, *12*(6), 1205–1220.

Wood, A. W., L. R. Leung, V. Sridhar, and D. P. Lettenmaier (2004), Hydrologic implications of dynamical and statistical approaches to downscaling climate model outputs, *Clim. Change*, *62*(1–3), 189–216.

Wood, E. F., J. K. Roundy, T. J. Troy, L. P. H. Van Beek, M. F. P. Bierkens, E. Blyth, A. de Roo, P. Döll, M. Ek, and J. Famiglietti (2011), Hyperresolution global land surface modeling: Meeting a grand challenge for monitoring Earth's terrestrial water, *Water Resour. Res.*, *47*(5).

World Economic Forum (2018), *Global Risks Report 2018*, Geneva.

Xu, C.-Y., and V. P. Singh (2004), Review on regional water resources assessment models under stationary and changing climate, *Water Resour. Manag.*, *18*(6), 591–612.

Yadav, R. K. (2013), Emerging role of Indian ocean on Indian northeast monsoon, *Clim. Dyn.*, *41*(1), 105–116, doi:10.1007/s00382-012-1637-0.

Yamazaki, D., S. Kanae, H. Kim, and T. Oki (2011), A physically based description of floodplain inundation dynamics in a global river routing model, *Water Resour. Res.*, *47*(4), 1–21, doi:10.1029/2010WR009726.

Yamazaki, D., G. A. M. Almeida, and P. D. Bates (2013), Improving computational efficiency in global river models by implementing the local inertial flow equation and a vector-based river network map, *Water Resour. Res.*, *49*(11), 7221–7235, doi:10.1002/wrcr.20552.

Yamazaki, D., T. Sato, S. Kanae, Y. Hirabayashi, and P. D. Bates (2014), Regional flood dynamics in a bifurcating mega delta simulated in a global river model, *Geophys. Res. Lett.*, *41*(9), 3127–3135, doi:10.1002/2014GL059744.

Yang, D., C. Li, H. Hu, Z. Lei, S. Yang, T. Kusuda, T. Koike, and K. Musiake (2004a), Analysis of water resources variability in the Yellow River of China during the last half century using historical data, *Water Resour. Res.*, *40*(6), n/a-n/a, doi:10.1029/2003WR002763.

Yang, D., B. Ye, and A. Shiklomanov (2004b), Discharge Characteristics and Changes over the Ob River Watershed in Siberia, *J. Hydrometeorol.*, *5*(4), 595–610, doi:10.1175/1525-7541(2004)005<0595:DCACOT>2.0.CO;2.

Yang, J., P. Gong, R. Fu, M. Zhang, J. Chen, S. Liang, B. Xu, J. Shi, and R. Dickinson

(2013), The role of satellite remote sensing in climate change studies, *Nat. Clim. Chang.*, *3*(10), 875.

Ye, H., H. Cho, and P. E. Gustafson (1998), The Changes in Russian Winter Snow Accumulation during 1936 – 83 and Its Spatial Patterns, *J. Clim.*, *11*, 856–863, doi:10.1175/1520-0442(1998)011<0856:TCIRWS>2.0.CO;2.

Yevjevich, V. M. (1967), An objective approach to definitions and investigations of continental hydrologic droughts, *Hydrol. Pap. (Colorado State Univ. no. 23*.

Yossef, N. C., L. P. H. Van Beek, J. C. J. Kwadijk, and M. F. P. Bierkens (2012), Assessment of the potential forecasting skill of a global hydrological model in reproducing the occurrence of monthly flow extremes, *Hydrol. Earth Syst. Sci.*, *16*(11), 4233.

Yossef, N. C., H. Winsemius, A. Weerts, R. Beek, and M. F. P. Bierkens (2013), Skill of a global seasonal streamflow forecasting system, relative roles of initial conditions and meteorological forcing, *Water Resour. Res.*, *49*(8), 4687–4699.

Yuan, Y., H. Yang, W. Zhou, and C. Li (2008), Influences of the Indian Ocean dipole on the Asian summer monsoon in the following year, *Int. J. Climatol.*, *28*(14), 1849–1859.

Zaitchik, B. F., M. Rodell, and F. Olivera (2010), Evaluation of the Global Land Data Assimilation System using global river discharge data and a source-to-sink routing scheme, *Water Resour. Res.*, *46*(6).

Zarfl, C., A. E. Lumsdon, J. Berlekamp, L. Tydecks, and K. Tockner (2015), A global boom in hydropower dam construction, *Aquat. Sci.*, *77*(1), 161–170.

Zelenhasić, E., and A. Salvai (1987), A method of streamflow drought analysis, *Water Resour. Res.*, *23*(1), 156–168.

Zhang, R., and T. L. Delworth (2007), Impact of the Atlantic multidecadal oscillation on North Pacific climate variability, *Geophys. Res. Lett.*, *34*(23).

Zhang, Y., J. M. Wallace, and D. S. Battisti (1997), ENSO-like interdecadal variability:

1900–93, *J. Clim.*, *10*(5), 1004–1020.

Zhang, Y., S. Liu, and Y. Ding (2006), Observed degree-day factors and their spatial variation on glaciers in western China, *Ann. Glaciol.*, *43*, 301–306.

Zhou, T., B. Nijssen, H. Gao, and D. P. Lettenmaier (2016), The contribution of reservoirs to global land surface water storage variations, *J. Hydrometeorol.*, *17*(1), 309–325.

Zhou, Y., M. Hejazi, S. Smith, J. Edmonds, H. Li, L. Clarke, K. Calvin, and A. Thomson (2015), A comprehensive view of global potential for hydro-generated electricity, *Energy Environ. Sci.*, *8*(9), 2622–2633.

Zhu, C., T. Nakazawa, J. Li, and L. Chen (2003), The 30–60 day intraseasonal oscillation over the western North Pacific Ocean and its impacts on summer flooding in China during 1998, *Geophys. Res. Lett.*, *30*(18).

Zhu, Y., and R. E. Newell (1998), A Proposed Algorithm for Moisture Fluxes from Atmospheric Rivers, *Mon. Weather Rev.*, *126*(3), 725–735, doi:https://doi.org/10.1175/1520-0493(1998)126<0725:APAFMF>2.0.CO;2.

Zubair, L., S. A. Rao, and T. Yamagata (2003), Modulation of Sri Lankan Maha rainfall by the Indian Ocean dipole, *Geophys. Res. Lett.*, *30*(2).